Airfoil Self-Noise Prediction Using Neural Networks for Wind Turbines

Leonardo Antonio Errasquin

Thesis submitted to the Faculty of the Virginia Polytechnic Institute and State University in partial fulfillment of the requirements for the degree of

Master of Science
In
Mechanical Engineering

Dr. Ricardo A. Burdisso, Chair
Dr. William J. Devenport
Dr. Martin E. Johnson

September 10, 2009
Blacksburg, Virginia

Keywords: Noise, airfoil, neural network, wind turbine.

Airfoil Self-Noise Prediction Using Neural Networks for Wind Turbines

Leonardo Antonio Errasquin

Abstract

A neural network prediction method has been developed to compute self-noise of airfoils typically used in wind turbines. The neural networks were trained using experimental data corresponding to tests of several different airfoils over a range of flow conditions. The experimental data corresponds to the NACA 0012, Delft DU96, Sandia S831, S822 and S834, Fx63-137, SG6043 and SD-2030 airfoils. The chord of these airfoils range from 0.025 to 0.91 m and they were tested at Reynolds numbers of up to 3.8 million and angle of attack up to 15^o depending on the airfoil. Using experimental data corresponding to different airfoils provides to the neural network the capacity to take into account the geometry of the airfoils in the predictions. The input parameters to the network are the flow speed, chord length, effective angle of attack and parameters describing the geometrical shape of the airfoil. In addition, boundary layer displacement thickness was used for some models. The parameters used for taking into account the airfoil's geometry are based on a conformal mapping method or a polynomial approximation. The output of the neural network is given by sound pressure level in $1/3^{rd}$ octave bands for nine frequencies ranging from 630 to 4000 Hz.

The present work constitutes an application of neural networks to aeroacoustics. The main objective was to assess the potential of using neural networks to model airfoil noise. Therefore, this work is focused in the modeling of the problem, and no mathematical analyses about neural networks are intended. To this end, several models were investigated both in terms of the configuration and training approach. The performance of the networks was evaluated for a range of flow conditions. The neural network technique was first investigated for the NACA 0012 airfoil only. For this case, the geometry of the airfoil was not incorporated as input into the model. The neural network approach was then extended to account for airfoils of any geometry by including data from all airfoils in the training.

The results show that the neural networks are capable of predicting the airfoils self-noise reasonably well for most of the flow conditions. The broadband noise due to the turbulent boundary layer interacting with the trailing edge is estimated very well. The tonal vortex shedding noise due to laminar boundary layer-trailing edge interaction is not predicted as well, most likely due to the limited data available for this noise source. In summary, the research here demonstrated the potential of the neural network as a tool to predict noise from typical wind turbine airfoils.

Acknowledgement

I would like to start expressing my gratitude to Dr. Ricardo Burdisso, Professor in the Mechanical Engineering department, Virginia Tech, who has been my advisor since the beginning of my graduate studies. His guidance and support allowed me to develop my research skills and autonomy. The present work would not have been possible without his patience and respectful suggestions.

I also wish to express my appreciation to Dr. William Devenport of the Aerospace and Ocean Engineering department, Virginia Tech and Dr. Marty Johnson of the Mechanical Engineering department, Virginia Tech, who integrated my committee. They made many valuable suggestions and gave constructive advice.

Kind acknowledgements are extended to the National Renewable Energy Laboratory (NREL) that provided the data corresponding to the NLR tests and founded the VT tests. The collaboration of Dr. Pat Moriarty who provided the code NAFNoise is also gratefully acknowledged. In addition, my appreciation goes to Dr. Mark Drela for making of public access his code XFOIL.

Facing this challenging project was possible because of the solid background in mechanical engineering obtained during my undergraduate studies at the National University of Rio Cuarto, Argentina. My gratitude goes to the professors and faculty of this institution whose vocation and dedication inspired me. I specially thank to professors Leonardo Molisani, Sergio Preidikman and Julio Massa who helped me to start my masters program.

Many friends have provided help and support. My appreciation goes to all my fellow graduate students of the Vibrations and Acoustics Laboratory, Virginia Tech. I am especially indebted to Mr. Ryan Haac for his friendship and help. I am also grateful to Mr. Marcel Remillieux who provided me of valuable guidance based on his rich experience and knowledge. In addition, I kindly thank to Mr. Cristian Gebhardt for his constant support and encouragement.

Finally, I want to thank to my family. This thesis would not have been possible without their help and support.

Table of contents

List of figures

List of tables

1. Introduction

During the last two decades, the technology of large wind turbine generators has seen considerable development. This technological development in combination with the increase in the cost of other sources of energy has made wind energy generation one of the world's fastest growing energy sectors as attested by the statistics shown in Figures 1.1 and 1.2 (Wind power targets for Europe: 75,000 MW by 2010, 2003). The growth of wind energy projects has been very significant and it will be even higher in the coming years (Onat and Canbazoglu, 2007).

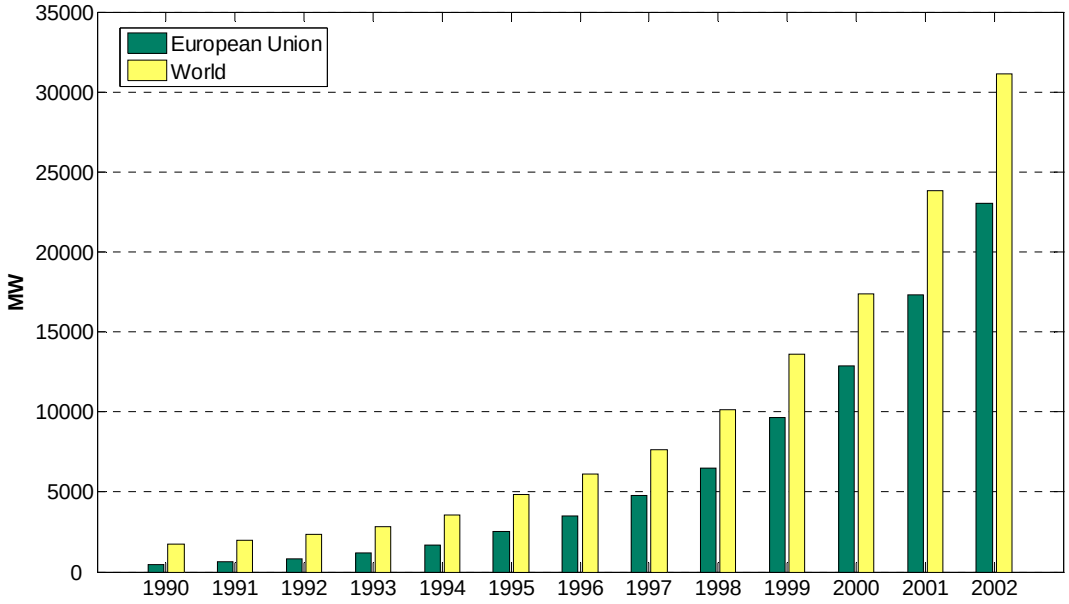

Figure 1.1: *Evolution of the cumulative wind power installed capacity in the European union and in the world during the period 1990-2002. Magnitudes given in MWatts. ('Wind power targets for Europe: 75,000 MW by 2010', 2003).*

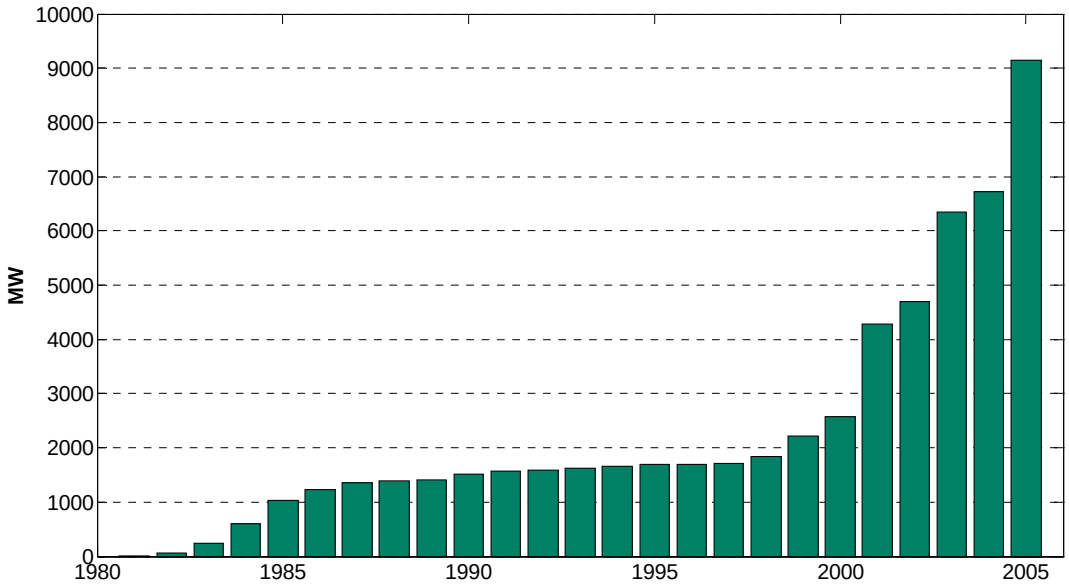

Figure 1.2: *Growth in the wind power capacity in the United States during the period 1981- 2005. Magnitudes given in MWatts. ('United States market sets new horizons', 2006).*

The wind power targets set by the industry and by the European commission during the last decade have all been exceeded. The European Wind Energy Association has set new targets for the European Union (EU) to have installed 75 GW for 2010 and 180 for 2020 as shown in Figures 1.3 and 1.4 (Wind power targets for Europe: 75,000 MW by 2010, 2003). These targets are 25% higher than the ones decided in 2000 and about 50% higher than the targets established in 1997 (Figure 1.2). Furthermore, it is forecasted a higher installed capacity than the target for 2010 (van den Berg, 2004.). This growth implies the potential investment of 49 billon Euros for the 2010 target and savings of 109 million ton of green house gases per year (Wind power targets for Europe: 75,000 MW by 2010, 2003).

With regard to the United States, a significant growth is also forecasted. By 2010, the cumulative installed capacity is expected to reach 28 GW. This means a significant increase considering the 12 GW of installed capacity in 2006 (United States market sets new horizons, 2006).

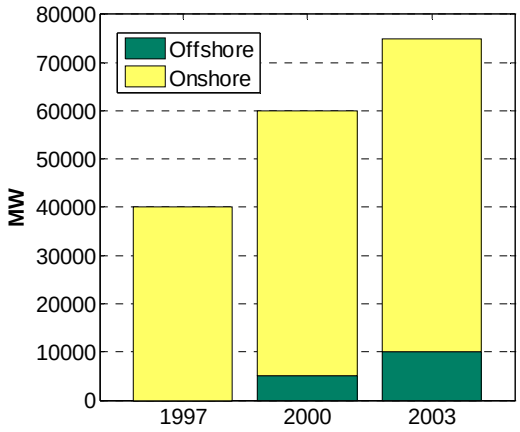

Figure 1.3: *Targets of installed capacity in the European Union established for 2010 by European Wind Energy Association. Magnitudes given in MWatts. ('Wind power targets for Europe: 75,000 MW by 2010', 2003).*

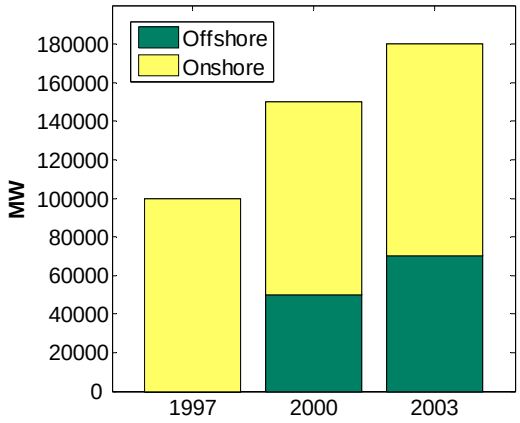

Figure 1.4: *Targets of installed capacity in the European Union established for 2020 by European Wind Energy Association. Magnitudes given in MWatts. ('Wind power targets for Europe: 75,000 MW by 2010', 2003).*

Unfortunately, wind generation projects resulted in adverse community reactions. These reactions where usually associated with the visual impact (Johansson and Laike, 2007), noise emission (van den Berg, 2004; Wind power brings prosperity, anger, 2008), and birds population's mortality (Drewitt and Langston, 2006). Noise emission is considered the most important problem in wind farms located in populated areas (van den Berg, 2004). Consequently, the growth of wind energy installed power, especially in regions with a high population density such as Europe, can be hindered by the noise emissions. In some cases, complaints have been documented from residences located more than two kilometers away from a wind generator (Shepherd and Hubbard, 1991). Furthermore, the low frequency component of the noise emitted can excite resonances associated with walls and windows in buildings increasing the annoyance of the acoustic phenomena (Shepherd and Hubbard, 1991). This is an important problem considering that installing wind farms at a large distance from populated areas greatly reduces the generation potential of a region.

The noise emitted by wind generators is basically produced in the mechanical components inside the nacelle and through the interaction of the blades with the flow, i.e. aerodynamic sources. During the last few years, the mechanical noise produced inside the

nacelle has been successfully controlled. Therefore, the aerodynamic noise sources are the main problem for large wind turbines. Thus, the prediction and reduction of noise due to aerodynamic phenomena is of main importance.

1.1 Literature review

Noise generation in wind turbines has been widely studied within the last decades and the bibliography available about the subject is extensive. According to the bibliography, the aerodynamic noise mechanisms present during the operation of a wind generator can be divided in two groups: Low frequency noise and Broadband noise (Voutsinas, 1995).

The generation of low frequency noise (harmonic impulsive aerodynamic noise) by wind turbines is analogous to noise generated by propellers, compressors, and rotors, except the blades are much larger and rotate at much lower speed. The rotating blades encounter localized flow deficiencies due to either atmospheric inflow gradients or the wake of the tower (Blade-Tower Interaction). Acoustic pulses arise from rapidly changing aerodynamic loads on the blades as they traverse the regions of disturbed flow. The periodic repetition of these pulses produces the characteristic harmonic noise (Shepherd and Hubbard, 1991). All the studies performed in recent years demonstrated that if the fluctuating pressures can be predicted from an aerodynamic model, then the acoustic field can be accurately simulated. Thus, the problem of low frequency noise prediction involves an accurate estimation of the fluctuating aerodynamic pressures on the blades (Voutsinas, 1995).

The broadband noise is caused by self-induced noise and turbulent inflow noise. The term self induced noise describes the noise due to the motion of the rotor blade through the air independent of other interactions and ignoring the local accelerations due to the rotary motion. Thus, the noise radiation process for any blade section becomes identical to that of an airfoil in a uniform flow. In this case, the main mechanisms that produce noise are direct radiation by the attached boundary layer on the blade, scattering of the turbulence in the boundary layer with the trailing edge, noise from separated flow on the blade (separation stall noise and tip noise), and

radiation due to trailing edge instabilities in quasi-discrete frequencies. This last source consists of laminar boundary layer vortex shedding noise and trailing edge bluntness noise (Voutsinas, 1995).

In the past, the prediction of noise emitted by wind turbines was limited to relating noise measured experimentally to the corresponding wind speed or output power of the wind generator. This rough method was provably the first tool available for predicting noise in wind turbines, and it is still used in some engineering standards (Lowson and Bullmore, 1996).

In 1981, Brooks and Hodgson conducted an extensive research about trailing edge noise supported with experimental measurements. The tests were performed in an open jet wind tunnel with anechoic treatment. The experiments explored the effect of the shape of the trailing edge by the addition of supplements, allowing the comparison of results for a sharp trailing edge to several different blunt edges. A noise prediction method was developed based on measurements of surface pressure. These predictions were successfully compared with the noise measurements corresponding to the tests from which the pressure measurements were obtained. Moreover, the half baffled dipole type directivity model (Meecham et al., 1981.) was successfully contrasted to experimental results, proving its validity.

The aforementioned noise mechanisms are very difficult to predict theoretically. However, Brooks et al. (1989) developed a semi-empirical method based on wind tunnel measurements of NACA 0012 airfoils that has been applied and compared to experimental measurements with good agreement (Voutsinas, 1995). The semi-empirical method has been incorporated into a code for predicting the noise emitted by a wind generator. To this end, a three-dimensional inviscid analysis of the flow interacting with the wind turbine was preformed comprising the velocity distributions along the span of the blades as well as the equivalent two-dimensional angles of attack. The blades were discretized along the span, and with the aerodynamic data of each discretized section, the semi-empirical formulas were applied to calculate the noise produced. Then, all the contributions of the sections were summed assuming they were uncorrelated.

During the last two decades, the semi-empirical method developed by Brooks et al. (1989) has been used in most of the attempts to predict the noise emitted by wind turbines (Voutsinas, 1995; Fuglsang and Madsen, 1996; Moriarty and Migliore, 2003; Leloudas et al., 2007; Herr, 2005; 2007a and 2007b). In general, the predictions compared reasonably well with experimental results (Voutsinas, 1995). Furthermore, some authors consider it as the best tool available to predict self induced noise (Leloudas et al., 2007). In 2007, Herr compared the semi-empirical predictions with experiments made with an airfoil of geometry similar to a NACA 0012 of 40 cm chord (Herr, 2005; 2007a and 2007b). The predictions showed good agreement with experiments in terms of the spectral shape and difference in the levels of only 3 dB. The predictions were implemented using the code NAFNoise developed by Moriarty (2005).

Though these semi-empirical formulas have proven to be an acceptable method to be applied to wind turbines, in some cases it has been reported to give inaccurate results. In the work of Leloudas et al. (2007), a systematic problem was found associated with the prediction of blunt trailing edge noise for frequencies above 3 kHz. In the work of Moriarty and Migliore (2003), the predictions were compared to wind tunnel test data of 20 cm chord airfoils (NACA 0012 and S822). The results for the NACA 0012 were reported not to be very accurate for relatively low Reynolds numbers. In the case of the S822 airfoil, poor agreement between predictions and experimental data was reported in general. One possible reason for this discrepancy was assumed to be that in the prediction code the boundary layer thickness was empirically modeled from NACA 0012 data. Therefore it was incorrectly predicted for the S822 airfoil. In fact, Fuglsang and Madsen (1996) argued that the method of Brooks et al. (1989) should be limited to airfoils similar to the NACA 0012.

Recently, a new turbulent boundary layer trailing-edge noise model was presented by Moriarty et al. (2004 and 2005). This model is more complex than the semi-empirical method developed by Brooks et al. (1989). The model uses boundary layer parameters to estimate the trailing edge noise on both sides of a given airfoil. These parameters are calculated by a boundary layer prediction routine, XFOIL (A brief description of XFOIL is presented in Appendix B). The predictions were contrasted with experiments and with predictions using the method developed by Brooks et al. (1989). It was reported that the new prediction method

provided the same accuracy than Brooks et al. (1989) and in some cases it was slightly better. (Moriarty et al., 2005).

In the work performed by Herr (2005, 2007a and 2007b), some scaling laws used for predicting trailing edge noise were analyzed. He concluded that the test data provided some evidence that the boundary-layer displacement thickness used by Brooks et al. (1989) does not represent the most relevant scaling parameter for noise spectra prediction. Noise levels were shown to scale with Strouthal number based on a constant reference length. On the other hand, in the work of Brooks et al. (1989), the Strouthal number scaling is based on variable boundary layer parameters.

The semi-empirical formulas developed by Brooks et al. (1989) for predicting laminar boundary layer vortex shedding bounds the range in which the vortex shedding is present. For 0^o angle of attack, it was assumed that vortex shedding occurs up to chord Reynolds numbers of $6x10^5$. Nevertheless, Devenport et al. (2008a and 2008b) and Paterson (1973) clearly proved that vortex shedding occurs at Reynolds numbers higher than the upper bounds assumed by Brooks et al. (1989). Consequently, Brooks et al (1989) fail in predicting laminar boundary layer vortex shedding at high Reynolds numbers.

Prediction of noise is important during the design process of a wind turbine to asses if noise regulations are met. As an example of noise legislation, the Wisconsin's draft model ordinance limits the wind energy facility sound levels to a maximum sound pressure level of 50 dBA at noise sensitive receptors (e.g. residences), and it sets the limit for tonal sounds at 45 dBA. This ordinance even sets a definition for tonal sound (Barnes and Gomez, 2007). Furthermore, new studies are being performed that could lead to more stringent noise regulations An example of these studies is the assessment of the impact of tonal noise in the perception by human beings performed by Mckenzie (1996).

In the work presented by Brooks et al. (1989), the formulas were developed using experimental data obtained from wind tunnel tests of NACA 0012 airfoils of up to 0.3 m of chord and moderate Reynolds numbers (from $5x10^4$ to $2x10^6$). But, in modern large wind

turbines other airfoils are used. Furthermore, chords of more than 2 m are common leading to Reynolds numbers considerably larger than $2x10^6$. Therefore, when attempting to predict broadband noise in modern wind generators, the semi empirical formulas are used outside the range of the data used to develop them. As a result, a lower accuracy could be expected.

Finally, it is important to consider that modern large wind turbine blades are composed by a region in which the airfoil's shapes have large blunt trailing edges. This region is located in the transition between the circular sections of the root and the typical aerodynamic sections of the rest of the blade. Figure 1.5 shows a picture of this transition region. It is expected that the noise contribution of these sections would not be important due to the relatively low flow speeds in this region close to the hub. Nevertheless, the method developed by Brooks et al (1989) would not be the proper tool if an analysis taking in account the contribution from the transition region of the blade was desired.

Property of LMS

Figure 1.5: *Root region of a modern large wind turbine's blade. It can be observed the region in which the airfoil's shapes used have large blunt trailing edges. This region is located in the transition between the circular sections of the root and the typical aerodynamic sections of the rest of the blade. (Used with permission of Jack Mowry, Editor, Sound & Vibrations Magazine, March 2008 and LMS international)*

Therefore, the semi-empirical formulas need to be improved in order to be more accurate for high Reynolds numbers and airfoils other than the NACA 0012. Moreover, a laminar boundary layer vortex shedding predicting method capable to be applicable for relatively large chord Reynolds numbers is required. These improvements would give more accurate results when trying to predict the broadband noise emitted by large wind turbines.

After the publication of the work of Brooks et al. (1989), several wind tunnel aeroacoustic experiments were performed. These experiments provide a more complete source of information to be used in improving the predictions. In 2004, Oerlemans reported tests of 6 different airfoils of potential use in wind turbines (Oerlemans, 2004). In 2007, Herr reported experiments for a 40 cm chord airfoil of geometric shape close to the NACA 0012 airfoil for several flow conditions (Herr, 2007a and 2007b). Finally, Devenport et al. (2008a and 2008b) conducted an extensive set of experiments for several airfoils of 0.9 m chord at high Reynolds numbers (Devenport, 2008a and 2008b).

1.2 Thesis Objectives

Currently, the semi-empirical approach developed by Brooks et al. (1989) is the "engineering" state of the art approach to predict wind turbine noise. However, the method needs to be improved for the analysis of modern large wind turbines.

In this thesis, it was intended to develop a new method to predict the self noise of airfoils typically used in wind turbines. The tool was expected to be able to predict the noise emitted by airfoils of any geometrical shape for different chord length and flow conditions. Furthermore, the method should be capable of being applied to different airfoil's geometries. To this end, a neural network predictive tool based on experimental data was developed. This method constitutes a new approach in the prediction of self noise in airfoils.

The neural network tool was trained using experimental measurements of airfoil self noise. The airfoils considered were the NACA 0012, Delft DU96, DU97-W300, Sandia S831,

S822 and S834, Fx63-137, SG6043 and SD 2030. Except for the NACA0012, these airfoils are commonly used in the wind energy industry. The reason for considering these airfoils was the availability of aeroacoustic experimental data. To take into account the influence of the geometry of the airfoils in the neural network training, two different parameterization approaches were assessed. The first method is based in a conformal mapping technique and the second is based in polynomial approximation of the surface of the airfoils.

Finally, the modeling accuracy of the implemented self-noise prediction method was assessed by comparing predictions and experimental data for the complete database.

1.3 Thesis organization

This thesis is organized in six chapters and four appendices. **Chapter 1** is an introduction to the problem studied and a comprehensive literature review on wind generator's airfoil noise mechanisms and prediction. In addition, the objectives of this study are presented. **Chapter 2** describes the self noise mechanisms responsible for sound emission in wind turbine blades. Then, the semi-empirical method developed by Books et al. (1989) is described and analyzed in depth. **Chapter 3** presents the experimental results used in this work. **Chapter 4** presents the implementation of a neural networks method. **Chapter 5** presents the main conclusions of the present work. **Chapter 6** discusses recommendations for future work. **Appendix A** presents the nomenclature associated with the geometrical shape of an airfoil and definitions of aerodynamic concepts applied in the present thesis. **Appendix B** presents a brief description of the software XFOIL and predictions made with it. **Appendix C** presents figures showing the results of applying a conformal mapping method to approximate the airfoils shape. **Appendix D** presents figures showing comparisons between predictions obtained with the neural network tool developed and the corresponding experimental data. In addition, it presents comparisons between predictions obtained with Brooks et al. (1989) method and the corresponding experimental data.

2 A review of the prediction tool of Brooks et al. (1989)

As indicated in the previous chapter, self-noise modeling is still in the early stages, and a successful theoretically based prediction tool is still years away. Therefore, the semi-empirical approach developed by Brooks et al. (1989) is essentially the main tool currently used for predictions. This prediction tool is reviewed here because it provides useful insight on the self-noise mechanisms and scaling characteristics. Brooks et al. (1989) performed aero-dynamical and acoustic measurements for a set of NACA 0012 airfoils of different chord for different flow speeds and angles of attack. These tests are described in chapter 3. The set of measurements resulted in a group of spectral scaling formulas for the calculation of the noise generated by an airfoil. In addition, in order to have a complete understanding of the noise generated by airfoils, it is important to study the radiation directivity characteristics. This is very important for the understanding of the noise directivity of wind generators. Therefore, this chapter also analyzes the radiation directivity of airfoils.

2.1 Airfoil Self-Noise Mechanisms

Airfoil self-noise consists of five mechanisms that are briefly described in the next sub-sections.

2.1.1 Turbulent boundary layer- trailing edge noise (TBL-TE)

Airfoils develop a boundary layer over their surface and a transition from laminar to turbulent occurs at certain chord-wise position. When a turbulent boundary layer is developed over the surface, the eddies that compose it are inefficient sound sources. However, if there is a sharp edge in the vicinity, they will become more efficient sources as they scattered on the trailing edge. Thus, the trailing edge of an airfoil intensifies the noise level of the turbulences convecting along the airfoil. The aforementioned process is schematically depicted in Figure 2.1

Trailing edge noise is perceived by people as a swishing sound. It is of broadband nature having the peak frequency typically in the range of 500 to 1500 Hz depending on the airfoil. The TBL-TE noise will dominate in the high frequency region if the flow is attached over the rotor blade. The factors that most influence trailing edge noise are the convection speed of the eddies and the structure of the boundary layer turbulence close to the edge. The exact shape of the trailing-edge is thought to be of importance only for relatively high frequencies (Wagner et al., 1996).

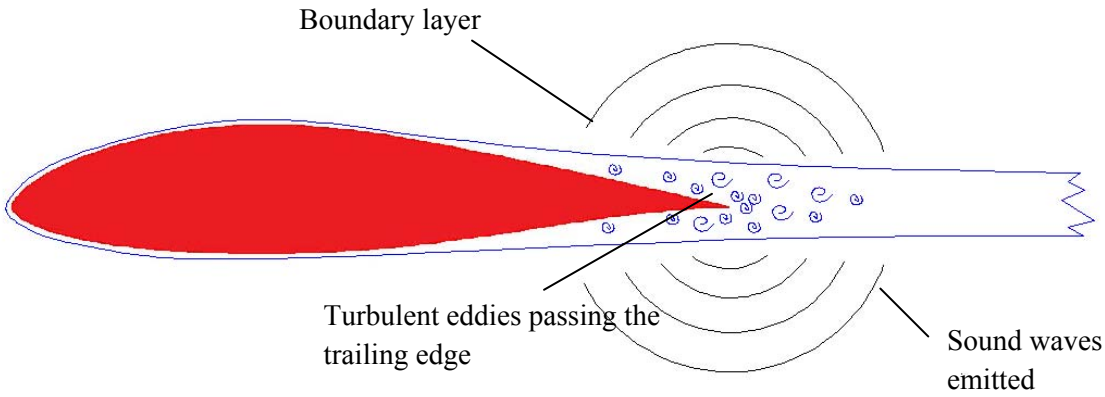

Figure 2.1: *Turbulent-boundary-layer—trailing-edge noise.*

2.1.2 Separated / stalled flow noise (S/SF)

This noise mechanism depends mainly on the angle of attack. As the angle of attack increases, stall conditions occur at a certain point causing a substantial level of unsteady flow around the airfoil. This phenomenon is represented in Figure 2.2.

In the work of Wagner et al. (1996), it is indicated that mildly separated flow causes sound radiation from the trailing edge, whereas deep stall causes radiation from the whole airfoil. Stalled flow noise is of broadband nature and is the only mayor contributing noise mechanism beyond limiting angles of attack.

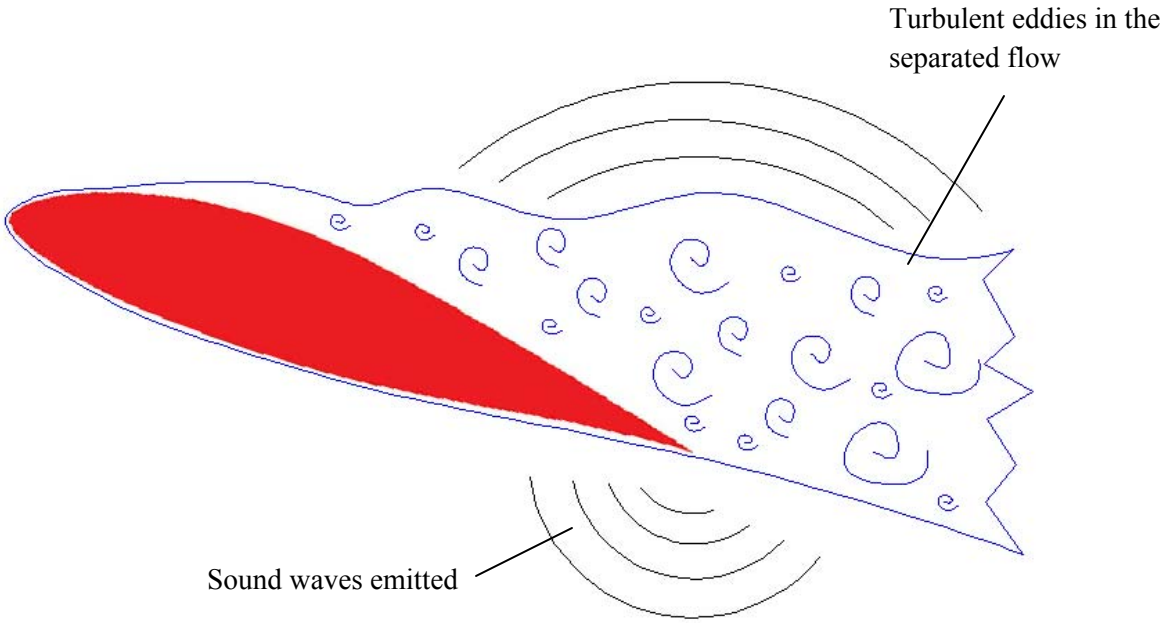

Figure 2.2: *Separated / stalled flow noise.*

2.1.3 Laminar boundary layer – vortex shedding noise (LBL-VS)

When an airfoil operates at relatively low Reynolds numbers, the laminar flow regions extend to the trailing edge. A resonant interaction of the trailing edge noise with the unstable laminar-turbulent transition can then occur. An upstream traveling acoustic wave couples with the instabilities resulting in tonal noise. The aforementioned instabilities can lead to separation bubbles generating noise. High levels of noise can occur if the instabilities are triggered by the acoustic field and vice versa (Wagner et al., 1996). This interaction is schematically represented in Figure 2.3. The LBL-VS noise is of tonal nature.

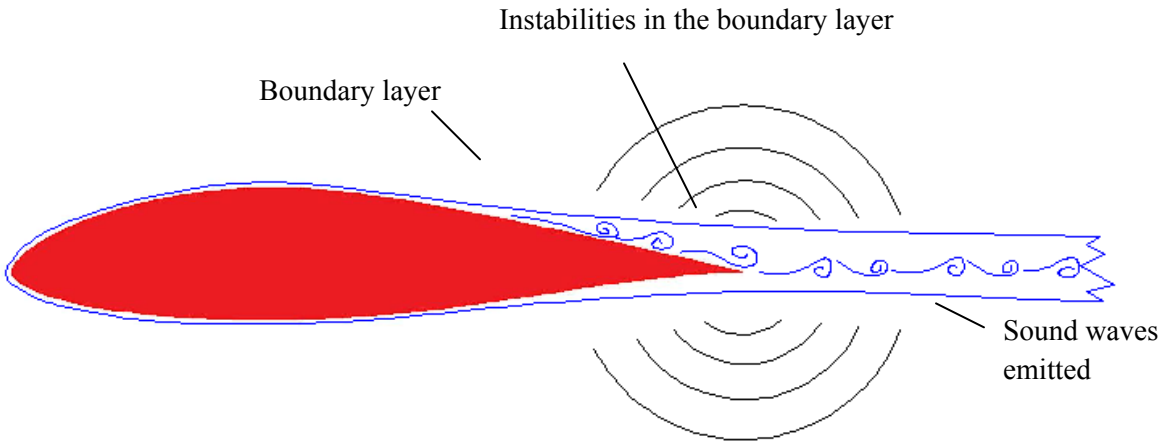

Figure 2.3: *Laminar-boundary-layer—vortex-shedding noise.*

2.1.4 Trailing edge bluntness – vortex shedding noise (TEB-VS)

This noise mechanism is based on the noise emission by von Karman type vortex shedding from the trailing edge. The shedding of vortices from the trailing edge depends on the bluntness, shape of the edge, and Reynolds number. The alternating vortices produces pressure fluctuations in the trailing edge zone as depicted in Figure 2.4. According to Wagner et al. (1996), a spike is present in the total noise spectra if the trailing edge thickness of the airfoil is higher than certain cut off value. This cut off value is specific for each airfoil and flow condition. The frequency of the spike originated depends on the flow conditions and the trailing edge thickness to displacement thickness ratio, b/δ^*. The smaller the trailing edge thickness to displacement thickness ratio the higher is the shedding frequency. Therefore, if the trailing edge is sharp enough, the spike will be displaced to high frequency region in which noise is not audible for humans.

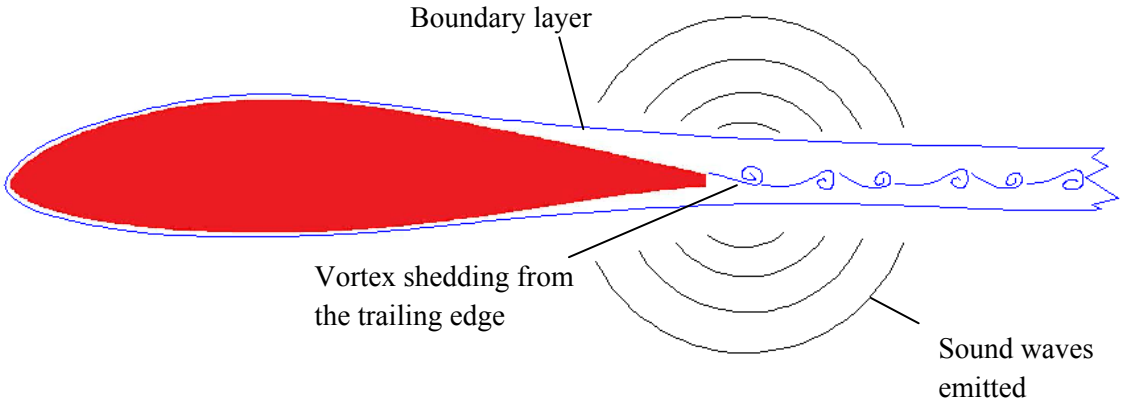

Figure 2.4: *Trailing-edge-bluntness—vortex-shedding noise.*

2.1.5 Tip vortex noise

At the tip of a blade, a vortex is generated due to the difference in pressure between the pressure and suction side. Brooks et al. (1989) suggested that this vortex interacts with the tip surface generating noise is analogous to the TBL-TE noise mechanism. This interaction is schematically represented in Figure 2.5.

Tip vortex noise is of broadband nature and it is assumed to be mostly influenced by the convective velocity of the vortex and its strength (Wagner et al., 1996).

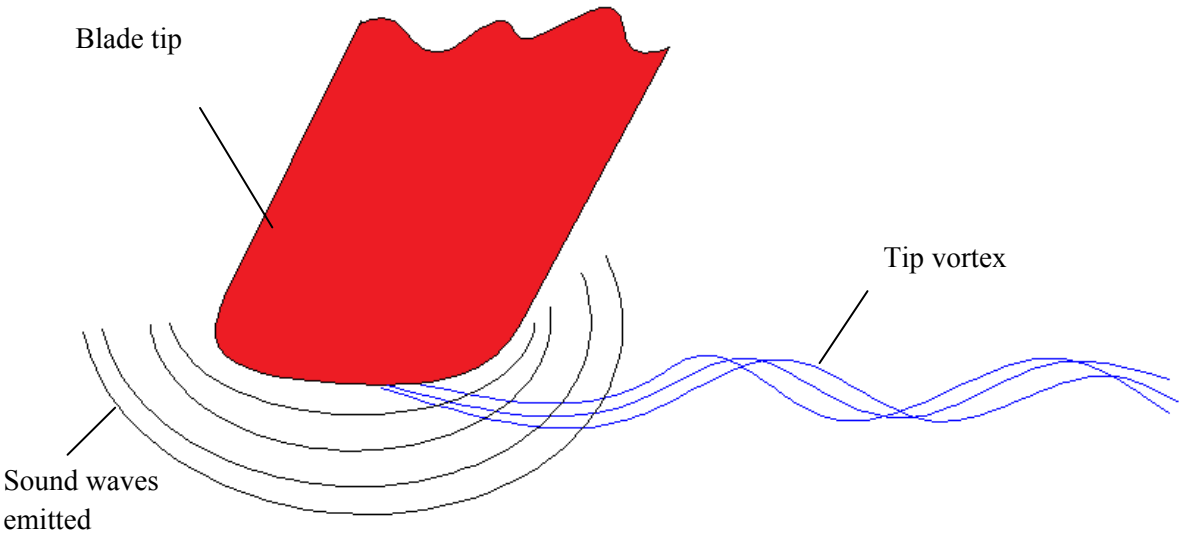

Figure 2.5: *Tip vortex formation noise.*

2.2 Directivity

An important aspect in the understanding of the noise emitted by wind turbines is the radiation directivity characteristics of trailing edge noise. This noise is usually modeled as a dipole source located at the trailing edge (Yildiz and Mawardi, 1960; Meecham W., Bui and Miller, 1981). If the acoustic wavelengths produced are much shorter than the chord length of the airfoil, then the trailing edge noise emission behaves as a baffled dipole. On the other hand, if the acoustic wavelengths are comparable to the airfoil's chord, then the noise emitted follows a pure dipole directivity behavior (Brooks et al., 1989). Nevertheless, these dipole-type directivities are influenced by the convective effect of the medium in which the airfoil is moving.

Equations describing the baffled-dipole and pure-dipole directivities were presented in the work of Brooks et al. (1989). These functions take in account the attenuation or amplification produced by the convective effect depending on the direction of propagation considered. The directivity function for the baffled-dipole directivity is

$$\bar{D}_h = \frac{2\sin^2\left(\frac{\theta_r}{2}\right)\sin^2\varphi_r}{\left(1+M\cos\theta_r\right)\left[1+\left(M-M_c\cos\theta_r\right)\right]^2} \tag{2.3}$$

where $M = U/c_o$ is the Mach number, U is the free stream velocity, M_c is the convection Mach number. The convection Mach number is based on the convection velocity of the turbulence present in the boundary layer with respect to the surface of the airfoil. In the work of Brooks et al. (1989), the convection Mach number was assumed to be equal to $0.8M$. The angles θ_r and φ_r defines the position of the observer as showed in Figure 2.6. Equation (2.3) is considered valid for high frequency noise when the wavelength is larger than the airfoil chord.

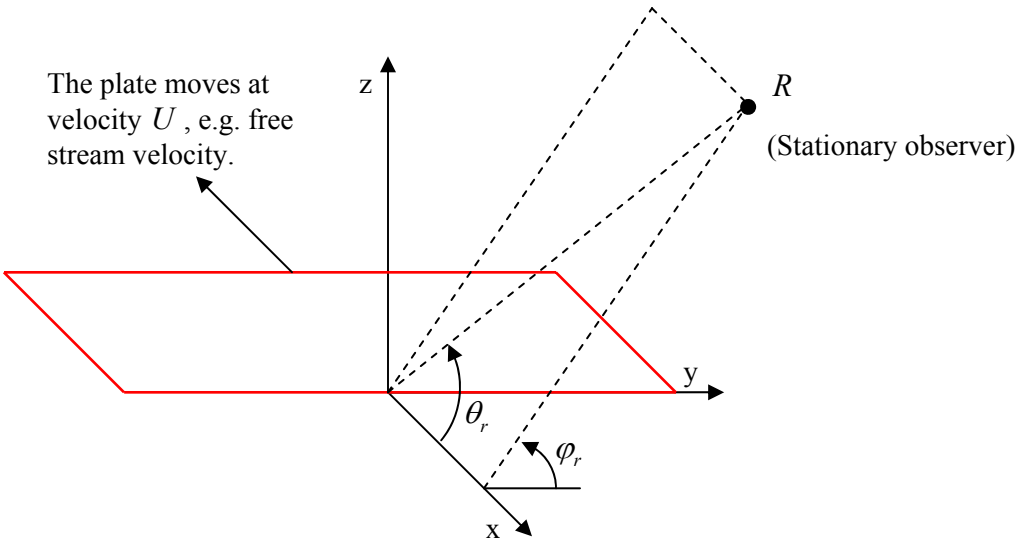

Figure 2.6: *Local coordinate system for a flat plate in rectilinear motion. Angles indicating the position of the retarded source (Retarded coordinates).*

When the airfoils chord and the wavelength are comparable, the noise directivity has a pure dipole behavior. The directivity function for this low frequency case is

$$\bar{D}_l = \frac{\sin^2\theta_r\sin^2\varphi_r}{\left(1+M\cos\theta_r\right)^4} \tag{2.2}$$

Figure 2.7 and 2.8 illustrate these directivity functions. Figures 2.9 and 2.10 illustrate the x-y and x-z cut view corresponding to figures 2.7 and 2.8, respectively.

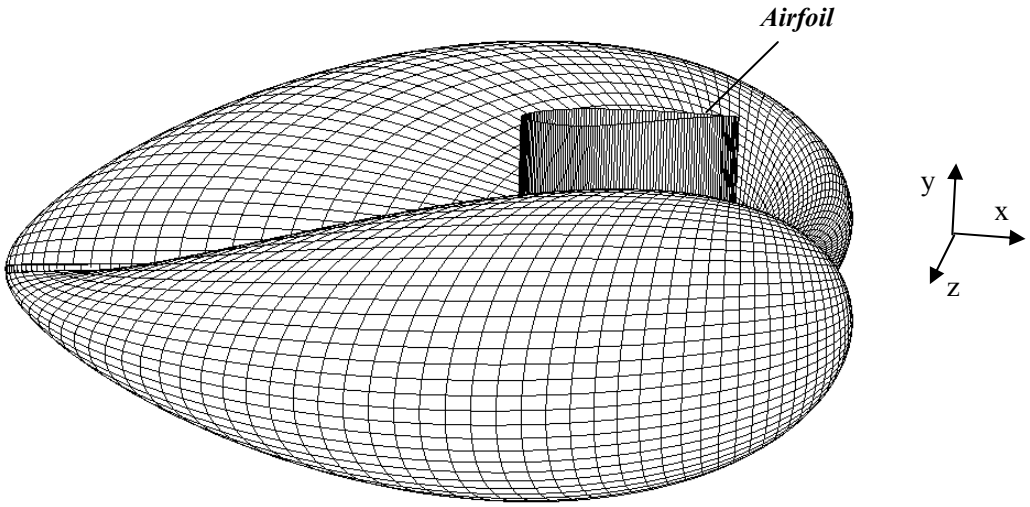

Figure 2.7: *Representation of the directivity function for the case of high frequency noise ($\bar{D}_f$).*

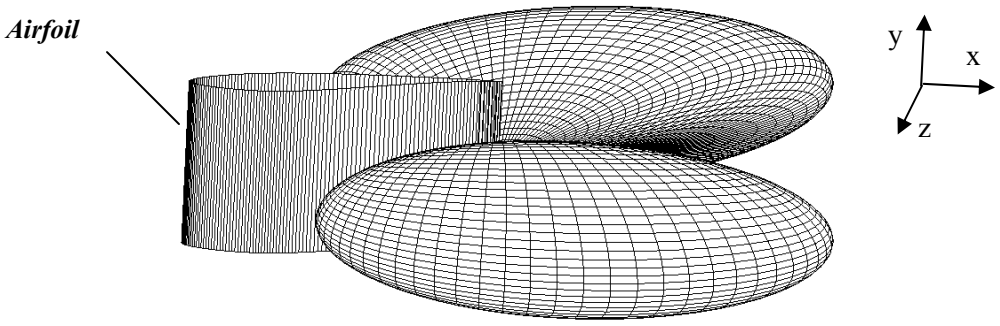

Figure 2.8: *Representation of the directivity for the case of low frequency noise ($\bar{D}_l$).*

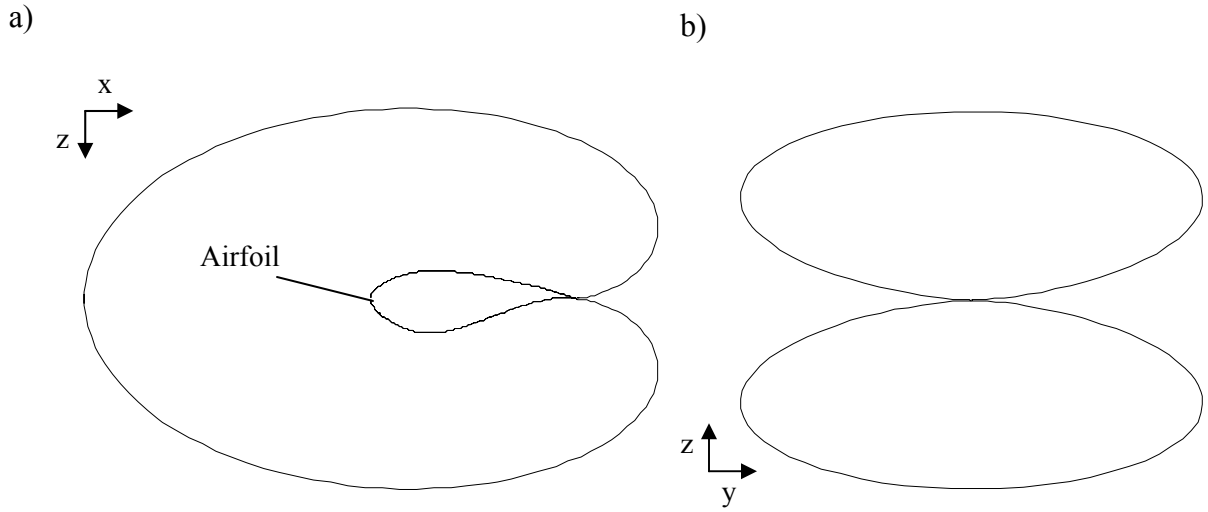

Figure 2.9: *Representation of the directivity for the case of high frequency noise ($\bar{D}_f$). a) x-z cut view. b) z-y cut view.*

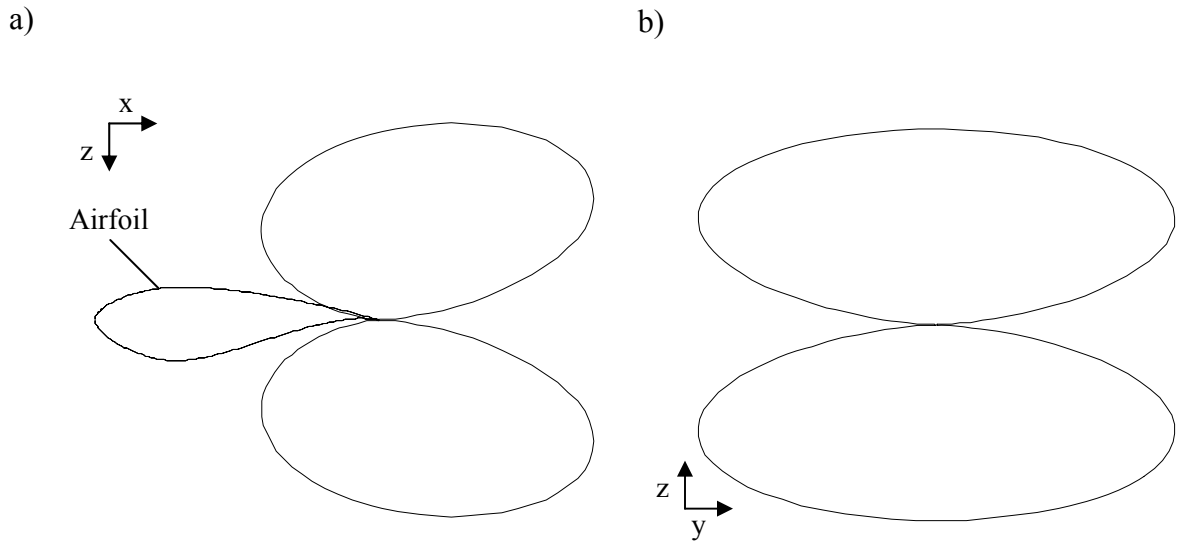

Figure 2.10: *Representation of the directivity for the case of low frequency noise ($\bar{D}_l$).a) x-z cut view. b) z-y cut view.*

2.3 Semi-empirical Predictions

As it was indicated previously, Brooks et al. (1989) developed semi-empirical formulas based on experiments performed with NACA 0012 airfoils. All five noise mechanisms were considered and formulas for each mechanism developed. The present section provides a description of the aforementioned work. It is important to mention that the predictions are in the form of 1/3rd octave bands in all cases.

The scaling method of Brooks et al. (1989) is based on the scattering from the trailing edge of a flat plate investigated by Ffowcs Williams and Hall (1970) and treated in a more general way by Blake (1986). They proposed the following law for the acoustic intensity of sound due to turbulent flow in the vicinity of a scattering flat plate

$$I \propto \rho_o c_o^3 M^5 \frac{sl}{r_r^2} \varepsilon^2 \tag{2.3}$$

where

ε : Normalized turbulence intensity.

r_r : Distance to the observer

ρ_o : Density of the air.

The parameters s and l describe the dimensions of the turbulent region in the plane perpendicular to the flow direction as depicted in Figure 2.11.

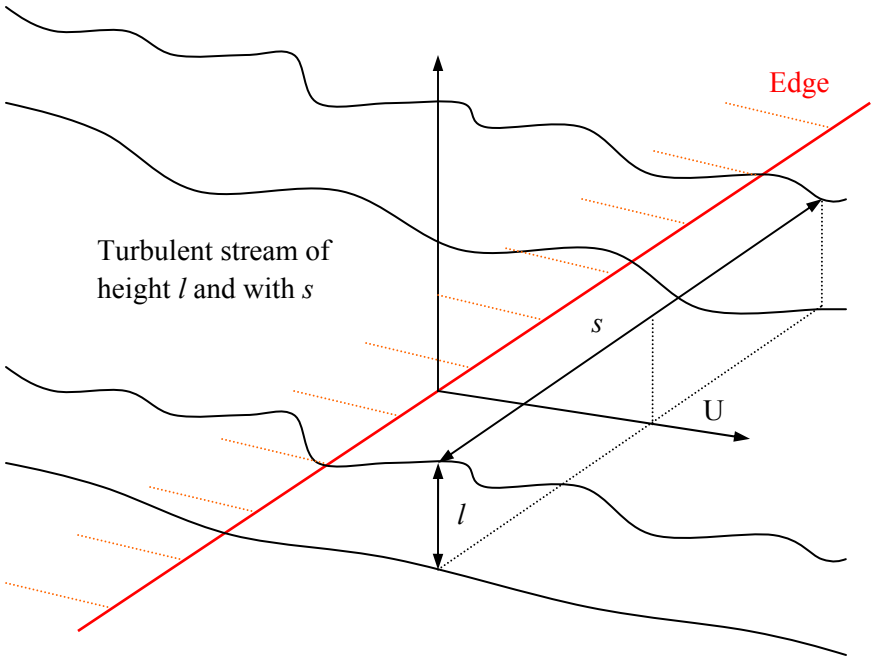

Figure 2.11: *Geometry used for the modeling of the interaction of turbulence with an edge.*

Equation (2.3) corresponds to the cases in which the predominant noise is emitted by eddies located close to the trailing edge. But in some cases, the turbulent boundary layer is wide enough for the noise produced by eddies located far away from the trailing edge to be important. For this case, the following relation was developed (Blake, 1986; Ffowcs Williams and Hall, 1970)

$$I \propto \rho_o c_o^3 M^8 \frac{sl}{r_r^2} \alpha^2 \tag{2.4}$$

It is important to consider that, in general, the boundary layer thickness δ or the boundary layer displacement thickness δ^* are used as a measure of l (Wagner et al., 1996). Furthermore, when this theory is applied to airfoils, s is replaced by the span length L of the

airfoil. When the length of the turbulent boundary layer, measured in the convection direction, is larger than $\frac{16}{\pi^4} M^{-3}\delta$, the effects modeled by equation (2.4) become important.

2.3.1 Turbulent boundary layer- trailing edge noise and separated / stalled flow noise

Turbulent boundary layer and S/SF noise were both assumed to be caused by turbulent effects. Therefore, the development of semi-empirical formulas describing these noise sources was based in the experimental results for tripped airfoils. Since separating the contributions of each noise mechanism is difficult, Brooks et al. (1989) approach was to model these noise mechanisms as a single one.

Brooks et al. (1989) proposed to separate the data to be normalized in two groups. The first normalization was applied to the cases corresponding to 0^o angle of attack and the second normalization was applied to the cases of angle of attack other than 0^o. Based on these normalizations, the following formula for modeling TBL-TE and S/SF noise was used

$$L_p^{TBL-TE\ /\ S/SF} = 10\log_{10}\left\{10^{L_p^s/10} + 10^{L_p^p/10} + 10^{L_p^\alpha/10}\right\}, \tag{2.5}$$

where L_p^s and L_p^p are the noise contributions of the pressure and suction sides of the normalized data corresponding to 0^o angle of attack, respectively. The contribution based on the normalized data corresponding to angles of attack other than 0^o is given by the third term L_p^α.

This equation is valid for angles of attack up to α_o, a cut off angle of attack for witch the transition from attached to stalled flow is supposed to occur. The value of this angle will be defined later in the present section. At angles above α_o, separation occur and therefore S/SF noise becomes dominant. Therefore, the terms corresponding to the 0^o degree of angle of attack in equation (2.5) become negligible.

Based on equation (2.3), the experimental data for 0^o angle of attack was normalized in amplitude as follows

$$L_p^{Scaled} = L_p^{Measured} - 10\log_{10}\left(\frac{\delta_o^* M^5 L}{r_r^2}\right). \tag{2.6}$$

where the boundary layer displacement thickness is noted as δ_o^*, e.g. same for pressure and suction sides due to symmetry. In addition, the frequency was normalized using the Strouthal number, St, based on the displacement thickness δ_o^*. That is

$$St = \frac{f\delta_o^*}{U}, \tag{2.7}$$

where f is the frequency.

The normalized noise spectra were found to coalesce to approximately the same spectral shape. This result is illustrated in the example presented in Figure 2.12 corresponding to a 30 cm chord airfoil at various flow speeds. It can also be noticed in Figure 2.12 that the scaled spectra present a maximum (indicated with markers) almost at the same Strouthal number for all cases. This value was denoted as Peak Strouthal Number, St_1.

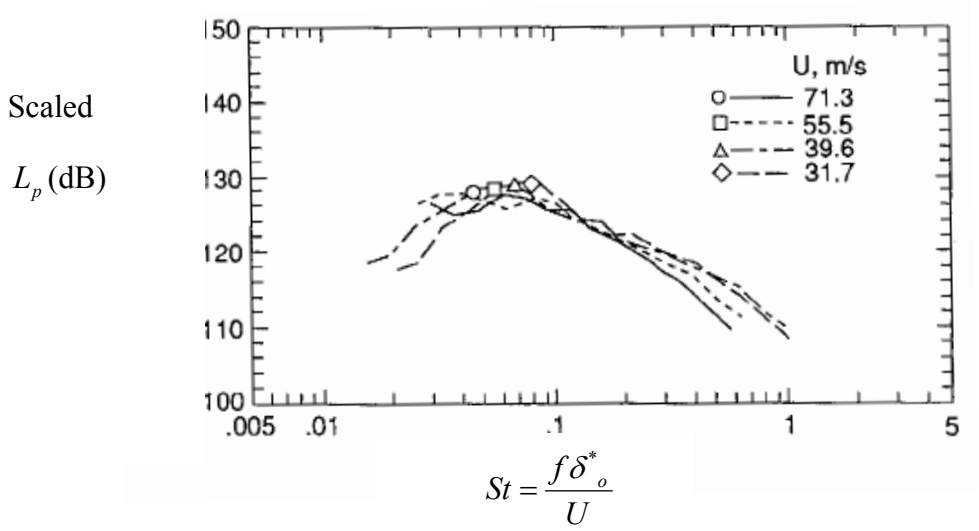

Figure 2.12: *Noise level* L_p^{Scaled} *normalized with respect to the Strouthal number. Peaks indicated with markers. The data corresponds to a 30 cm chord airfoil at* 0^o *angle of attack and different flow speeds. (Extracted from Brooks et al., 1989.)*

It was also found that the Peak Strouthal number St_1 didn't collapse with the chord Reynolds number, R_C. However, St_1 was found to have a dependency on the Mach number. This dependency is depicted in Figure 2.13 where peak Strouthal numbers are indicated for the corresponding chord Reynolds numbers. The horizontal lines indicate the Mach numbers for the 0^o angle of attack cases. The cases for the other angle of attack are showed for the sake of completeness. A relationship between St_1 and the Mach number was obtained as

$$St_1 = 0.02M^{-0.6} \tag{2.8}$$

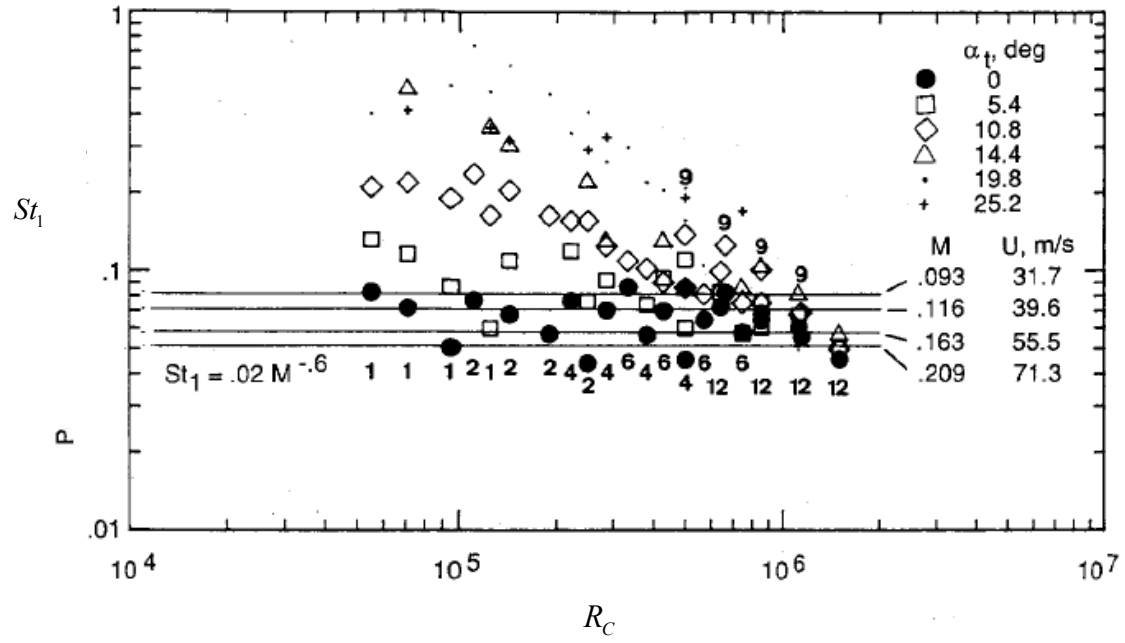

Figure 2.13: *Peak Strouthal number, St_1, vs. Reynolds number, R_c* for different values of M *. The numbers aligned with data are chord sizes in inches. (Extracted from Brooks et al., 1989.)*

Finally, the spectral level at the Peak Strouthal number was plotted as a function of the chord Reynolds number as shown in Figure 2.14. This figure shows a dependency of the peak level on the Reynolds number. This dependence was approximated by parts as shown by the solid lines denoted as the function $K_1(R_c)$. The results for angles of attack other than 0^o are again presented for the sake of completeness.

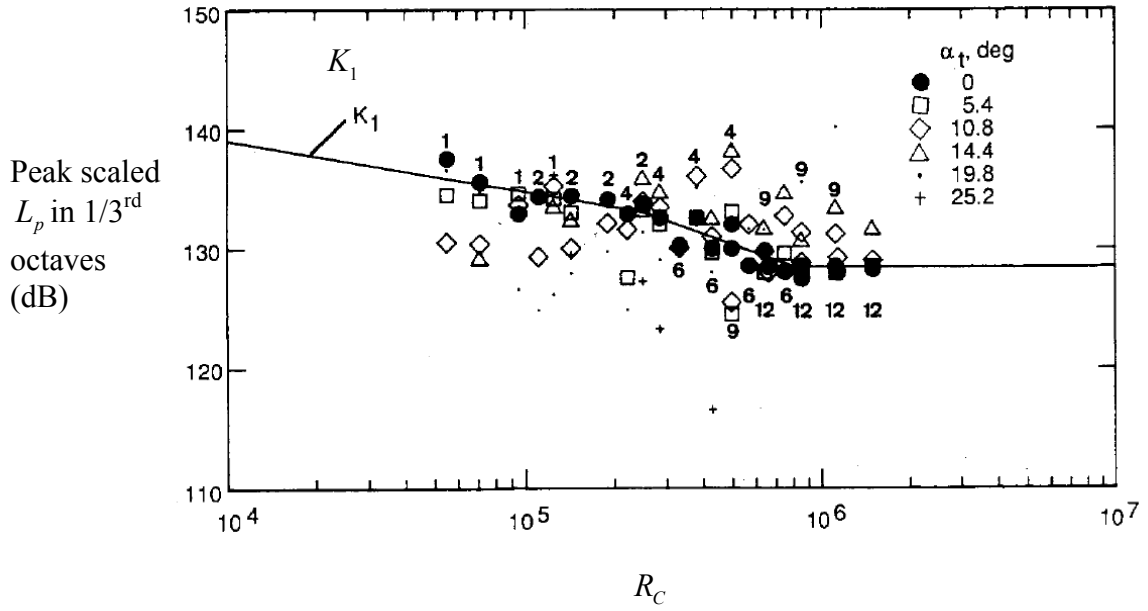

Figure 2.14: *Peak scaled L_p in 1/3rd octaves (function K_1) scaled with respect to the Chord Reynolds number for 0^o angle of attack. (Extracted from Brooks et al., 1989.)*

Finally, the noise corresponding to 0^o angle of attack that was scaled in equation (2.6) is subsequently scaled with respect to the ratio of the Strouthal number to the peak Strouthal number, St/St_1. From the previous scaling, all the cases coalesce to a spectral shape that dependent only on the chord Reynolds number. This spectral shape is represented by the function G_A. A representation of this function is shown in Figure 2.15. This function was defined for the maximum and minimum Reynolds numbers. Shapes for a specific Reynolds number should be interpolated. Numerical expressions for $G_{A\min}$ and $G_{A\max}$ are presented in page 60 of Brooks et al. (1989).

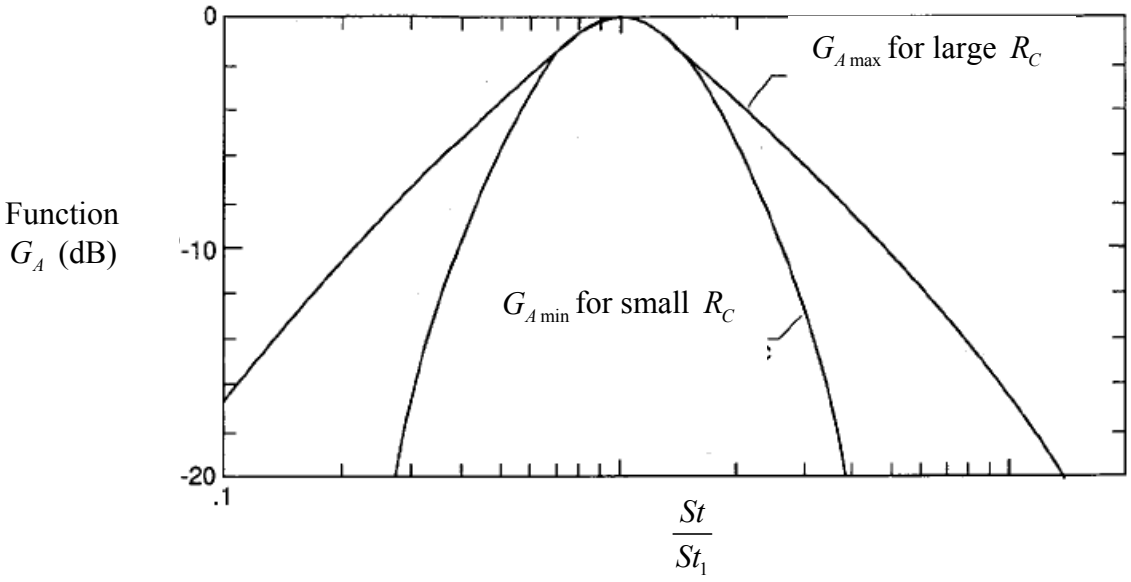

Figure 2.15: *Shape function G_A as a function of the scaled peak Strouthal number. (Extracted from Brooks et al., 1989.)*

The result of the previous normalizations is that the noise spectra for 0^o angle of attack can be separated into three terms as expressed in the following equations

$$L_p^s = 10\log_{10}\left(\frac{\delta^*_s M^5 L\,\bar{D}_h}{r_r^2}\right) + G_A\left(\frac{St_s}{St_1}\right) + \left(K_1\left(R_C\right) - 3\right) \tag{2.9}$$

and

$$L_p^p = 10\log_{10}\left(\frac{\delta^*_p M^5 L\,\bar{D}_h}{r_r^2}\right) + G_A\left(\frac{St_p}{St_1}\right) + \left(K_1\left(R_C\right) - 3\right) + \Delta K_1\left(R_{\delta_p^*}, \alpha\right) \tag{2.10}$$

for the suction and pressure sides, respectively, and with the Strouthal numbers given as

$$St_s = \frac{f\delta^*_s}{U},\ St_{\mathrm{p}} = \frac{f\delta^*_{\mathrm{p}}}{U} \tag{2.11 and 2.12}$$

In equations (2.9) and (2.10), the first term was generalized to be applied for angles of attack other than 0^o by replacing δ_o^* for δ_s^* and δ_p^* , e.g. the displacement thickness of the pressure and suction sides, respectively. The function $\overline{D}_h$ represents the directivity as presented in Section 2.2. The term expressed by the function G_A defining the spectral shape of this noise and the function K_1 indicating its levels. The subtraction of 3 dB is an adjustment of the noise level due to breaking the noise into pressure and suction side components from a single side component. According to the work of Brooks and Hodgson (1981), each side of an airfoil with well developed boundary layers produces noise independently, e.g. uncorrelated. In addition, the term ΔK_1 is an empirical level adjustment for the pressure-side contribution for non zero angles of attack. It is a function of the angle of attack and the Reynolds number based on the displacement thickness.

With regard to the experimental data corresponding to angles of attack other than 0^o , it was also normalized in amplitude based on equation (2.3) as follows

$$L_p^{Scaled} = L_p^{Measured} - 10\log_{10}\left(\frac{\delta_s^* M^5 L}{r_r^2}\right). \tag{2.13}$$

where the boundary layer displacement thickness corresponding to the suction side is noted as δ_s^*. In addition, the frequency was normalized using the Strouthal number, S_t, based on the displacement thickness δ_s^*. That is

$$St = \frac{f\delta_s^*}{U} \tag{2.14}$$

The normalized noise spectra were again found to coalesce to approximately the same spectral shape. This result is illustrated in the example presented in Figure 2.16 corresponding to a 30 cm chord airfoil at various angles of attack. It can also be noticed in Figure 2.16 that the scaled spectra present a maximum (indicated with markers) almost at the same Strouthal Number

for all cases. This value was denoted as Peak Strouthal number, St_2, e.g. for angles of attack other than 0^o.

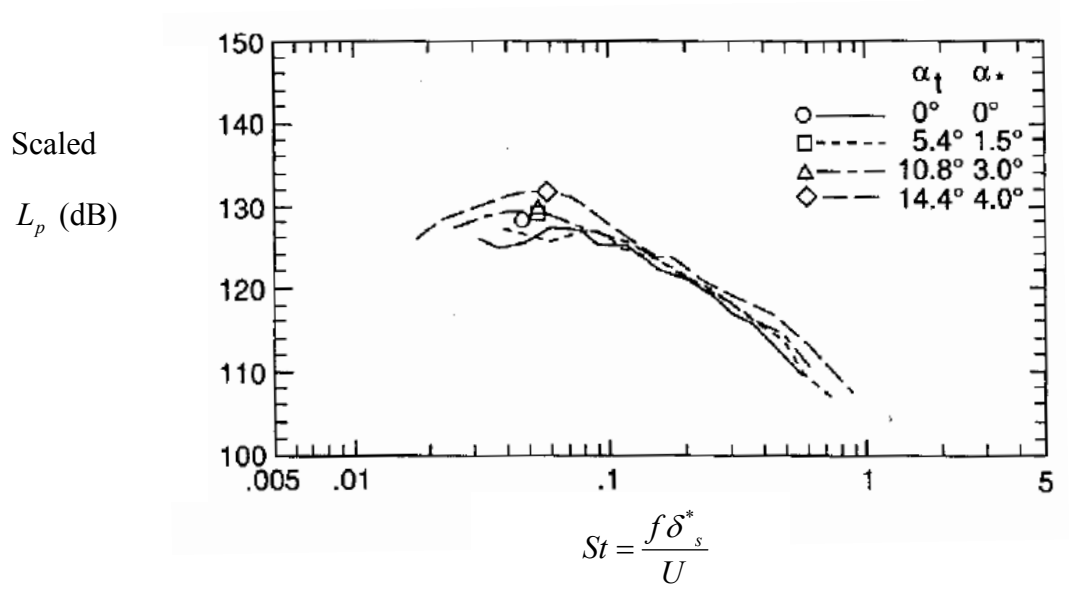

Figure 2.16: *Scaled L_p normalized with respect to the Strouthal number. The data corresponds to a 30 cm chord airfoil submerged in a flow with a free stream velocity of 71 m/s and different angles of attack. (Extracted from Brooks et al., 1989.)*

When St_2 is represented versus the angle of attack, a dependency on the Mach number was once again observed. This dependency is depicted in Figure 2.17 where peak Strouthal numbers are indicated for the corresponding angles of attack. The horizontal lines approximate the trend follower by the peak Strouthal numbers corresponding to the same Mach number. The peak Strouthal number St_2 was then expressed in terms of the Mach number, angle of attack, and St_1 as follows

$$St_2 = St_1 \begin{cases} 1 & (\alpha < 1.33^o) \\ 10^{0.0054(\alpha - 1.33)^2} & (1.33^o < \alpha < 12.5^o) \\ 4.72 & (\alpha > 12.5^o) \end{cases} \qquad (2.15)$$

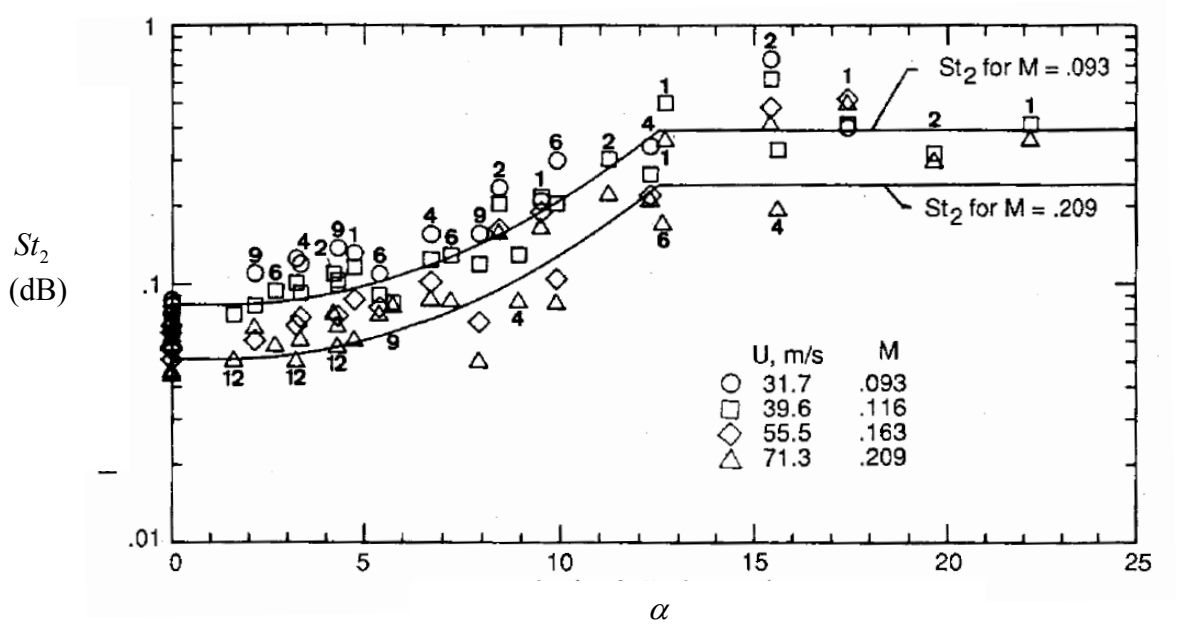

Figure 2.17: *Peak Strouthal number, St_2, versus angle of attack α for different values of M (Mach number). (Extracted from Brooks et al., 1989.)*

Finally, the spectral level at the Peak Strouthal number was plotted as a function of the angle of attack as shown in Figure 2.18. In this figure, the dependency the spectral level was normalized with respect to the previously calculated K_1 in order to eliminate the dependency on the Reynolds number. In Figure 2.18, it can be observed that the scaled spectral level at the Peak Strouthal number presents a dependency on the Mach number. This dependency was accounted for using the function $K_2(K_1, M, \alpha)$. The use of the function K_1 summarizes the dependency of K_2 on the Reynolds number. This is depicted in Figure 2.18 where the curves approximating K_2-K_1 for different Mach numbers are showed. This dependency was represented by the equation given in page 62 of Brooks et al. (1989).

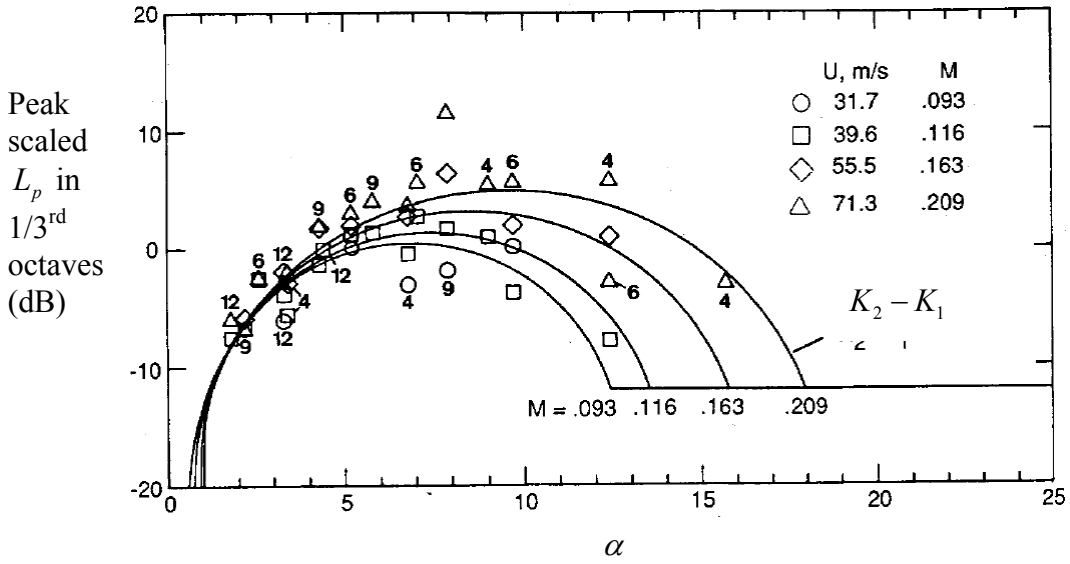

Figure 2.18: *Peak scaled L_p in 1/3rd octaves (function K_2) scaled with respect to the angle of attack and expressed as a function of K_1. (Extracted from Brooks et al., 1989.)*

As done before, the noise corresponding to angles of attack other than 0^o that was scaled in equation (2.13) is subsequently scaled with respect to the ratio St/St_2. The result of the previous scalings, all the cases collapse to a spectral shape that is a function of the chord based Reynolds number. This shape is represented by the function G_B as shown in Figure 2.19. Two functions are shown corresponding to the two limits for Reynolds numbers. Shapes for a specific Reynolds number should be interpolated. Numerical expressions for $G_{B\min}$ and $G_{B\max}$ are presented in page 61 of Brooks et al. (1989).

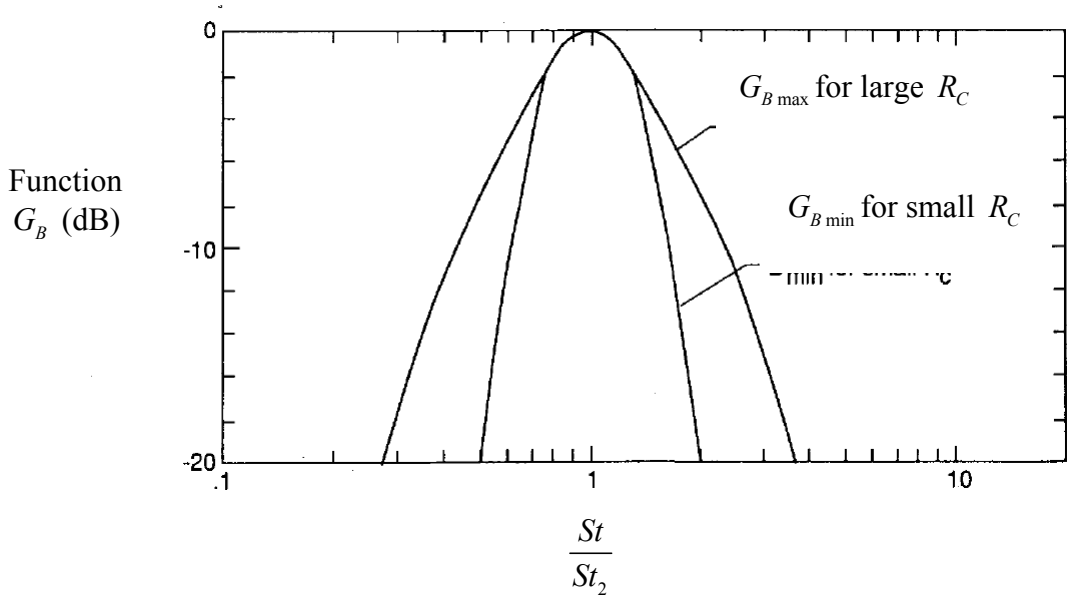

Figure 2.19: *Shape function G_B as a function of the scaled peak Strouthal number. (Extracted from Brooks et al., 1989.)*

The end results of the previous normalizations is that the noise spectra for angles of attack other than 0^o can be expressed as

$$L_p^{\alpha} = 10\log_{10}\left(\frac{\delta^*{}_s M^5 L\,\bar{D}_h}{r_r^{\,2}}\right) + G_B\left(\frac{St_s}{St_2}\right) + K_2\left(\alpha, R_C, M\right) \qquad for\ \alpha < \alpha_o \tag{2.16}$$

$$L_p^{\alpha} = 10\log_{10}\left(\frac{\delta^*{}_s M^5 L\,\bar{D}_l}{r_r^{\,2}}\right) + G'_A\left(\frac{St_s}{St_2}\right) + K_2\left(\alpha, R_C, M\right) \qquad for\ \alpha > \alpha_o \tag{2.17}$$

The terms expressed by the functions G_B and G_A' define the spectral shape and the function K_2 defines the levels. The function G'_A is the same function as G_A but for a Reynolds number tree times the actual value. Finally, the angle α_o previously introduced was empirically defined as the value for which K_2 is a maximum or α exceeds 12.5^o, whichever occur first.

2.3.2 Laminar boundary layer – vortex shedding noise

In contrast to TBL-TE noise, there are no scaling laws to describe LBL-VS noise. The reason is the erratic behavior of the multiple tones in the noise spectra and the complexity of the mechanism. The scaling used is based in two key results extracted from literature. The first is that the noise spectra seems to scale on the Strouthal number based on the laminar boundary layer thickness, δ. The second result is that the noise levels tend to coalesce to a function of R_C when they are scaled in a similar way to the used for TBL-TE noise.

For the prediction of LBL-VS, it is taken advantage of using 1/3rd octave bands. The use these broad bands overlap the tonal frequency spacing smoothing the tones and giving as a result a single peak in the spectra. As this noise mechanism is produced by the presence of a laminar boundary layer, the data used in the normalization corresponded to no-tripped cases.

Based on equation (2.3), the experimental data for no-tripped cases was normalized in amplitude as follows

$$L_p^{Scaled} = L_p^{Measured} - 10\log_{10}\left(\frac{\delta_p M^5 L}{r_r^2}\right). \tag{2.18}$$

where the boundary layer thickness at the pressure side is used and it is noted as δ_p. In this case δ_p was used instead of δ^*_p because it was found empirically that it conduces to better results. In addition, the frequency was normalized using the Strouthal number, St, based on the displacement thickness δ_p. That is

$$St' = \frac{f\delta_p}{U}, \tag{2.19}$$

The normalized noise spectra were found to coalesce to approximately the same spectral shape. This result is illustrated in the example presented in Figures 2.20 and 2.21 corresponding to a 10 cm. In Figure 2.20, the angle of attack is zero and the results are presented for several

flow speeds. In Figure 2.21, the flow speed is kept constant and the angle of attack is varied. It can also be noticed in these figures that the scaled spectra present a maximum (indicated with markers) almost at the same Strouthal number for all cases. This value was denoted as Peak Strouthal Number, St'_{peak}.

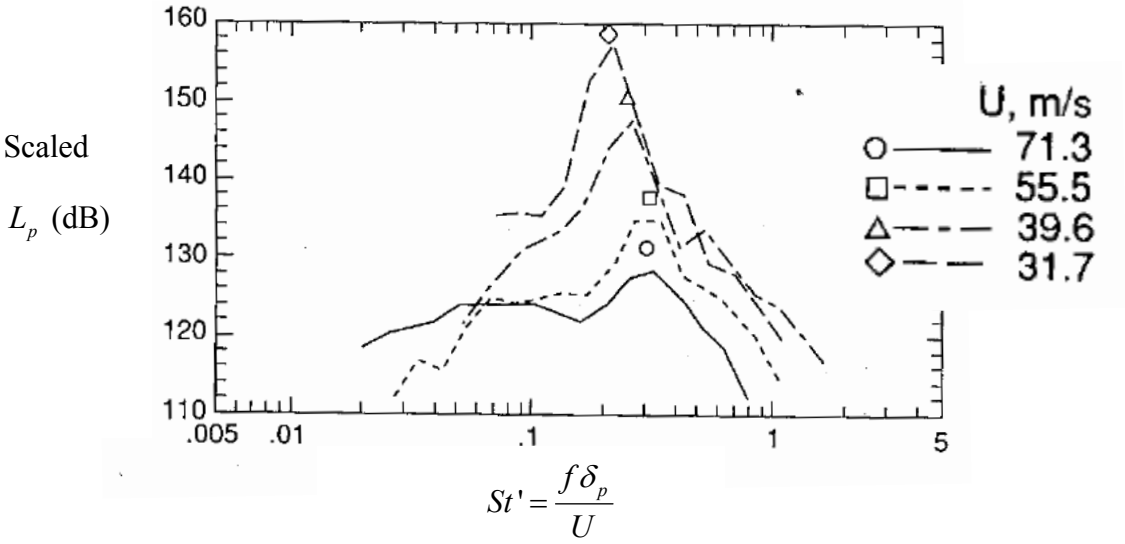

Figure 2.20: *Noise level* L_p^{Scaled} *normalized with respect to* St'*. The data corresponds to a 10 cm chord airfoil at* 0^o *angle of attack. Airfoil no-tripped. (Extracted from Brooks et al., 1989.)*

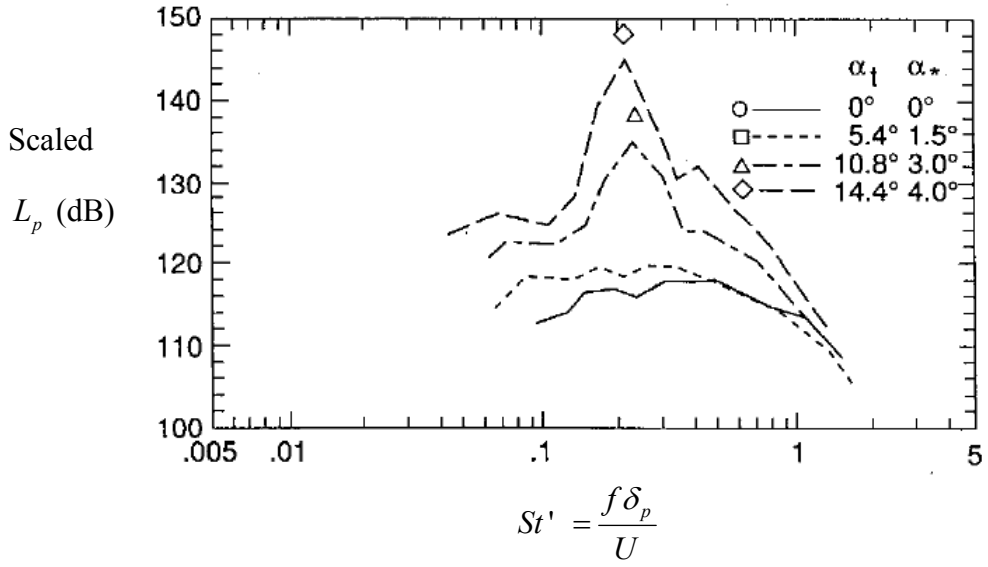

Figure 2.21: *Noise level L_p^{Scaled} normalized with respect to St' . The data corresponds to a 10 cm chord airfoil submerged in a flow with a free stream velocity of 71 m/s and different angles of attack. Airfoil no-tripped. (Extracted from Brooks et al., 1989.)*

Using the normalized data as in Figures 2.20 and 2.21, the peak Strouthal number levels for the spectra were found to be a function of the angle of attack and on the flow speed. In consequence, one function representing the dependency on the Reynolds number and other representing the dependency on the angle of attack were used for describing its variation law. To this end, an auxiliary function St'_o was used. This function represents the dependency of St'_{peak} on the Reynolds number for cases with 0^o angle of attack. The function St'_o is shown in Figure 2.22.

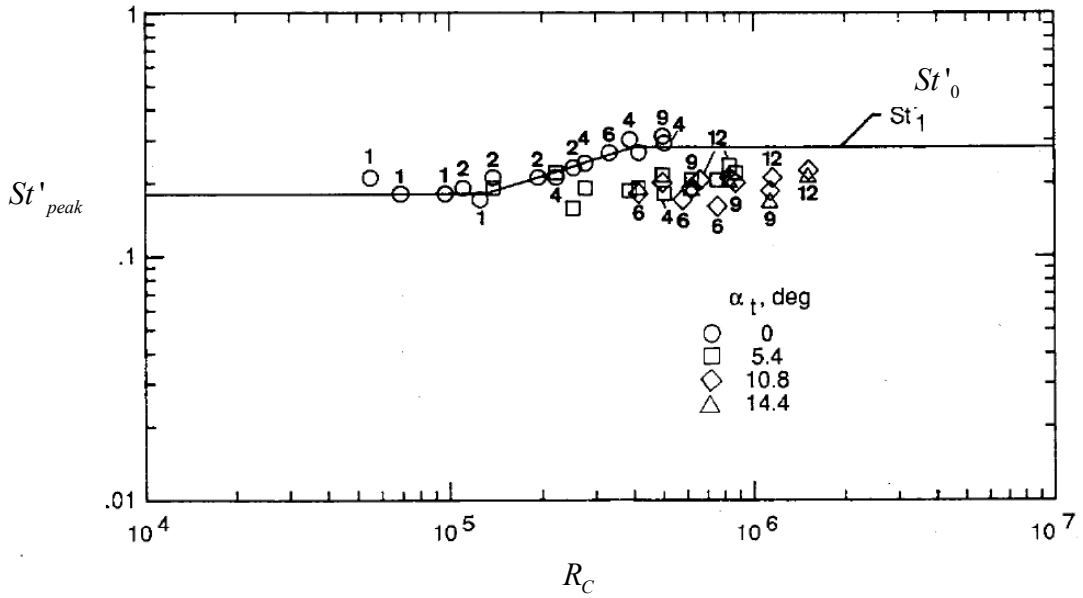

Figure 2.22: *Peak Strouthal number St'_{peak} versus R_C. The function that represents the St'_{peak} versus R_C dependency for 0^o angle of attack is scalled St'_0. (Extracted from Brooks et al., 1989.)*

Once St'_o was obtained, St'_{peak} was normalized with respect to St'_o and this normalization plotted as a function of α. This process was applied for each chord length tested and the results are presented in Figure 2.23.

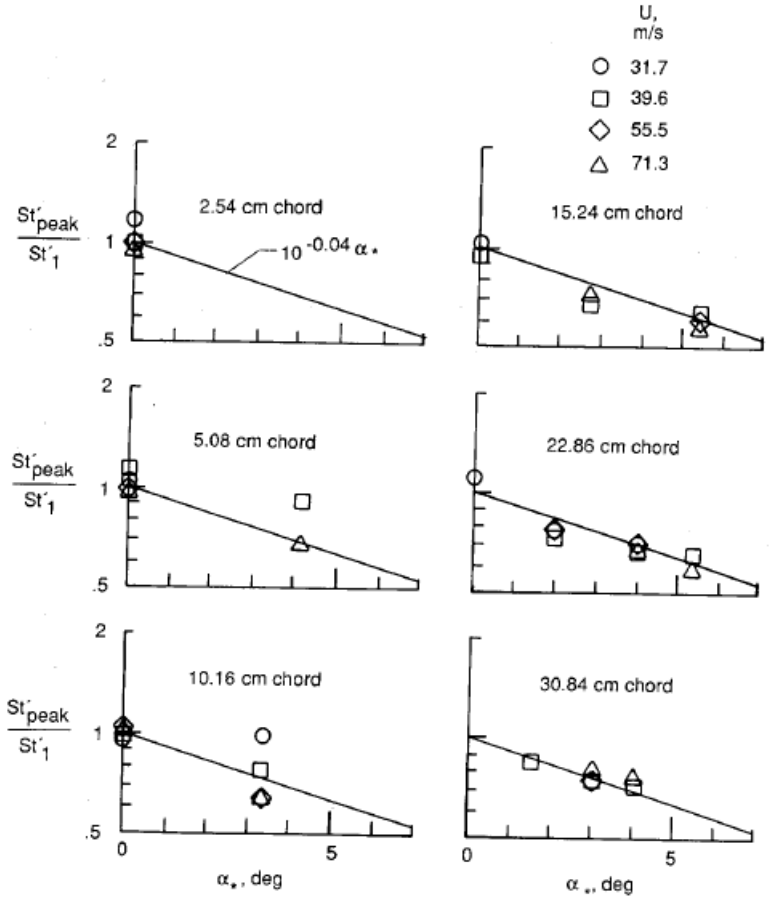

Figure 2.23: *Normalized peak Strouthal number versus angle of attack (α) for each airfoil tested. (Extracted from Brooks et al., 1989.)*

It was found that for all cases the α dependence could be approximated by

$$\frac{St'_{peak}}{St'_o} = 10^{-0.04\alpha} \tag{2.20}$$

Then, the peak scaled levels $\left(St'_{peak}\right)$ were plotted versus the angle of attack as presented in Figure 2.24. As a result of the aforementioned normalization, it was noticed in the curves presented in Figure 2.24 that the shape of the function representing the normalized peak Strouthal number was governed by R_C. Additionally, α governs the levels of this function. These two dependencies were expressed separately by the use of the functions G_D and G_E. The

function G_D specifies the curve's shape, while G_E is the angle dependence for the levels represented by G_D. The expressions for G_D and G_E can be found in page 70 of Brooks et al. (1989).

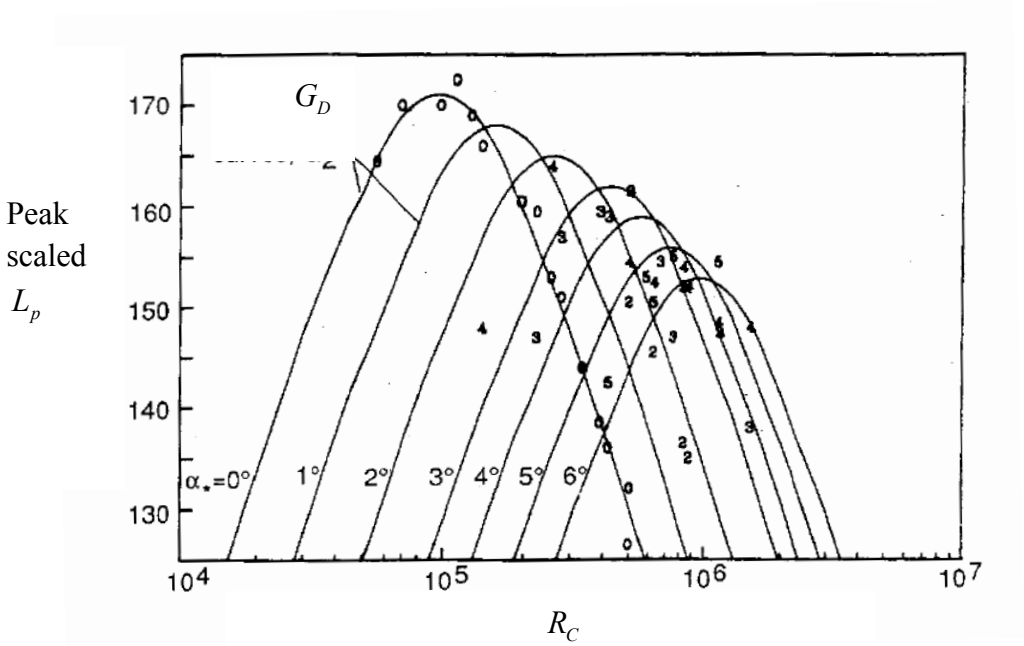

Figure 2.24: *Normalized peak Strouthal number versus R_C. (Extracted from Brooks et al., 1989.)*

Based on the shape of the scaled L_p, i.e. the scaled L_p presented in Figures 2.20 and 2.21, the shape of the normalized spectra were expressed by the function G_C that is presented in Figure 2.25.

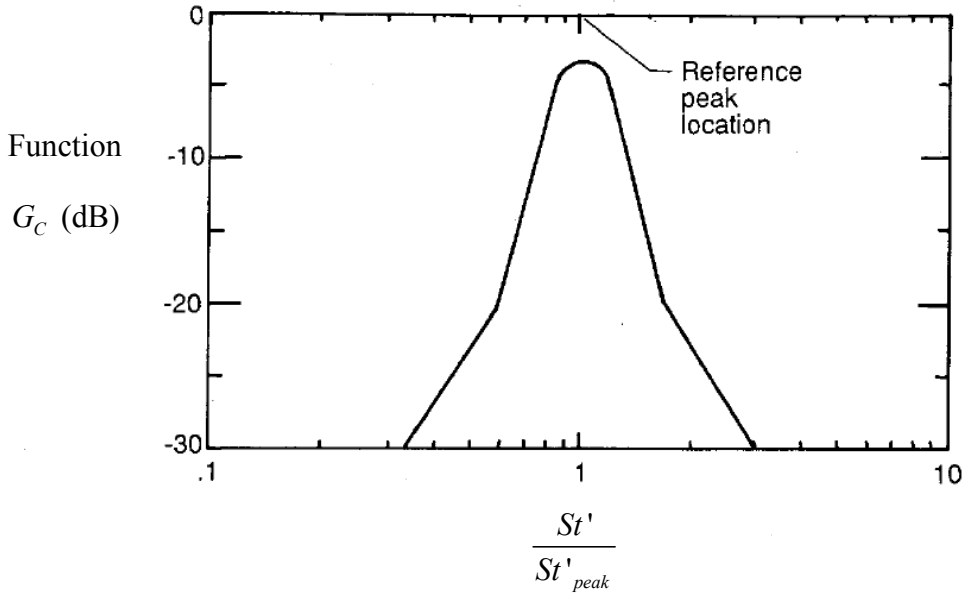

Figure 2.25: *Shape function G_C for LBL-VS noise mechanism. (Extracted from Brooks et al., 1989.)*

Finally, the noise spectra for LBL-TE can be separated into four terms as expressed by

$$L_p^{LBL-VS} = 10\log_{10}\left(\frac{\delta_p M^5 L \bar{D}_h}{r_r^2}\right) + G_C\left(\frac{St'}{St_{peak}'}\right) + G_D\left(\frac{R_C}{(R_C)_0}\right) + G_E(\alpha) \tag{2.21}$$

The first term in equation (2.21) is based on equation (2.3). The term expressed by the function G_C defines the spectral shape of this noise and the functions G_D and G_E indicate its levels as a function of the Reynolds number and angle of attack, respectively.

2.3.3 Trailing edge bluntness – vortex shedding noise

This noise mechanism is based on the experiments performed by Brooks and Hodgson (1981). In these experiments, noise spectra were measured for an airfoil with different trailing edge blunt sizes as shown in Figure 2.26. These different trailing edge blunts were obtained by the successive attachment of extensions to a NACA 0012 airfoil model. Furthermore, flat plates were used as attachments in some cases. These experiments were similar to the experiments

performed by Brooks et al. (1989) in terms of hardware setup. The main difference was that the airfoil tested was larger (0.6 m chord) than the airfoils tested by Brooks et al. (1989).

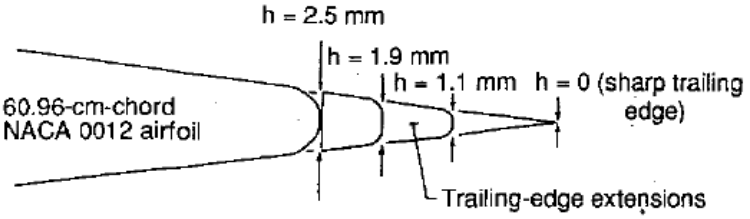

Figure 2.26: *Trailing edge extensions witch were alternatively attached during the experiments performed. (Extracted from Brooks et al., 1989.)*

Based on equation (2.3), the experimental data was normalized in amplitude as follows

$$L_p^{Scaled} = L_p^{Measured} - 10\log_{10}\left(\frac{bM^{5.5}L}{r_r^2}\right). \tag{2.22}$$

where b denotes the trailing edge thickness. A 5.5 power law of M is used instead of 5 as in the noise mechanisms previously exposed because it was found to lead to better scaling results. The results of these scalings are presented in Figure 2.27. It can be noticed in Figure 2.27 that the levels corresponding to the trailing edge of the NACA 0012 are considerably different to the cases in which a flat plate extension was used. This is believed to be caused by the difference in the angle of the terminations. For the trailing edge of the NACA 0012, the angle Ψ is 14^o while for the flat plate the angle is 0^o. The angle Ψ is the angle between the tangents to the pressure and suction curves that defines the geometry of the airfoil at the trailing edge. It is schematically described in Figure A1 of Appendix A.

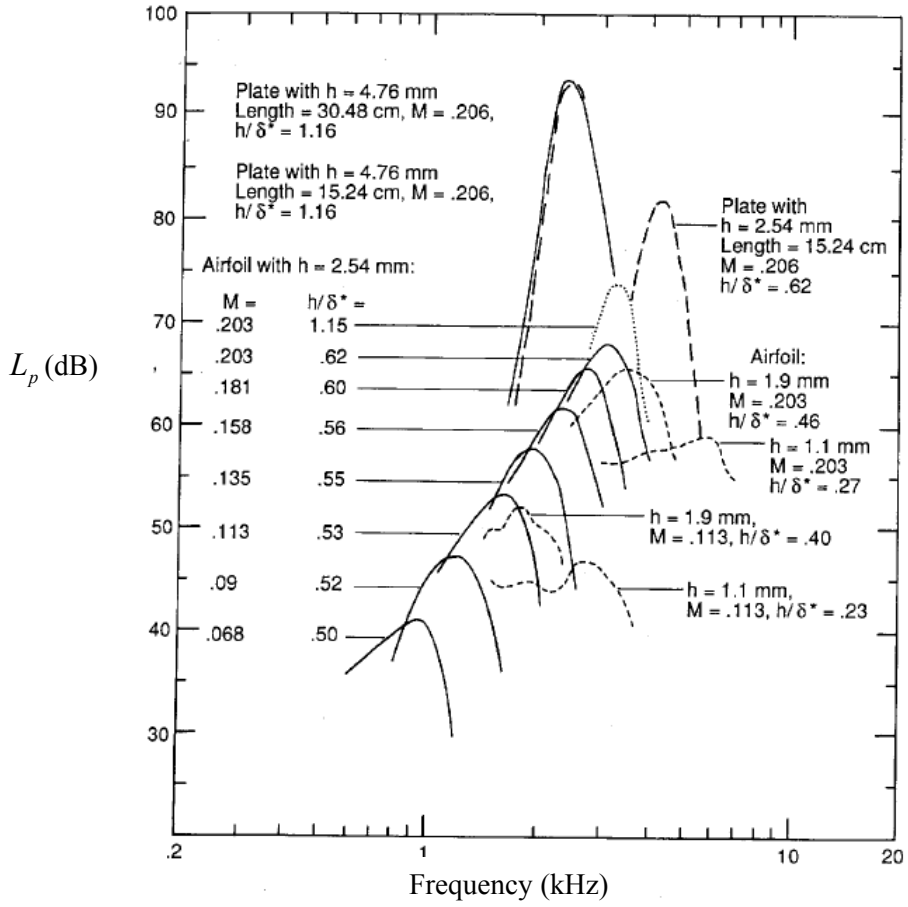

Figure 2.27: *Scaled BTE noise based in equation (2.3). (Extracted from Brooks et al., 1989.)*

In addition to the previous scaling, the frequency was normalized using the Strouthal number, St, based on the trailing edge thickness b. That is

$$St'' = \frac{f\,b}{U} \quad . \tag{2.23}$$

Then, the peak Strouthal number, St''_{peak}, and the corresponding Peak scaled levels were plotted as a function of b/δ^*_{avg} as shown in Figures 2.27 and 2.28, respectively. The average displacement thickness, δ^*_{avg}, is defined as

$$\delta^*_{avg} = \frac{\delta^*_p + \delta^*_s}{2} \quad . \tag{2.24}$$

In Figure 2.28, it is possible to note that when the aforementioned normalization is applied, the peak Strouthal number, St''_{peak}, presents a clear dependency on the angle Ψ. This dependency also appeared for the peak Strouthal levels, and it was represented with lines in Figure 2.29 and denoted as G_F. The function G_F was presented as a function bounded by limits given by $\Psi = 0^o$ and $\Psi = 14^o$. Levels for a specific Ψ should be interpolated.

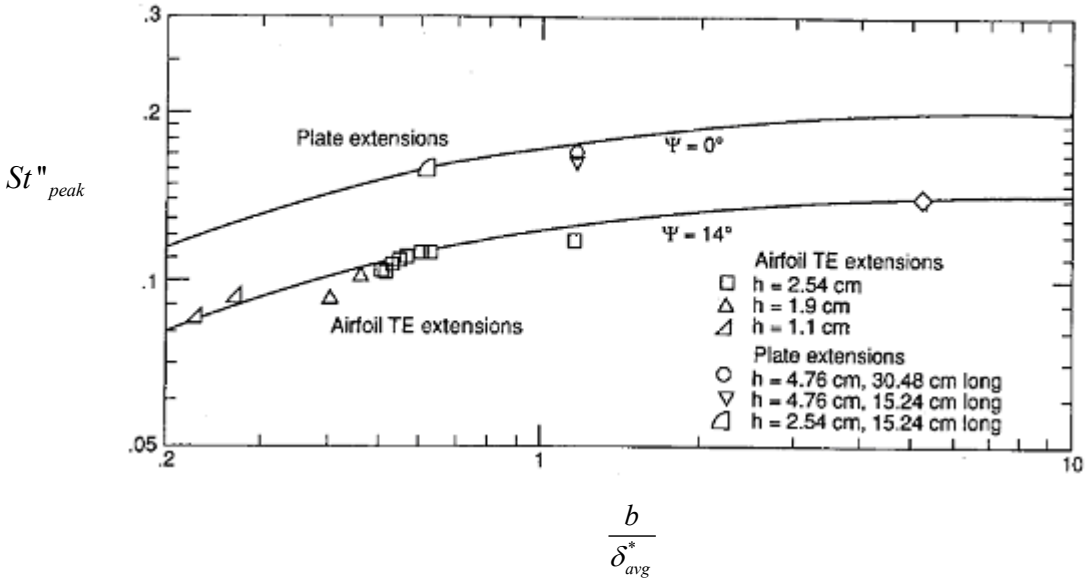

Figure 2.28: *Peak Strouthal number versus thickness ratio* $\frac{b}{\delta^*_{avg}}$ *determined from Figure 2.27. (Extracted from Brooks et al., 1989.)*

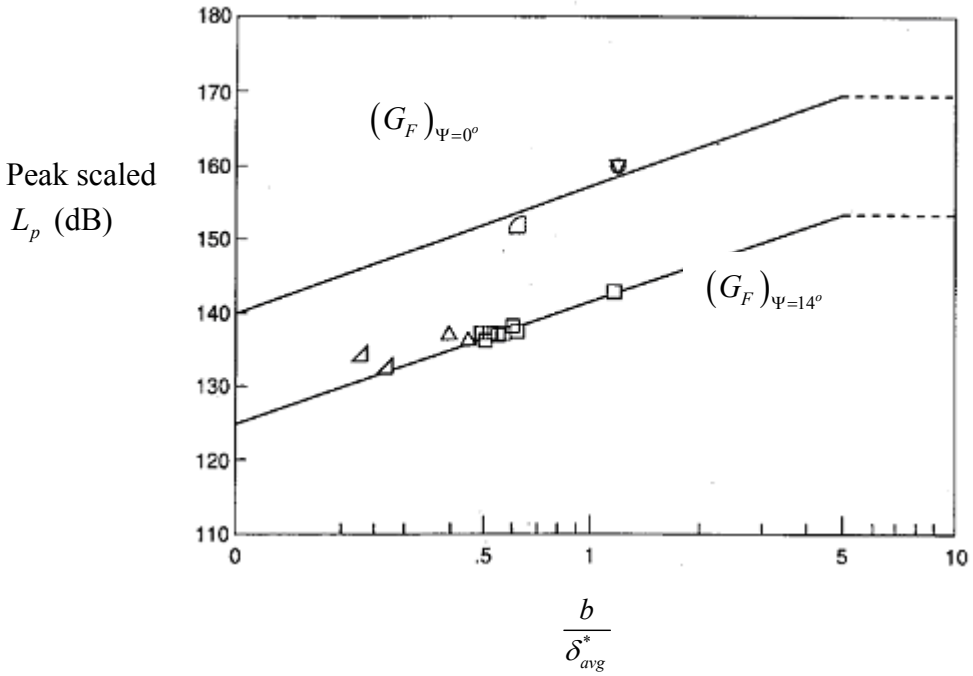

Figure 2.29: *Scaled Peak levels corresponding to* $St"_{peak}$ *versus thickness ratio* $\frac{b}{\delta^*_{avg}}$ *determined from Figure 2.27. (Extracted from Brooks et al., 1989.)*

Finally, the scaled levels presented in Figure 2.27 we normalized with respect to the ratio $St"/St"_{peak}$ as presented in Figure 2.30. The results of this scaling were modeled using function G_G. This shape function is bounded between $\Psi = 0^o$ and $\Psi = 14^o$ and varies as a function of $\frac{b}{\delta^*_{avg}}$ and $\frac{St"}{St"_{peak}}$. Numerical expressions for G_F and G_G are presented in pages 78 and 80 of Brooks et al. (1989).

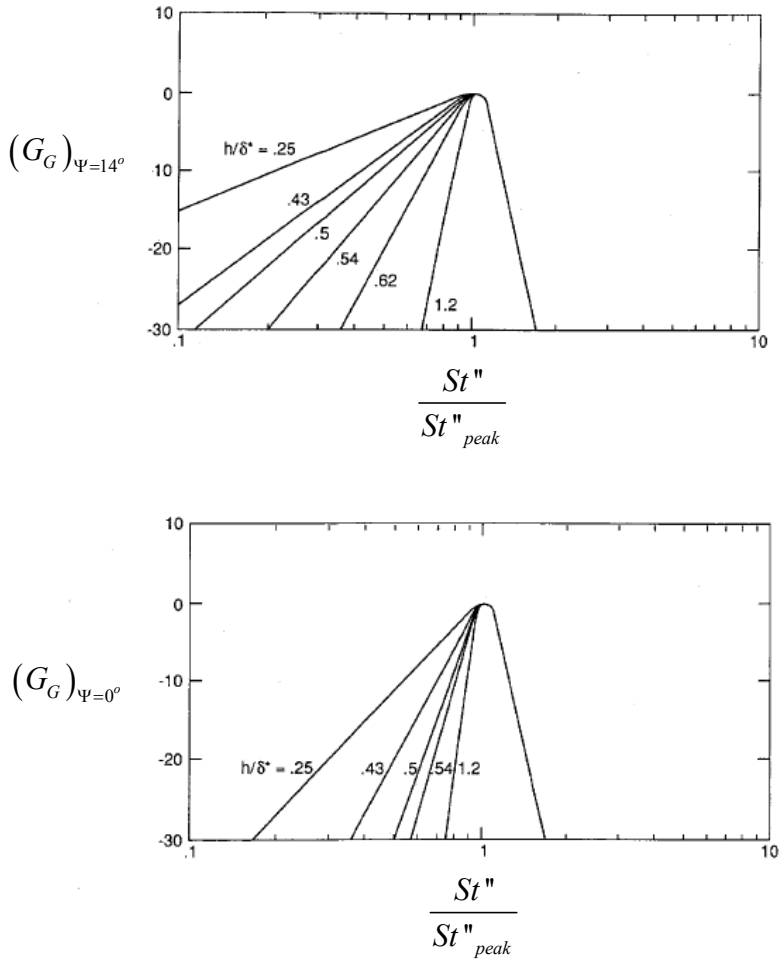

Figure 2.30: *Spectral shape functions* G_F *. (Extracted from Brooks et al., 1989.)*

Therefore, the TEB-VS noise spectra was separated into three terms as expressed by

$$L_p^{BTE} = 10\log_{10}\left(\frac{bM^{5.5}L\bar{D}_h}{r_r^{\,2}}\right) + G_F\left(\frac{b}{\delta_{ave}}, \Psi\right) + G_G\left(\frac{b}{\delta_{ave}}, \Psi, \frac{St''}{St''_{peak}}\right) \tag{2.25}$$

The first term in equation (2.25) is based on equation (2.3). The term expressed by the function G_G describe the 1/3rd octave spectral shape of the normalized BTE noise in terms of $\frac{b}{\delta_{ave}}$ Ψ and $\frac{St''}{St''_{peak}}$, and the function G_F indicates its levels as a function of $\frac{b}{\delta_{ave}}$ and Ψ.

2.3.4 Tip vortex noise

This noise mechanism was modeled by scaling experimental results obtained for different blade tips. In order to isolate the noise emitted by a blade's tip from the noise emitted along the chord of the blade during the experiments, it was proposed to compare results corresponding to a tip (3-D model) with the results corresponding to a 2-D model like the ones considered in all the previous scaling. This comparison is presented in Figure 2.31. The noise spectra corresponding to a 15 cm chord 3-D airfoil is represented with triangular markers. In addition, the noise spectra corresponding to a 2-D airfoil is presented using square markers. These noise spectra were conveniently corrected to represent the same span length. The circular markers represent the difference in noise levels between the two aforementioned spectra. It was assumed that this is the noise contribution of the tip.

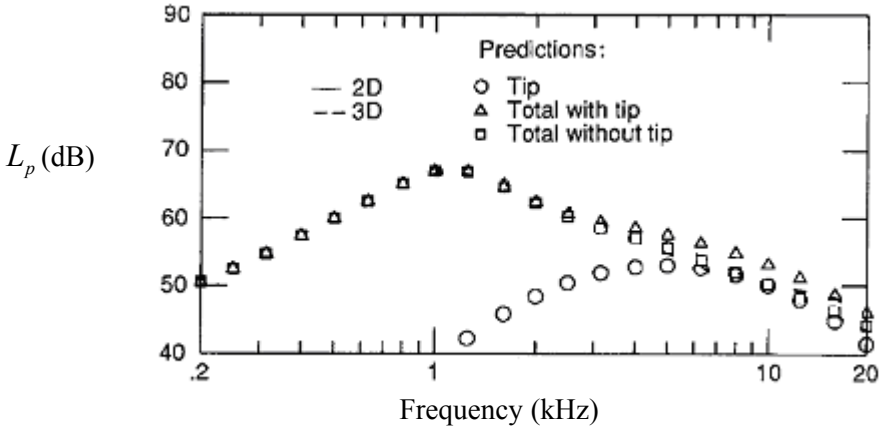

Figure 2.31: *Noise spectra of a 2-D and a 3-D airfoil. Acoustic corrections were applied with regard to chord length and span length in order for the spectra to be comparable. (Extracted from Brooks et al., 1989.)*

The noise attributed to the tip that was calculated previously, was normalized once again based on equation (2.3) as follows

$$L_p^{Scaled} = L_p^{Measured} - 10\log_{10}\left(\frac{M^2 M_{\max}^3 q^2 \bar{D}_h}{r_r^2}\right). \tag{2.26}$$

where q is the extension of the tip vortex that is defined as

$$q = C\,0.008\,\alpha_{tip} \tag{2.27}$$

with α_{tip} being the angle of attack of the blade at the tip section. The definition of this parameter holds if the blade considered is untwisted and encounters uniform flow over the span. Otherwise, a more complex consideration, which is exposed in Brooks et al. (1989), is necessary. The maximum Mach number, $M_{\max}$ is defined as

$$\frac{M_{\max}}{M} \approx 1 + 0.036\,\alpha_{tip}. \tag{2.28}$$

Then, the normalized data was subjected to a further normalization by the use of the Strouthal number St''' that is defined as follows

$$St''' = \frac{f\,q}{U_{\max}}. \tag{2.29}$$

with $U_{\max}$ being the maximum velocity within or about the separated flow region at the trailing edge that is defined as

$$U_{\max} = M_{\max} c_o. \tag{2.30}$$

The consequence of the previous normalizations is that the noise spectra was separated into two terms by

$$L_p^{Tip} = 10\log_{10}\left(\frac{M^2 M_{\max}^3 q^2 \bar{D}_h}{r_r^2}\right) - 30.5(\log St''' + 0.3)^2 + 126 \tag{2.31}$$

The first term in equation (2.32) is based on equation (2.3). The second term gives the frequency dependence. This term, is a parabolic fit about a peak Strouthal number of 0.5.

2.4 Normalization of Boundary layer parameters at the trailing edge

The semi-empirical formulas developed by Brooks et al. (1989) requires knowledge of the boundary layer displacement thickness, δ^*, and boundary layer thickness, δ, corresponding to the airfoil. This boundary layer parameters needs to be predicted. Different methods can be applied for performing these predictions. One of the most widely used methods is computerized flow dynamics (CFD) simulations or using XFOIL. Nevertheless, a simpler method was developed by Brooks et al. (1989) based on the extensive boundary layer measurements of the NACA 0012 airfoils. It was found that when boundary layer thickness and displacement thickness data were normalized with respect to the chord, dependence on the Reynolds number and angle of attack become clear. The normalization was carried out separately for the tripped and no-tripped cases.

The boundary layer parameters were first normalized with respect to the chord length for the 0^o angle of attack and plotted as a function of the chord Reynolds number as shown in Figure 2.32. The subscript "*o*" indicating that the parameter corresponds to 0^0 angle of attack. It can be noticed that the data collapsed relatively well in particular at high Reynolds numbers and for tripped cases.

The boundary layer parameters for the various angles of attack (α) are then normalized with respect to the value at 0^o angle of attack and plotted as a function of the angle of attack. The subscripts s and p are indicating that the parameter corresponds to the suction and pressure side, respectively. To illustrate this, curves resulting from this normalization of tripped cases are presented in Figure 2.33. It can be seen that for the pressure side, the data can be approximated by a single curve. For the suction side, a function's approximation is possible if it is done by parts. A similar situation occurs for no-tripped cases.

The curves in Figures 2.32 and 2.33 can be used to estimate the boundary layer parameters for the NACA 0012 airfoil of different chord, angle of attack, and Reynolds numbers.

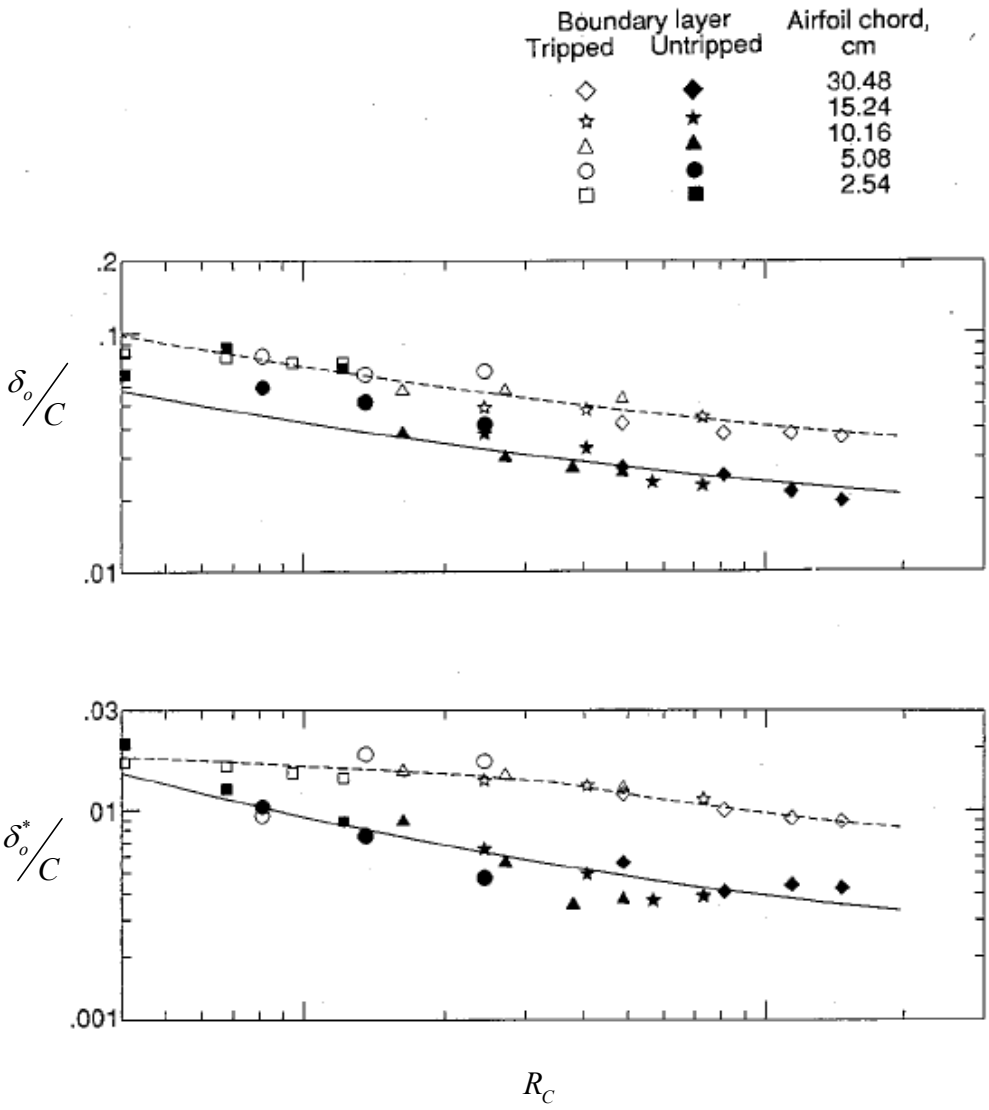

Figure 2.32: *Boundary layer thicknesses at the trailing edge for 2-D airfoil models at an angle of attack of* 0^o *versus chord Reynolds number. Solid lines are for no-tripped Boundary layer and broken lines are for the tripped cases. (Brooks et al., 1989.)*

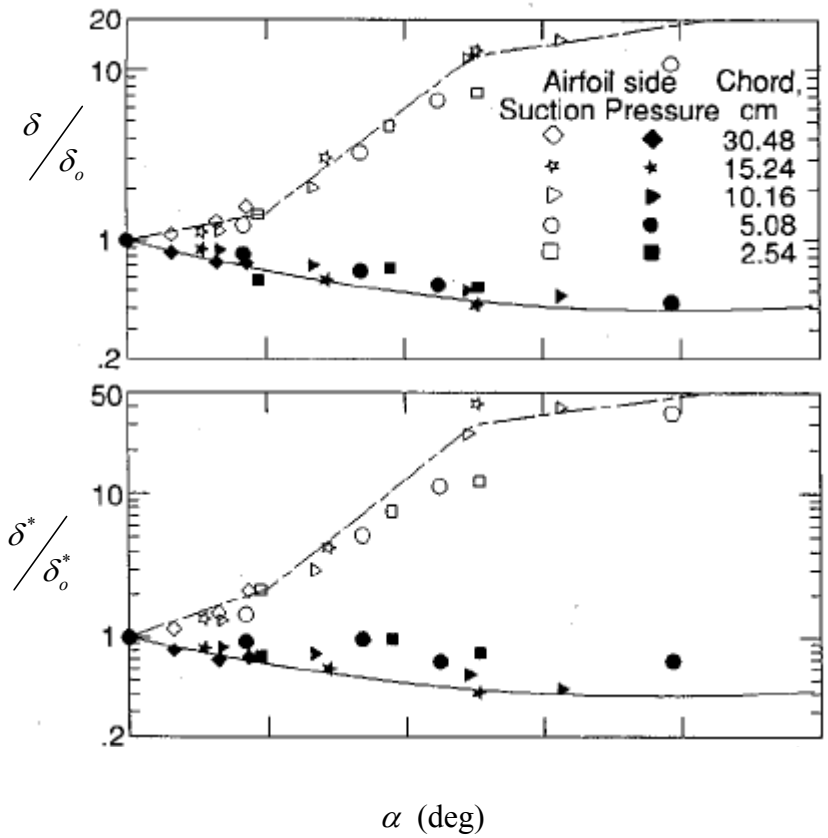

Figure 2.33: *Tripped Boundary layer thicknesses at the trailing edge for 2-D airfoil models versus angle of attack. Solid lines are for pressure side and broken lines are for suction side. (Brooks et al., 1989.)*

3. Experimental data

As discussed earlier, the main aim of the present thesis is to develop a tool for the prediction of wind turbine noise using neural networks. Experimental data is required for the training of the neural network. To this end, three experimental data sets are used. They are the NASA data of NACA 0012 airfoils (Brooks and Hodgson, 1981; Brooks et al., 1989), the test of large chord wind turbine airfoils at Virginia Tech (Devenport et al., 2008a and 2008b), and the data obtained from test of small wind turbine airfoils at Netherlands National Aerospace Laboratory (Oerlemans, 2004). In this chapter, the experimental data used to develop the network is described. Corrections applied to the data to make them consistent are also presented.

3.1 Experimental data obtained by NASA

In 1989 Brooks et al. performed experiments of six NACA 0012 airfoils of chord length ranging from 0.025 m to 0.3 m with a span of 0.45 m. The experiments were performed in an acoustic open jet wind tunnel. Acoustic measurements were made for different effective angles of attack ranging from 0^o to 22^o and chord Reynolds numbers up to 1.5×10^6. All tests were performed for conditions of clean and tripped leading edge. The tripping of the leading edge had the objective of forcing the development of a turbulent flow regime. The tripping of the boundary layer was achieved by a random distribution of grit in strips from the leading edge to 20% chord. This tripping is considered heavy because of its extension along the chord. Noise spectra in $1/3^{rd}$ octave frequency bands were published together with the semi-empirical prediction code. The frequency range of the experimental data presented varies according to the cases. In all cases, these frequencies were contained within a range from 0.2 to 20 kHz.

The experiments were carried out at the low-turbulence potential core of a free jet located in an anechoic chamber. The jet section was of 0.3 x 0.45 m of section. Airfoil NACA 0012 models of constant transversal section and 0.025, 0.05, 0.1, 0.15, 0.23 and 0.3 m of chord were tested. The trailing edge bluntness of the models was constructed with a thickness of less than

0.05 mm which allows considering them as sharp trailing edges. Figure 3.1 depicts the NACA 0012 airfoil's shape.

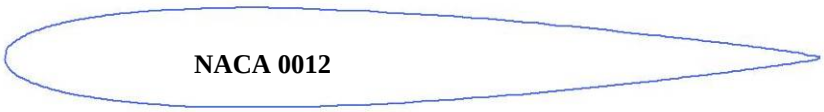

Figure 3.1: *NACA 0012 airfoil profile.*

For each model, data were collected at various effective angles of attack ranging from 0^o to 22^o depending on the airfoil and various flow speeds ranging from 32 to 71 m/s for nominal chord Reynolds numbers of 0.055 to 1.5 million. Table 3.1 shows a summary of the cases tested. The data was collected with eight microphones distributed around the model. Then, the data was processed using correlation functions in order to eliminate the background noise and isolate the trailing edge noise component. The results are presented as the sound pressure level (L_p) in 1/3rd octave frequency bands corresponding to an observer's distance of 1.23 m normal to the plane that contains the chord and span lines when the airfoil is at 0^o of angle of attack.

Aerodynamic flow measurements were performed consisting of hot-wire measurements. The boundary layer thickness was measured in the proximity of the trailing edge. For most cases, this measurement was made at 1.3 mm downstream from the trailing edge. Experiments are reported to have an accuracy of 5% for turbulent cases and 10% for laminar or transitional cases. The boundary layer thickness, δ, displacement thickness, δ^*, and momentum thickness, θ, were calculated from the measured mean velocity profiles.

Table 3.1: Ranges of flow speeds and effective angles of attack considered in the tests performed by Brooks et al. (1989).

Airfoil	Chord	No-tripped		Tripped	
		Flow speed	Effective angle of attack	Flow speed	Effective angle of attack
		(m/s)	(deg)	(m/s)	(deg)
NACA 0012	0.025	32 to 71	0 to 12	32 to 71	0 to 22
NACA 0012	0.05	32 to 71	0 to 19	32 to 71	0 to 20
NACA 0012	0.1	32 to 71	0 to 15	32 to 71	0 to 16
NACA 0012	0.15	32 to 71	0 to 12	32 to 71	0 to 13
NACA 0012	0.23	32 to 71	0 to 7	32 to 71	0 to 7
NACA 0012	0.3	32 to 71	0 to 4	32 to 71	0 to 4

The data collected by Brooks et al. (1989) is only available in the corresponding publication as figures showing noise spectra for each airfoil for each condition. Therefore, it is only possible to extract the data by copying the noise levels manually from the figures. This procedure would be time consuming. Thus, the experimental results were replaced by predictions using the semi-empirical tool for the corresponding airfoils and test conditions. Specifically, the predictions were made with the software NAFNoise (Moriarty, 2005) that implements the method developed by Brooks et al. (1989) based on the aforementioned experimental results. In the work of Brooks et al. (1989), the experimental data are presented together with predictions for the corresponding cases. Observation of these results shows that predictions obtained with Brooks et al. (1989) method lead to errors of less than 5 dB with respect to the experimental data in most cases and up to about 20 dB in a few cases.

3.2 Experimental data obtained at Virginia Tech (VT)

Funded by the National Renewable Energy Laboratories (NREL) and Sandia Laboratories, from June to December of 2007, the Advanced Turbulent Flow Research Group and the Vibrations and Acoustics Laboratories of VT conducted aerodynamic and aeroacoustic measurements of a series of large chord wind turbine airfoils. The results of the tests are presented in two reports (Devenport et al., 2008a and 2008b) and summarized in this work.

The experiments were carried out at the VT Stability Wind Tunnel in its anechoic configuration. The objectives of the tests were to study the aerodynamic and acoustic performance of various wind turbine airfoil models at high Reynolds numbers. For each model, data were collected at various effective angles of attack ranging from zero lift to stall condition, and various flow speeds ranging from 28 to 66 m/s for nominal chord Reynolds numbers of 1.5 to 3.8 million. Some of tests were performed tripping the leading edge. Table 3.2 shows a summary of the cases tested.

Table 3.2: Ranges of flow speeds and effective angles of attack tested by VT.

	No-tripped		Tripped	
	Flow speed	Effective angle of attack	Flow speed	Effective angle of attack
	(m/s)	(deg)	(m/s)	(deg)
NACA 0012	15 to 66	-8 to 5	10 to 66	-14 to 12
NACA 0012 (0.2 m chord)	41 to 55	0 to 7	40 to 52	0 to 5
S831	29 to 60	-7 to 8	30 to 56	-2 to 5
DU96	26 to 59	1 to 12	29 to 58	3 to 10
DU97-W300	28 to 56	4 to 12	28 to 56	4 to 8
DU97-W900 Flat-back	28 to 58	4 to 12	28 to 57	10
DU97-W900 Splitter plate	28 to 57	4 to 10	28 to 57	4 to 10

The airfoils tested were NACA 0012, Sandia S831 (developed by NREL), Delft DU97 (W300, W900, W900 with splitter plate), and Delft DU96 (Devenport et al., 2008a and 2008b). For the sake of completeness, all section shapes are shown in Figure 3.2 together with a picture of the splitter plate attached to a DU97 airfoil. Nevertheless, some of the airfoil's test results are not used in the present work because of reasons that are explained in chapter 5. The cases excluded correspond to the DU97-W900 and DU97-W900 with splitter plate airfoils.

The models were designed to span the complete vertical height of the test section as shown in Figure 3.3. In Figure 3.3a it is presented a view the model mounted between end plates and located inside the wind tunnel seen from the trailing edge side. Figure 3.3b presents a view of the leading edge side of the corresponding model. They have a 1.8 m span and 0.914 m chord. Models were instrumented with approximately 80 pressure taps of 0.5 mm internal diameter located near the mid-span.

As it was previously mentioned, for certain measurements the airfoils were tripped to ensure a stable and span-wise uniform transition location and a fully turbulent boundary layer at the trailing edge. Two different types of trip were used. The first tripping methods consisted of serrated trip tape (Glasfaser-Flugzeug-Service GmbH 3D Turbulator Tape). It was applied along the entire span at the 5% chord location measured from the leading edge on the airfoil suction side and at the 10% chord location on the pressure side. The tape has a thickness of 0.5 mm and is 12 mm in overall width. The second consisted of a random distribution of number 60 silicon carbide grit particles applied in a 100 mm-wide span-wise band centered on the leading edge. The grit size and pattern are designed to simulate soiling of the airfoil leading edge by insects. When applied, the soiled trip covered only the middle half-span of the airfoil models.

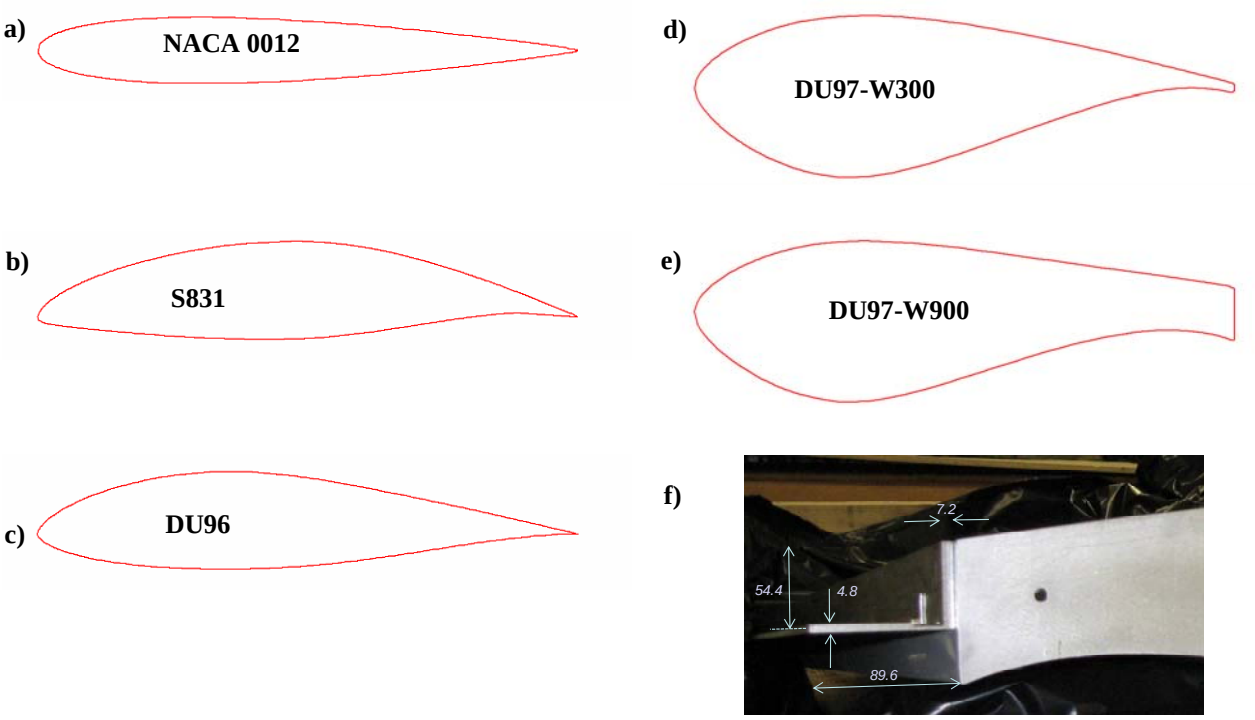

Figure 3.2: *Airfoils profiles for a) NACA 0012, b) Sandia S831, c) DU96, d) DU97-W300. e) DU97-W900. f) Splitter plate attachment used with the DU97-W900.*

Since the aeroacoustic configuration of the VT Stability Wind Tunnel is relatively new, noise measurements of a small 0.2 m chord NACA 0012 airfoil were also carried out to provide benchmark data. Results from this small size airfoil were compared to data obtained by Brooks et al. (1989) for a NACA 0012 model of almost the same chord with relatable agreement. For tripped case the difference was above 6 dB. With regard to no-tripped case, the results presented a similar pattern, but differed significantly in terms of levels.

The aerodynamic flow measurements of the airfoils consisted of static pressure distributions on the airfoil surfaces; wake profile measurements downstream of the airfoil mid-span, and single hot-wire measurements in the vicinity of the trailing edge. The data obtained by the hot-wire anemometry measurements were used by the authors of the experiments to calculate the boundary layer displacement thickness. In Appendix C, this experimentally measured boundary layer parameter is used to control the accuracy of CFD predictions performed with the program XFOIL (Drela, 2001). Hot-wire profiles were measured in the vicinity of the trailing edge of the DU96, S831 and DU97-W300 airfoils.

Noise measurements were carried out with 63-element microphone phased arrays located at 3 m from the model as shown in Figure 3.4. The data from the microphones in the arrays was processed to compute the average noise spectra, the acoustic maps, and the integrated noise spectra over a volume enclosing the trailing edge. The average spectra was computed to provide an estimate of the noise results at low frequency (<500 Hz) where the array resolution is very poor and noise maps are not computed. The acoustic maps were computed over a plane along the center of the test section as illustrated in Figure 3.5 in the 500 to 5000 Hz range. An example of trailing edge noise is depicted in Figure 3.5. In the figure, a noise map is presented in its location in the wind tunnel. The red region in the noise map represents the noise emitted by the trailing edge. In this work, the levels were integrated 10 dB down from the peak value to avoid adding the effects of the side-lobes from other sources. The integrated spectra were computed over a volume enclosing the trailing edge of the airfoil as shown in Figure 3.4. It has a square cross section and it is aligned with the airfoil trailing edge (green box in Figure 3.4). The parts of the trailing edge next to the junction with the tunnel were excluded to avoid noise due to end effects as well as other spurious noise sources seen on the test section floor and ceiling. Therefore, the integrated spectra represent the trailing edge noise radiated by the center 2/3 of the airfoil as measured at the array position. The noise data were computed for all the configurations in $1/12^{th}$ and $1/3^{rd}$ octave bands in the 500 to 5000 Hz range.

a) b)

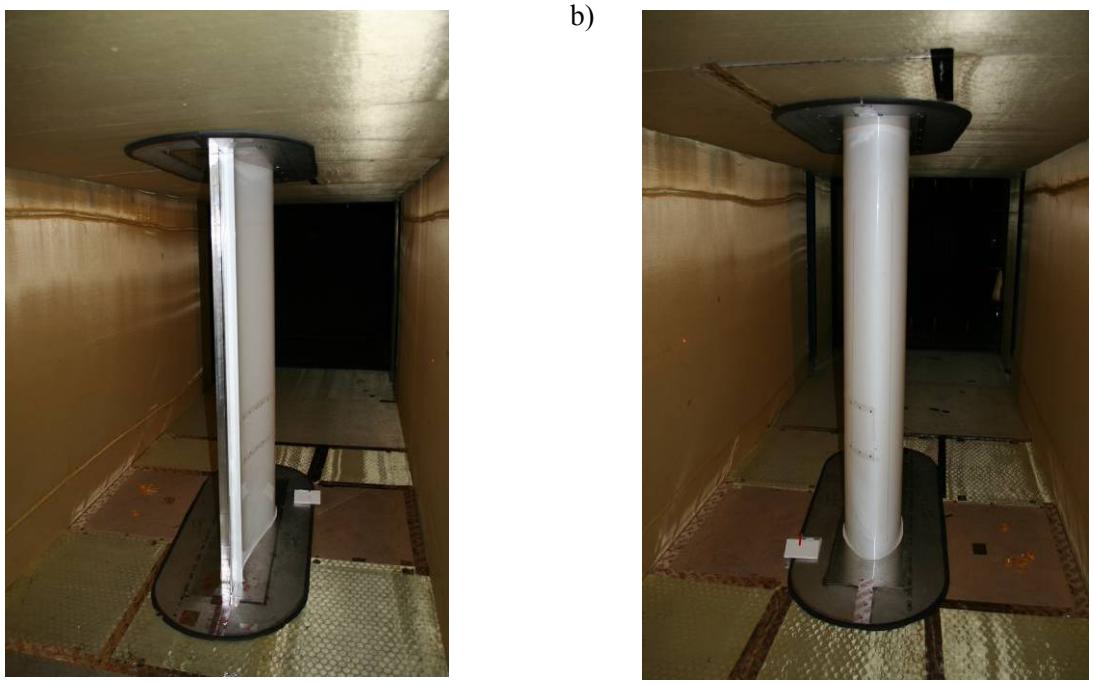

***Figure 3.3**: Wind turbine airfoil models tested in the VT Wind Tunnel seen from the trailing edge (a) and from the leading edge (b). (Extracted from Devenport et al., 2008b.)*

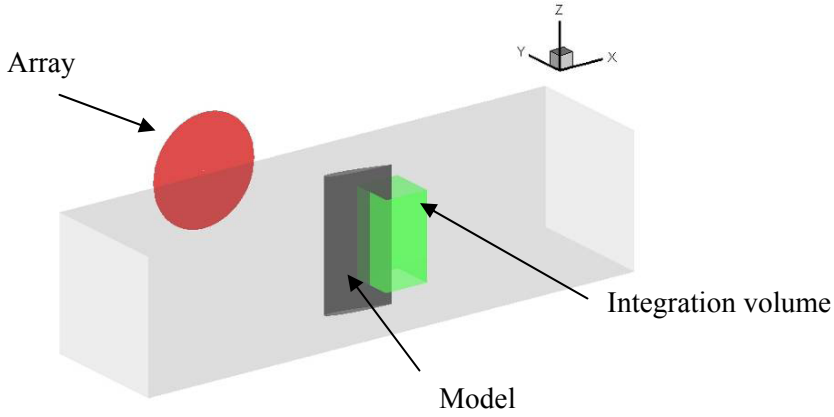

***Figure 3.4:** Measuring beamforming volume enclosing the central 2/3of span of the trailing edge of a model for the computation of the integrated spectra. (Extracted from Devenport et al., 2008b.)*

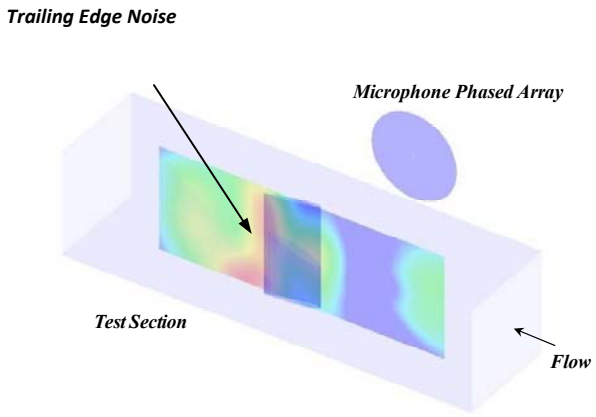

Figure 3.5: *Schema of an Airfoil inside the wind tunnel and a typical acoustic map. (Extracted from Devenport et al., 2008b.)*

3.3 Experimental data obtained at NLR

Promoted by the National Renewable Energy Laboratories, aeroacoustic tests of seven airfoils were performed at the National Aerospace Laboratory of The Netherlands (Oerlemans, 2004; Migliore and Oerlemans, 2004). The experiments were conduced in an open jet anechoic wind tunnel for several flow speed and angle of attack. Seven airfoils were tested and they are shown in Figure 3.6 except for the SH 3055 airfoil. They were NACA 0012, Sandia S822 and S834 (developed by NREL), FX63-137, SG 6043, SH 3055, and SD 2030. The NACA 0012 airfoil was tested for benchmarking purposes while the rest are candidate airfoils for wind turbines. They had a span of 0.51 m and 0.23 m chord. The trailing edges were built respecting tolerances that assure a blunt thickness lower than 0.375 mm. In the cases that the airfoils were tripped, the trips were located at 2% and 5% chord on the suction and pressure sides of the airfoils, respectively. The stream-wise peak-to-peak length of the zigzag tape used was 11 mm. The standard trip thickness was 0.25 mm, but for some cases trips of up to 0.5 mm were used.

In the present thesis, the data corresponding to the airfoil SH 3055 was not used because the geometry was not found in the open literature.

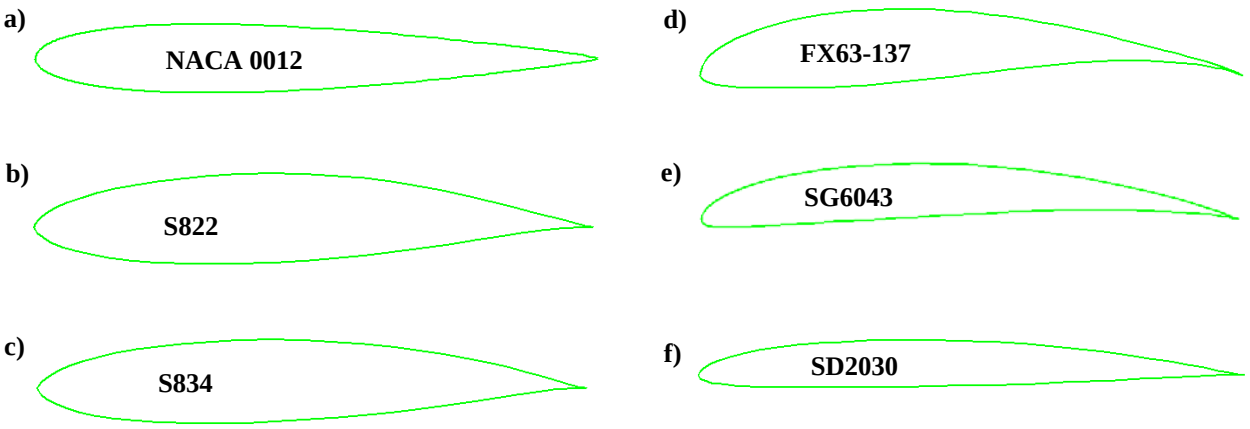

Figure 3.6: *Airfoils tested: a) NACA 0012. b) S822. c) S834. d) FX63-137. e) SG6043 f) SD2030.*

The objectives of the tests were to study the acoustic performance of various wind turbine airfoil models. For each model, data were collected at various effective angles of attack ranging from 0° to 9° depending on the airfoil, and various flow speeds ranging from 7 to 64 m/s, corresponding to Reynolds numbers from 0.2 to 1.0 million. Table 3.3 shows a summary of the cases tested. Furthermore, in some cases a turbulent flow was induced by the use of a grid placed upstream of the model to investigate the mechanism of leading edge turbulence noise. The noise measurements consisted of far-field acoustic data using a 48-element microphone phased array system. The array was placed outside the tunnel's flow at a distance of 0.6 m from the model's rotating axis at the suction side of the airfoils. The integrated noise spectra were performed for a volume enclosing the central 0.1 m of span. The results were reported as sound power level (L_w) in 1/3rd octave bands (Migliore and Oerlemans, 2004). The measurements were made in the frequency range from 80 to 20000 Hz. Nevertheless, the facility used was considered anechoic only above 500 Hz. Furthermore, the microphone array used was designed for maximum side-lobe suppression at frequencies between 1 and 20 kHz. Therefore the data is valid between 500 and 20000 Hz, with a higher accuracy above 1000 Hz.

Table 3.3*: Ranges of flow speeds and effective angles of attack tested by NLR.*

	No-tripped		Tripped	
	Flow speed	Effective angle of attack	Flow speed	Effective angle of attack
	(m/s)	(deg)	(m/s)	(deg)
NACA 0012	32 to 71	0 to 7	32 to 71	0 to 7
S822	13 to 63	0 to 8	12 to 63	0 to 8
S834	13 to 48	0 to 8	13 to 48	0 to 8
FX63-137	13 to 48	0 to 8	13 to 48	0 to 8
SG 6043	7 to 32	0 to 8	7 to 32	0 to 8
SH 3055	32 to 64	0 to 8	32 to 64	0 to 8
SD 2030	12 to 32	0 to 8	12 to 32	0 to 8

3.4 Summary of Experimental Data

To gain a better understanding of the data used in the training of the neural network, the range of test parameters for all three tests is summarized here. Figure 3.7 shows the range of chord Reynolds numbers versus the range of angle of attacks covered for each airfoil tested for tripped cases. Each polygon represents a Reynolds number versus angle of attack enveloped corresponding to each airfoil tested. It can be observed that the VT data cover the largest range in particular towards the higher Reynolds numbers. The figure also reveals some gaps in the data such as in the 1 to 1.5 million Reynolds number and angles of attack above 5°. A similar result is shown for the tripped cases in Figure 3.8.

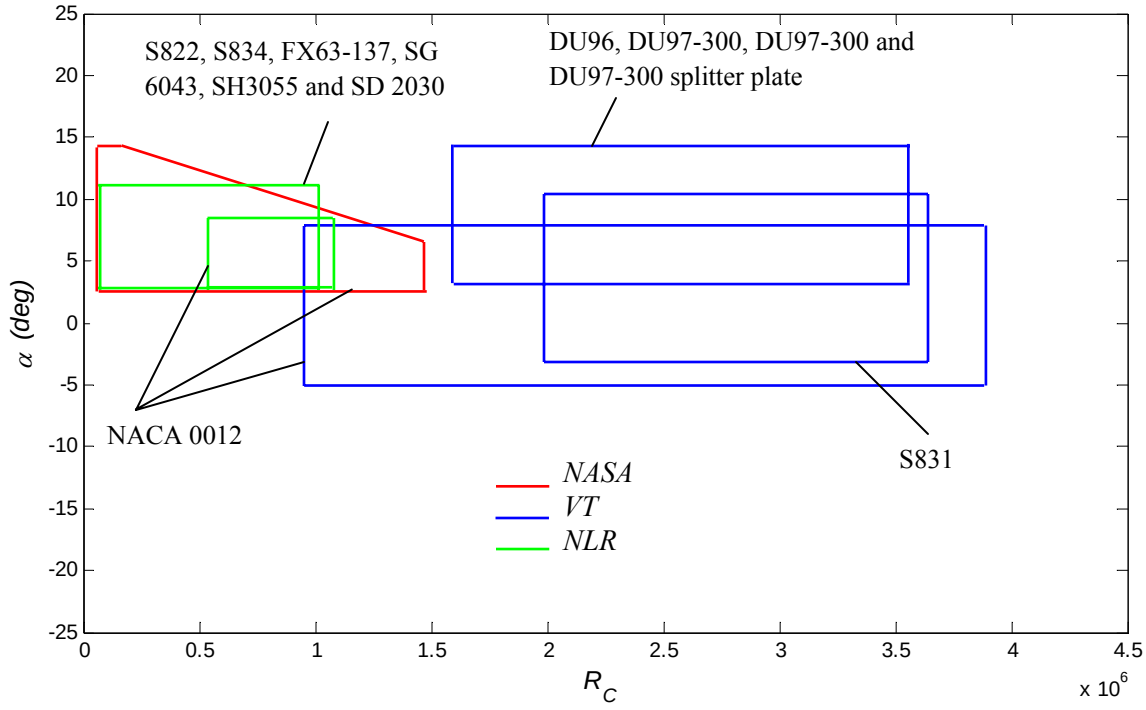

Figure 3.7: *Summary of the Reynolds number versus angle of attack range for the tests presented in the present chapter. Tripped cases.*

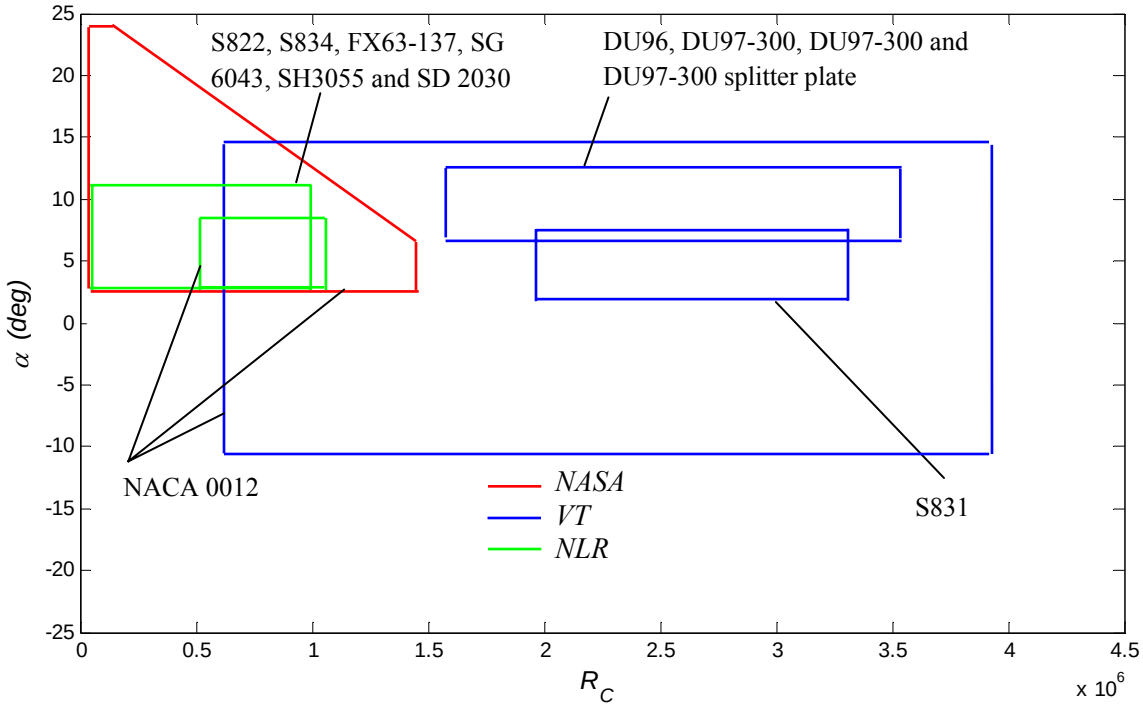

Figure 3.8: *Summary of the Reynolds number versus angle of attack range for the tests presented in the present chapter. No-tripped cases.*

3.5 Corrections applied to the experimental data

The experimental data must be first adjusted to account for the different measurement methods, locations, and processing. To this end, the data were corrected for an observer's position at 3 m from the trailing edge in direction perpendicular to the plane containing the chord and span lines of the airfoil. This position corresponds to $r_r = 3\,m$, $\theta_r = \pm 90^o$ and $\varphi_r = 90^o$ following the coordinates system presented in Figure 2.7. The source's span length was set at 1.23 m. These are the conditions corresponding to the VT tests for 0^o effective angle of attack. For the NASA data, the reference airfoil span length and observer's location are obtained by using the correct input to the semi-empirical code. Therefore, no corrections are necessary. On the other hand, some corrections were applied to the VT and NLR data.

3.5.1 Interference correction for angle of attack

It is important to clarify that in the present thesis the effective angle of attack is used to characterize each test. When a wind tunnel test is performed, the aerodynamic behavior of the airfoils is different than at free flight. This is due to the interference caused by the walls of a hard walled wind tunnel, the turning of the jet in an open jet tunnel, or the Kevlar cloth of the VT hybrid configuration. Therefore, this interference effect is accounted for by adjusting the geometry angle of the airfoil (geometric angle of attack, e.g. actual physical angle of the airfoil in the tunnel) until it best matches the expected pressure distribution in free flight for a certain angle of attack, known as effective angle of attack. Therefore, interference correction is the ratio of the effective to geometric angle of attack, e.g. correction to be applied to the angle of attack measured at a wind tunnel test for the data to represent free flight conditions. These corrections have already been applied by the authors of each test. For the NASA tests, the interference correction was of 37%. This means that the effective angle of attack is 0.37 times the geometric angle of attack used during the tests. For the VT tests the correction factor was 77% and for the NLR test it was 44%.

3.5.2 Corrections to VT's data

The data obtained at the VT's wind tunnel were affected by the losses through the Kevlar cloth and the shear layer (Remilleux et al., 2006; Devenport et al., 2008a; Burdisso and Errasquin, 2009). The acoustic losses through the Kevlar cloth and the boundary layer were first determined experimentally by Remilleux et al. (2006) and later improved by Burdisso and Errasquin (2009). The improved corrections can be calculated as follows

$$L_p^{corrected} = L_p^{measured} + \Delta_{Kevlar} + \Delta_{BL} \tag{3.1}$$

where

$$\Delta_{Kevlar}(dB) = 0.0196\left(\frac{f}{1000}\right)^2 - 0.0391\left(\frac{f}{1000}\right) \tag{3.2}$$

and

$$\Delta_{BL}(dB) = 0.00154471\left(1 - e^{-\left(f/1000\right)^{1.057}}\right)e^{43.28\,M} \tag{3.3}$$

.

In these expressions, $L_p^{measured}$ is the noise measured experimentally, f is the band center frequency, and M is the free stream flow Mach number. In Figure 3.9 the corrections are presented as functions of frequency. The positive values in the curves indicate the magnitude of the losses in decibels.

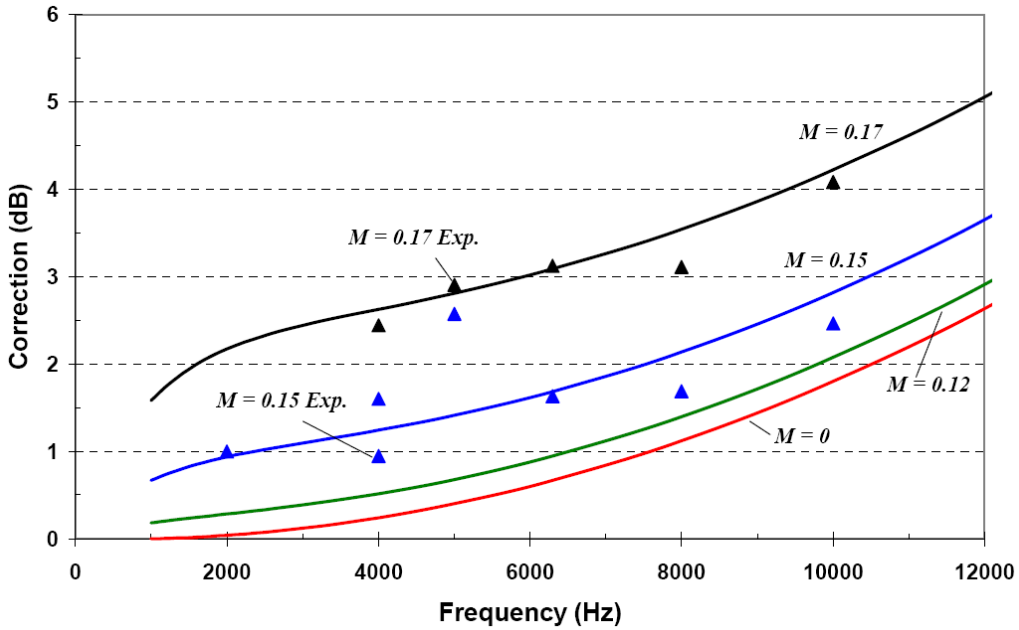

Figure 3.9: *Attenuation of sound passing through the acoustic Kevlar window as a function of frequency in 1/3 octave bands. The summation of the effects of the Kevlar's wall and the boundary layer are considered. (Extracted from Burdisso and Errasquin, 2009)*

In addition, correction for the position of the observer as a function of the geometric angle of attacks is required as illustrated in Figure 3.10. The microphone array center is at the

distance r_1 from the center of rotation of the model (1/4 chord from leading edge). As the geometric angle of attack is changed the actual distance and angle of the observer to the trailing edge also changes.

For this correction, the noise propagation is modeled as spherical waves emitted from the center span. The actual directivity of the noise emitted by an airfoil is that of a dipole or a baffle dipole depending on the case. Nevertheless, these directivity functions are much like spherical waves at the observer's direction considered in this work, e.g. normal to the airfoil. Considering the spherical spreading law, and calling r_r to the distance from the source (trailing edge) to the observer and r_e' to the distance form source to the microphone array center, then the correction is given as follows

$$L_p^{3m} = L_p^{r_e} + 20\log\left(\frac{3}{r_r}\right) \tag{3.4}$$

where L_p^{3m} corresponds to the noise level at the observer distance of 3 meters and $L_p^{r_r}$ is the measured level at the r_r distance. This distance is easily computed using the cosine rule as follows

$$r_r = \sqrt{3^2 + \left(\frac{3}{4}C\right)^2 - 2\left(3\left(\frac{3}{4}C\right)\right)\cos\left(\frac{\pi}{2} - \alpha\right)} \tag{3.4}$$

It should be noted that this correction is not very important with a maximum adjustment of 0.3 dB for a geometric angle of attack of 15°.

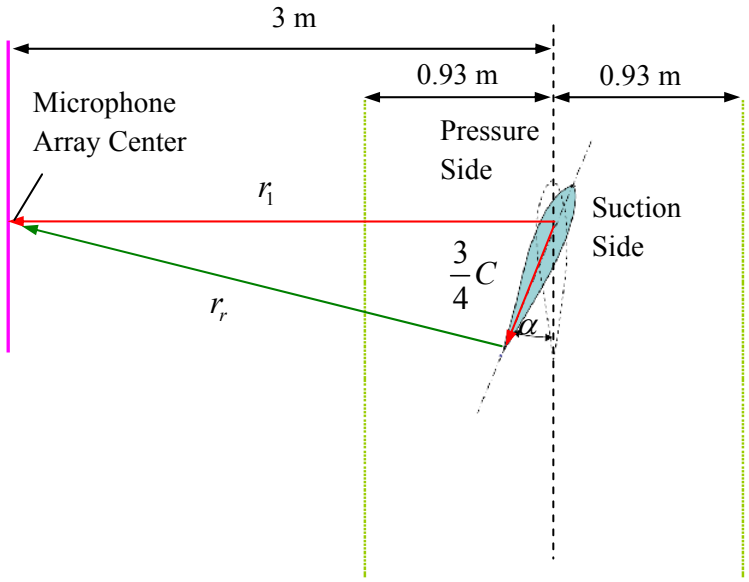

Figure 3.10: *Schematic view of the VT wind tunnel configuration depicting the array position with respect to the center and trailing edge of the model. During the tests, the array was located either on the pressure of suction side depending on the test.*

3.5.3 Corrections to NLR's data

The experimental measurements obtained at NLR were expressed in sound power level (L_w) assuming a monopole behavior of the source (Spherical waves). Therefore, at a distance of 0.282 m $\left((4\pi)^{-\frac{1}{2}}\right)$ the sound pressure level has the same value as the sound power level. Thus, the sound pressure level at the observer's position of 3 m is computed as

$$L_p^{3m} = L_p^{0.282m} - 20\log\left(\frac{3}{0.282}\right) = L_W - 20\log\left(\frac{3}{0.282}\right) \tag{3.11}$$

In addition, a correction for length of the source in the span direction is necessary. This correction takes into account that for the NLR tests the map integration was made over the center 0.1 m of the airfoil's span while for the VT tests the span length considered was 1.23 m. This correction is simply

$$L_p^{1.23} = L_p^{0.1} + 10\log_{10}\left(1.23/0.1\right) \tag{3.15}$$

4 Neural Networks Prediction Method

The objective of this chapter is to investigate the potential of using neural networks as a computational tool to predict self noise for airfoils of any geometrical shape, chord length, flow speed, and angle of attack. The neural networks are trained using experimental data obtained at VT (Devenport et al., 2008a and 2008b), NLR (Oerlemans, 2004 and Migliore and Oerlemans, 2004), and NASA (Brooks et al., 1989). The neural networks types and configurations are chosen according to the experience of the author and following advises found in literature. This work is an application of neural networks and, thus, the theory of this technique is presented only to the extent that is needed for the proper understanding of the method.

Since the neural network implementation is a new approach, it is intended to develop this tool in a step by step approach. This means that the first step is to develop a simple model applicable only to the NACA 0012 airfoils. Then, this model is then extended to include any airfoil shape. The airfoil shape is considered by incorporating parameters describing the geometry into the training data. Two different approaches are used here. They are based on a conformal mapping and polynomial approximations of the surfaces of the airfoil, respectively. Several different neural networks models are studied in order to identify the ones that are more appropriate.

4.1 Neural Network Review

Artificial neural networks can be considered as simplified models of the networks of neurons of animals and human beings. From the engineering point of view, artificial neural networks offer an alternative form for solving highly non linear problems (Gurney, 1997). Over the last years, the method of Neural Networks has been increasingly applied to all kind of engineering problems (Rai, 2002). Following Sundararajan et al. (1999) a typical neuron is shown in Figure 4.1. A scalar input s_i is transferred through a connection that multiplies the input by a scalar w (weight). The weighted input $s_i w$ receives the addition of a scalar bias s_b.

Then, a transfer function f_T, chosen according to the problem to be solved, is applied to the product of the previous steps giving an output s_o. The transfer function can be either linear or nonlinear. The process can be expressed mathematically as

$$s_o = f_T\left(ws_i + s_b\right) \tag{4.1}$$

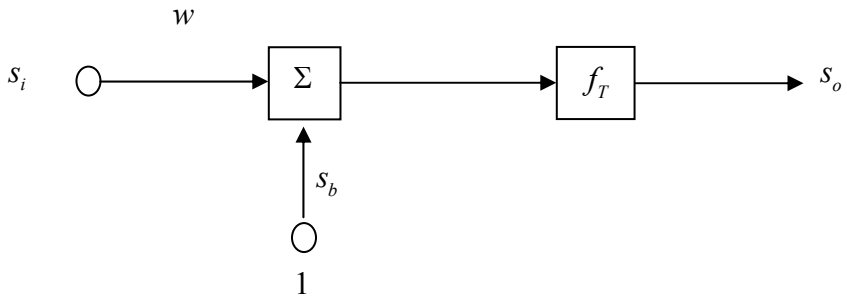

Figure 4.1: *Schematic representation of an artificial neuron.*

In a neural network, several neurons are interconnected in order to mimic more complex behavior than the one that the neurons could reach individually. The functioning of the network depends on the connections between elements. Figure 4.2 shows a schematic representation of a typical neural network. The network must be trained by adjusting the bias and the connections (weights) between elements. A neural network is adjusted so that given a specific input the network produces a specific output. Then, the output is compared to an expected result or target. This process is repeated, adjusting the weights, until the difference between output and target reaches a desire error tolerance. Typically, several pairs of input/target data are needed to reach an expected behavior. Usually the whole set of input/target data is presented to the network repeatedly in order to improve the training. Each process of presenting the set of input/target data is called epoch. Figure 4.3 shows a flow diagram representing the training process.

It can be observed in Figure 4.2 that the network can be composed of several layers. Frequently, all the neurons in the same layer have the same transfer function. Thus, the transfer functions are specified by layer. The layer that receives the input data is called Input layer. In the

same way, the layer that outputs the results is called Output layer. The layers between them are commonly called hidden layers. The simplest neural network will be composed of an input and an output layer. The hidden layers usually improve the capacity of the network to solve complex problems. Though input parameters feed into the input layer, it is important to clarify that the number of input parameters is not related to the number of neurons in the input layer. In fact, it is possible to have several input parameters and a single neuron in the input layer. On the other hand, the number of neurons in the output layer has to match the number of output parameters that are expected. The number of neurons in the hidden layers does not follow any special rule and it is chosen based in the experience of the user. The same situation occurs with the election of the number of hidden layers (Kasnakogluand and Onder Efe, 2008; Sundararajan et al., 1999; Gurney, 1997).

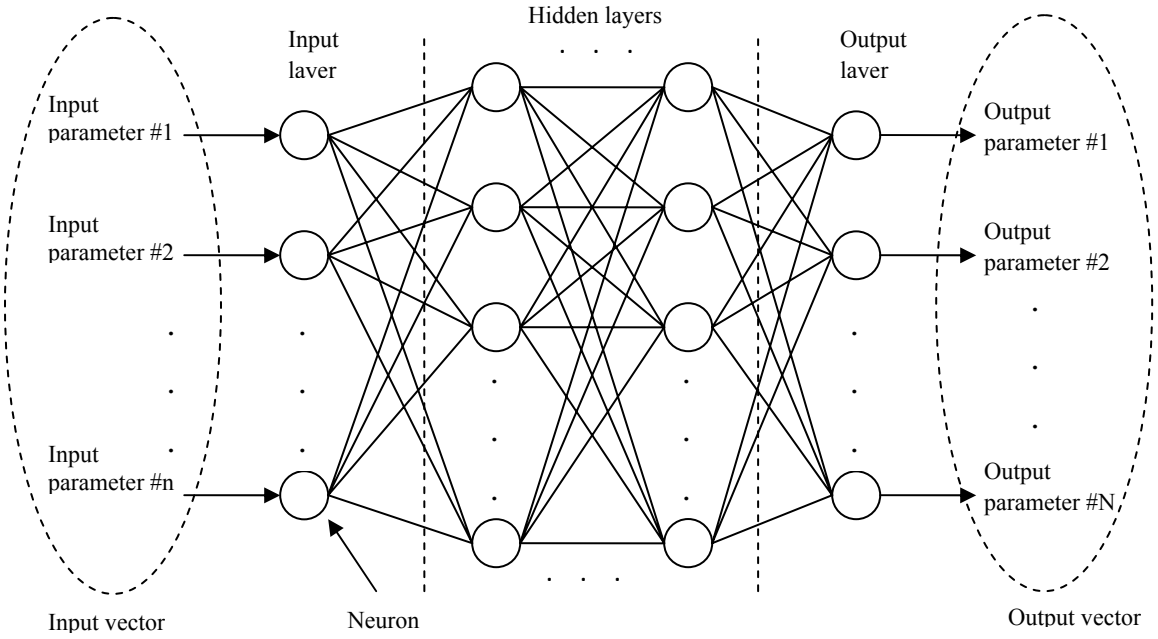

Figure 4.2: *General schematic representation of a neural network.*

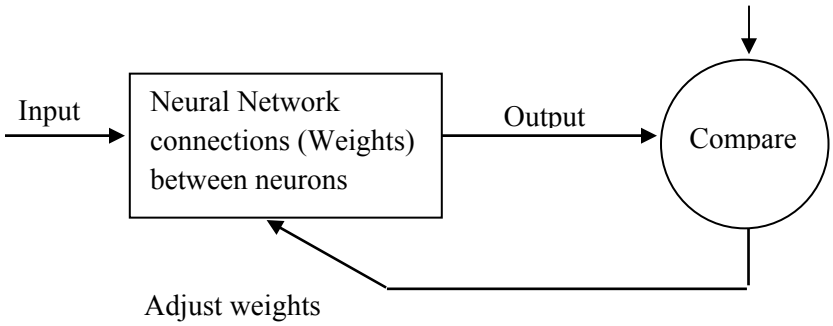

Figure 4.3: *Schematic representation of a neural network training.*

Each set of input and output parameter corresponding to a set of target parameters is grouped as an input, output, and target vector, respectively. In this work, it is adopted the convention of calling input matrix to the set of input vectors and target matrix to the set of target vectors. The conjunction of the two matrixes is the called training matrix.

4.2 Prior Applications of Neural Networks in Aerodynamic and Aeroacoustics

Artificial neural networks have been widely used in aerodynamics. Recent applications in aerodynamics include flow control, estimation of aerodynamic coefficients, compact functional representations of aerodynamic data for rapid interpolation, grid generation, aerodynamic design, and the interpolation of wind tunnel data (Rai, 2002).

One of the first applications of neural networks to aerodynamics is the work of Chong et al. (1992). In this work, a multilayer neural network was applied to airfoil design. The network was trained using aerodynamic parameters such as drag and lift coefficients as inputs while the output was the airfoil geometry. The aerodynamic parameters were calculated using XFOIL (Drela and Youngren, 2001). The geometry was represented by conformal mapping. The results of this work showed that choosing the optimal neural network configuration is, to some extent, a random process. Furthermore, it was showed that the network had a much better behavior

making predictions inside the limits of the training data than outside these limits. This is that the network was better interpolating than extrapolating (Chong et al., 1992).

In 1993, Meade successfully applied neural networks to the approximation of pressure coefficients based on experimental data corresponding to NACA 0012 airfoils of different chord length. Nevertheless, several uncertainties about how to manipulate the neural networks were reported as a factor that would limit the acceptability of the method. The technique of weighted residual learning was used. The main advantage of this method would be the possibility of incorporating some theoretical models to the networks. The possibility of representing the integral and derivative of the output function was presented as another advantage of the method (Maede, 1993).

Huang et al. (1994) used a neural network to address the problem of predicting the aerodynamic parameters given the airfoil's geometry. In this case, parameters that indirectly describe the geometry of the airfoil are used as input for the neural networks. The outputs are lift coefficient, drag coefficient, and pitching moment. It was found that it is uncertain which and how many input parameters are necessary in order to properly define the problem and guarantee uniqueness (Huang et al., 1994).

Other application of neural networks was the geometrical design of airfoils by Di Stefano and Di Angelo (2003). The input of the network is given by angle of attack, lift, drag, and so forth. The output is represented by the coordinates set of control points of a Bèzier curve. In this work, it is stated that a multi-layer feed-forward neural network with an arbitrary large number of units in the hidden layers can approximated any real continuous function. It has been verified that the implemented neural network had little capability to reproduce the geometries expected when it is operating in the extremes or outside the range of the parameters used for the training process. Nevertheless, in the case of input parameters located away from the extremes of the range, the results were reported to be satisfactory.

A different problem was studied by Kasnakoglu and Onder Efe (2008). In this work, different *intelligent methods*, including neural networks among them, are contrasted for the

problem of predicting pressure at a specific location in a 3-element airfoil. A 3-element airfoil is an arrangement of 3 airfoils interacting between each other like the ones found in the wings of commercial airplanes. Based on the pressure measured in some locations, it is attempted to predict the pressure in a different location. The results reported show that a Multilayer Perceptron network provides better results than a Radial Basis Function Neural Network (Kasnakoglu and Onder Efe, 2008).

Different methods have been used to take into account the shape of airfoils in neural network simulations. Chong et al. (1992) used a conformal mapping method. The main reason for using this method is that it only requires the use of five parameters to define the geometry. The conformal mapping is described in depth by Jones (1990). This mapping is dependent on two parameters defining the thickness of the airfoil, two parameters defining the camber, and a single parameter defining the trailing edge thickness. In the work presented by Rai and Madavan (1998), two methods for parameterization of airfoils geometry are presented that use up to 13 parameters to describe the geometry. Other method of airfoil representation that has been found in literature is the use of Bezier curve representation. This method is used in the previously described work of Stefano and Di Angelo (2003) and in the work of Hacioglu (2007). Finally, there is a method based in the use of PARSEC airfoils that was used in the work of Khurana et al. (2008).

With regard to the characteristics of the neural networks used in aerodynamics, according to all the literature reviewed, in most cases the chosen neural network was a feed forward network using a back-propagation algorithm (i.e. Rai, 2002 and Meade, 1993). Moreover, the present literature review shows that a neural network method in aerodynamics would not be advisable for extrapolating results.

In 2008, Khurana et al. presented an airfoil's optimization method that included a neural networks module implemented in Matlab. In this work, a thumb-of-rule assumption is that the number of neurons in the hidden layer equals five times the number of input neurons. This rule is reported to have been successful.

It is important to notice that in most of the works reviewed, the data set used for training was obtained by simulations rather than experiments.

To the author best knowledge, no prior work was found in the open literature for the implementation of neural networks to noise prediction from airfoils.

4.3 Neural Networks Implementation

The objective of this section is to describe the general structure of the neutral networks and the approach used here to train them. The accuracy of the networks is assessed by developing several simple metrics as presented here. The data excluded from the training is also described.

4.3.1 General description of the models

The neural network implementation was performed using the Neural Networks tool box in Matlab. Although several different models have been developed, all of them have the same structure as illustrated in Figure 4.4. The general characteristics of the neural networks models are the following:

i. The neural network implemented is only able of predicting TBL-TE and LBL-VS noise because the training data corresponding to the presence of only these noise mechanisms.

ii. The input to the networks is given by aerodynamic parameters, i.e. effective angle of attack, Reynolds number based on the chord length, displacement thickness, and the airfoil geometry.

iii. The output is given by sound pressure level in 1/3rd octave band in the same range of frequency than the available training data, e.g. 630 to 4000 Hz. Working in this range

is acceptable considering that according to Lowson and Bullmore (1996), broadband noise between 500 and 1000 Hz would be the dominant noise for a typical wind generator. Therefore, most parts of the dominant frequency range would be covered.

iv. The predictions are valid for an observer located at 3 m from the trailing edge in direction perpendicular to the plate containing the chord and span lines of the airfoil. This is $r_r = 3m$, $\theta_r = \pm 90^o$ and $\varphi_r = 90^o$ following the coordinates system presented in Figure 2.7. The reason for considering the predictions valid at both sides of the airfoil is that the directivity function of airfoils can be considered symmetric with respect to the chord as presented in section 2.2. This is the reason for using training data that correspond to locations of the observer at the suction or pressure side indistinctly.

v. In all models, two neural networks are used. One is trained with data corresponding to tripped cases and the other is trained with data corresponding to the no-tripped cases.

vi. Hidden layers are present only in some models.

vii. The experimental noise spectra were not normalized before being presented to the networks.

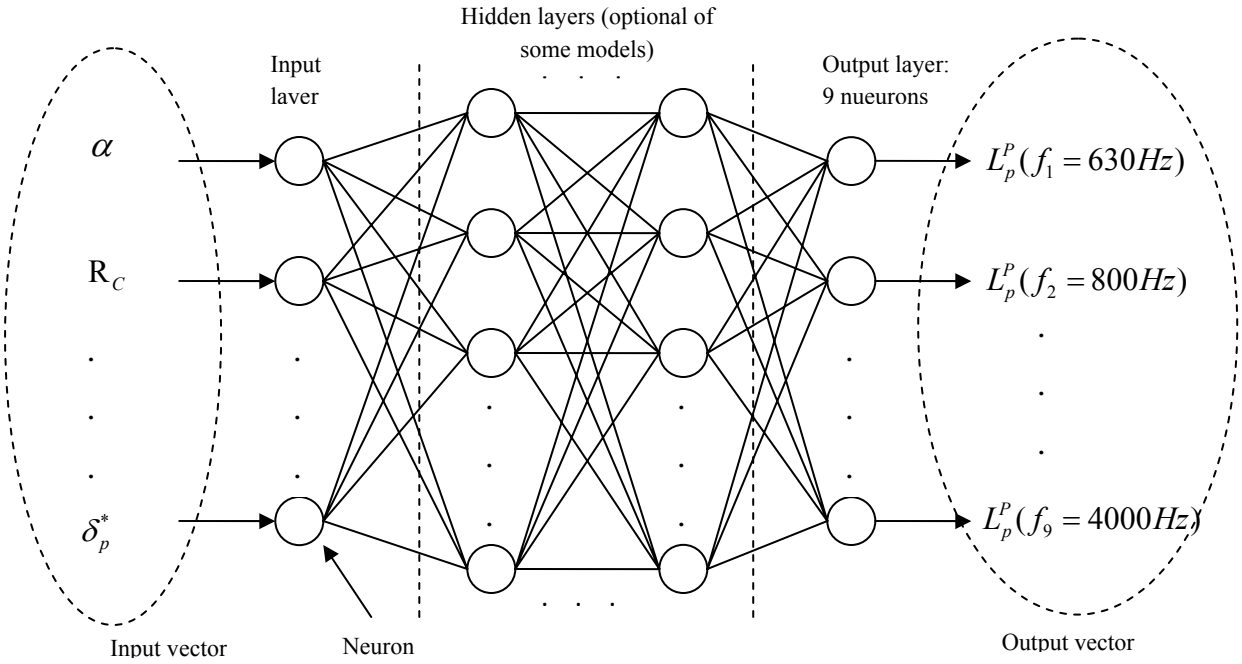

Figure 4.4: *Schematic representation of the general neural network model applied in the present work*

4.3.2 Training the Networks

An important problem when developing a neural network is to asses the capacity of the network to predict the phenomenon of interest. In contrast to other numerical models, it is important to consider that the neural networks do not include any theoretical modeling of physical phenomena. The neural networks are mathematical entities trained to reproduce a trend given by a data set. Consequently, it is uncertain how the neural network will respond in its predictions, especially if the input data is not close to the training data used. In general, a group of data is excluded from the training set to be used to contrast the predictions obtained with the trained network. This process is very convenient when sufficient training data is available. If the quantity of training data is limited, excluding some data from the training set can potentially lead to an inadequate training.

The experimental data to be used in the training of the neural networks for noise predictions were described in Chapter 3. Since these data are not very extensive, it was decided

not to exclude a subset for the purpose of assessing the accuracy of the networks. Therefore, two different approaches were used for the training and assessing the accuracy of the networks. These approaches are:

a) Conventional Training of the Neural Network (CTNN)

The training of the neural network will be carried out by using the complete data set. This procedure will be referred as CTNN. This is the typical method for training and commonly found in the literature reviewed. This method is the most adequate when the objective is just to reach the training targets with the highest precision. This approach will be used to create the network for airfoil noise predictions. However, the method does not provide any means to assess the capacity of the network to predict the response to input data other than the one included in the training set.

b) Alternative Training for Assessing Network Accuracy (ATANA)

To assess the accuracy of the network, it is trained again using all the data except for one test vector. This network training is referred as ATANA. The vector excluded from the training is known as control vector. In order to test the network for different conditions, multiple control vectors are considered. In this way, the capacity of the network to predict new inputs is tested for all the cases available. Each network created by this approach is expected to be similar to the network created by the CTNN approach since the training matrix differs in a single vector. In consequence, it is expected that the networks developed by the ATANA approach will provide some information about how well the network created by the CTNN approach will behave.

As mentioned earlier, the network created by the CTNN approach will be ultimately used for airfoil self noise predictions. Here, all the m vectors available for training are used as control vector. Thus, there will be m neural networks trained with $m-1$ data points to asses the accuracy of the network using all m data points (CTNN network).

4.3.3 Metrics to Assess Neural Network Accuracy

One of the most important steps in the development of the neural networks tool is to assess the accuracy of each model. This is necessary in order to determine if the changes implemented improve the network behavior. The assessment of the networks performance can be carried out by visually inspecting the network output to the experimental data used as control vectors. However, this process is time consuming due to the large number of vectors, e.g. more than 500. Therefore, it is proposed to asses the accuracy of the predictions by using simple metrics as described here.

Average Level Difference

This metric is based on computing the difference in the average spectra level as follows

$$\Delta\bar{L}_p = \bar{L}_p^E - \bar{L}_p^P \tag{4.2}$$

where superscript *E* and *P* indicates the experimental and predicted results, respectively, and the line over the levels indicate that they are averages.

Using the illustrative spectra in Figure 4.5, the average spectra level is computed as

$$\bar{L}_p = 10\log_{10}\left(\frac{1}{n}\sum_{i=1}^{n} 10^{L_{p\,i}/10}\right) \tag{4.3}$$

where $L_{p\,i}$ is the sound pressure level in the i^{th} band and the summation goes over the 1/3 octave bands from $f_1 = 630$ to $f_n = 4000$ Hz and n is the number of bands in the frequency range. The physical interpretation of this metric is shown in Figure 4.5.

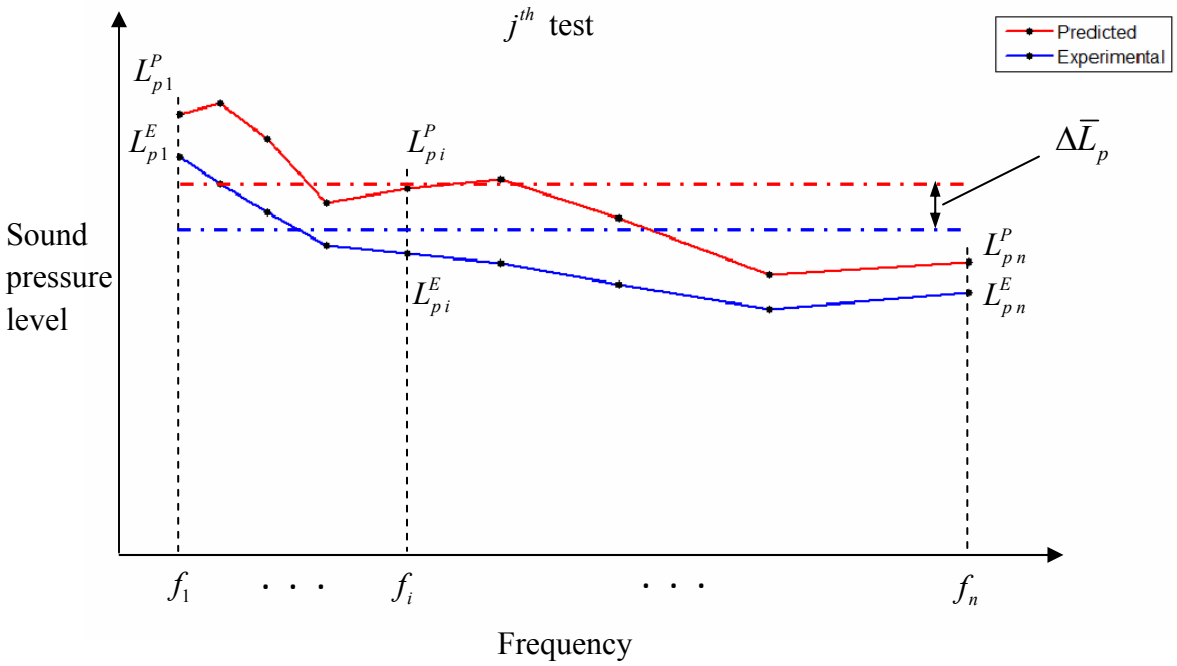

Figure 4.5: *Schematic representation of the physical meaning of the average level difference metric correspond to the* j^{th} *test of a set of* m *tests with frequencies ranging from* f_1 *to* f_n*. Predicted and experimental noise spectra indicated with continuous red and blue lines respectively. Predicted and experimental average level difference* $\left(\overline{L}_p\right)$ *represented in red and blue dashed lines respectively.*

This average spectra difference is computed for all m control vectors. To assess the overall performance of the network, the average of the absolute value of the m calculated $\Delta\overline{L}_p$ is computed as follows

$$\left(\Delta\overline{L}_p\right)_{avg} = \frac{\sum_{j=1}^{m}\left|\left(\Delta\overline{L}_p\right)_j\right|}{m} \tag{4.4}$$

where the subscript j indicates that the summation is performed for the $\Delta\overline{L}_p$ corresponding to each of the m tests. Though not strictly correct mathematically, this overall value provides a simple number that represent the expected difference in decibels between the predicted and

experimental data in an average sense over frequency range and aerodynamic envelope of the data set.

Maximum Level Difference

This metric is based on computing the maximum difference between the predicted and experimental spectra in disregard of what frequency band this maximum difference takes place on. That is

$$\Delta L_{p\,Max} = \max \left| L_{p\,i}^{E} - L_{p\,i}^{P} \right|. \tag{4.5}$$

The maximum level difference of the spectra $\Delta L_{p\,Max}$ is graphically depicted in Figure 4.6. It is clear that this metric is always equal or larger than the average one presented previously.

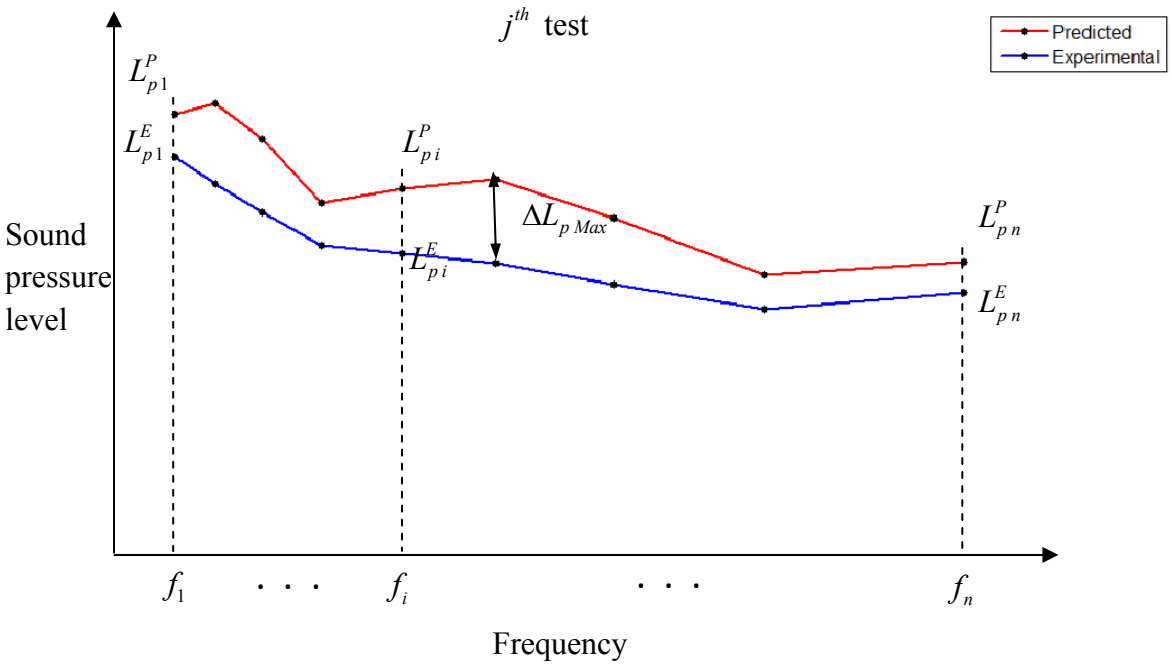

Figure 4.6: *Schematic representation of the physical meaning of the maximum level difference metric correspond to the j^{th} test of a set of m tests with frequencies ranging from f_1 to f_n. Predicted and experimental noise spectra indicated with continuous red and blue lines respectively.*

As before, an overall average is computed as

$$\left(\Delta L_{p\,\max}\right)_{avg} = \frac{\sum_{j=1}^{m}\left|\Delta L_{p\,\max}\right|}{m} \tag{4.6}$$

R-square correlation

The use of R-squared correlation has become common in the field of neural networks and it is also implemented in this problem. The metric is obtained by computing the linear regression between each element of the network output and the corresponding target for the training set. Then, the difference between response and target is calculated and expressed in root-mean-

square (rms) terms. Therefore, if the output of the network is composed of n 1/3th octave band levels, then n R-squared correlation values are calculated.

$$\left(r_{rms}\right)_i = \frac{\sqrt{\sum_{j=1}^{m}\left(L_{p\,ij}^{E} - L_{p\,ij}^{P}\right)^2}}{\sqrt{m}} \quad \text{for} \quad i = 1,\cdots,n \tag{4.7}$$

where *norm* is the Euclidean norm, and i denotes each of the n frequencies bands. The levels $\vec{L}_{p\,i}^{E}$ and $\vec{L}_{p\,i}^{P}$ are vectors containing the levels for the i^{th} band frequency and for all the m data vectors available. Therefore, $\vec{r}_{rms}$ is a vector of length n containing the R-squared correlation obtained for each frequency. Then, on order to transform this in a single value, a subsequent rms calculation is applied.

$$R_{RMS} = \frac{\sqrt{\sum_{i=1}^{n}\left(r_{rms}\right)_i^2}}{\sqrt{n}} = \frac{\sqrt{\sum_{i=1}^{n}\sum_{j=1}^{m}\left(L_{p\,ij}^{E} - L_{p\,ij}^{P}\right)^2}}{\sqrt{nm}} \tag{4.8}$$

It is important to note that this metric was used in the training of the networks, i.e. used by the Matlab routines.

4.3.4 Data excluded

As indicated in the previous chapter, some of the experimental data was not used in the training of the networks. In this section, the experimental data that was not included are described. They are:

i. One of the parameters that are intended to be used for the neural networks implementation is the boundary layer displacement thickness. Here, the boundary layer parameters were predicted using the code XFOIL (Drela and Youngren, 2001). In Appendix B, a brief description of XFOIL is presented, and the validity of the predictions is assessed by comparing them with experimental data available in literature. For some airfoils at high

angles of attack, XFOIL failed to converge. Therefore, for the neural networks implementations only the tests cases for which the displacement thickness could be predicted are included in the training matrix.

ii. The acoustic data corresponding to the SH3055 airfoil could not be used because the geometry coordinates were not found in the open literature.

iii. The acoustic data corresponding to the DU97-W300, DU97-W900 and the DU97-W900 with splitter plate were also excluded because these airfoils do not have sharp trailing edges. The vortex shedding due to blunt trailing edges is not considered in this initial study.

iv. Some results for the NACA 0012 airfoil for the same conditions were available from NASA and NLR tests. Thus, only the NLR data was used for the aforementioned test condition. The NLR data was chosen because it provided a richer database in terms of angles of attack and flow speeds.

The data used in the development of the neural networks is shown in Figures 4.7 and 4.8 corresponding to tripped and no-tripped cases. Each polygon represents a Reynolds number versus angle of attack range for witch the corresponding airfoil was tested. Each test is depicted with a different color.

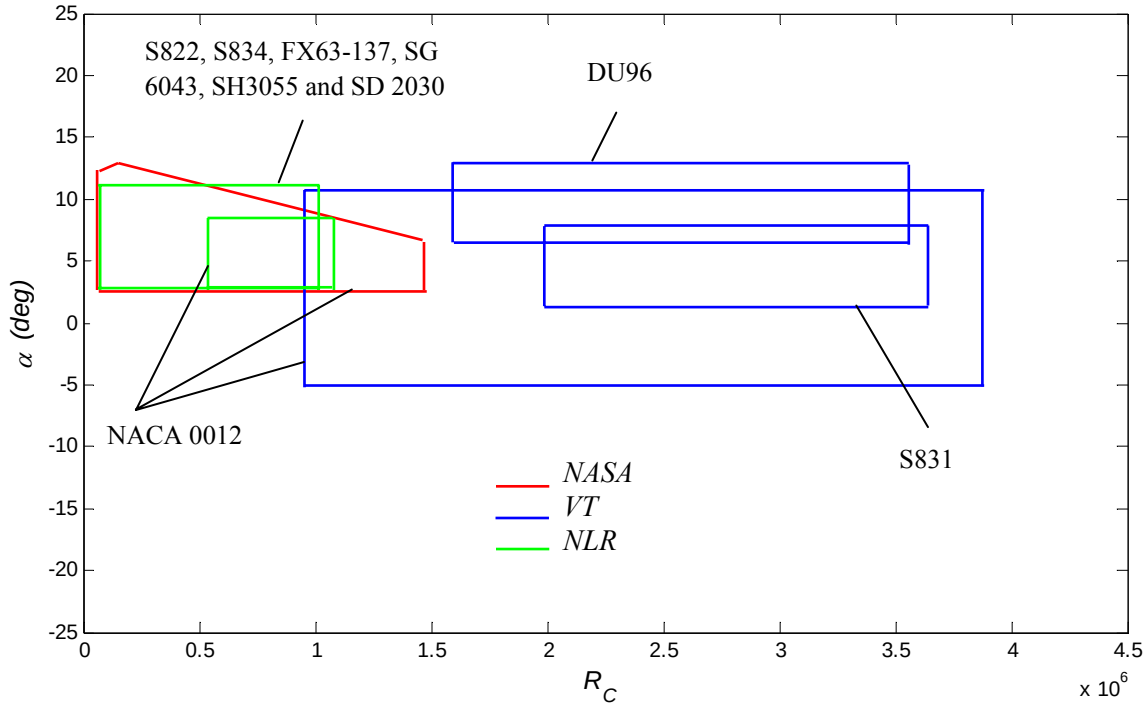

Figure 4.7: *Summary of the Reynolds number versus angle of attack range of the tests results used for training the networks. Tripped cases.*

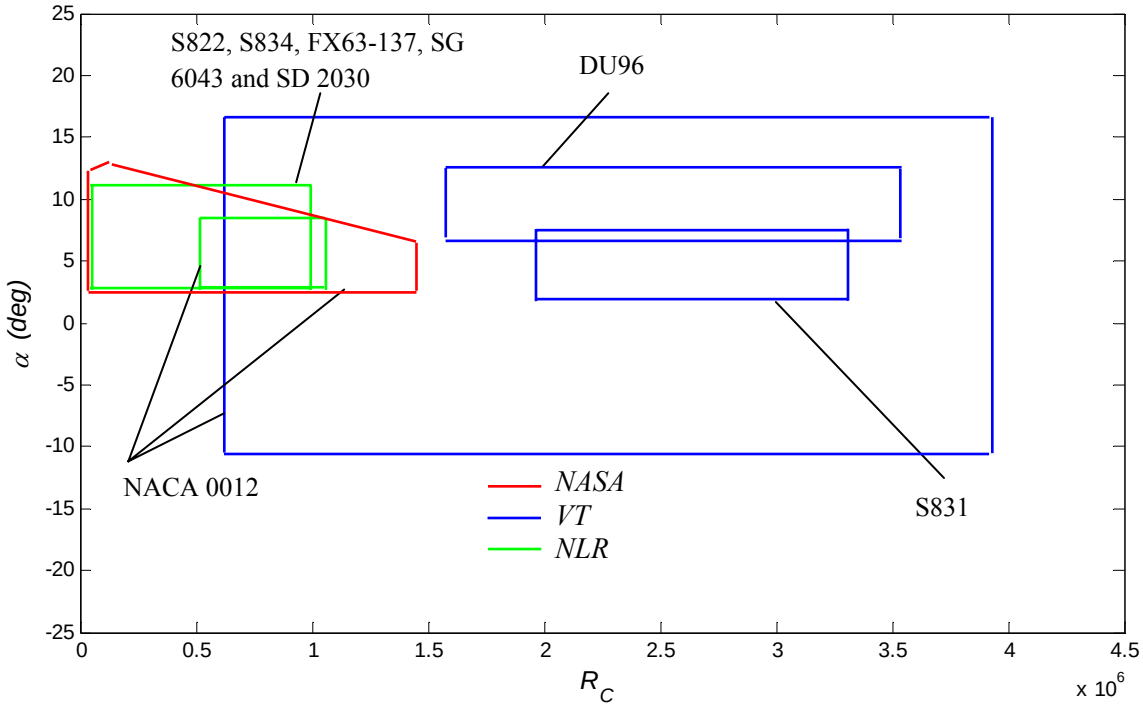

Figure 4.8: *Summary of the Reynolds number versus angle of attack range of the tests results used for training the networks. No-tripped cases.*

4.4 Airfoil Self Noise Neural Networks

The present section describes the implementation of two neural networks models of increasing complexity. The first model is trained with experimental data obtained for NACA 0012 airfoils. The second model incorporates training data corresponding to several different airfoils. In order to take in account the shape of the airfoils, this model includes parameters describing the geometry of the airfoils.

4.4.1 Neural Network for NACA0012 Airfoil

Several neural network configurations were developed using only NACA 012 airfoil data. The main aim of these initial studies is to investigate the performance of the network excluding the effect of the airfoil shape.

The first models implemented are simple configurations used to get familiarized with the neural networks. The training matrix used consists of the experimental data obtained at the VT wind tunnel for the 0.91 m chord airfoil and the data obtained by NASA for airfoils of chord ranging from 0.025 m to 0.3 m. As the present model is a first assessment of the neural networks capacity, the data corresponding to a NACA 0012 airfoil tested at NLR (Oerlemans, 2004) is not included for simplicity in the calculations. Furthermore, the chord of the NACA 0012 airfoil tested at NLR is the same than for one of the airfoils tested at NASA.

Due to the symmetry of the NACA 0012 airfoil, it is expected to have the same acoustic behavior for negative and positive angles of attack. Therefore, data for negative angles was used by simply taking the absolute value of the angle of attack.

Table 4.1 summarizes the main characteristics of the neural network models. The input parameters consisted of flow speed, chord length, effective angle of attack, and in some cases the boundary layer displacement thickness at the trailing edge at the suction side and/or pressure side.

Table 4.1: Description of the neural network model I developed. The same model is used for the tripped and the no-tripped networks.

Model I	
Input	Flow speed
	Chord
	Effective angle of attack
	Boundary layer displacement thickness at the trailing edge at the suction side
	Boundary layer displacement thickness at the trailing edge at the pressure side
Output	L_p in 1/3rd octave bands for 9 frequencies ranging from 630 to 4000 Hz
Number of layers	2 to 4
Training data	0.9 m chord NACA 0012 tested by VT
	0.025 to 0.3 m chord NACA 0012 airfoil tested by NASA

To seek the optimal configuration of the network, eight models (denoted as I-*a* thought I-*h*) were developed. The differences among the models are based on training settings or input data used. The eight models are presented in Table 4.2. For Models I-*a* thought I-*g*, the networks consist of two layers with 20 neurons in the input layer and 9 neurons in the output layer. The number of input neurons was empirically chosen. The 9 output neurons correspond to the 9 frequencies for which the acoustic data is considered. In the last model (I-*h)*, two hidden layers are incorporated.

For all models, the training algorithm used was *trainlm* and the transfer functions for the input-output layer were *tansig-purelin.* These configurations were found to be the most effective among several tried. For I-*h* model, *tansig-logsig* transfer functions were used in the hidden layers. It can be seen in Figure 4.9 that the transfer functions *tansig* and *logsig* are nonlinear

functions while *purelin* is linear. The number of epochs used for the training process was varied between 25 and 500 depending on the case. It is important to note that for Model I-*h,* no training epochs number was set. In this case, a target error was used for stopping the training process. The reason for this difference is that when hidden layers are used, the training for each epoch is very slow. Therefore, it is necessary to set an error target in order not to go over an excessive number of training epochs.

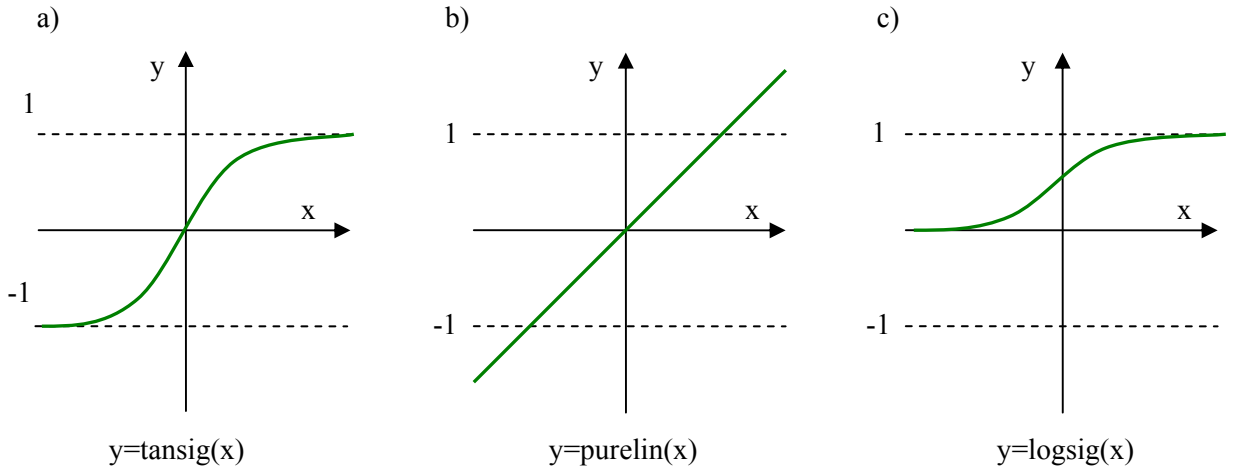

Figure 4.9: *Transfer functions used in the neural networks implemented. a) Tansig transfer function. b) Purelin transfer function. c) Logsig transfer function.*

In all models, flow speed, chord length, and effective angle of attack are used in the input matrix. In addition, for Models I-*e* to I-*h*, boundary layer displacement thicknesses for the suction and/or pressure side are used as shown in Table 4.2. The reason for adding the boundary layer parameters to some cases is that the noise spectra seem to scale well with the boundary layer displacement. The boundary layer displacement thickness corresponding to the pressure and suction sides of the airfoil required as inputs were predicted using XFOIL (Drela and Youngren, 2001).

The metrics presented in Section 4.3.2 are also presented in Table 4.2, e.g. equations 4.3, 4.5, and 4.7. Note that the metrics were computed for the ATANA networks and the CTNN

network. However, it is important to clarify that the results for the ATANA approach are considered more important to assess the network accuracy.

The results in Table 4.2 show that when the boundary layer displacement thickness is not used for training the networks (cases I-*a* to I-*d*), increasing the number of epochs above 50 does not improve the accuracy of the networks. Moreover, using more than 100 epochs could over train the neural networks leading to less accurate predictions. Another case of over-training can be observed by comparing the metrics of case I-*f* and I-*g*. In this cases, increasing the number of epochs from 50 to 500 lead to a high reduction in the prediction accuracy, i.e. 0.95 to 0.57 in the R-square correlation for the tripped case.

The assessment of the influence of using hidden layers can be performed by comparing cases I-*e* and I-*h*. For both these cases, the pressure side boundary layer displacement thickness is used. Comparison of the aforementioned cases shows no significant improvement of the predicting capacity by incorporating hidden layers. In fact, adding the hidden layers degraded the metrics, i.e. from 0.98, 1.4 dB, and 3.7 dB to 0.95, 1.8 dB, and 4.3 dB for the R-square, average level difference, and maximum level difference for tripped cases, respectively.

Comparison of the metrics between tripped and no-tripped cases shows a higher level of accuracy in the predictions for tripped cases. For model I-*a,* the metrics for tripped cases are 0.98, 1.5 dB, and 4.2 dB, and for no-tripped cases 0.91, 3.5 dB, and 7.7 dB, respectively.

In the overall evaluation of the metrics, Model I-*e* provides the most accurate network for both the tripped and no-tripped cases. However, all the other models seem to perform reasonably well with results only slightly poorer than the model I-*e*. This observation suggests that the actual network configuration to be used for noise predictions is not very sensitive.

Table 4.2: Comparison of the results obtained for different network configurations and training settings for Model I using the Alternative Training for Assessing Network Accuracy (ATANA) approach.

Model I

Case	***a***	***b***	***c***	***d***	***e***	***f***	***g***	***h***
NN Architecture	20-9	20-9	20-9	20-9	20-9	20-9	20-9	20-30-30-9
Training Algorithm	trainlm	trainlm	trainlm	trainlm	trainlm	trainlm	trainlm	trainlm
Transfer functions	tansig-purelin	tansig-purelin	tansig-purelin	tansig-purelin	tansig-purelin	tansig-purelin	tansig-purelin	Tansig-tansig-logsig-purelin
Number of epochs	25	50	100	500	50	50	500	About 15
Error target	-	-	-	-	-	-	-	10^{-5}
Displacement thickness	Not used	Not used	Not used	Not used	Pressure side	Pressure and suction side	Pressure and suction side	Pressure side
Configuration	tripped/ no-tripped	tripped/ no-tripped	tripped/ no-tripped	tripped/ no-tripped	tripped/ no-tripped	tripped/ no-tripped	tripped/ no-tripped	tripped/ no-tripped
R-Square correlation	0.977/ 0.908	0.980/ 0.913	0.968/ 0.886	0.948/ 0.897	0.979/ 0.876	0.949/ 0.905	0.566/ 0.793	0.953/ 0.893
Average Level difference (dB)	1.5/ 3.5	1.3/ 3.4	1.6/ 4.2	1.4/ 3.8	1.4/ 3.3	1.9/ 3.5	4.9/ 4.1	1.8/ 2.9
Maximum Level difference (dB)	4.2/ 7.7	3.9/ 7.7	4.1/ 8.5	3.8/ 7.8	3.7/ 7.9	4.4/ 7.6	8.8/ 9.8	4.3/ 7.2

The results in Table 4.2 present the average metric for all *m* control vectors. Figures 4.10 through 4.13 present the average and maximum level difference metrics for the individual control vectors using Model I-e. In these figures, the control vector case is defined as a circle in a plot of the angle of attack (α) versus chord Reynolds number (R_c). A color scheme is used to plot the magnitude of the calculated metric. The color scheme ranges from 0 to 10 dB for the figures representing the average level difference metrics and from 0 to 20 for the maximum level difference metrics. Nevertheless, there were few cases for which the levels of the metrics were outside this range, e.g. the case indicated as *d* in Figure 4.10 for which the average difference level metric is 25 dB. The cases that are indicated with letters in these figures will be analyzed in detail later in the section. For the sake of completeness, Appendix E presents results similar to Figures 10 through 13 but with a color-bar that shows a larger range.

Figures 4.10 and 4.11 present the results of the average and maximum difference level metrics for the no-tripped case, respectively. Figures 4.12 and 4.13 present similar results but for tripped cases. Inspection of these figures shows that the lower levels of accuracy tend to occur almost exclusively at the boundaries of the training set. This result is not unexpected since it has been reported the limitation of the neural networks to extrapolate.

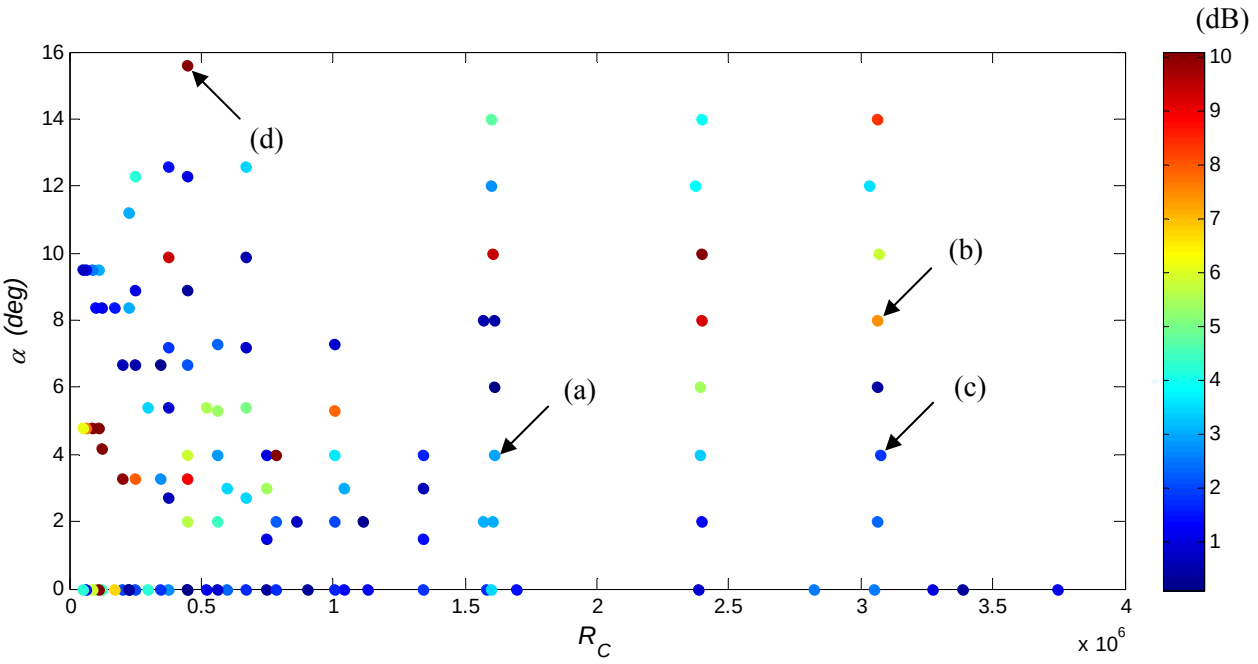

Figure 4.10: *Average Level difference metric for each control vector using Model I-e for no-tripped case. Training using the ATANA approach.*

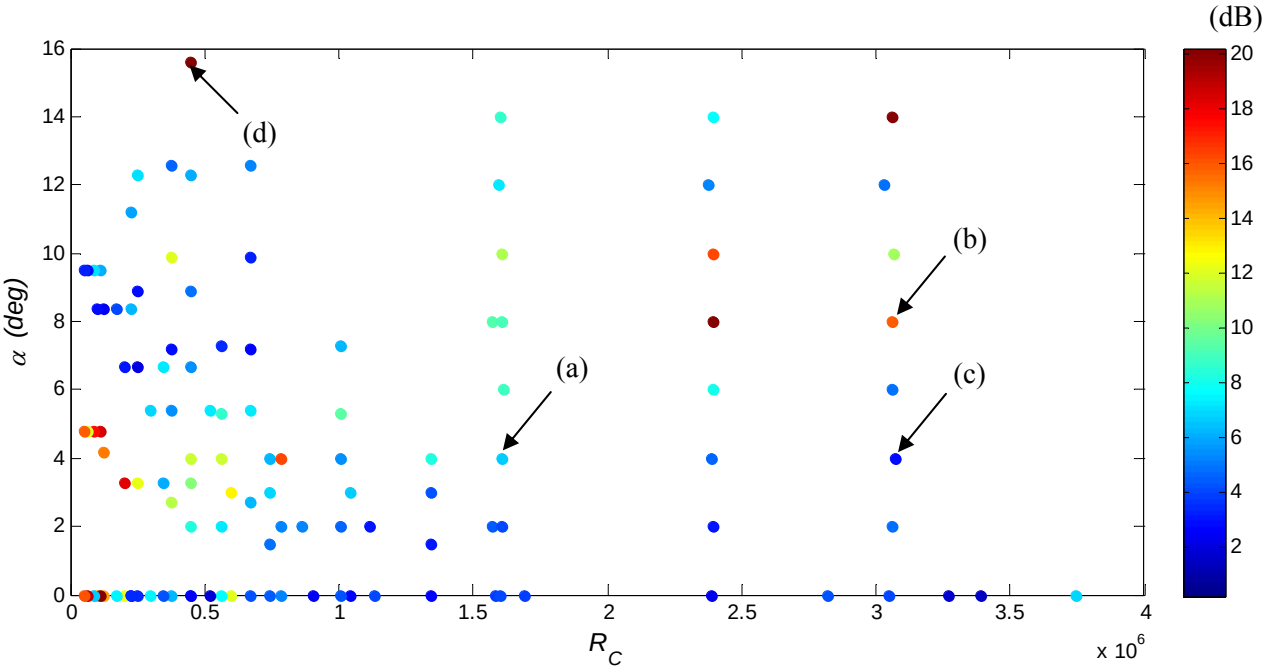

Figure 4.11: *Maximum Level difference metric for each control vector using Model I-e for no-tripped case. Training using the ATANA approach.*

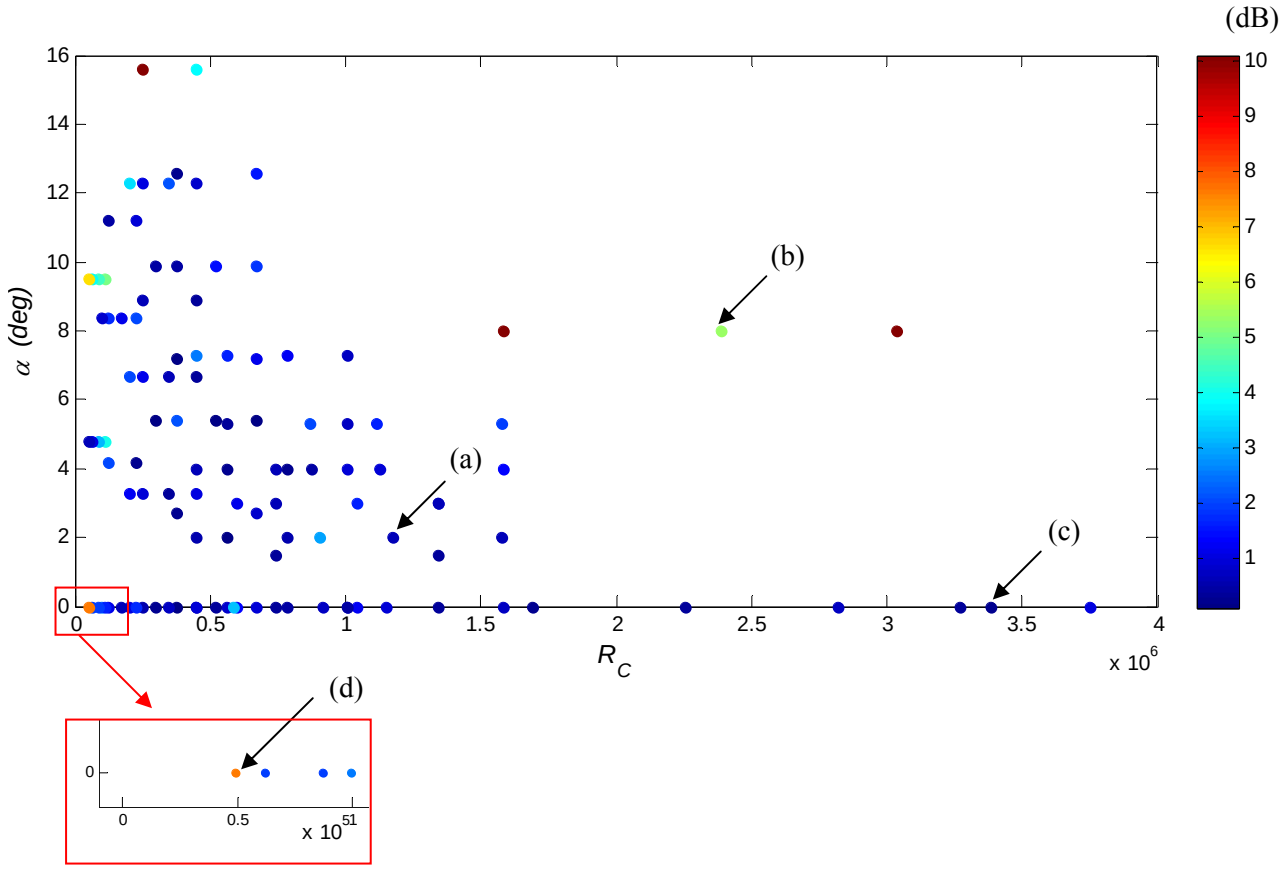

Figure 4.12: *Average Level difference metric for each control vector using Model I-e for tripped case. Training using the ATANA approach.*

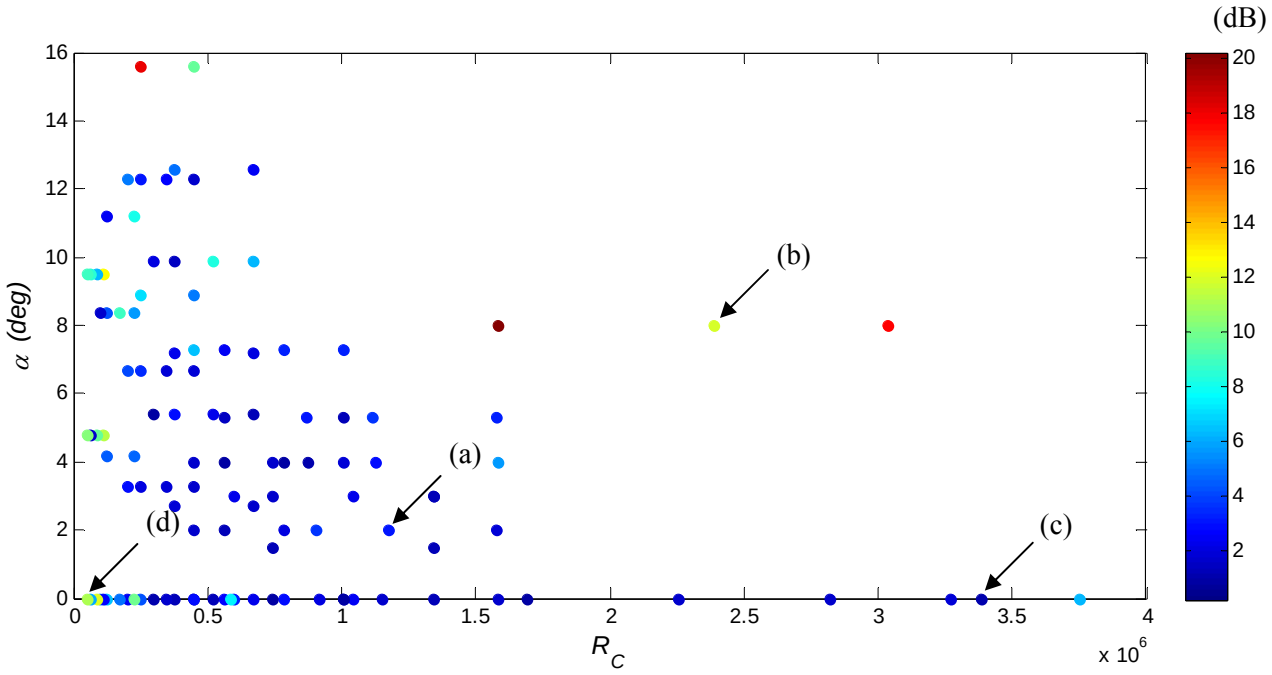

Figure 4.13: *Maximum Level difference metric for each control vector using Model I-e for tripped case. Training using the ATANA approach.*

To gain more in depth understanding of the accuracy of the network, comparison between experimental and predicted spectra for the control vectors are presented in Figures 4.14 and 4.15. In all cases, predictions were obtained with Model I-e. Figure 4.14a presents the case for $\alpha = 4°$ and $R_c = 1.6$ million in the no-tripped configuration. This case is indicated in Figures 4.10 and 4.11 with the letter *a*. It can be noticed that the predictions are within 7 dB for all frequency bands. In this case, the calculated average level difference is 4 dB and the maximum level difference is 8 dB. Figure 4.14b shows a case in which the experimental data presents vortex shedding noise. The case presented corresponds to 8^o of angle of attack and $R_c = 3.0$ million and it is indicated in Figures 4.10 and 4.11 with the letter *b*. It can be seen that in this case the prediction obtained with the neural network fails in approximating the vortex shedding peaks present in the experimental measurements. In this case, the calculated average level difference is 7 dB and the maximum level difference is 14 dB. Figure 4.14c presents the case for $\alpha = 4°$ and $R_c = 3.1$ million in the no-tripped configuration. This case is indicated in Figures 4.10 and 4.11 with the letter *c*. The predictions for this case are within 3 dB for all frequency bands (Average

and maximum level difference are 2 and 4 dB, respectively). Figure 4.14d shows a case that is located at the boundary of the data set. The case presented corresponds to 16^o of angle of attack and $R_c = 0.4$ million (letter *d* in Figures 4.10 and 4.11). It can be observed that the network completely fails in predicting outside the range of the training data.

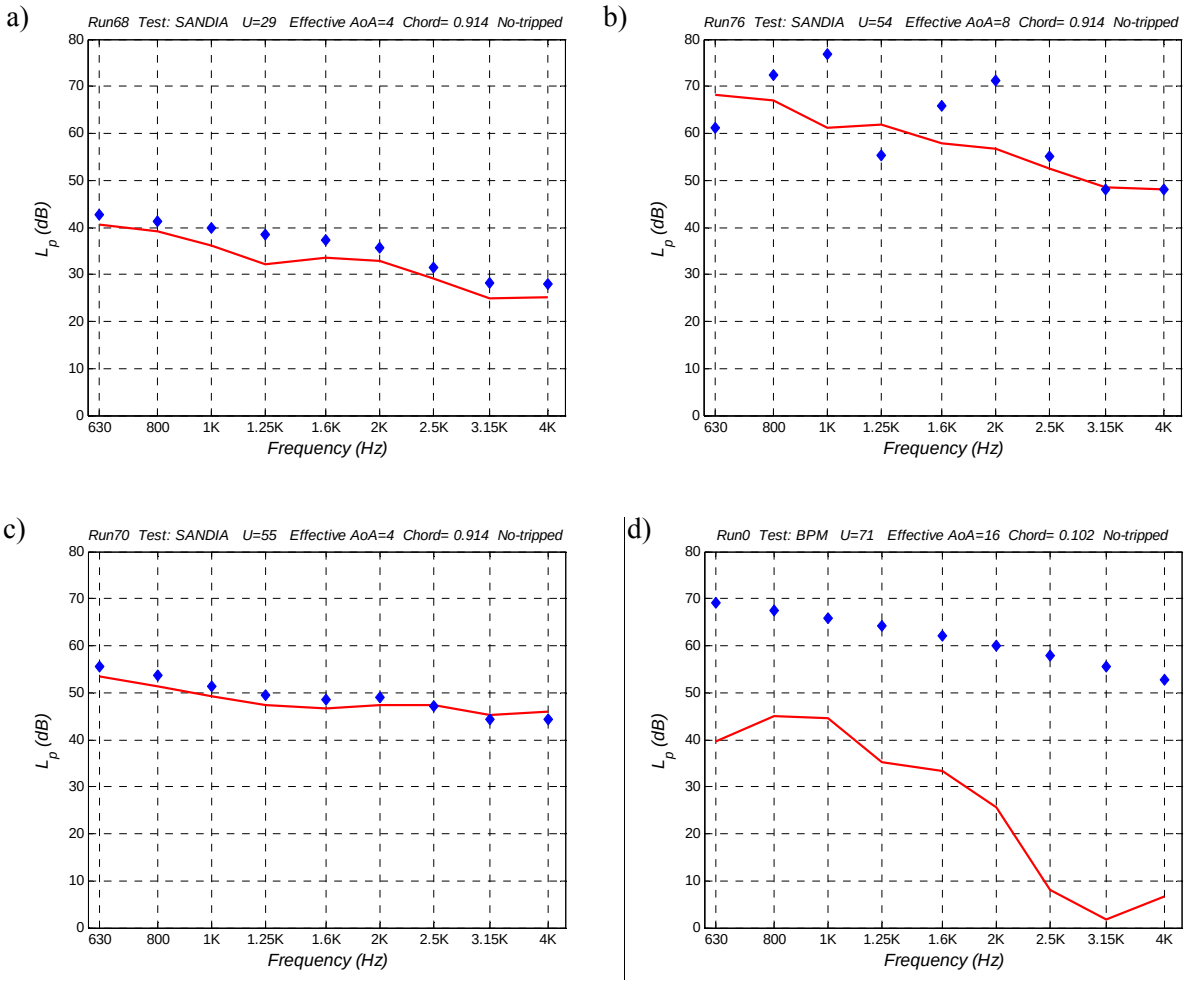

Figure 4.14: *Comparison of experimental results and predictions using Model I-e and ATANA training approach for no-tripped case: Control vectors a)* $\alpha = 4°$ *and* $R_c = 1.6$ *million, b)* $\alpha = 8°$ *and* $R_c = 3$ *million. c)* $\alpha = 4°$ *and* $R_c = 3.1$ *million, and d)* $\alpha = 16°$ *and* $R_c = 0.4$ *million.*
♦ *Experimental* —— *Prediction*

The results in Figure 4.15 present similar sample spectra for the tripped condition. The cases shown are indicated with the letters *a*, *b*, *c,* and *d* in Figures 4.12 and 4.13. The results

reveal the same trends as for the tripped cases. The network predicts very well all cases while failing to capture the vortex shedding mechanism is the few cases it takes place.

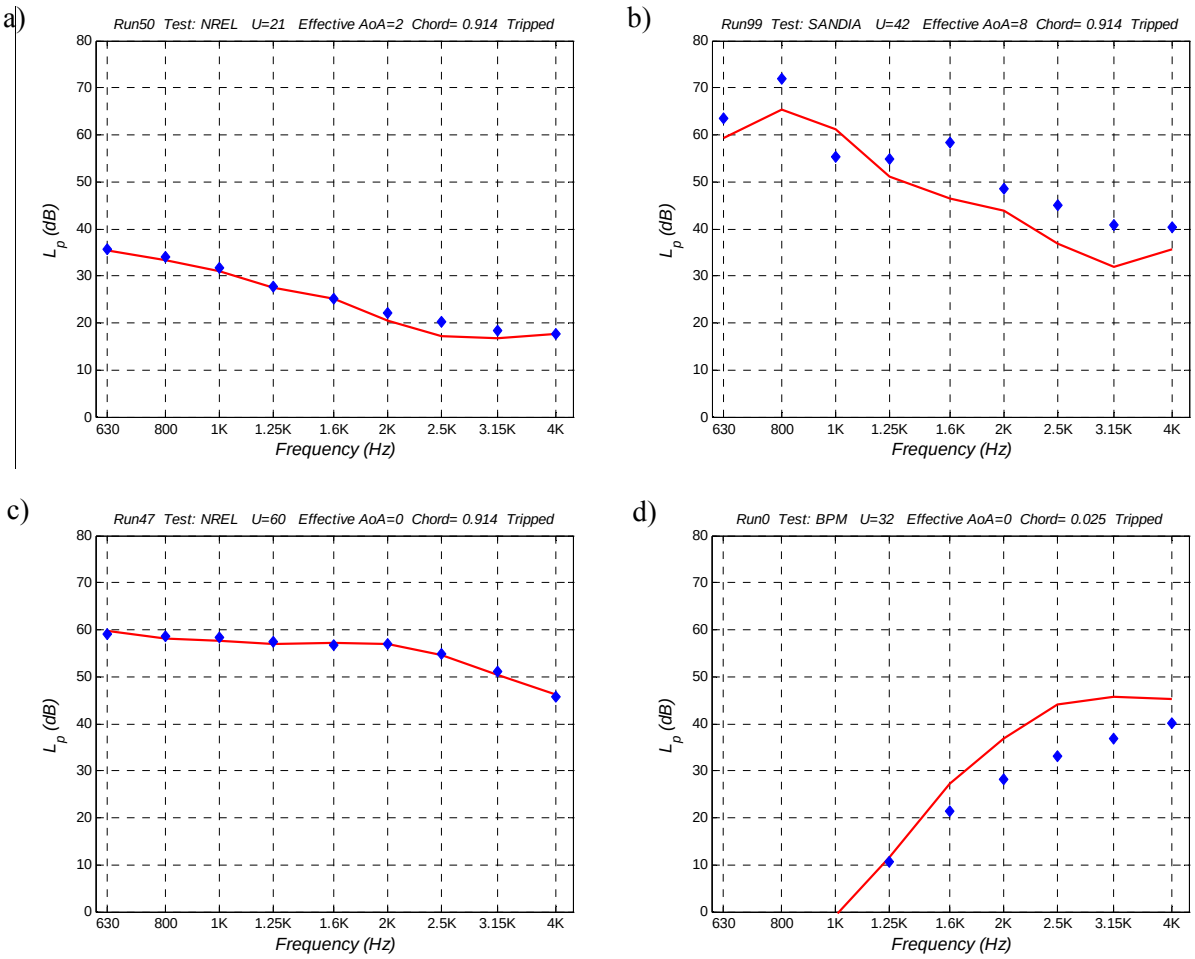

Figure 4.15: *Comparison of experimental results and predictions using Model I-e and ATANA training approach for tripped case: Control vectors a)* $\alpha = 2°$ *and* $R_c = 1.2$ *million and b)* $\alpha = 8°$ *and* $R_c = 2.4$ *million. c)* $\alpha = 0°$ *and* $R_c = 3.4$ *million and d)* $\alpha = 0°$ *and* $R_c = 0.05$ *million.*
♦ *Experimental* —— *Prediction*

Figures 4.16 through 4.19 present the average and maximum level difference metrics for the final network, e.g. CTNN training approach for Model I-e. These results are presented using the same format as in Figures 4.10 through 4.13. Figures 4.16 and 4.17 present the results for the no-tripped case while Figures 4.18 and 4.19 are for tripped cases. As expected, the results are about the same in Figures 4.10 through 4.13. This demonstrates that the network trained using all

the data (CTNN) and the ones used to assess the accuracy of the networks (ATANA) are similar. Sample spectra are presented in Figure 4.20 corresponding to the cases indicated with the letters *a* through *d*.

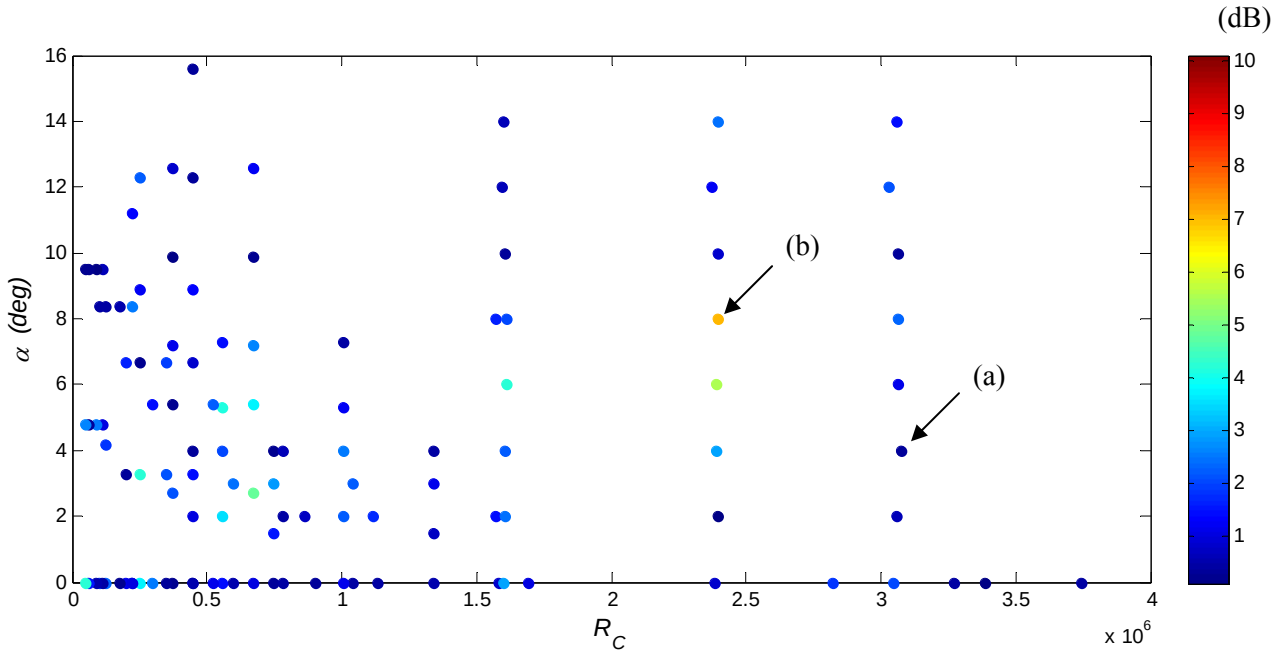

Figure 4.16: *Average Level difference metric for each test case vector using Model I-e for no-tripped case. Training using the CTNN approach.*

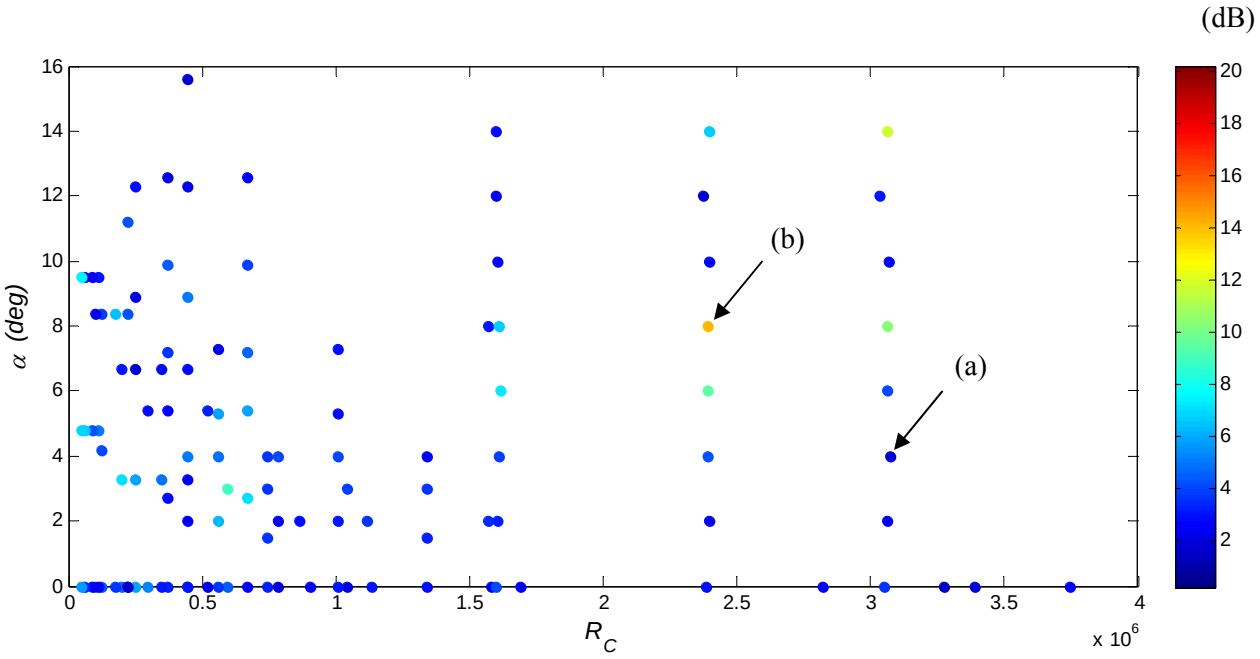

Figure 4.17: *Maximum Level difference metric for each test case vector using Model I-e for no-tripped case. Training using the CTNN approach.*

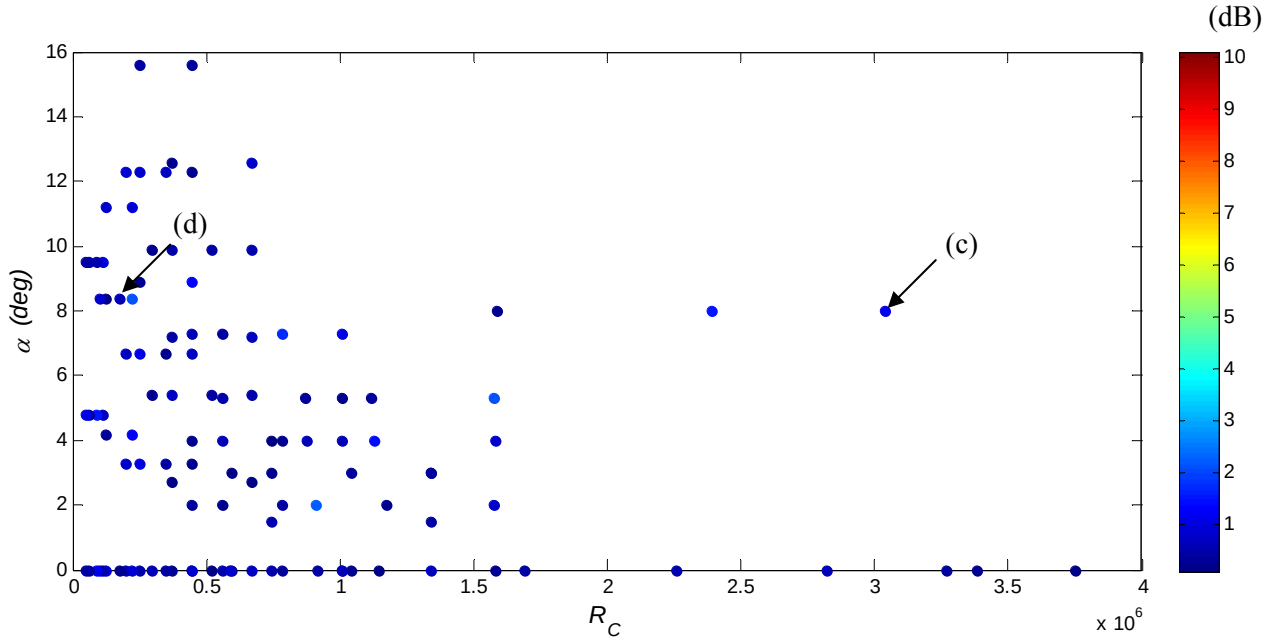

Figure 4.18: *Average Level difference metric for each test case vector using Model I-e for tripped case. Training using the CTNN approach.*

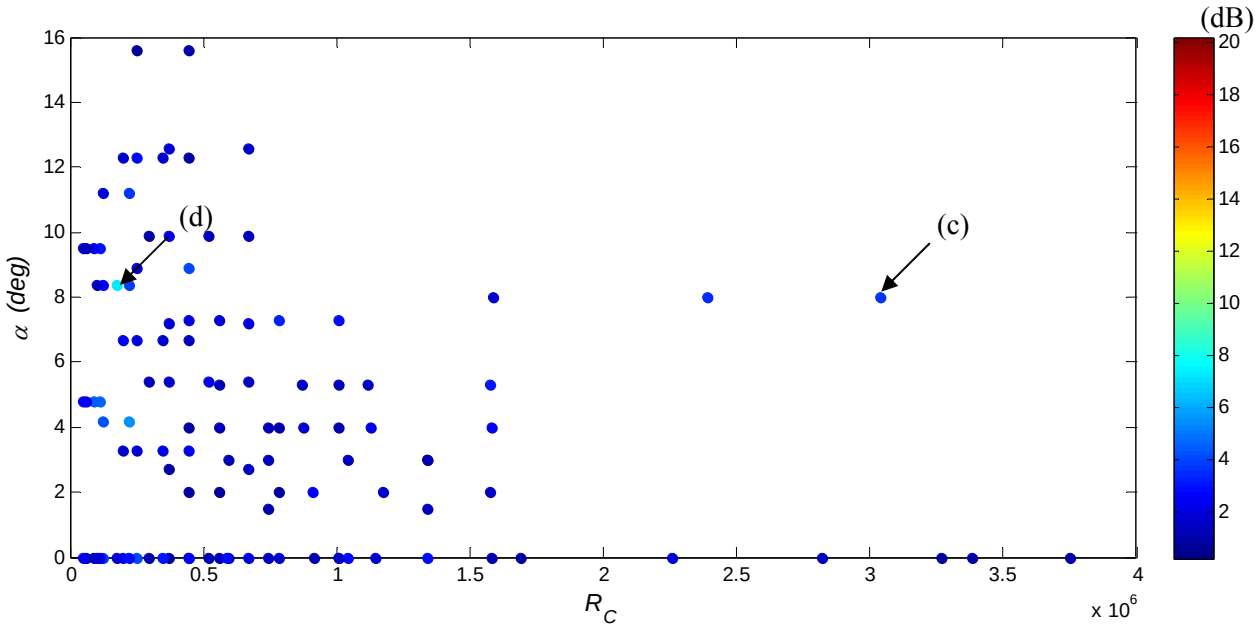

Figure 4.19: *Maximum Level difference metric for each test case vector using Model I-e for tripped case. Training using the CTNN approach.*

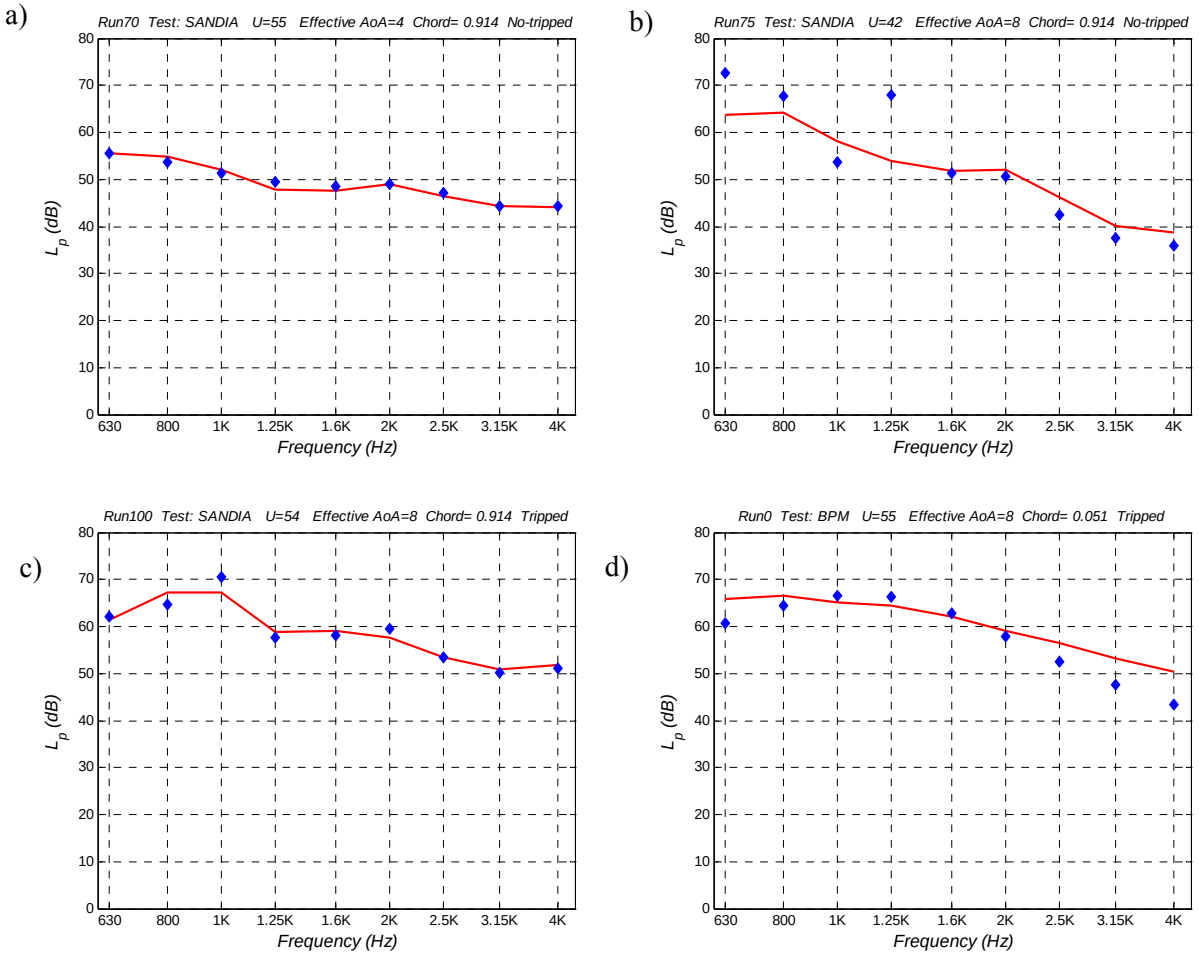

Figure 4.20: *Comparison of experimental results and predictions using Model I-e and CTNN training approach: Control vectors a) No-tripped case,* $\alpha = 4°$ *and* $R_c = 3.1$ *million, b) No-tripped case,* $\alpha = 8°$ *and* $R_c = 2.4$ *million, c) Tripped case,* $\alpha = 8°$ *and* $R_c = 3.1$ *million and d) Tripped case,* $\alpha = 8°$ *and* $R_c = 0.18$ *million.*

♦ *Experimental* —— *Prediction*

4.4.2 Implementation including airfoils other than NACA0012

This case constitutes a generalization of the previous models for different airfoil's geometry. The data used for training the network correspond to the NACA 0012, Sandia S831, S822 and S834, Delft DU96, FX63-137, SG 6043, and SD 2030 airfoils.

As nonsymmetrical airfoils are included in the training set of the present model, data corresponding to positive and negative angles of attack are considered. Therefore, the data corresponding to NACA 0012 airfoils for VT and NLR tests was doubled by using the original data set plus a data set similar to the original but with the sign of the angle of attack changed. This process was not applied to the data corresponding to NASA because it was desired to keep the size of the data reasonable for the computation time point of view.

The airfoil geometry is taken in account by parameters obtained through a Karman-Trefftz conformal mapping or by polynomial approximation of the pressure and suction surfaces.

The Karman-Trefftz conformal mapping is a technique typically used in aerodynamics for mapping a circle (contained in the ζ -plane) into an airfoil with a specific trailing edge angle (z-plane) and vice versa as it is depicted in Figure 4.21. This procedure allows simplifying the aerodynamic calculations by performing them in the ζ domain where the boundary conditions are simple. Then, the results can be mapped into the physical domain (z-plane). The Karman-Trefftz transformation is given by

$$\frac{z-nD}{z+nD}=\frac{(\zeta-D)^n}{(\zeta+D)^n}, \tag{4.9}$$

where

$$\Psi=\pi(2-n), \tag{4.10}$$

and Ψ is the trailing edge angle (Angle Ψ in Figure A.1 of Appendix A).

The shape of the airfoil can be controlled through the position of the circle, ζ_1, the parameter D, and the angle Ψ. The real part of ζ_1 controls the thickness of the airfoil, the imaginary part controls the camber, and D controls the chord of the airfoil. The trailing edge angle is controlled by Ψ as it was previously stated.

The approach used in the present work is finding values for the conformal mapping parameters to approximate the airfoil's shape. The explicit expression necessary for the transformation can be obtained by a series expansion of equation (4.9) (Karamcheti, 1980). In the present work, the first two terms of the series were used as follows

$$z = \zeta + \frac{n^2 - 1}{3}\frac{D^2}{\zeta} + \ldots \tag{4.11}$$

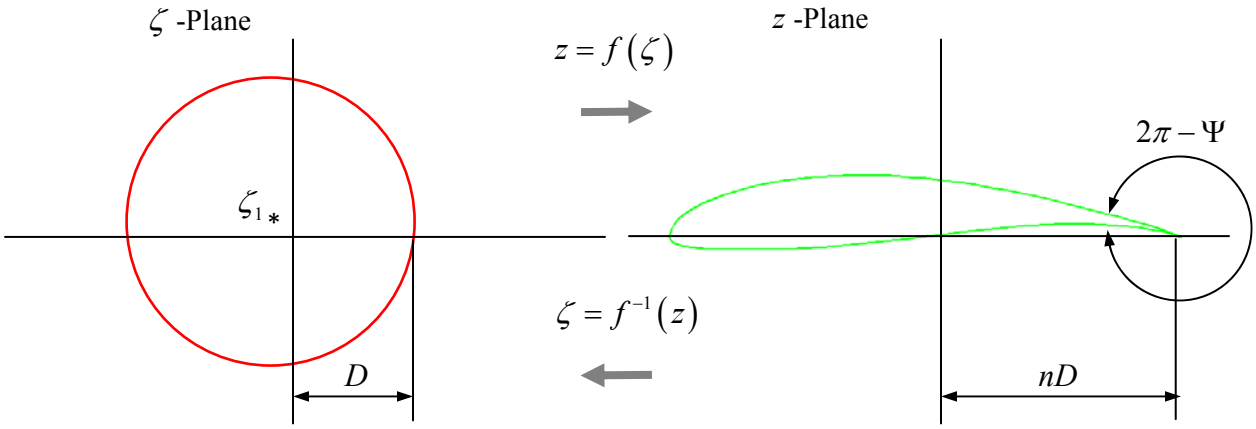

Figure 4.21: *Schematic description of the Karman-Trefftz conformal mapping.*

It is important to clarify that the Karman-Trefftz conformal mapping has limitations in terms of the geometries that it can produce. Some geometrical characteristics can not be controlled. Therefore, the Karman-Trefftz conformal mapping conduces to geometries that are only an approximation to the actual airfoil shapes. Figure 4.22 shows an example of the FX63-137 airfoil and the conformal mapping approximation. In Appendix C, comparison of the airfoil geometry with the approximate geometry obtained is presented for all airfoils.

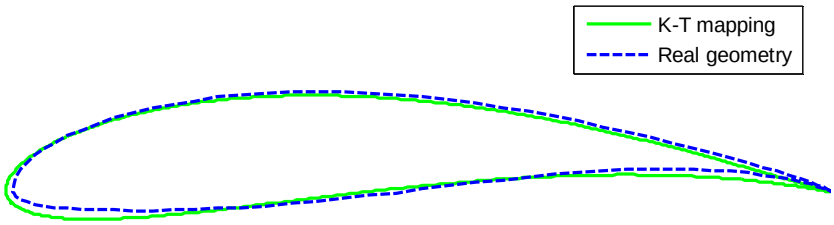

Figure 4.22: *Example of the shape of an FX63-137 airfoil originated through Karman-Trefftz conformal mapping compared with the desired geometry.*

The second approach to define the airfoil geometry consisted of using polynomials for the pressure and suction surfaces of the airfoils. For simplicity, the same order, *u*, were assumed for the pressure and suction side polynomials. That is,

$$p_p = a_{p0} + a_{p1}x + a_{p2}x^2 + \ldots + a_{pu}x^u \tag{4.12}$$

and

$$p_s = a_{s0} + a_{s1}x + a_{s2}x^2 + \ldots + a_{su}x^u \tag{4.13}$$

for the pressure and suction sides, respectively. Therefore, $2(u+1)$ parameters are used to define the airfoil geometry. In the present work, polynomials of order 6 are used. The error in approximating the airfoils used is of less that 2% of the chord in the regions near the leading and trailing edges. The error reduced to less than 0.05% on the rest of the airfoil. Better accuracy was obtaining using the polynomials as compared to the conformal mapping approach. Figures of the airfoil shape and the polynomial approximation are not presented since they are virtually identical.

Table 4.3 summarizes the main characteristics of the neural network model that incorporates the airfoil geometry. Several sub-models were investigated to asses the effect of using hidden layers and incorporating the displacement thickness. The nine sub-models are presented in Table 4.4.

Table 4.3: Description of the neural network model developed based on the data of Brooks et al. (1989), VT and NLR. The same model is used for the tripped and the no-tripped networks.

Model II	
Input	Flow speed Chord length Effective angle of attack Boundary layer displacement thickness in the trailing edge at the suction side Boundary layer displacement thickness in the trailing edge at the pressure side $p_p = a_{p0} + a_{p1}x + a_{p2}x^2 + ... + a_{pu}x^u$ or $D \quad \tau$ $p_s = a_{s0} + a_{s1}x + a_{s2}x^2 + ... + a_{su}x^u$ $Re(\zeta_1) \quad \mathrm{Im}(\zeta_1)$
Output	L_p in 1/3rd octave bands for 9 frequencies ranging from 630 to 8000 Hz
Number of layers	2 to 3
Training data	NACA 0012, Sandia S831 and Delft DU96 tested at VT NACA 0012, Sandia S822 and S834, FX63-137, SG 6043, and SD 2030 tested at NLR. NACA 0012 airfoil tested by Brooks et al. (1989) (Except 0.33 m chord airfoil)

For Models II-*a* thought II-*f* and II-*i*, the networks consist of two layers with 20 neurons in the input layer and 9 neurons in the output layer. The number of input neurons was empirically chosen. The 9 output neurons correspond to the 9 frequencies for which the acoustic data was considered as in Model I. In Models II-*g* and II-*h*, a hidden layer was incorporated. For all models, the training algorithm used was *trainlm* and the transfer functions for the input-output layer were *tansig-purelin.* For II-*g* and II-*h* models, *tansig* transfer function was used in the hidden layer. In all models, flow speed, chord length, and effective angle of attack were used in

the input matrix. In addition, for Models II-*c* and II-*d* boundary layer displacement thickness at the trailing edge on the pressure side was used. For Models II-*e* to II-*h*, boundary layer displacement thickness at the trailing edge on both the pressure and suction sides was used. The boundary layer displacement thickness corresponding to the pressure and suction sides of the airfoil required as inputs were predicted using XFOIL (Drela and Youngren, 2001). The number of epochs used for the training process was 20. This number of epochs was previously found to lead to good results with acceptable computing time. It is important to note that for Models g and *h,* the limit for the iterations was set to 20 epochs or until a target error was reached, whatever occurred first.

The average metrics used to asses the network accuracy are presented in Table 4.4. The results presented show no significant differences in the accuracy of the different models. The average and maximum level difference metrics for tripped cases are almost the same for all the models. With regard to no-tripped cases, it can be observed that the inclusion of a hidden layer improves the accuracy of the predictions, i.e. the average and maximum level difference metrics for Models II-*b* and II-*h* go from 4.7 and 9.6 dB to 2.9 and 7.3 dB, respectively. Another interesting observation is that the results are again very similar for the conformal mapping and polynomial approximation geometry parameterizations. In all cases, the difference in the metrics between these two methods is less than 0.4 dB.

In the overall evaluation of the metrics, Model II-*h* provides the most accurate network for both the tripped and no-tripped cases. However, all the other models seem to perform reasonably well with results only slightly poorer than the model II-*h*. This observation suggests that the actual network configuration to be used for noise predictions is not very sensitive.

Table 4.4: Comparison of the results obtained for different network configurations and training settings for Model II using the Alternative Training for Assessing Network Accuracy (ATANA) approach.

Model II

Case	***a***	***b***	***c***	***d***	***e***	***f***	***g***	***h***	***i***
NN Architecture	20-9	20-9	20-9	20-9	20-9	20-9	20-30-9	20-30-9	20-9
Training Algorithm	trainlm	trainlm	trainlm	trainlm	trainlm	trainlm	trainlm	trainlm	trainlm
Transfer functions	tansig-purelin	tansig-purelin	tansig-purelin	tansig-purelin	tansig-purelin	tansig-purelin	tansig-tansig-purelin	tansig-tansig-purelin	tansig-purelin
Number of epochs	20	20	20	20	20	20	About 20	About 20	20
Error target		-	-	-	-	-	10^{-5}	10^{-5}	-
Displacement thickness	Not used	Not used	Pressure side	Pressure side	Pressure and suction side	Pressure and suction side	Pressure and suction side	Pressure and suction side	Suction side
Geometry parameters	Conformal mapping	Polynomials	Conformal mapping	Polynomials	Conformal mapping	Polynomials	Conformal mapping	Polynomials	Conformal mapping
Configuration	tripped/ no-tripped	tripped/ no-tripped	tripped/ no-tripped	tripped/ no-tripped	tripped/ no-tripped	tripped/ no-tripped	tripped/ no-tripped	tripped/ no-tripped	tripped/ no-tripped
R-Square correlation	0.960/ 0.880	0.963/ 0.868	0.964/ 0.905	0.964/ 0.902	0.960/ 0.905	0.961/ 0.876	0.912/ 0.854	0.950/ 0.923	0.953/ 0.897
Average Level difference (dB)	1.9/ 4.6	1.9/ 4.7	1.8/ 4.0	1.9/ 4.2	1.9/ 3.8	1.9/ 3.9	2.2/ 3.2	1.9/ 2.9	2.0/ 4.1
Maximum Level difference (dB)	4.7/ 9.4	4.7/ 9.6	4.5/ 8.7	4.5/ 8.8	4.4/ 8.3	4.4/ 8.6	5.0/ 7.8	4.4/ 7.3	4.6/ 8.8

The results in Table 4.4 present the average metric for all *m* control vectors. Figures 4.23 through 4.30 present the average level difference metric for all the airfoils using Model II-*h* for no-tripped cases. The color scheme ranges from 0 to 10 dB in order to be consistent with the levels used for representing the results for Model I-*e*. Nevertheless, there are some cases for which the levels of the metrics were higher. For the sake of completeness, Appendix E presents the same results with the full scale range.

Figure 4.23 shows the results for the NACA 0012 airfoil. Comparing this figure to the Figure 4.10, it can be observed that Model-II (for all airfoils) performed similarly to Model-I (exclusively for the NACA0012 airfoil). This results proofs of the robustness of the network. The results in Figures 4.24 through 4.30 show similar trends as previously observed. The network predicts well the self-noise in the absence of vortex shedding.

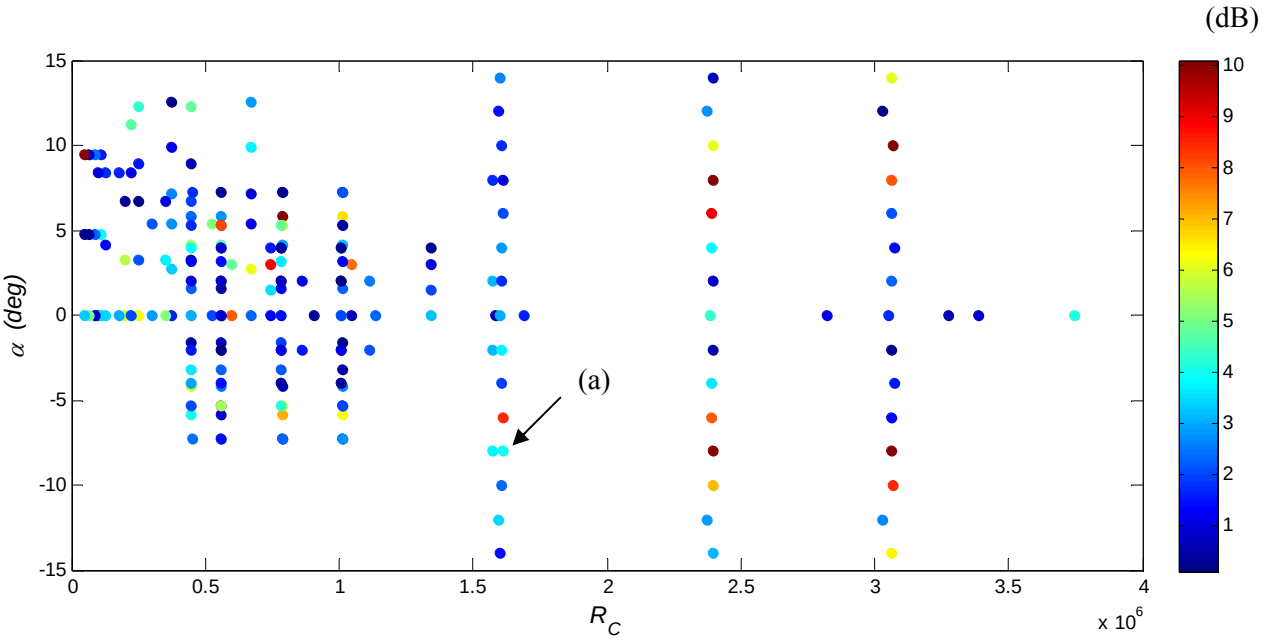

Figure 4.23: *Average level difference metric for each control vector using Model II-h for no-tripped case for the NACA 0012 airfoil. Training using the ATANA approach.*

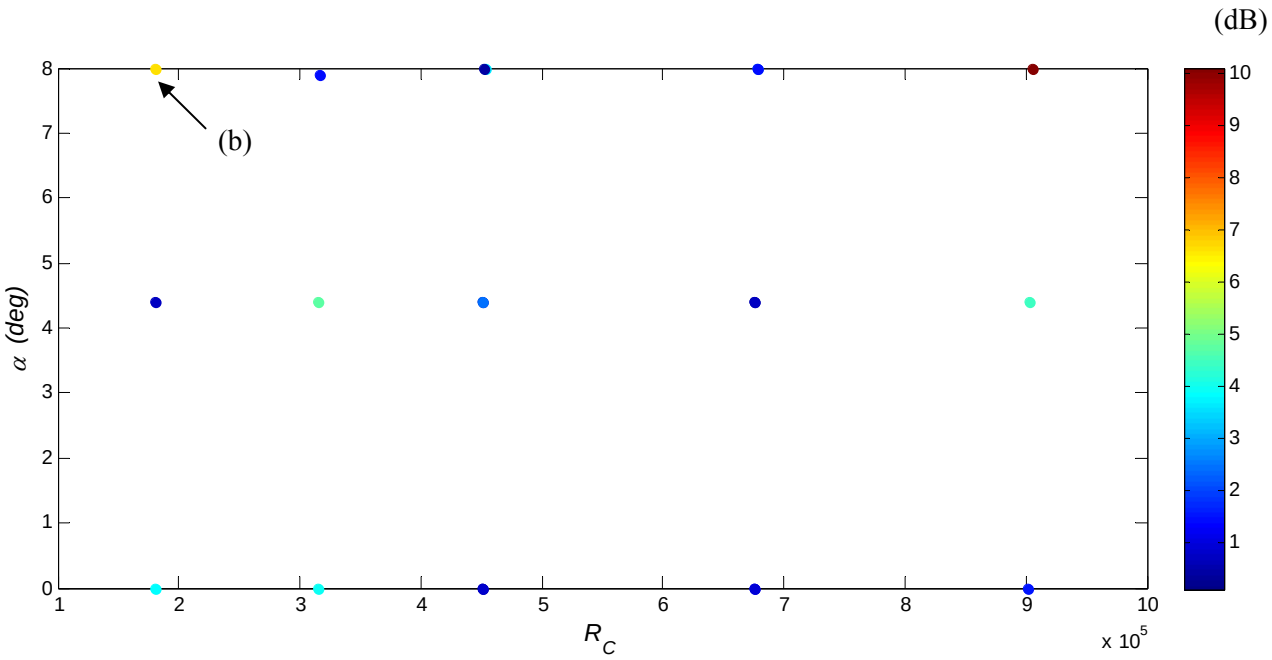

Figure 4.24: *Average level difference metric for each control vector using Model II-h for no-tripped case for the S822airfoil. Training using the ATANA approach.*

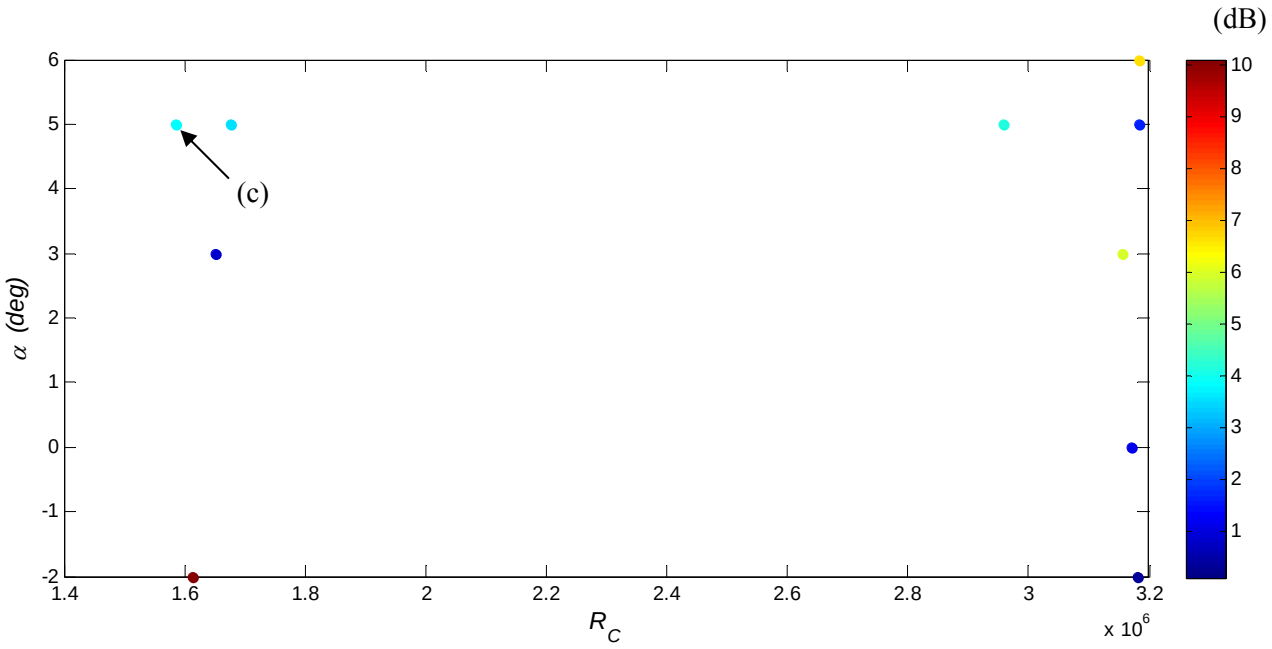

Figure 4.25: *Average level difference metric for each control vector using Model II-h for no-tripped case for the S831 airfoil. Training using the ATANA approach.*

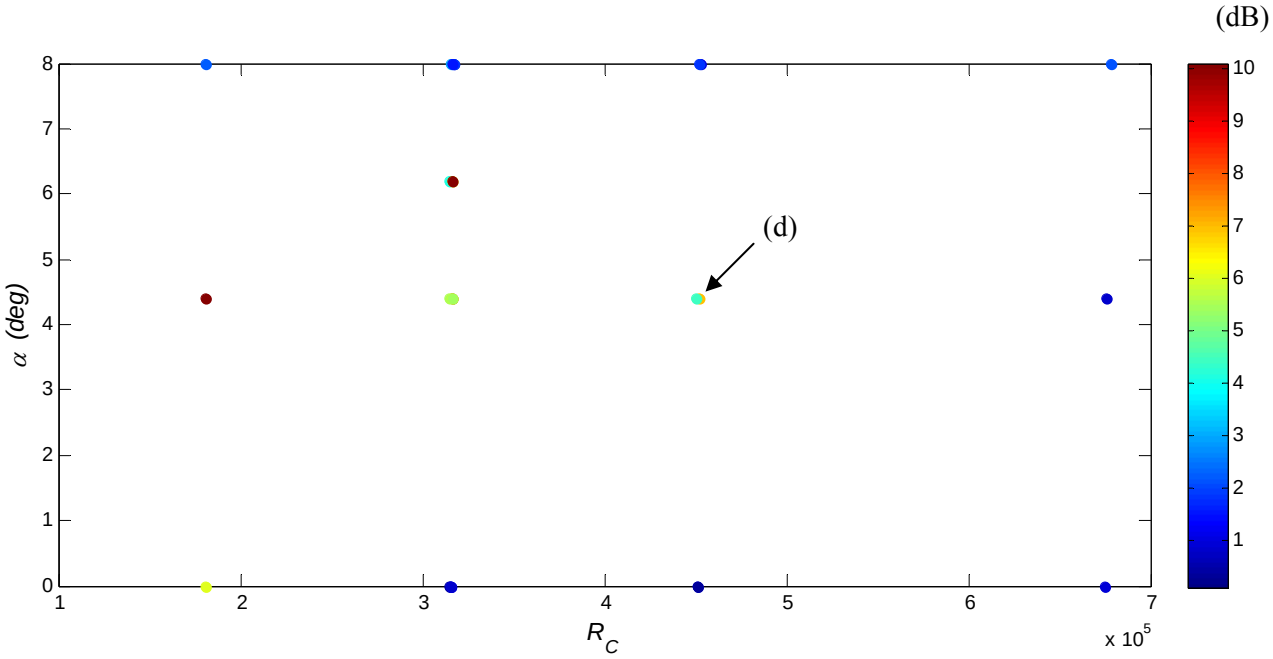

Figure 4.26: *Average level difference metric for each control vector using Model II-h for no-tripped case for the S834 airfoil. Training using the ATANA approach.*

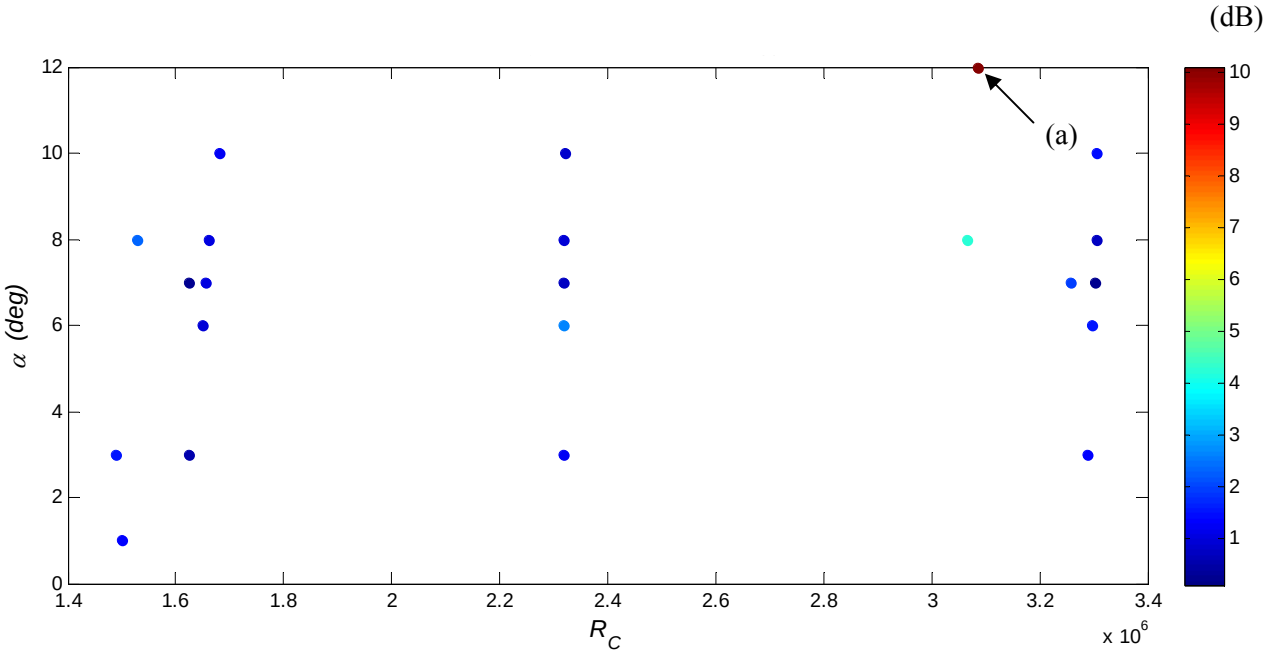

Figure 4.27: *Average level difference metric for each control vector using Model II-h for no-tripped case for the DU96 airfoil. Training using the ATANA approach.*

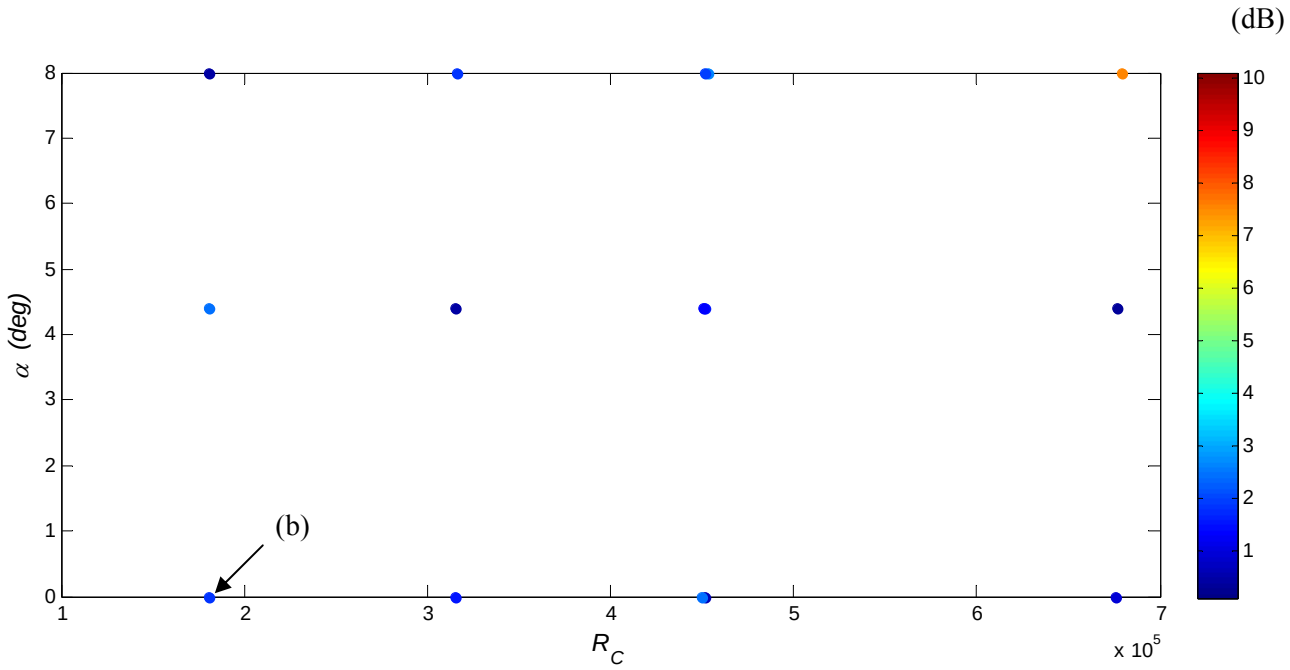

Figure 4.28: *Average level difference metric for each control vector using Model II-h for no-tripped case for the Fx63-137 airfoil. Training using the ATANA approach.*

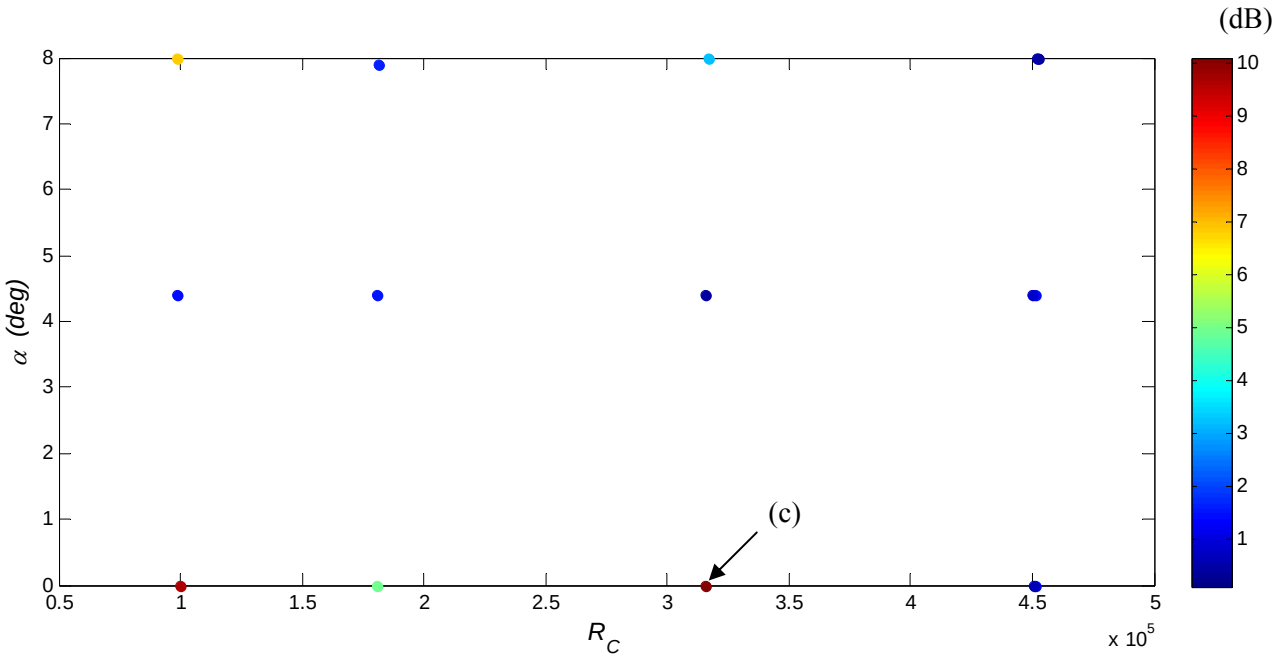

Figure 4.29: *Average level difference metric for each control vector using Model II-h for no-tripped case for the SG 6043 airfoil. Training using the ATANA approach.*

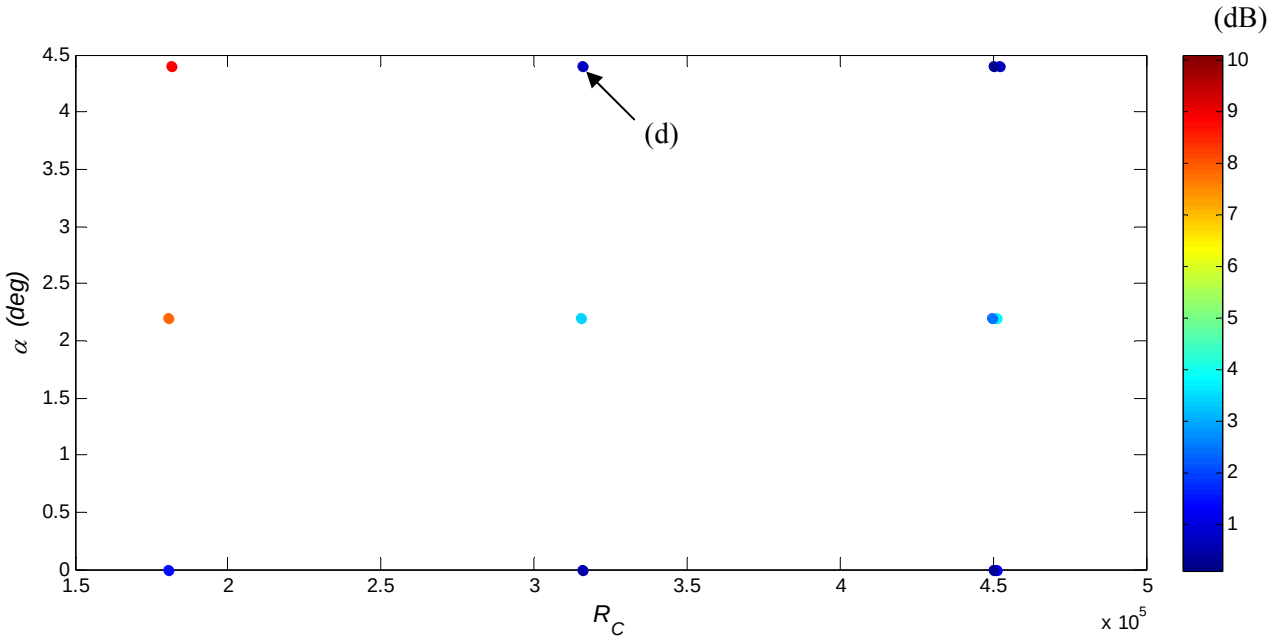

Figure 4.30: *Average level difference metric for each control vector using Model II-h for no-tripped case for the SD2030 airfoil. Training using the ATANA approach.*

To gain more in depth understanding of the accuracy of the network, comparison between experimental and predicted spectra for the control vectors are presented in Figures 4.31 and 4.32. In all cases, predictions were obtained with Model II-*h,* and the results presented correspond to no-tripped configurations. As before, letters *a* through *d* in Figures 4.23 through 4.30 indicate the control vector presented.

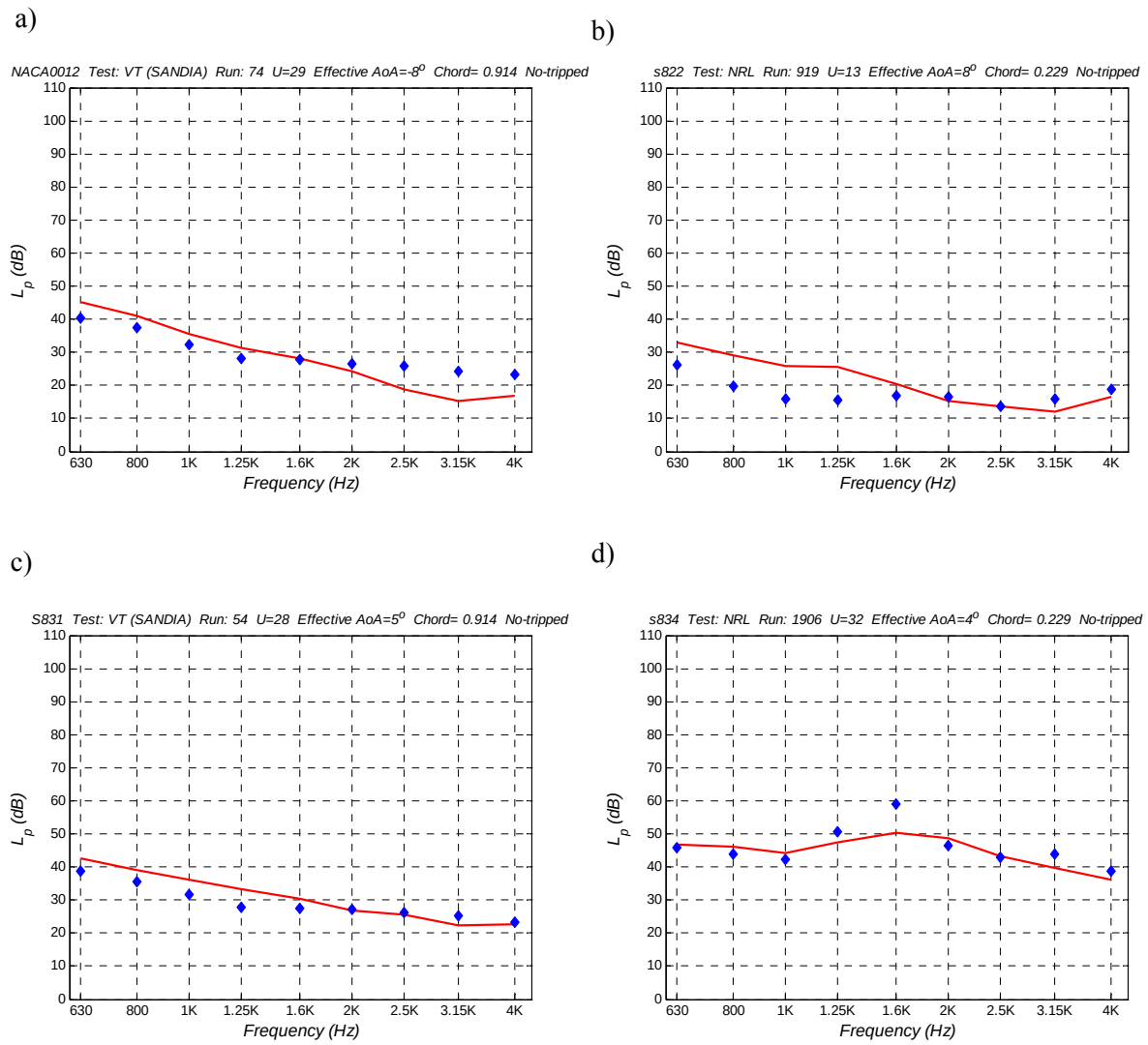

Figure 4.31: *Spectral comparison of experimental results and prediction using Model II-e for no-tripped case: Control vectors a) NACA 0012,* $\alpha = -8°$ *and S822,* $R_c = 1.6$ *million, b)* $\alpha = 8°$ *and* $R_c = 0.18$ *million, c) S831,* $\alpha = 5°$ *and* $R_c = 1.5$ *million and d) S834,* $\alpha = 4°$ *and* $R_c = 0.45$ *million.*
♦ *Experimental* —— *Prediction*

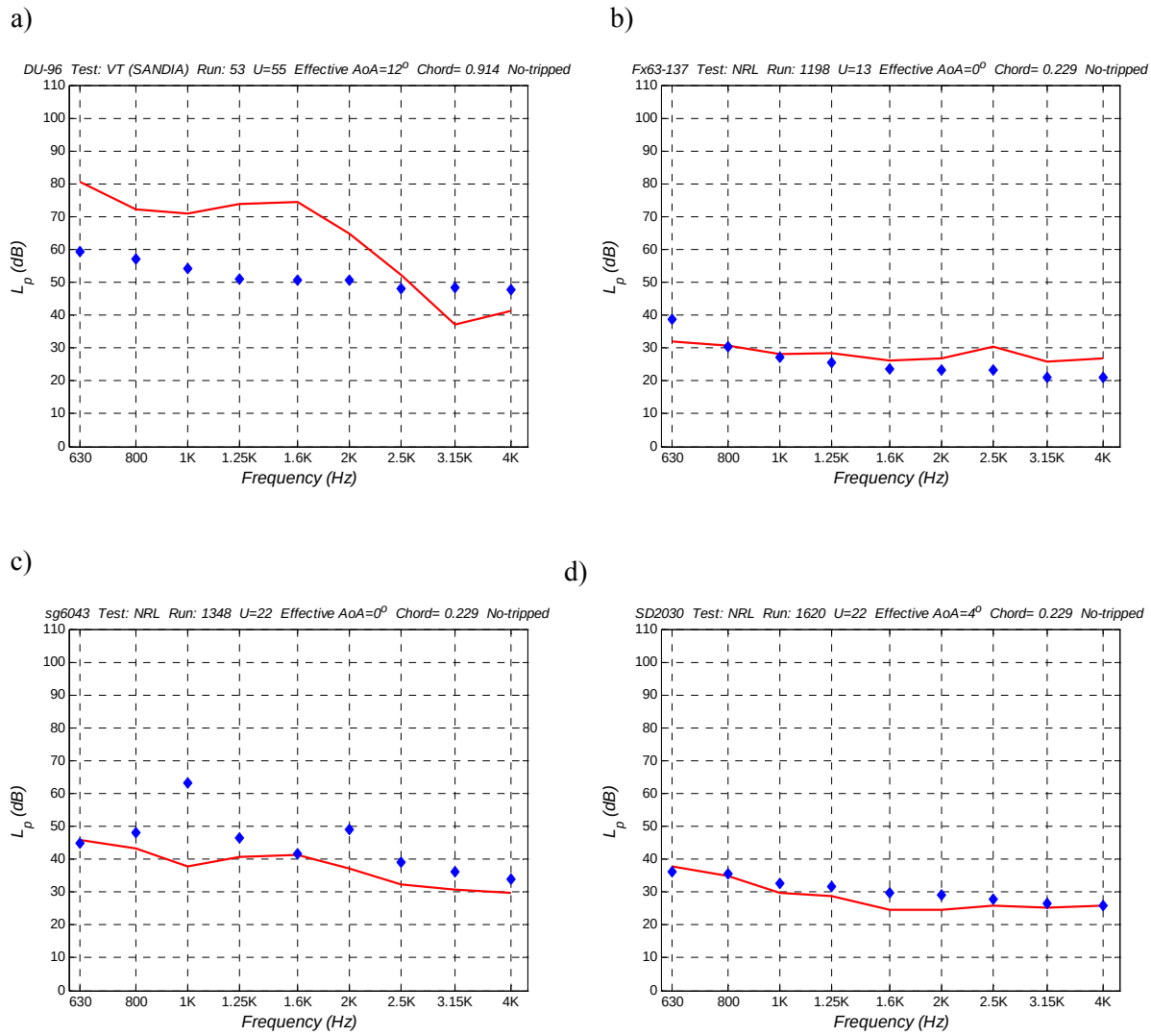

Figure 4.32: *Spectral comparison of experimental results and prediction using Model II-e for no-tripped case: Control vectors a) DU-96,* $\alpha = 12°$ *and* $R_c = 3.1$ *million, b) Fx63-137,* $\alpha = 0°$ *and* $R_c = 0.18$ *million, c) sg6043,* $\alpha = 0°$ *and* $R_c = 3.1$ *million and d) SD2030,* $\alpha = 4°$ *and* $R_c = 3.1$ *million.* ♦ *Experimental* —— *Prediction*

For the reader interested in additional results, Appendices E and F present comparison between experimental data and predictions for representative subsets of the results obtained with Models I-*e* and II-*h*.

4.4.3 Comparing the neural networks prediction accuracy with the method of Brooks et al. (1989)

It was stated in Chapter 1 that the method of Brooks et al. (1989) is the most used tool for predicting airfoils self noise. Therefore, in this section the prediction accuracy of the neural networks tool developed here is compared with the prediction accuracy of the method of Brooks et al. (1989). To this end, the same metrics presented in Section 4.4.2 are computed using Brooks et al. approach. The results are compared in Table 4.5. The metrics were computed for all the cases except the ones corresponding to the tests performed by Brooks et al. (1989). The reason was that in the present thesis the data corresponding to the tests performed by Brooks et al. (1989) was simulated using the semi-empirical method of Brooks et al. (1989). Therefore, experimental data and predictions obtained by the method of Brooks et al. (1989) are the same for the NASA data.

The results of the comparison show that the neural networks tool predicts the cases considered with a higher level of accuracy in an average sense. The reason for this is likely because the neural networks were developed using a richer experimental database than the one used by Brooks et al. (1989). Another potential reason could be that the neural network is more capable of modeling the non-linear physics of the trailing edge noise than the normalization performed by Brooks et al. (1989).

Table 4.5: Comparison of the accuracy of the predictions obtained with the developed neural networks and the predictions obtained using the method of Brooks et al. (1989).

	Neural Networks (Training excluding a control vector (ATANA))	**Brooks et al. (1989)**
	tripped/no-tripped	tripped/no-tripped
R-Square	0.943/0.838	0.904/0.720
$\left(\Delta L_p\right)_{average}$	1.9/ 2.9	2.6/7.6
$\left(\Delta L_{Max}\right)_{average}$	4.3/6.8	8.2/14.6

5 Conclusions

A new method was developed to predict self noise of airfoils typically used in wind turbines. The developed tool is based on neural networks trained with experimental data. This experimental data corresponds to tests of several different airfoils and flow conditions. The resulting tool is capable of taking in to account the geometric characteristics of the airfoil. The input parameters received by the network are the flow speed, chord length, effective angle of attack, and parameters describing the geometrical shape of the airfoil. In addition, boundary layer displacement thickness is used for some models. The parameters used for taking in account the airfoil's geometry are based on a conformal mapping method or a polynomial approximation. The output of the neural network is given by sound pressure level in $1/3^{rd}$ octave bands for nine frequencies ranging from 630 to 4000 Hz.

No information about the trailing edge thickness was incorporated into the training data. Therefore, the neural networks tool is not capable of predicting TBE-VS noise. Furthermore, as no training data corresponding to stall condition was used, the neural network does not take in account this noise mechanism. The neural network does not predict tip noise either because no experimental data for this source was available.

Two models were developed; the first one was based on training data corresponding to NACA 0012 airfoils only. The second model incorporated experimental data corresponding to the NACA 0012, Delft DU96, Sandia S831, S822 and S834, Fx63-137, SG6043 and SD-2030 airfoils. The airfoil chords ranged from 0.025 to 0.91 m. For both models, the effects of different input data and training configurations were assessed. It was found that both conformal mapping and polynomial approximation for parameterization of the airfoils shape lead to similar levels of accuracy. Furthermore, it was found that the neural network models are not sensitive to the use of boundary layer parameters as input. This constitutes an advantage with respect to other prediction tools that require boundary layer information.

In some cases the neural network fails in predicting tonal vortex shedding noise produced by laminar boundary layer-trailing edge interaction. Moreover, it was found that the neural

network developed in the present work is not capable of making predictions outside of the domain defined by the training set. Furthermore, in contrast with the semi-empirical method presented in Chapter 2, the networks application developed in this thesis present the advantage of allowing flexibility for the incorporation of new experimental data into the training set. The neural networks can be successively improved by adding the new experimental data to the training matrix and retraining the networks.

Finally, the predicting accuracy of the neural networks tool developed in this thesis was compared with the semi-empirical method developed by Brooks et al. (1989). It was found that the neural networks tool produced more accurate predictions in an average sense for the cases that were considered.

The overall conclusion of the present work is that the developed neural network is capable of predicting self-noise accounting for the shape of airfoils. This demonstrates the potential of the neural network method as a tool for predicting wind turbine noise.

6 Future work

In this section, a set of research recommendations are made for future work.

As it was mentioned before, incorporating new training experimental data to the neural networks is a very simple process. It was mentioned that the neural networks could possibly fail in approximating tonal vortex shedding noise due to lack of enough data. Therefore, it could be convenient to incorporate more experimental data corresponding to test configurations for which this vortex shedding occurs, e.g. no-trip.

In addition, it is advised to normalize the experimental data to be used for training the networks. The objective is to present to the networks a more homogeneous data set. For example, the noise data could be normalized using the 5^{th} power law of the free stream velocity and the chord based Strouthal number. Another possible improvement would be to separate the tonal noise from the broadband noise. Then, separated neural network for predicting the broadband and tonal noise components could be developed. Moreover, as some neural networks are commonly used for yes-no decision making, it is advised to implement a decision making model to predict whether vortex shedding occur or not.

It is also recommended to create new neural networks models to predict blunt vortex shedding and tip noise. For the prediction of blunt vortex shedding noise, it would be necessary to use acoustic measurements corresponding to several trailing edge geometries. In the case of tip noise, the neural networks should be based on experimental measurements of noise emitted by blade's tips.

Upon further development of the neural network methods, it is recommended to use this predictive tool to estimate the noise from real wind generators and assess it fidelity. The ultimate goal is to develop a tool to accurately predict wind turbine noise emissions.

Finally, it is recommended to work on the development of a neural network application for designing quiet airfoils. It is proposed to implement an iterative or inverse method based on neural networks to minimize the sound emission. In the case of an iterative design tool, the

network would be trained using aerodynamic parameters such as drag and lift and geometrical parameters. The output would be the noise spectra. Once the network is trained, an iterative process would search for an optimal geometry, with aerodynamic performance constrains, i.e. drag and lift. In the case of an inverse process, the nets would be trained using aerodynamic parameters and noise spectra as input parameters. The output parameters would be given by the geometry. Once the net is trained, aerodynamic and acoustic targets would be inputted to the network in order to obtain a geometry satisfying these targets. Considering the limitations of the neural networks exposed in previous sections, the first method appears to be more realistic for a practical implementation.

References

Amiet R., ***"Acoustic Radiation from an Airfoil in a Turbulent Stream,"*** Journal of Sound Vibration, Vol. 41, No. 4, pp. 407-420, 1975

Barnes J. and Gomez R., ***"A variety of wind turbine noise regulations in the UnitedStates,"*** Second International Meeting on Wind Turbines Noise, Lyon, France, September 20-21, 2007.

Blake W., ***"Mechanics of Flow-induced Sound and Vibration,"*** Vol II: Complex flow structure mechanics. ACADEMIC Press INC. Harcourt Brace Jovanovich Publishers, 1986.

Brooks T. and Hodgson T., ***"Trailing edge noise prediction from measured surface pressures,"*** Journal of Sound and Vibration, 78(1), 69-117, 1981.

Brooks T., Pope D. and Marcolini M., ***"Airfoils self-noise and predictions,"*** NASA Reference Publication 1218, 1989.

Burdisso R., and Errasquin L., ***"Calibration of the VT Anechoic Wind Tunnel for the Corrections of Airfoil Noise Data,"*** Report for Sandia National Laboratories, 2009.

Candel S., ***"Application of Geometrical Techniques to Aero-Acoustic Problems,"*** 3rd Aero-acoustics Conference, Palo Alto, CA, July 20-23, AIAA 76-546, 1976.

Chong W., Rodriguez J. and Sivasundaran S., ***"Neural network simulation of airfoil properties,"*** Intelligent engineering systems through artificial neural networks, Volume 2, Proceedings of the Artificial Neural Networks in Engineering (ANNIE '92) conference, St. Louis, Missouri, USA, 1992

Devenport W., Burdisso R., Camargo H., Crede E., Remillieux M., Rasnic M. and Van Seeters P., ***"Aeroacoustic testing of wind turbine airfoils,"*** Report for NREL, 2008a.

Devenport W., Burdisso R., Camargo H., Crede E., Remillieux M., Rasnic M. and Van Seeters P., ***"Aeroacoustic Testing of Sandia National Labs wind turbine airfoils,"*** Report for Sandia National Labs, 2008b.

Di Stefano P. and Di Angelo L., ***"Neural Network based geometric primitive for airfoil design,"*** Proceedings of the Shape Modeling International 2003 (SMI.03), 2003.

Drela M. and Youngren H., ***"XFOIL 6.9 User Primer,"*** http://web.mit.edu/drela/Public/web/xfoil/ , 2001

Drewitt A. and Langston R., "***Assessing the impacts of wind farms on birds,"*** British Ornithologists' Union, Ibis, 148, 29–42, 2006.

Faszer A. and Hynes T., ***"Acoustic Beamforming and Holography Measurements of Modified Boundary Layer Trailing Edge Noise,"*** 27th AIAA Aeroacoustics Conference, Cambridge, Massachusetts, 8-10 May, 2006.

Ffowcs Williams J. and Hall L., ***"Aerodynamic sound generation by turbulent flow in the vicinity of a scattering half plane,"*** Journal of fluid mechanics, vol. 40, part 4, pp. 657-670, 1970.

Fuglsang P. and Madsen H., ***"Implementation and Verification of an Aeroacustic Noise Prediction Model for Wind Turbines,"*** Risø National Laboratory publication, R-867(EN), 1996.

Gurney K., ***"An Introduction to Neural Networks,"*** CRC Press, **ISBN:** 9781857285031, 1997.

Hacioglu A., ***"Fast Evolutionary Algorithm for Airfoil Design via Neural Network,"*** AIAA JOURNAL Vol. 45, No. 9, 2007

Herr M., ***"Design for low-noise trailing-edges,"*** 13th AIAA/CEAS Aeroacoustics conference, 2007a.

Herr M., ***"A noise reduction study on flow permeable trailing edge,"*** ODAS, 2007b.

Herr M., ***"Experimental investigations in low-noise trailing-edge design,"*** AIAA journal, Vol. 43, No. 6, 2005.

Huang S., Miller L. and Steck J., ***"An Exploratory Application of Neural Networks to Airfoil Design,"*** AIAA 94-0501, 32nd Aerospace Sciences Meeting & Exhibit, Reno, NV, 1994.

Johansson M. and Laike M., ***"Intention to respond to local wind turbines: The role of attitudes and visual perception,"*** Wind Energy 2007, 10:435–451, 2007.

Jones R., ***"Wing theory,"*** Princeton University Press, Princeton, 0-691-08536-6, 1990

Jonkman J. and Marshall L., ***"FAST User's Guide,"*** Technical Report NREL/EL-500-38230, http://wind.nrel.gov/designcodes/simulators/fast/FAST.pdf, National Renewable Energy Laboratory, Golden, CO, USA, 2005.

Karamcheti K., ***"Principles of Ideal-Fluid Aerodynamics,"*** Krieger Publishing Company, 9780898741131, 1980.

Kasnakoglu C. and Onder Efe M., ***" Prediction of Dynamical Properties of Flow Over a Three-element Airfoil via Computationally Intelligent Architectures,"*** International Conference on Control, Automation and Systems 2008, Seoul, Korea, 2008.

Khurana M., Winarto H. and Sinha A., ***"Application of Swarm Approach and Artificial Neural Networks for Airfoil Shape Optimization,"*** 12th AIAA/ISSMO Multidisciplinary Analysis and Optimization Conference, Victoria, British Columbia Canada, 2008.

Kinsler L., Frey A., Coppens A. and Sanders V., ***"Fundamentals of acoustics,"*** John Wiley and Sons, Inc., 9971-51-318-8, 2000.

Leloudas G., Zhu W., Sørensen J., Shen W. and Hjort S., ***"Prediction and reduction of noise from a 2.3 MW wind turbine,"*** The Science of Making Torque from Wind, IOP Publishing, Journal of Physics, Conference Series 75, 012083, 2007.

Lowson J. and Bullmore A., ***"Wind turbine noise source characterization,"*** Proceedings of the 18th wind energy association conference, Exeter University, UK, p. 451, 1996.

Lowson M., ***"Assessment and prediction of wind turbine noise,"*** Flow Solutions report, ETSU W/13/00284/REP, 1992.

McKenzie A., ***"Objective and subjective assessment of tonal components in noise from UK wind farm sites,"*** Proceedings of the 18th wind energy association conference, Exeter University, UK, p. 467, 1996.

Meade A. ***"An application of artificial neural networks to experimental data approximation,"*** 31 Aerospace Science Meeting & Exhibit, Reno, Nevada, 1993

"Matlab's Help," Matlab 7.4, The MathWorks, Inc.

Meecham W., Bui T. and Miller W., ***"Diffraction of dipole sound by the edge of a rigid baffle,"*** Journal Acoustic Soc. Am., Vol. 70, No 5, pp. 1531-1533, 1981.

Migliore P. and Oerlemans S., ***"Wind Tunnel Aeroacoustic Tests of Six Airfoils for Use on Small Wind Turbines,"*** AIAA Wind Energy Symposium, Reno, Nevada, January 5–8, 2004.

Moriarty P. and Migliore P., ***"Semi-empirical aeroacoustic noise prediction code for wind*** turbines," Technical report, NREL/TP-500-34478, 2003.

Moriarty P., Guidati G. and Migliore P., ***" Recent improvement of a semi-empirical aeroacoustic prediction code for wind turbines,"*** Proc., 10th AIAA/CEAS Aeroacoustics Conference, Manchester, UK, AIAA 2004-3041, 2004.

Moriarty P., Guidati G. and Migliore P., ***"Prediction of Turbulent Inflow and Trailing-Edge Noise for Wind Turbines"*** 11th AIAA/CEAS Aeroacoustics Conference (26th AIAA Aeroacoustics Conference), Monterey, California, 2005

Moriarty P., ***"NAFNoise user's guide,"*** NWTC Design Codes, National Renewable Energy Laboratory, Golden, CO, USA, http://wind.nrel.gov/designcodes/simulators/NAFNoise/, 2005.

Oerlemans S., ***"Wind Tunnel Aeroacoustic Tests of Six Airfoils for Use on Small Wind Turbines,"*** Subcontractor report, NREL /SR-500-35339, August 2004

Onat C. and Canbazoglu S., ***"An investigation on the economic analysis of wind turbines,"*** Energy Exploration & Exploitation, Volume 25, Number 1, pp. 27-37, 2007.

Paterson R., Vogt P. and Fink M., ***"Vortex Noise of Isolated Airfoils,"*** J. Aircraft, Vol. 10, No. 5, May 1973.

Pierce A., ***"Acoustics, An Introduction to its Physical Principles and Applications,"*** Acoustical Society of America, Woodbury, NY, 1989.

Remilleux M., ***"Aeroacoustic Study of a Model-Scale Landing Gear in a Semi-Anechoic Wind-Tunnel,"*** Masters dissertation, Virginia Polytechnic Institute and State University, 2007.

Rai M. and Madavan N., ***"Aerodynamic Design Using Neural Networks,"*** AIAA JOURNAL Vol. 38, No. 1, 2000.

Rai M., ***"Towards a Hibrid Aerodynamic Design procedure based on neural networks and evolutionary methods,"*** 20th AIAA Applied Aerodynamics Conference, St. Louis, Missouri, 2002.

Sclinker R. and Amiet R., ***"Helicopter rotor trailing edge noise 1981, "*** AIAA 7th Aero-acoustics Conference, Palo Alto, CA, October 5-7,1981.

Shepherd K. and Hubbard H., ***"Physical characteristics and perception of low frequency noise from wind turbines,"*** Noise control engineering journal, 1991.

Sclinker R. and Amiet R., ***"Refraction of sound by a shear layer,"*** Journal of Sound and Vibration, 58(4), 467-482, 1978.

"Sound & Vibration magazine," P.O. Box 40416, 27101 E. Oviatt Rd., Bay Village, OH 44140, USA http://www.sandv.com*, 2008*

Staubs J., ***"Real Airfoil Effects on Leading Edge Noise,"*** Ph.D. Dissertation, VT, 2008.

Sundararajan N., Saratchandran P. and Lu ying wei, ***"radial basis function neural networks with sequential learning,"*** World Scientific, 1999.

"United States market sets new horizons," American Wind Energy Association, 2006.

Van den Berg G., ***"Do wind turbines produce significant low frequency sound levels?,"*** 11th international Meeting on Low Frequency Noise and Vibration and its Control, 2004.

Voutsinas S, ***"Development of a vortex type aeroacustic model of HAWTs and its evaluation as a noise prediction tool,"*** Final technical report on the JOU2-CT92-0148 project, 1995.

Wagner S., Bareiβ R. and Guidati G., ***"Wind turbine noise,"*** Springer, 3-540-60592-4, 1996.

"Wind power brings prosperity, anger," Cable News Network. Turner Broadcasting System Inc., http://www.cnn.com, 2008.

"Wind power targets for Europe: 75,000 MW by 2010," The European Wind Energy Association, 2003.

Yildiz M. and Mawardi O., ***"On the Diffraction of Multipole Fields by a Semi-Infinite Rigid Wedge,"*** The journal of the acoustical society of America, Volume 32, Number 12, Arlington, Massachusells, 1960.

Appendix A: Airfoil Geometry, Abbreviations and Symbols

A.1 Parameters defining the geometry of an airfoil

Figure A1 depicts the main geometrical components of an airfoil and the corresponding nomenclature.

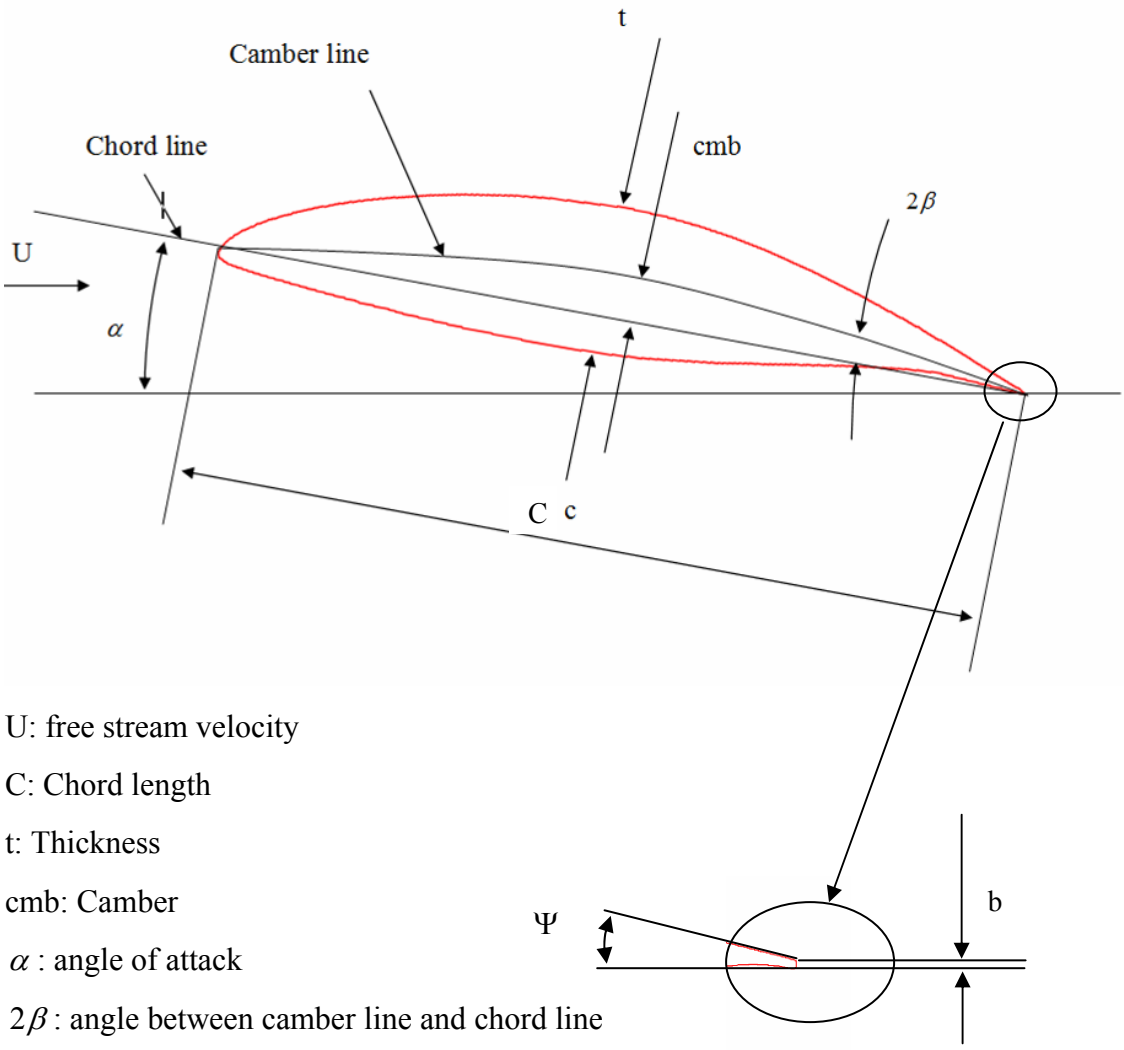

U: free stream velocity

C: Chord length

t: Thickness

cmb: Camber

α : angle of attack

2β : angle between camber line and chord line

b: Trailing edge bluntness thickness

Ψ : Angle of the trailing edge

Figure A1: *Schematic view of the geometry of an airfoil.*

A.2 Abbreviations

TBL-TE: Turbulent boundary layer trailing edge

S/SF: Separated / Stalled flow

LBL-VS: Laminar boundary layer – vortex shedding

TEB-VS: Trailing edge bluntness – vortex shedding

SPL: Sound pressure level

ATANA: Alternative Training for Assessing Network Accuracy

CTNN: Conventional Training of the Neural Network

VT: Virginia Tech

A.3 Symbols

c_o: Speed of sound

τ: Time that a wave front takes to travel from the source to the receiver

r_r: Distance to the observer

θ_r: Local coordinate for a flat plate in rectilinear motion

φ_r: Local coordinate for a flat plate in rectilinear motion

M: Mach number

$\bar{D}_h$: High frequency directivity function

$\bar{D}_l$: Low frequency directivity function

I : Acoustic intensity

U : Free stream velocity

ε : Normalized turbulence intensity

ρ_o : Density of the air

L : Span length

s , l : Parameters describing the dimensions of the turbulent region as depicted in Figure 2.6

δ : Boundary layer thickness. It is the distance from the airfoil surface where the mean velocity reaches the 99% of the potential flow stream velocity

δ^* : Boundary layer displacement thickness. It is the distance by which a surface would have to be moved parallel to itself towards a reference plane in an ideal fluid stream to give the same mass flow as occurs between the surface and the reference plane in a real fluid. In other words, it is the distance a streamline just outside the boundary layer is displaced away from the wall compared to the inviscid solution.

δ_o : Boundary layer thickness for 0^o of angle of attack

δ_o^* : Boundary layer displacement thickness for 0^o of angle of attack

δ_s : Boundary layer thickness at the suction side

δ_s^* : Boundary layer displacement thickness at the suction side

δ_p : Boundary layer thickness at the pressure side

δ_p^* : Boundary layer displacement thickness pressure side

δ_{avg}^* : Average displacement thickness

R_C : Chord Reynolds number

C : Chord

α : Effective angle of attack

α_{tip} : Angle of attack of the blade at the tip section

α_o : Angle of attack for witch the directivity effect is considered to change from high frequency to low frequency for S/SF noise

$L_p^{TBL-TE\ /\ S/SF}$: Turbulent-boundary-layer—trailing-edge --- Separated / Stalled-flow noise in sound pressure level.

L_p^{LBL-VS} : Laminar – Boundary – Layer – Vortex – Shedding Noise in sound pressure level

L_p^{BTE} : Blunt trailing edge noise in sound pressure level

L_p^{α} : Separated / Stalled-flow noise in sound pressure level

L_p^{Tip} : Tip noise in sound pressure level

L_p^{p} : Turbulent-boundary-layer—trailing-edge noise produced by the pressure side in sound pressure level

L_p^{s} : Turbulent-boundary-layer—trailing-edge noise produced by the suction side in sound pressure level

L_p^{scaled} : Scaled noise in sound pressure level in 1/3rd octaves bands

$L_p^{corrected}$: Corrected noise in sound pressure level in 1/3rd octaves bands

$L_p^{measured}$: Measured noise in sound pressure level in 1/3rd octaves bands

$L_p^{r_r}$: Noise level perceived at a observer's distance r_r

L_W : Sound power level

L_p^{3m} : Noise in sound pressure level at an observer's distance of 3 m

$L_p^{1.23}$: Noise in sound pressure level emitted by an airfoil of 1.23 m span

$L_p^{0.1}$: Noise in sound pressure level emitted by an airfoil of 0.1 m span

$L_{p\,i}$: Sound pressure level for each frequency expressed in dB

L_p^E : Experimental sound pressure level for each frequency expressed in dB

L_p^P : Predicted sound pressure level for each frequency expressed in dB

ΔL_p : Metric measuring difference between the measured and the predicted spectra in an average sense

$\Delta L_{p\,Max}$: Maximum sound pressure level difference of the spectra

$G_A \;\; G_{A\min} \;\; G_{A\max} \;\; K_1 \;\; \Delta K_1$: Functions used for scaling TBL-TE noise

$G'_A \; G_B \;\; G_{B\min} \;\; G_{B\max} \;\; K_2$: Functions used for scaling S/SF noise

$G_C \;\; G_D \;\; G_E$: Functions used for scaling LBL-VS noise

$G_F \;\; G_G$: Function used for scaling BTE noise

f : Frequency

St : Strouthal number

St_p : Strouthal number based in the boundary layer displacement thickness measured at the pressure side

St_s : Strouthal number based in the boundary layer displacement thickness measured at the suction side

St_1 : Peak Strouthal Number used in the scaling of TBLTE noise

St_2 : Peak Strouthal Number used for scaling S/SF noise

St'_p : Strouthal Number used for scaling LBL-VS noise

St'_{peak} : Peak Strouthal Number used for scaling LBL-VS noise

St'' : Strouthal Number used for scaling BTE noise

St''_{peak} : Peak Strouthal Number used for scaling BTE noise

St''' : Strouthal number used for scaling tip noise

St'_0 : Strouthal Number for case of 0^o of angle of attack used for scaling LBL-VS noise

$R_{\delta_p^*}$: Reynolds number based on the displacement thickness

b : Trailing edge's bluntness thickness

Ψ : Trailing edge angle

q : Extension of the tip vortex for tip noise

$U_{\max}$: Maximum velocity within or about the separated flow region at the trailing edge

$M_{\max}$: Maximum Mach number within or about the separated flow region at the trailing edge

Δ_{Keblar} : Attenuation due to the Kevlar's wall

Δ_{BL} : Attenuation due to the boundary layer

S_o : Unitary surface

s_i : Neural network scalar input

s_b : Neural network scalar bias

s_o : Neural network output

f_T : Neural network transfer function

w : Neural network weight

$\vec{i}_j$: Neural network j^{th} input vector

$\vec{o}_j$: Neural network j^{th} output vector

m : Number of experimental data vectors available

p^2_{rms} : Squared pressure in RMS

i : Subscript that indicates the frequency considered

n : Number of frequencies of the spectra analyzed

$\vec{r}_{RMS}$: R-square correlation for a frequency

R_{RMS} : R-square correlation for a all the frequencies

z , ξ : Variables used in conformal mapping

D , ζ_1 : Parameters used for conformal mapping

p_p , p_s : Polynomials used for approximating the shape of airfoils

Appendix B: XFOIL and Boundary Layer Predictions

XFOIL is a panel method's based program for the design and analysis of subsonic isolated airfoils. It was first developed in 1986 by Mark Drela of MIT and has been constantly improved since then. The program has an interactive interface that allows performing several types of design and analysis. It is possible to perform viscous or inviscid analysis of an existing airfoil, airfoil design and redesign, drag polar calculation. Furthermore, it is possible to write, read and plot airfoil's geometry, pressure distribution and boundary layer parameters (Drela and Youngren, 2001).

In the present thesis, XFOIL is used to predict the boundary layer properties in the trailing edge region of the airfoils considered. The airfoil's geometry is taken in account by the use of an input file containing the coordinates, except for the NACA0012 that can be generated internally by the program. As the program has an interactive interface that makes slow to operate it, a Matlab code was developed to run XFOIL automatically.

One of the parameters that are intended to be used for the neural networks implementation is the boundary layer displacement thickness. For some airfoil shapes in certain conditions, convergence in the simulations performed with X-Foil can not be reached. In consequence, for the neural networks implementations that include the displacement thickness, some test results are excluded.

It is important to assess the accuracy of the predictions obtained with XFOIL. To this end, the hot wire measurement performed by Brooks et al (1990) for the NACA 0012 and the measurements performed by Devenport et al. (2008, 1 and 2) for the DU-96 and S831 airfoils are compared with predictions.

In the case of the NACA 0012, Brooks et al. developed empirical curves based on the measurements that they performed. These curves are compared with XFOIL predictions in Figure B1 and B2. Inspection of these figures shows that the predictions obtained with XFOIL are acceptable. It can be noticed that for the no-tripped cases, the predictions do not follow the trend of the empirical curve for low Reynolds numbers. The predictions are considered

acceptable anyways because they are in the same order of magnitude. Moreover, in practice, such a lows Reynolds numbers are not present in large wind turbines.

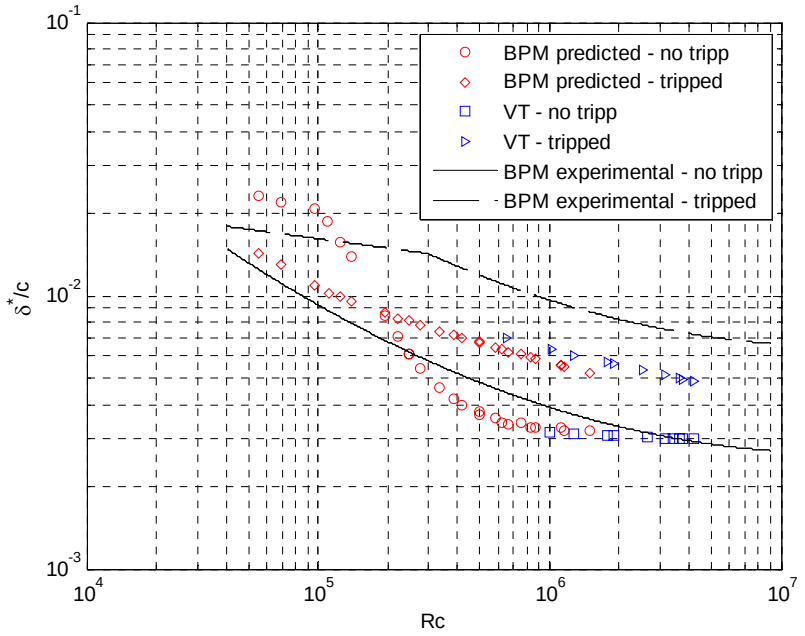

Figure B1: *Displacement thickness measured at the trailing edge of NACA 0012 airfoils normalized with respect to the chord length versus Reynolds number. The curves were obtained by Brooks et al. by curve-fitting experimental measurements. The results indicated with markers were obtained with XFOIL for the test conditions applied in the experiments of Brooks et al. (1990) and Devenport et al. (2008, 1 and 2).*

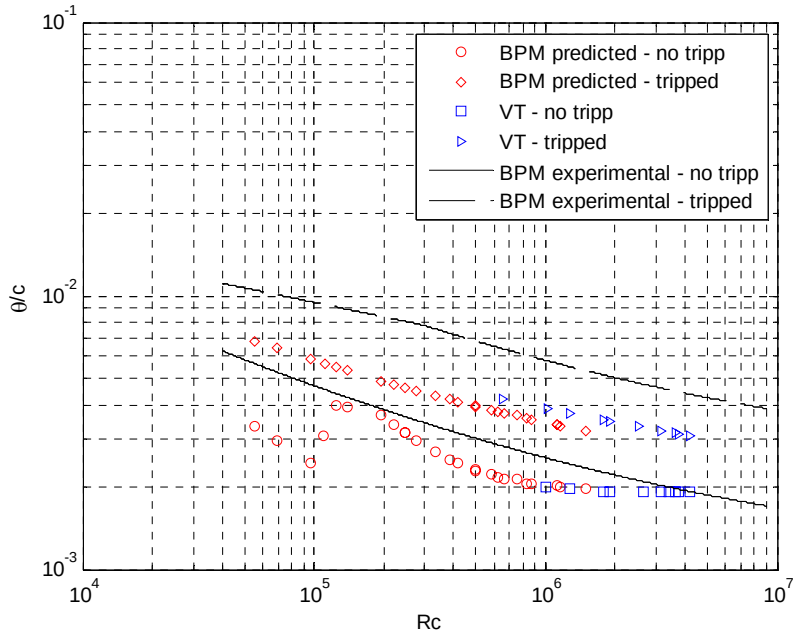

Figure B2: *Momentum thickness measured at the trailing edge of NACA 0012 airfoils normalized with respect to the chord length versus Reynolds number. The curves were obtained by Brooks et al. by curve-fitting experimental measurements. The results indicated with markers were obtained with XFOIL for the test conditions applied in the experiments of Brooks et al. (1990) and Devenport et al. (2008, 1 and 2).*

In the case of the DU-96 and S831 airfoils, predicted and experimental results are presented in Tables B1 and B2. It can be noticed that the predictions are in good agreement with the measured displacement thickness.

Table B.1: Boundary layer parameters for a DU-96 airfoil. Comparison between experimental measurements (Devenport et al., 2008, 2) and predictions made with XFOIL. Chord = 0.914 m

Effective angle of attack (deg)	R_C	Trip	Side	δ * (m) Experimental	δ * (m) Calculated with X-Foil
3.1	1600000	No	Pressure	0.002	0.002254
3.1	1600000	No	Suction	0.0084	0.009256
3.1	1580000	No	Pressure	0.0023	0.002262
3.1	1570000	No	Suction	0.0062	0.009313
7	1560000	No	Pressure	0.0015	0.001558
7	1560000	No	Suction	0.0118	0.013668
7	3140000	No	Pressure	0.0019	0.001305
7	3140000	No	Suction	0.0088	0.014315
7	3130000	Yes	Pressure	0.0033	0.00252
7	3130000	Yes	Suction	0.0197	0.022079

Table B2: Boundary layer parameters for a S831airfoil. Comparison between experimental measurements (Devenport et al., 2008, 2) and predictions made with XFOIL. Chord = 0.914 m

Effective angle of attack (deg)	R_C	Trip	Side	δ * (m) Experimental	δ * (m) Calculated with X-Foil
-2	1550000	No	Pressure	0.0021	0.00573
-2	1550000	No	Suction	0.0079	0.010322
-2	1590000	No	Pressure	0.0014	0.005706
-2	1630000	No	Suction	0.0105	0.010239
-2	3130000	No	Pressure	0.0032	0.005064
-2	3130000	No	Suction	0.0134	0.009136
5	1570000	No	Pressure	0.001	0.001282
5	3180000	No	Pressure	0.0015	0.001006
5	3180000	No	Suction	0.0309	0.04974
5	1620000	Yes	Pressure	0.0011	0.001833
5	1620000	Yes	Suction	Separated flow	0.057439
5	3160000	Yes	Pressure	0.0023	0.001637
5	3160000	Yes	Suction	Separated flow	0.05187

Appendix C: Karman-Trefftz Conformal Mapp Airfoils

In this section, results for the Karman-Trefftz conformal mapping approximation of the airfoil shapes are presented. Figures C1 through C8 shows the airfoil geometry, the approximated geometry using the conformal mapping, and the circle in the ζ domain.

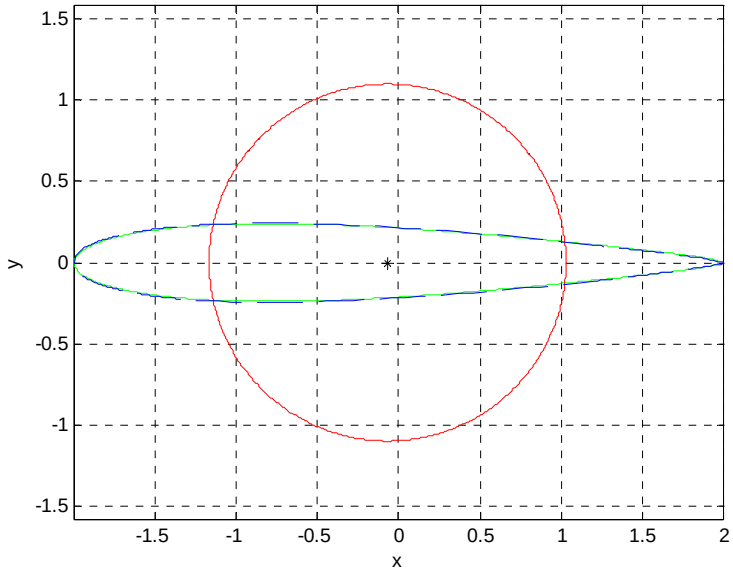

Figure C1: *NACA 0012 airfoil. Green: Airfoil's shape achieved through a Karman-Trefftz conformal mapping. Blue: Original shape of the airfoil. Red: Circle used for obtaining the airfoil through the Karman-Trefftz conformal mapping. *: Origin of the circle.*

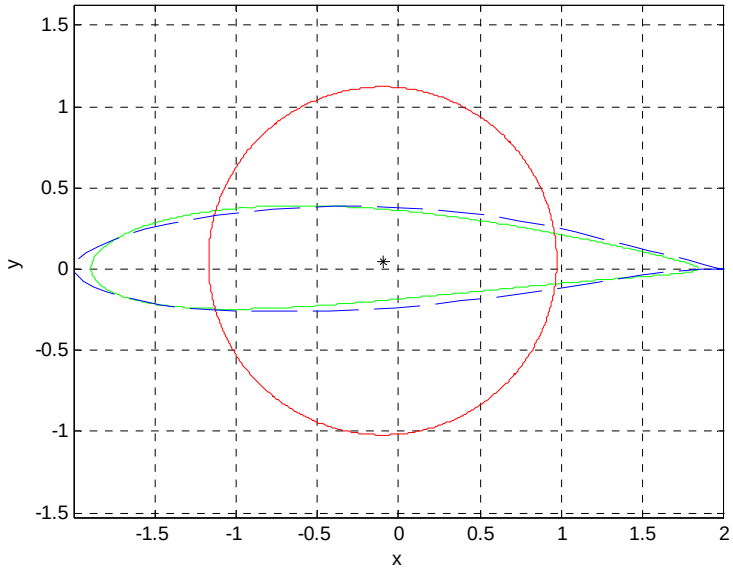

Figure C2: *S822 airfoil. Green: Airfoil's shape achieved through a Karman-Trefftz conformal mapping. Blue: Original shape of the airfoil. Red: Circle used for obtaining the airfoil through the Karman-Trefftz conformal mapping. *: Origin of the circle.*

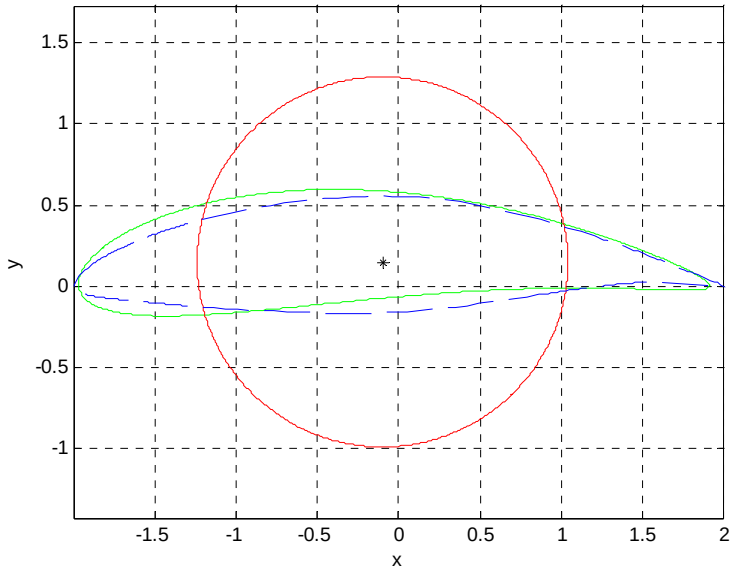

Figure C3: *S831 airfoil. Green: Airfoil's shape achieved through a Karman-Trefftz conformal mapping. Blue: Original shape of the airfoil. Red: Circle used for obtaining the airfoil through the Karman-Trefftz conformal mapping. *: Origin of the circle.*

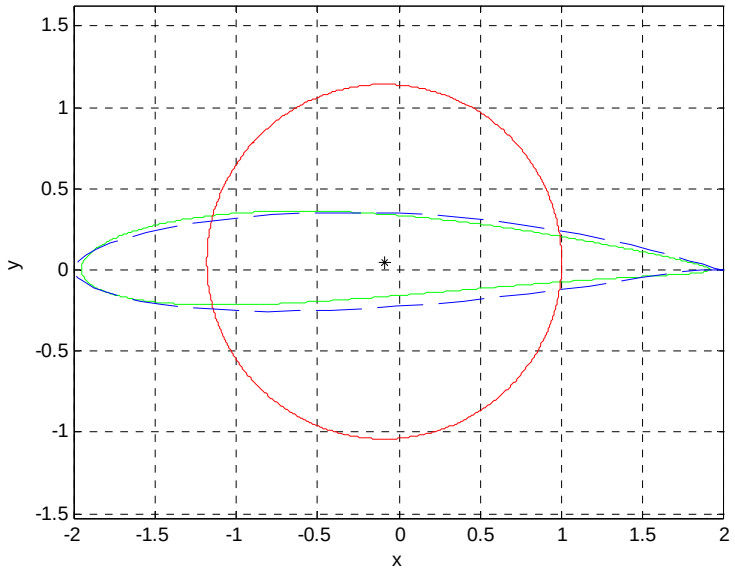

Figure C4: *S834 airfoil. Green: Airfoil's shape achieved through a Karman-Trefftz conformal mapping. Blue: Original shape of the airfoil. Red: Circle used for obtaining the airfoil through the Karman-Trefftz conformal mapping. *: Origin of the circle.*

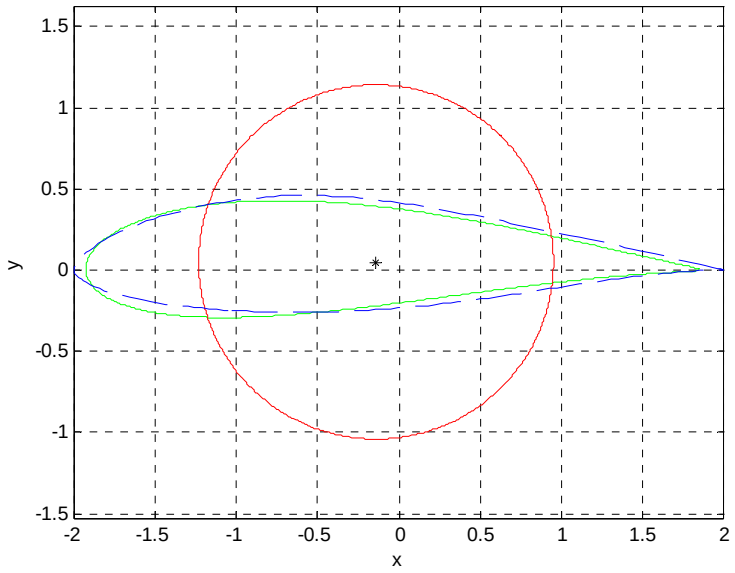

Figure C5: *DU96 airfoil. Green: Airfoil's shape achieved through a Karman-Trefftz conformal mapping. Blue: Original shape of the airfoil. Red: Circle used for obtaining the airfoil through the Karman-Trefftz conformal mapping. *: Origin of the circle.*

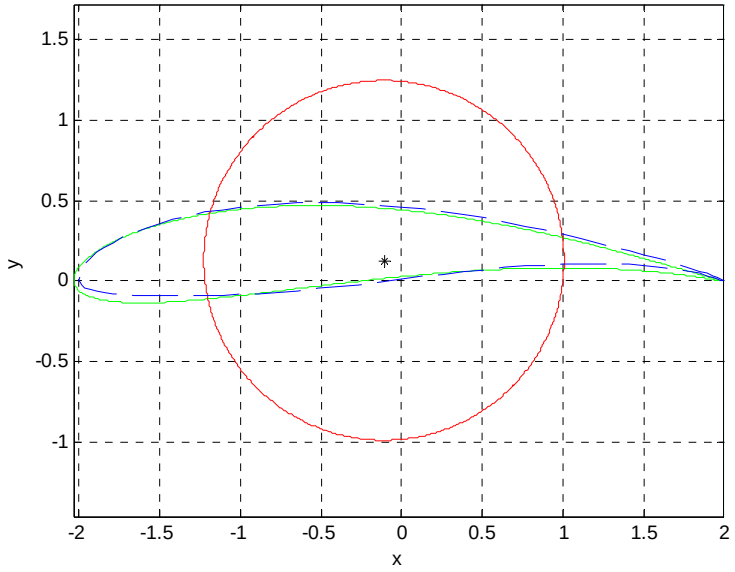

Figure C6: *FX63-137 airfoil. Green: Airfoil's shape achieved through a Karman-Trefftz conformal mapping. Blue: Original shape of the airfoil. Red: Circle used for obtaining the airfoil through the Karman-Trefftz conformal mapping. *: Origin of the circle.*

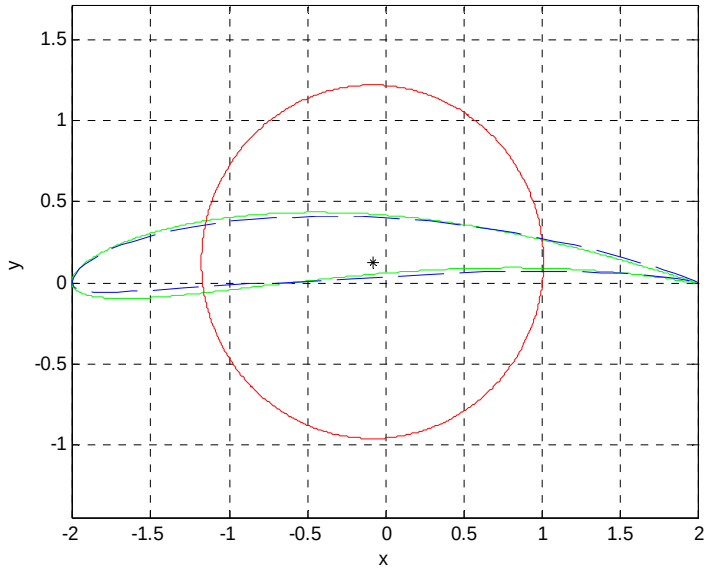

Figure C7: *SG6043 airfoil. Green: Airfoil's shape achieved through a Karman-Trefftz conformal mapping. Blue: Original shape of the airfoil. Red: Circle used for obtaining the airfoil through the Karman-Trefftz conformal mapping. *: Origin of the circle.*

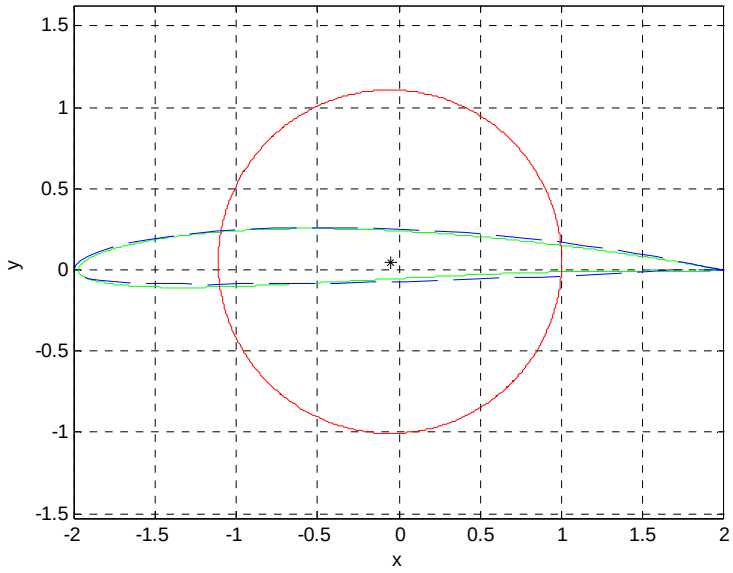

Figure C8: *SD2030 airfoil. Green: Airfoil's shape achieved through a Karman-Trefftz conformal mapping. Blue: Original shape of the airfoil. Red: Circle used for obtaining the airfoil through the Karman-Trefftz conformal mapping. *: Origin of the circle.*

Appendix D: NAFNoise

NAFNoise is a program developed by researchers at NREL to predict airfoil self noise (Moriarty and Migliore, 2003; Moriarty et al., 2004 and 2005, Moriarty, 2005). This software predicts the noise of any airfoil accounting for five noise mechanisms: TBL-TE noise, S/SF noise, LBL-VS noise, TEB-VS noise, and turbulent inflow noise.

Several different prediction models are available in the program. The first four aforementioned noise sources can be predicted using the semi empirical method developed by Brooks et al. (1989). Moreover, it is possible to choose the use of the method of Brooks et al. (1989), but with the boundary layer parameters being calculated by XFOIL (Appendix C shows a description of this program) instead of semi-empirical formulas (Moriarty et al., 2004). A newly developed method that relates the noise emitted with the pressure field over the whole airfoil's surface can also be used (Moriarty et al., 2005).

The prediction of turbulent inflow noise is made using a semi-empirical method based on the work of Amiet (1975). This method is improved using two modifications: the introduction of a turbulent inflow noise correction developed by Guidati (Moriarty et al., 2004 and 2005) and a simplified version of the same Guidati's method that is less computationally intensive. The method of Guidati provides a correction to Amiet's method for turbulent inflow noise to account for airfoil shape (Moriarty, 2005, Moriarty et al., 2004 and 2005).

The program utilizes an input file in ASCII format where it can be specified the combinations of models to use, the geometric characteristics of the airfoil (including the shape of the airfoil provided as a set of points), the characteristics of the flow, etc. The output of the program is an ASCII file that provides the predicted noise levels as sound pressure level in 1/3rd octave bands. The noise levels are printed separately for each noise mechanism, and a total noise level is printed too.

In the present thesis, the noise predictions made with NAFNoise are performed using the semi-empirical method of Brooks et al (1989), and no inflow noise predictions are made.

Appendix E: Accuracy of Predictions

In this appendix, results are presented for the average and maximum level difference metrics for the individual control vectors using Models I-*e* and II-*h*. In these figures, the control vector case is defined as a circle in a plot of the angle of attack α versus the chord Reynolds number R_c. A color scheme is used to plot the level difference. For each airfoil considered in the aforementioned model, four figures are presented corresponding to average level difference metrics for tripped cases, maximum level difference metrics for no-tripped cases, average level difference metrics for no-tripped cases, and maximum level difference metrics for no-tripped cases.

E.1 Model I-*e*

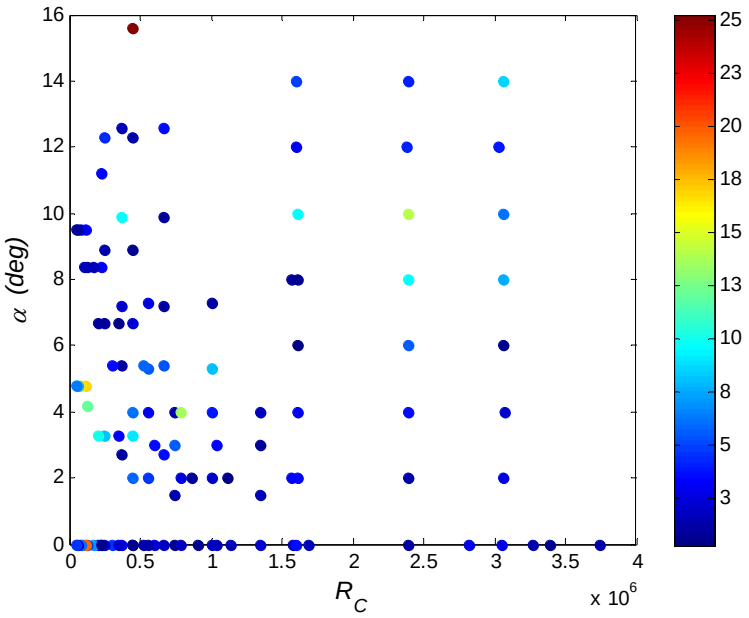

Figure E1: *Average Level difference metric for each control vector using Model I-e for no-tripped case. Training using the ATANA approach.*

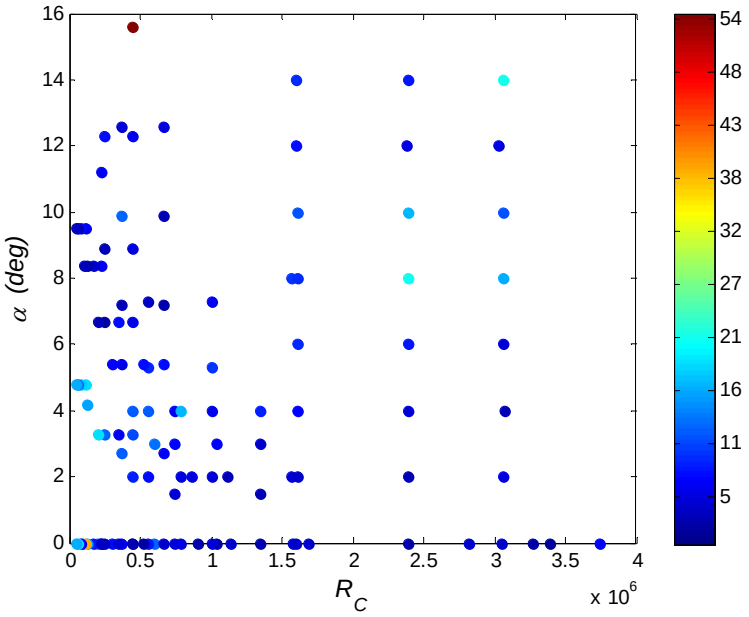

Figure E2: *Maximum Level difference metric for each control vector using Model I-e for no-tripped case. Training using the ATANA approach.*

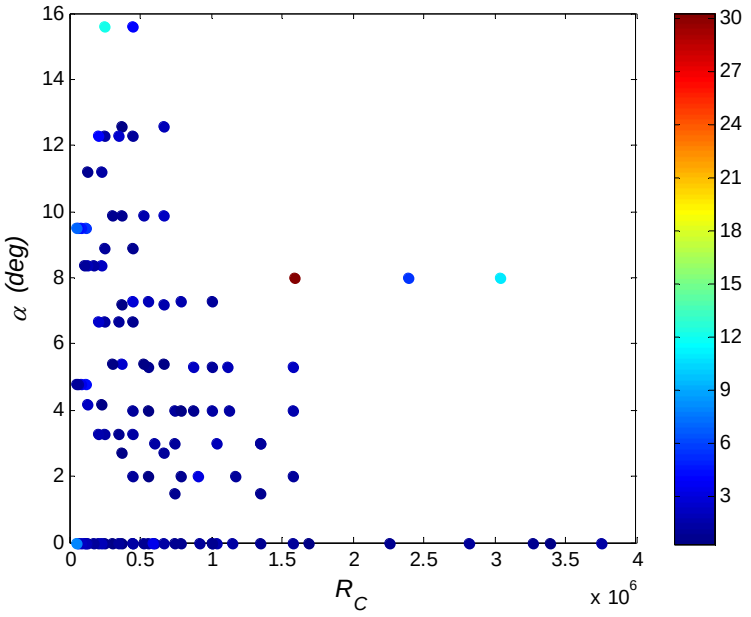

Figure E3: *Average Level difference metric for each control vector using Model I-e for tripped case. Training using the ATANA approach.*

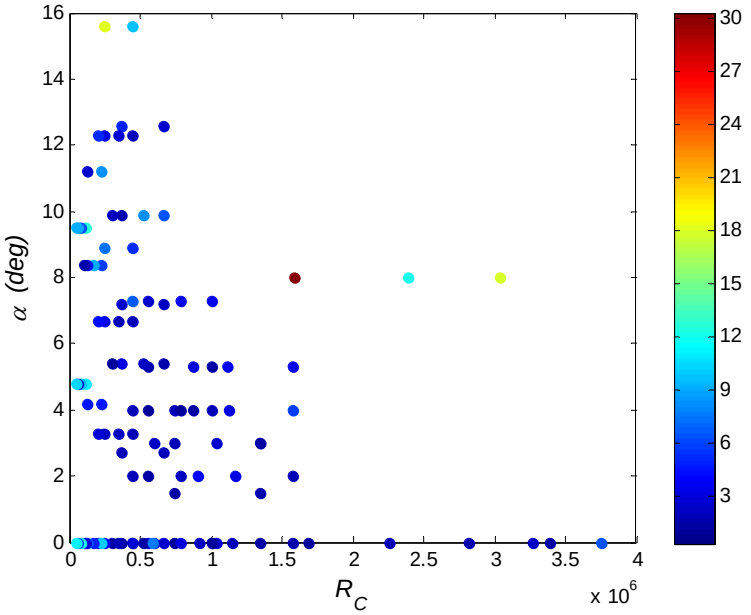

Figure E4: *Maximum Level difference metric for each control vector using Model I-e for tripped case. Training using the ATANA approach.*

E.2 Model II-*h*

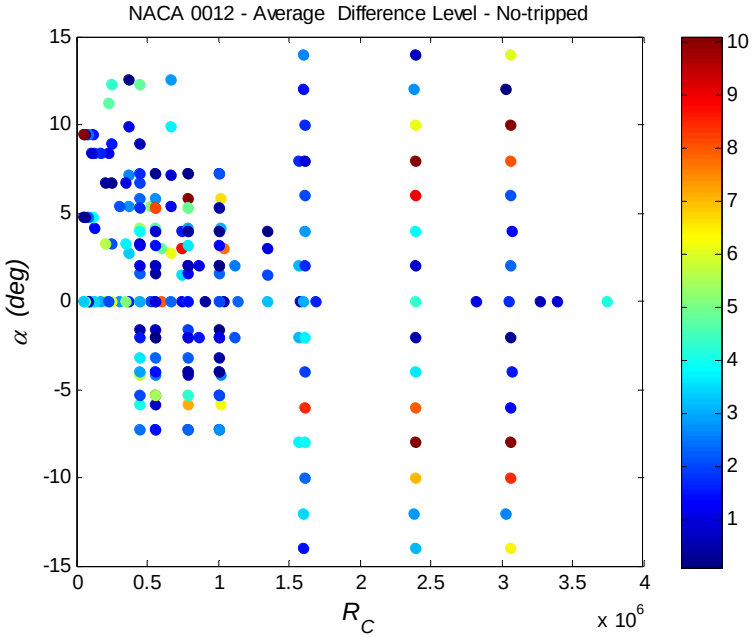

Figure E5: *Average level difference metric for each control vector using Model II-h for no-tripped case for the NACA 0012 airfoil. Training using the ATANA approach.*

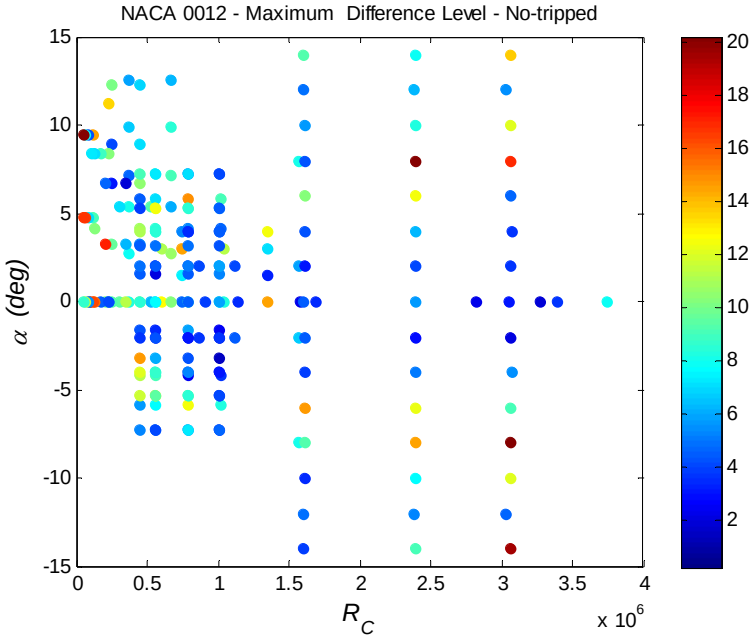

Figure E6: *Maximum level difference metric for each control vector using Model II-h for no-tripped case for the NACA 0012 airfoil. Training using the ATANA approach.*

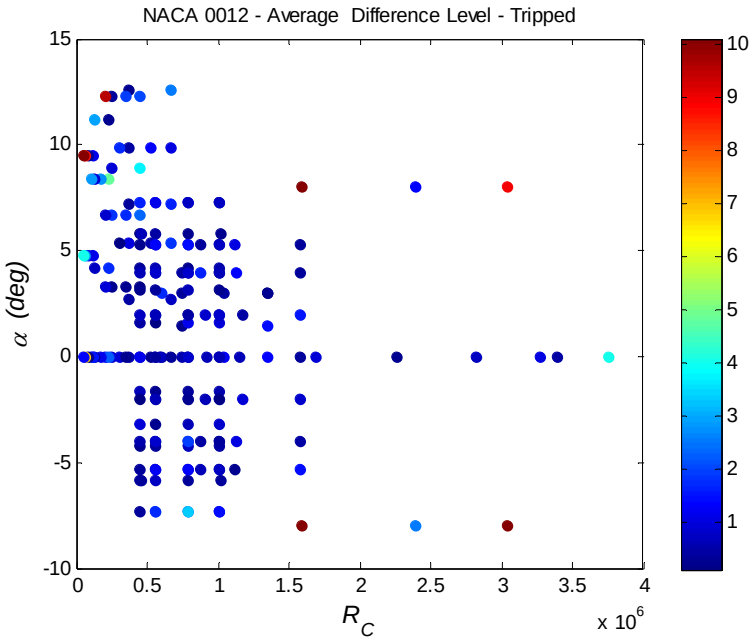

Figure E7: *Average level difference metric for each control vector using Model II-h for tripped case for the NACA 0012 airfoil. Training using the ATANA approach.*

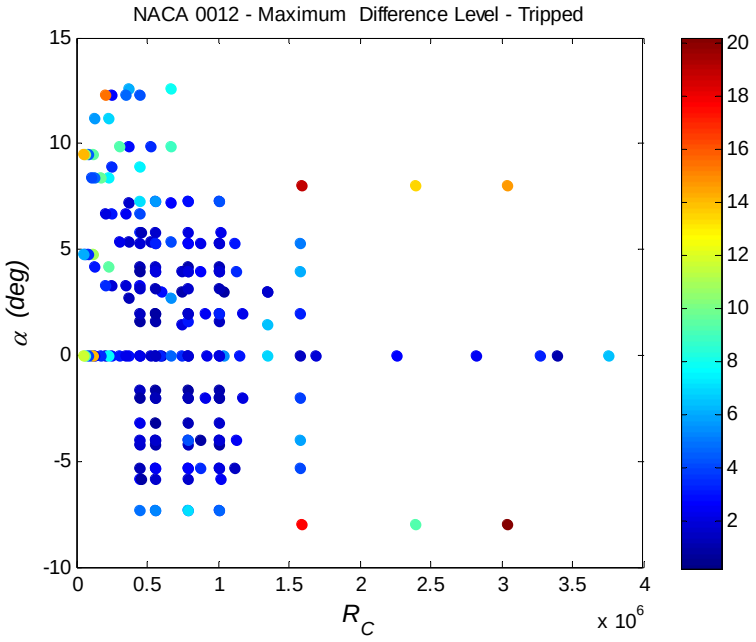

Figure E8: *Maximum level difference metric for each control vector using Model II-h for tripped case for the NACA 0012 airfoil. Training using the ATANA approach.*

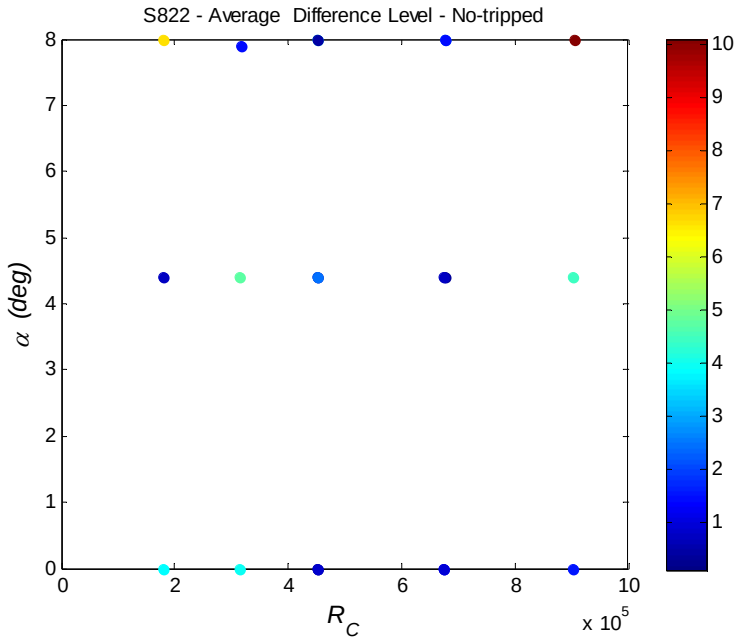

Figure E9: *Average level difference metric for each control vector using Model II-h for no-tripped case for the S822 airfoil. Training using the ATANA approach.*

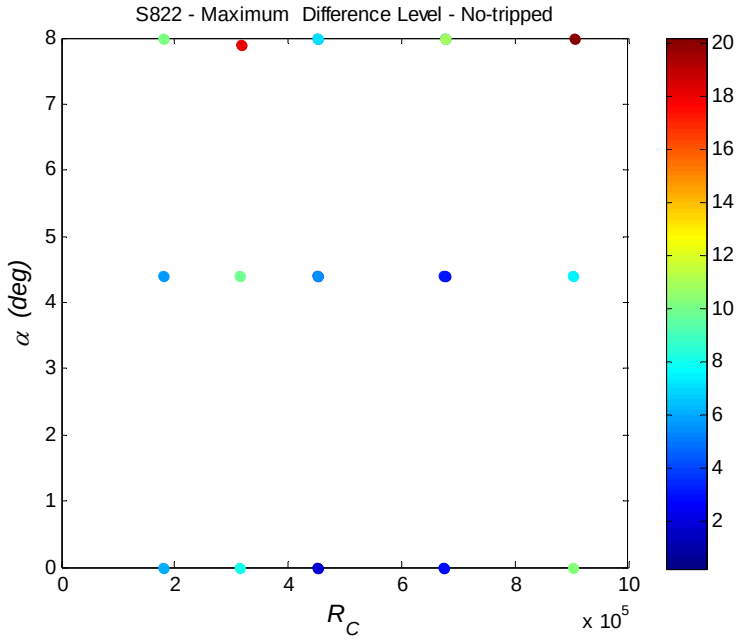

Figure E10: *Maximum level difference metric for each control vector using Model II-h for no-tripped case for the S822 airfoil. Training using the ATANA approach.*

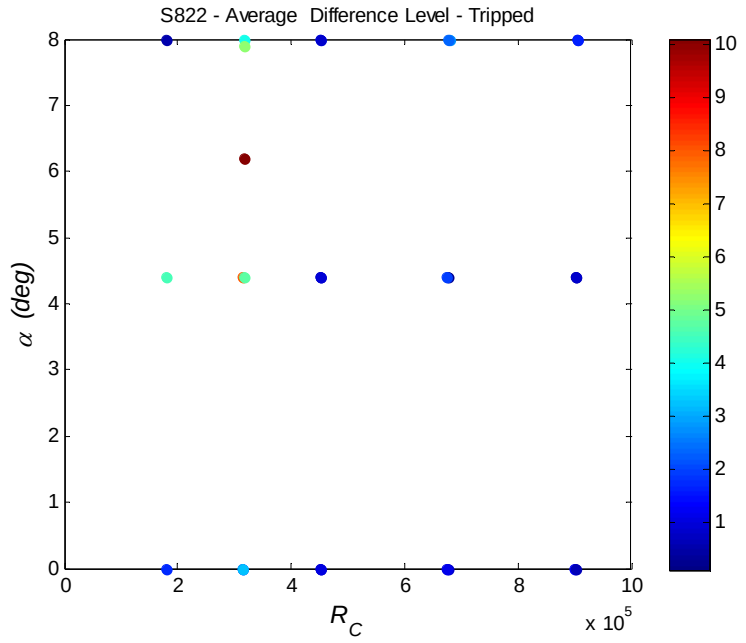

Figure E11: *Average level difference metric for each control vector using Model II-h for tripped case for the S822 airfoil. Training using the ATANA approach.*

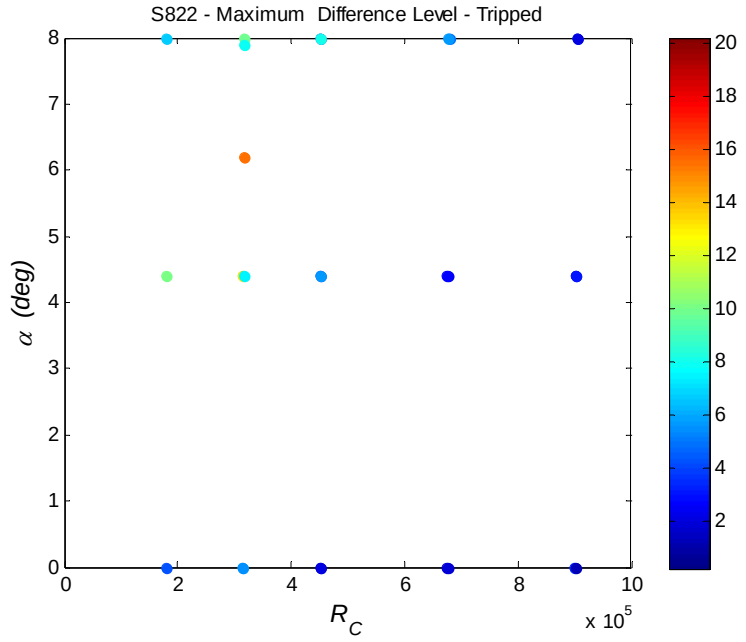

Figure E12: *Maximum level difference metric for each control vector using Model II-h for tripped case for the S822 airfoil. Training using the ATANA approach.*

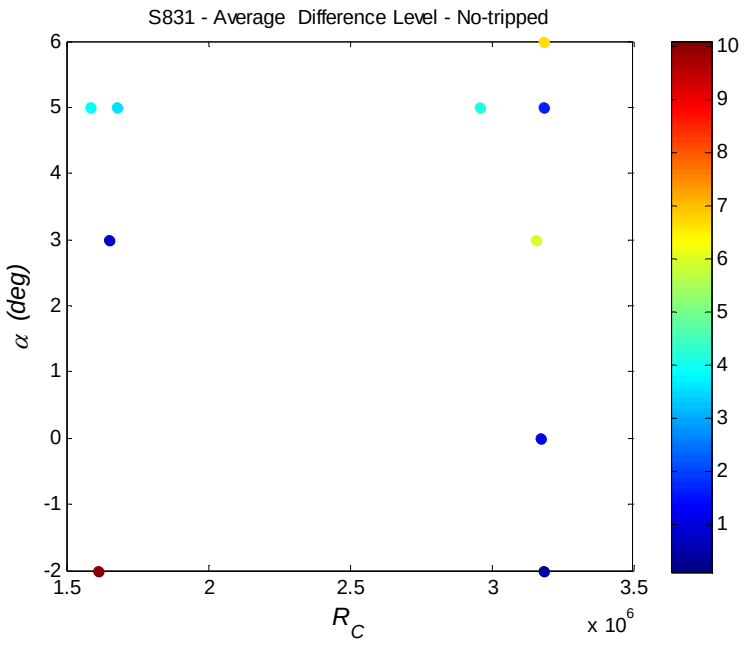

Figure E13: *Average level difference metric for each control vector using Model II-h for no-tripped case for the S831 airfoil. Training using the ATANA approach.*

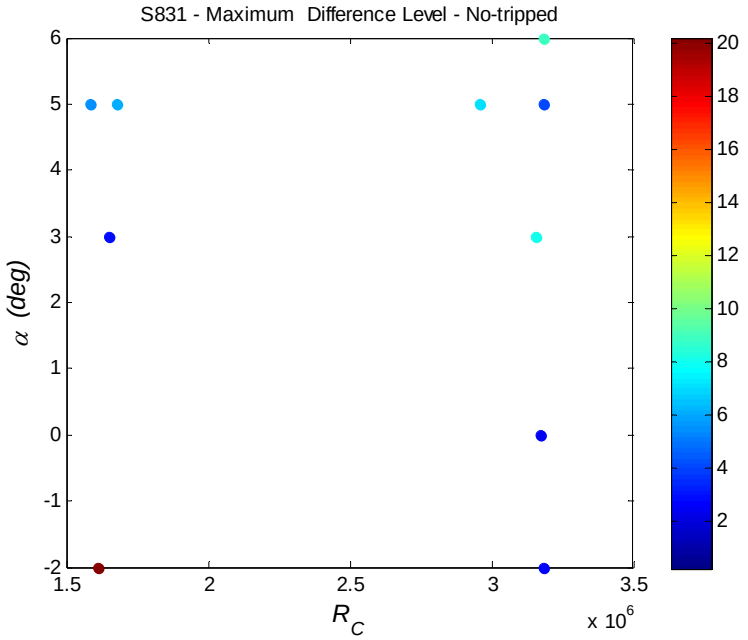

Figure E14: *Maximum level difference metric for each control vector using Model II-h for no-tripped case for the S831 airfoil. Training using the ATANA approach.*

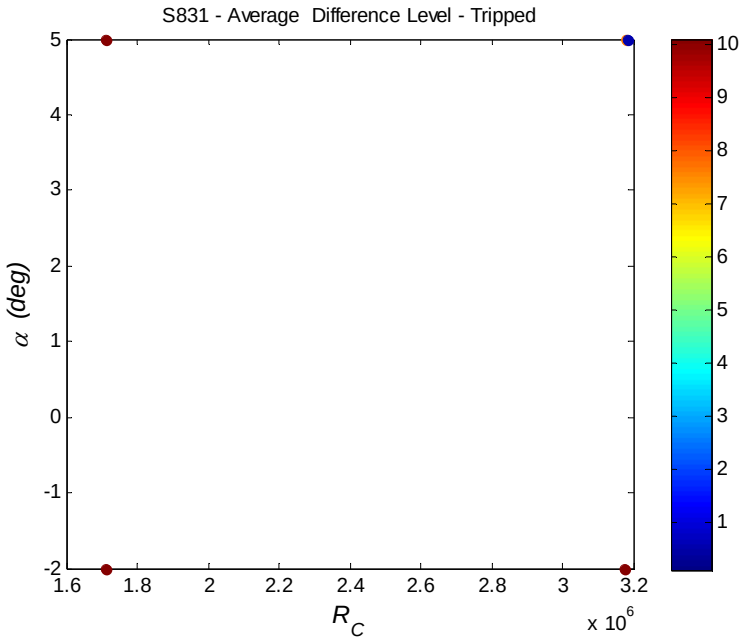

Figure E15: *Average level difference metric for each control vector using Model II-h for tripped case for the S831 airfoil. Training using the ATANA approach.*

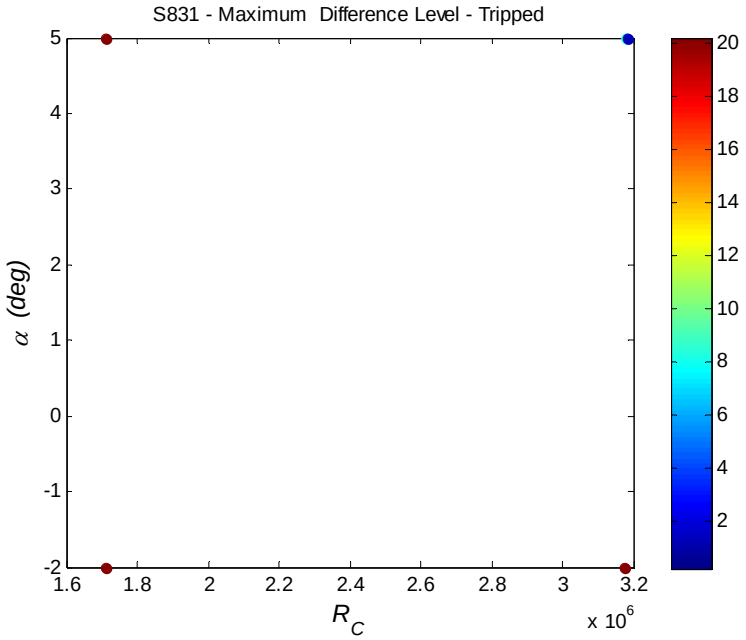

Figure E16: *Maximum level difference metric for each control vector using Model II-h for tripped case for the S831 airfoil. Training using the ATANA approach.*

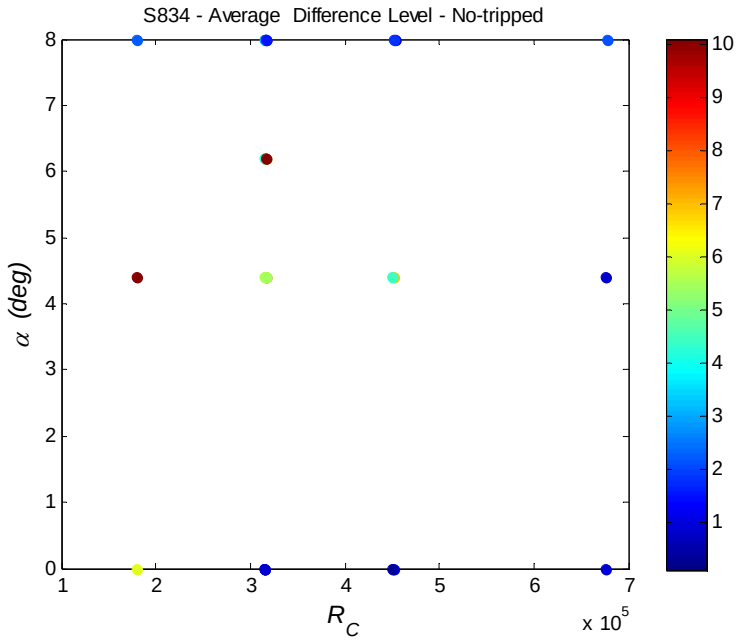

Figure E17: *Average level difference metric for each control vector using Model II-h for no-tripped case for the S834 airfoil. Training using the ATANA approach.*

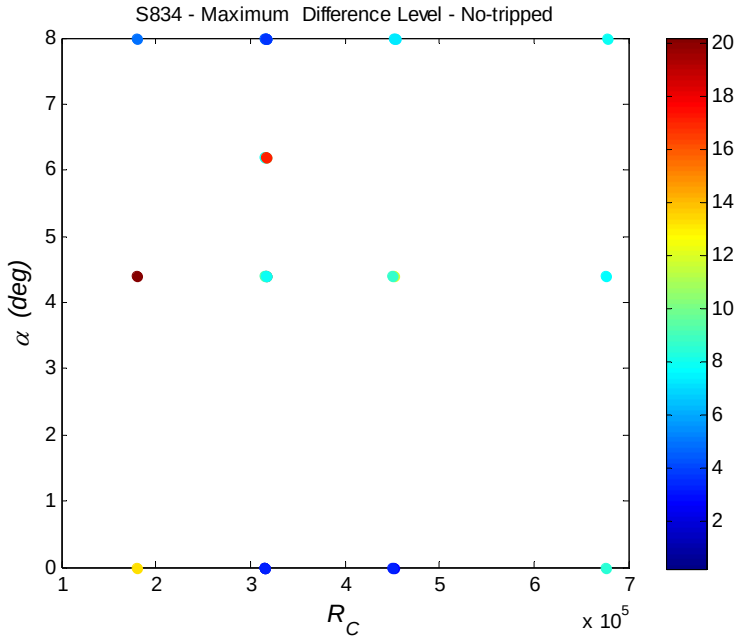

Figure E18: *Maximum level difference metric for each control vector using Model II-h for no-tripped case for the S834 airfoil. Training using the ATANA approach.*

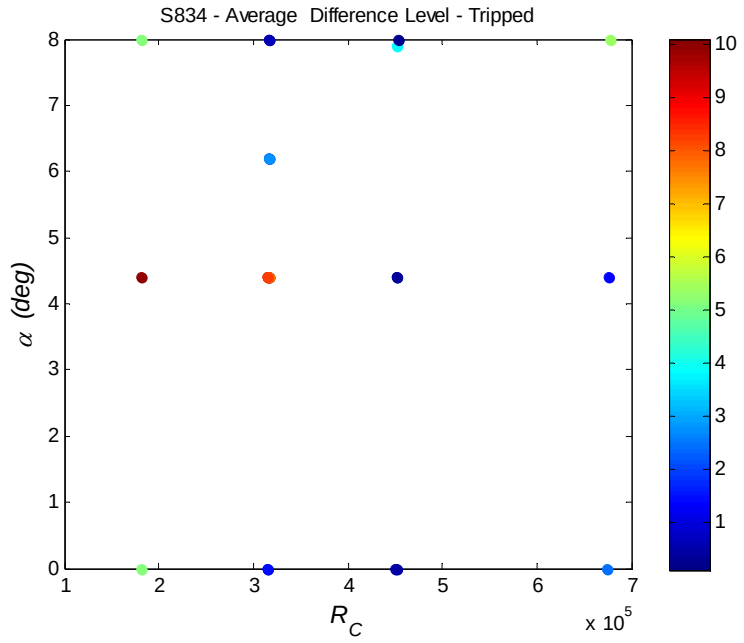

Figure E19: *Average level difference metric for each control vector using Model II-h for tripped case for the S834 airfoil. Training using the ATANA approach.*

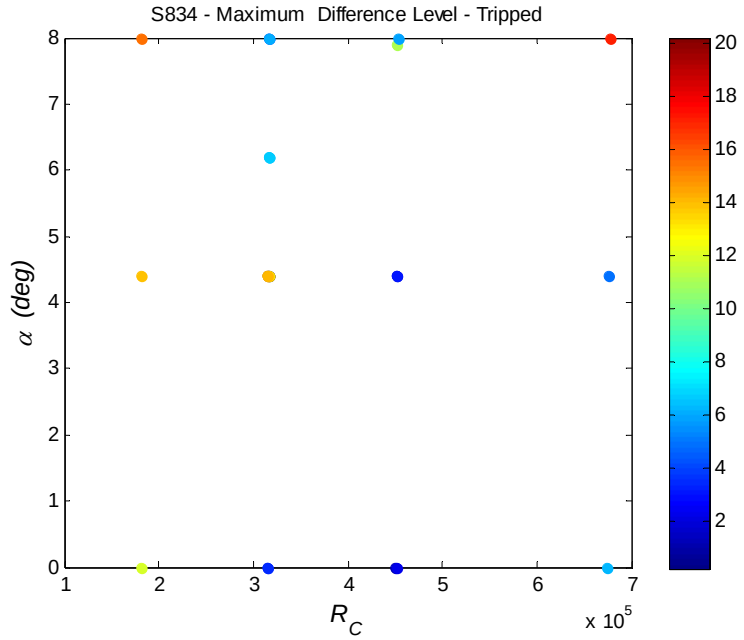

Figure E20: *Maximum level difference metric for each control vector using Model II-h for tripped case for the S834 airfoil. Training using the ATANA approach.*

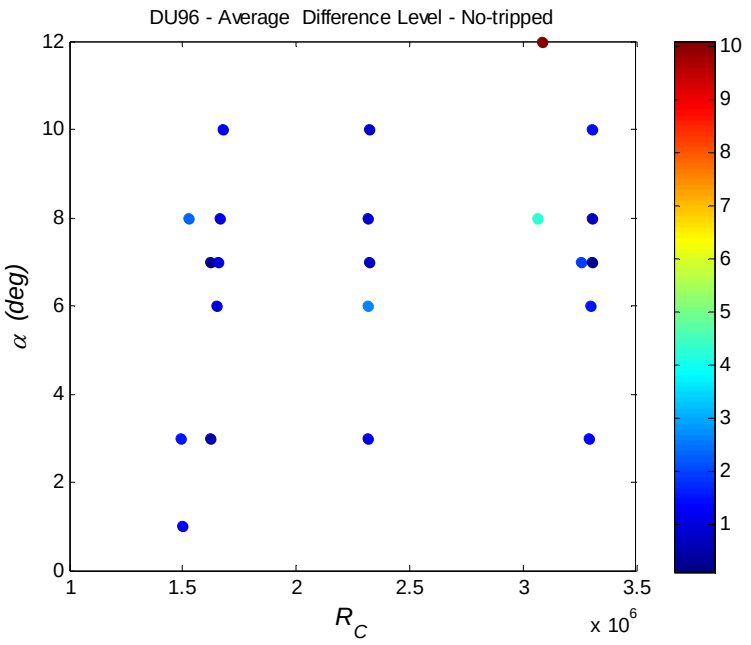

Figure E21: *Average level difference metric for each control vector using Model II-h for no-tripped case for the DU96 airfoil. Training using the ATANA approach.*

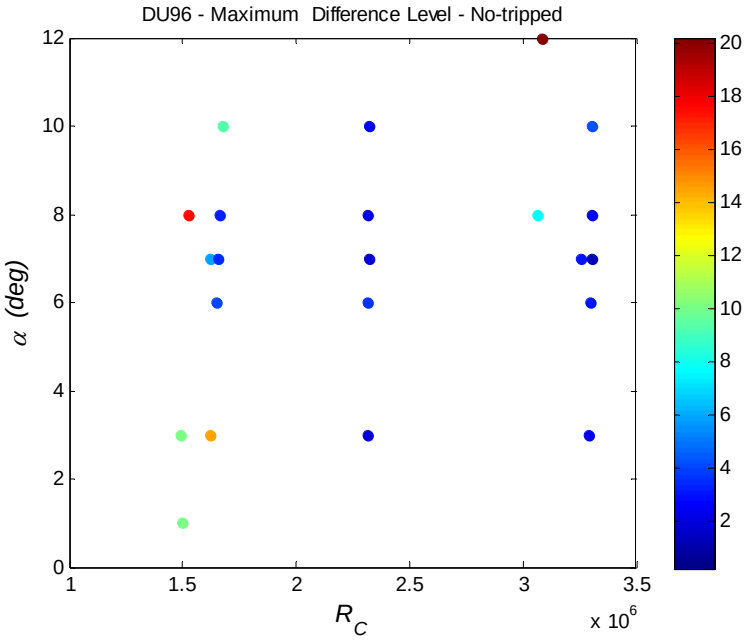

Figure E22: *Maximum level difference metric for each control vector using Model II-h for no-tripped case for the DU96 airfoil. Training using the ATANA approach.*

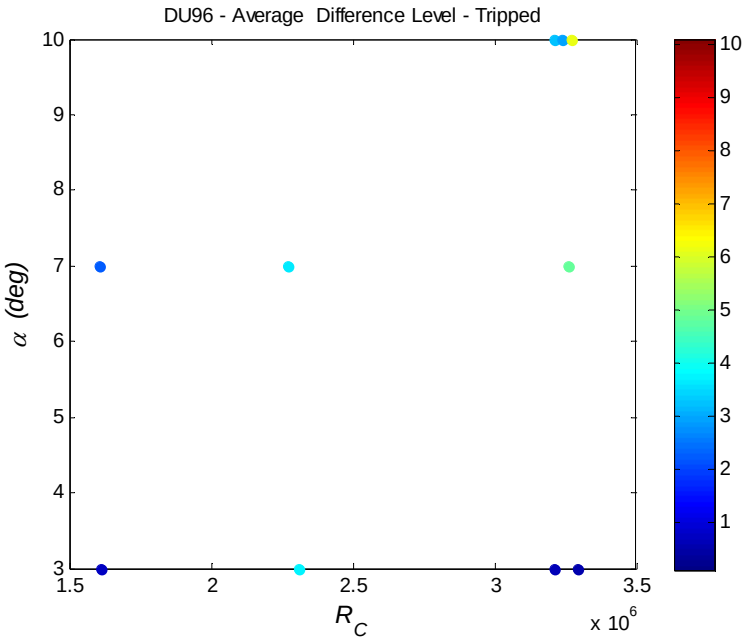

Figure E23: *Average level difference metric for each control vector using Model II-h for tripped case for the DU96 airfoil. Training using the ATANA approach.*

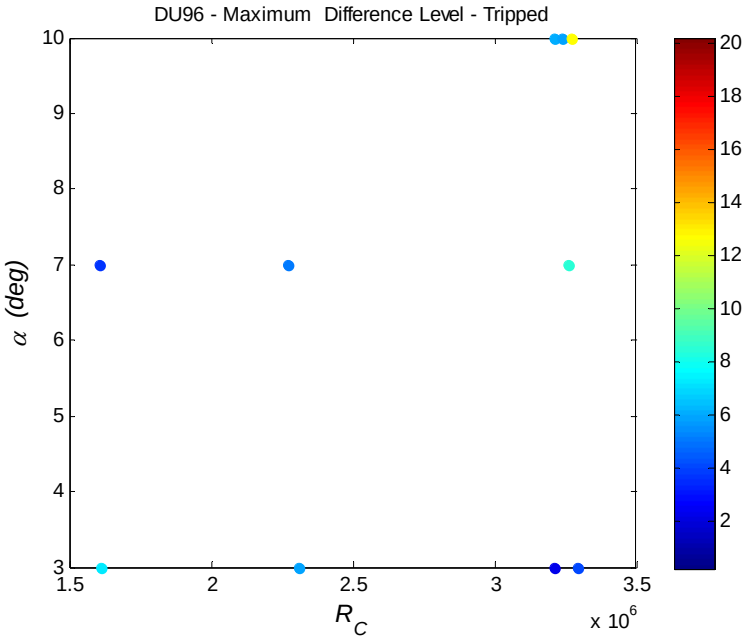

Figure E24: *Maximum level difference metric for each control vector using Model II-h for tripped case for the DU96 airfoil. Training using the ATANA approach.*

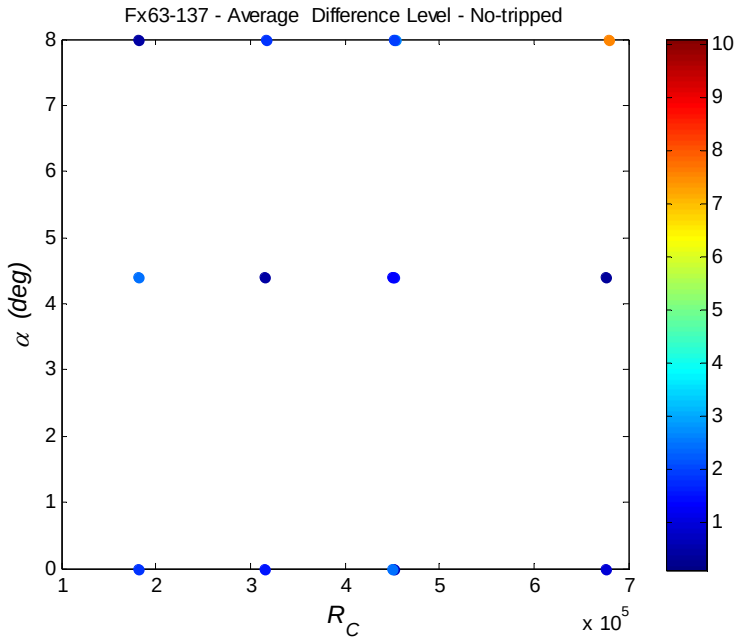

Figure E25: *Average level difference metric for each control vector using Model II-h for no-tripped case for the Fx63-137 airfoil. Training using the ATANA approach.*

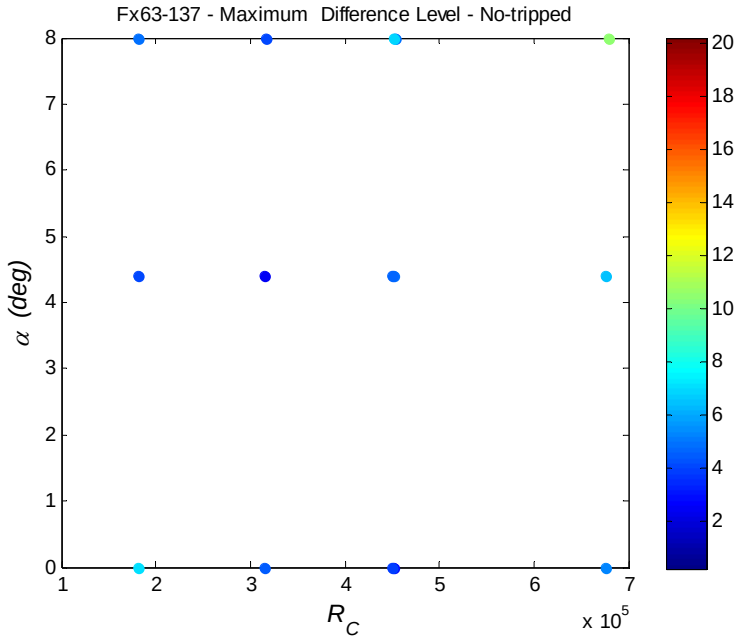

Figure E26: *Maximum level difference metric for each control vector using Model II-h for no-tripped case for the Fx63-137 airfoil. Training using the ATANA approach.*

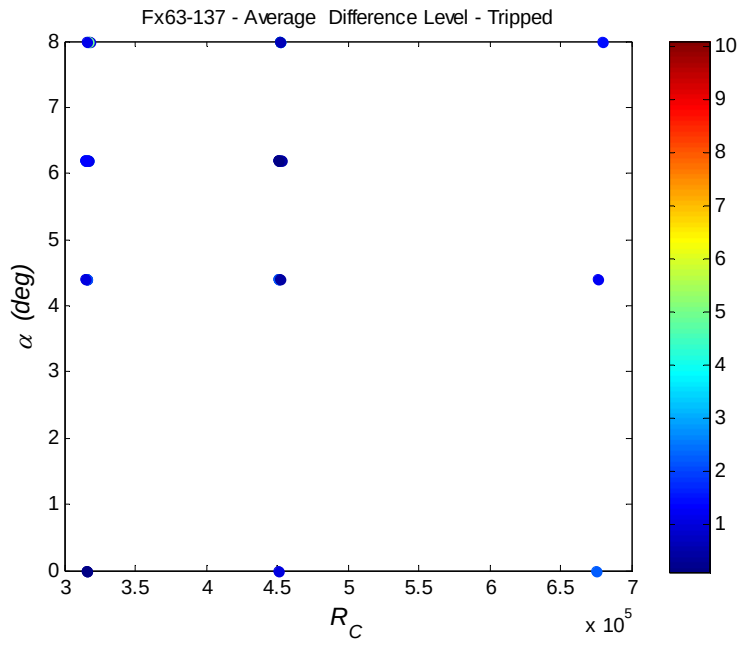

Figure E27: *Average level difference metric for each control vector using Model II-h for tripped case for the Fx63-137 airfoil. Training using the ATANA approach.*

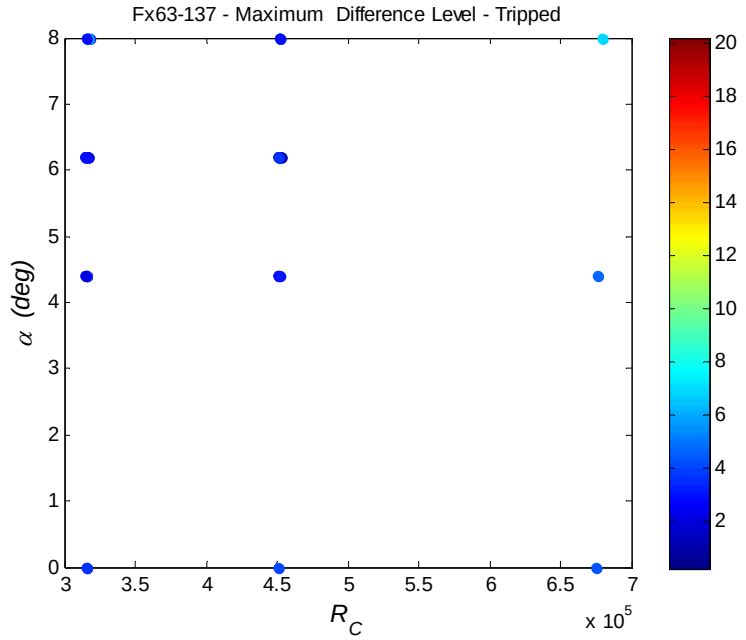

Figure E28: *Maximum level difference metric for each control vector using Model II-h for tripped case for the Fx63-137 airfoil. Training using the ATANA approach.*

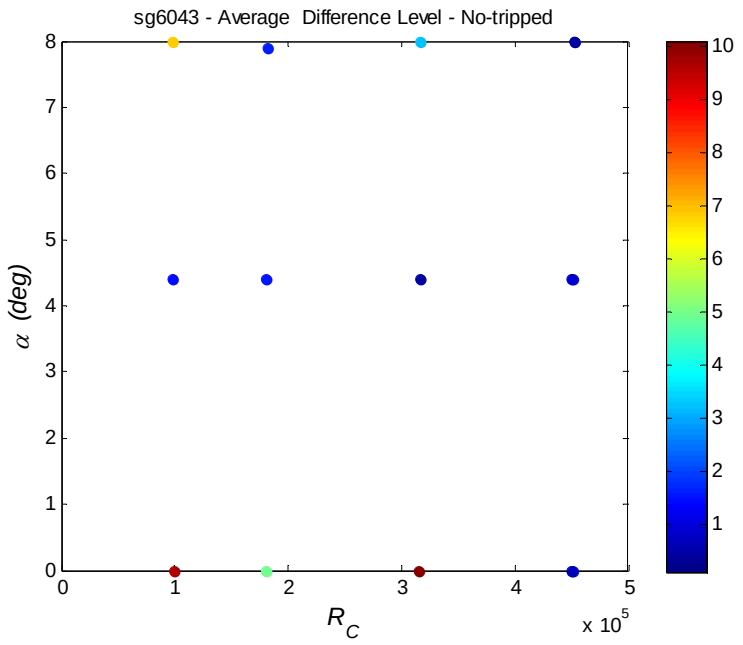

Figure E29: *Average level difference metric for each control vector using Model II-h for no-tripped case for the sg6043 airfoil. Training using the ATANA approach.*

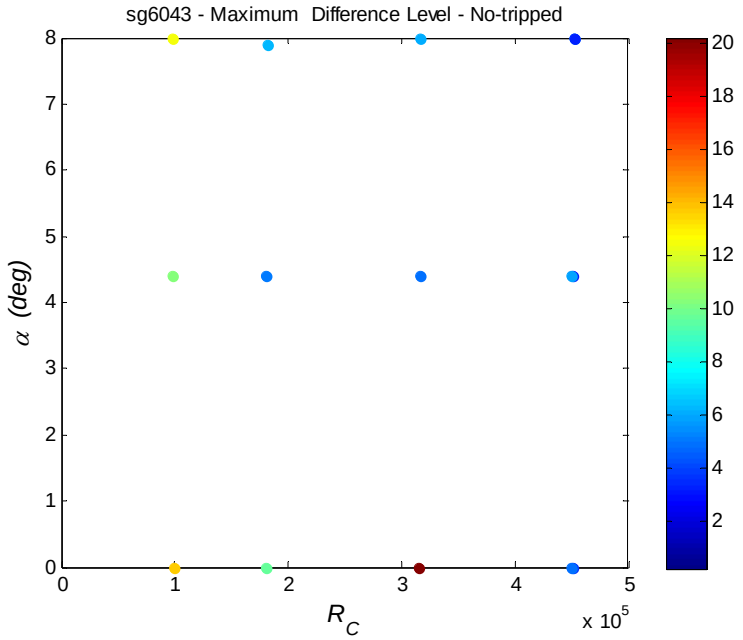

Figure E30: *Maximum level difference metric for each control vector using Model II-h for no-tripped case for the sg6043 airfoil. Training using the ATANA approach.*

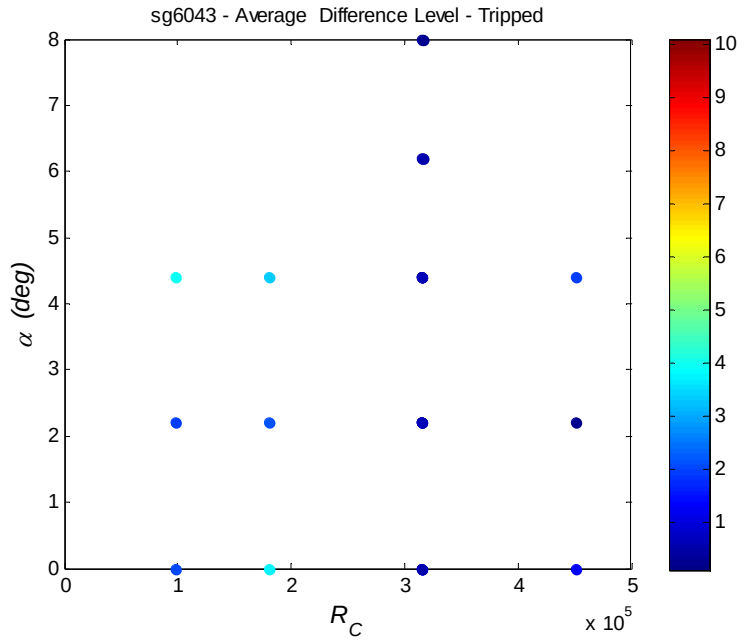

Figure E31: *Average level difference metric for each control vector using Model II-h for tripped case for the sg6043 airfoil. Training using the ATANA approach.*

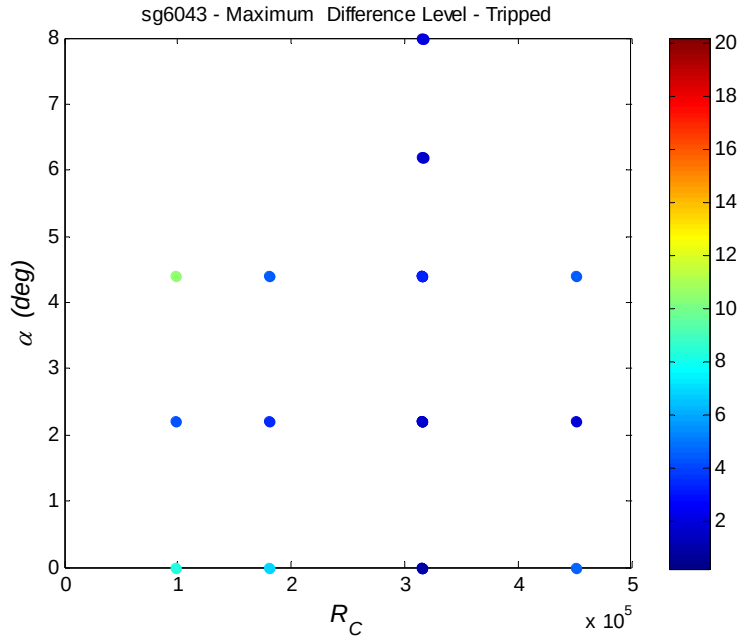

Figure E32: *Maximum level difference metric for each control vector using Model II-h for tripped case for the sg6043 airfoil. Training using the ATANA approach.*

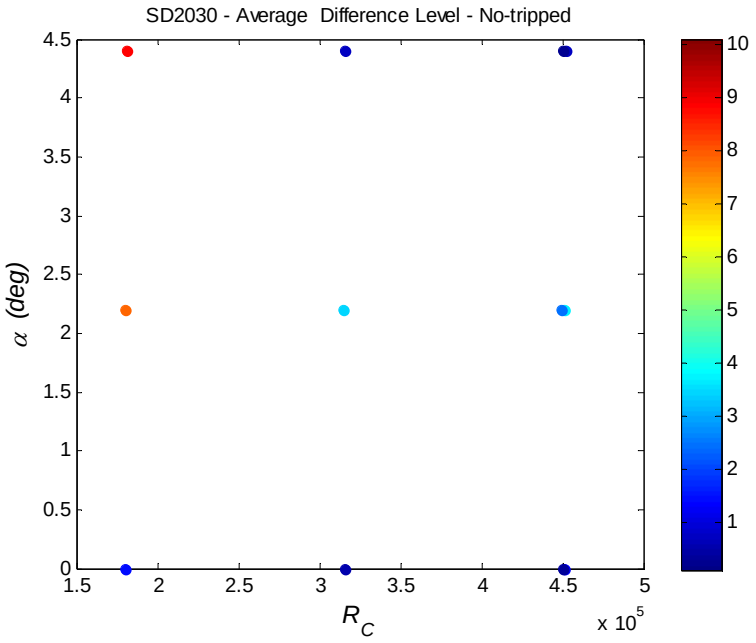

Figure E33: *Average level difference metric for each control vector using Model II-h for no-tripped case for the SD2030 airfoil. Training using the ATANA approach.*

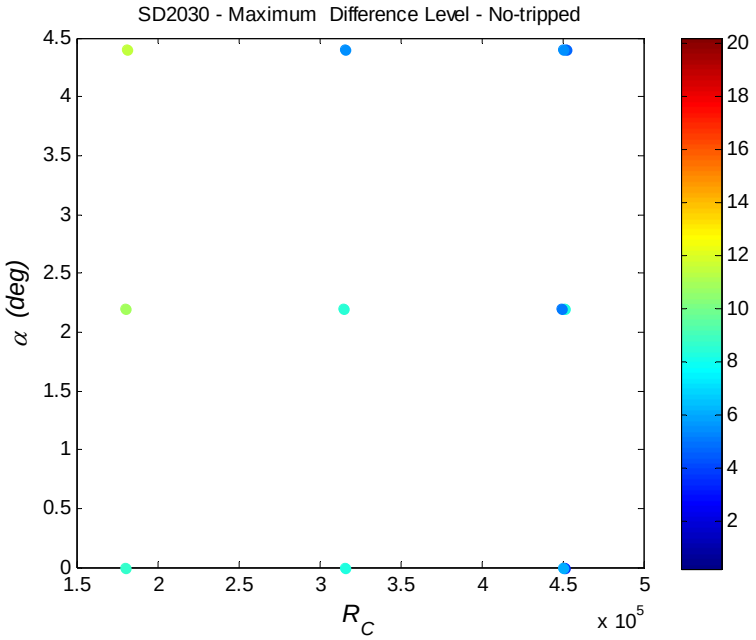

Figure E34: *Maximum level difference metric for each control vector using Model II-h for no-tripped case for the SD2030 airfoil. Training using the ATANA approach.*

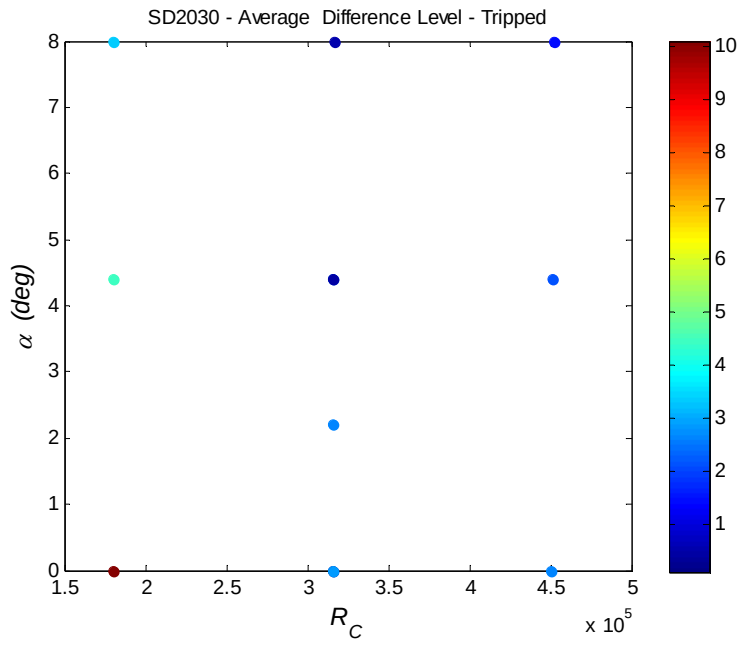

Figure E35: *Average level difference metric for each control vector using Model II-h for tripped case for the SD2030 airfoil. Training using the ATANA approach.*

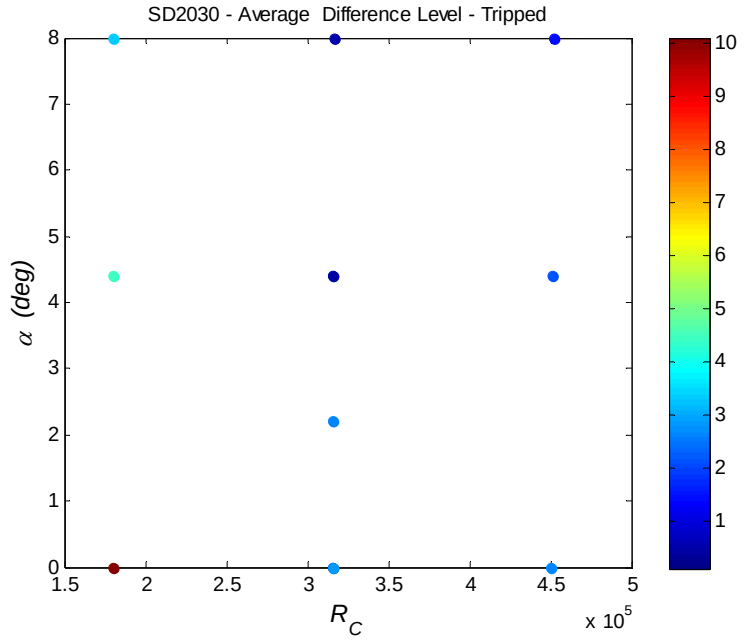

Figure E36: *Maximum level difference metric for each control vector using Model II-h for tripped case for the SD2030 airfoil. Training using the ATANA approach.*

Appendix F: Comparison of Experimental Data and Predictions

This appendix presents a comparison between experimental data and predictions. The figures presented correspond to representative subsets of the results obtained with Models I-*e* and II-*h*.

F.1 Model I-*e* using the ATANA approach

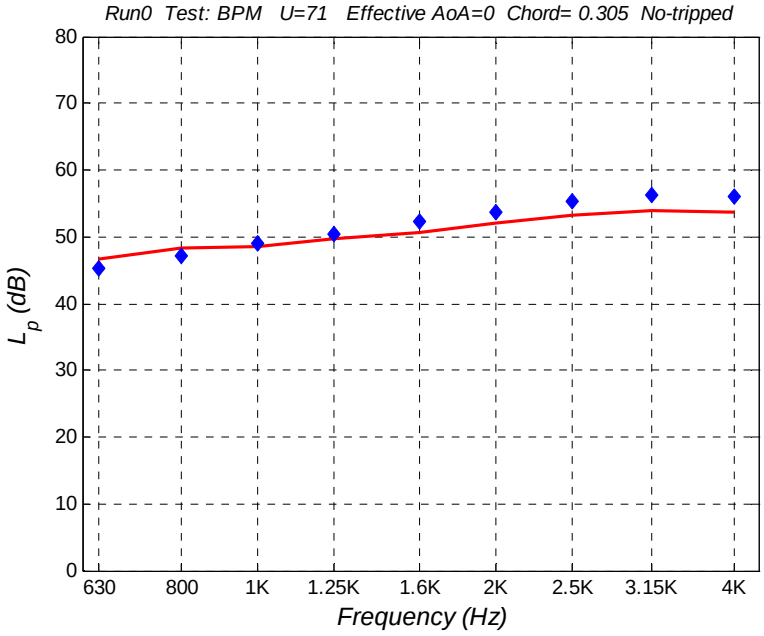

Figure F1: *Example of spectral comparison of experimental results and prediction using Model I-e and the ATANA approach.*

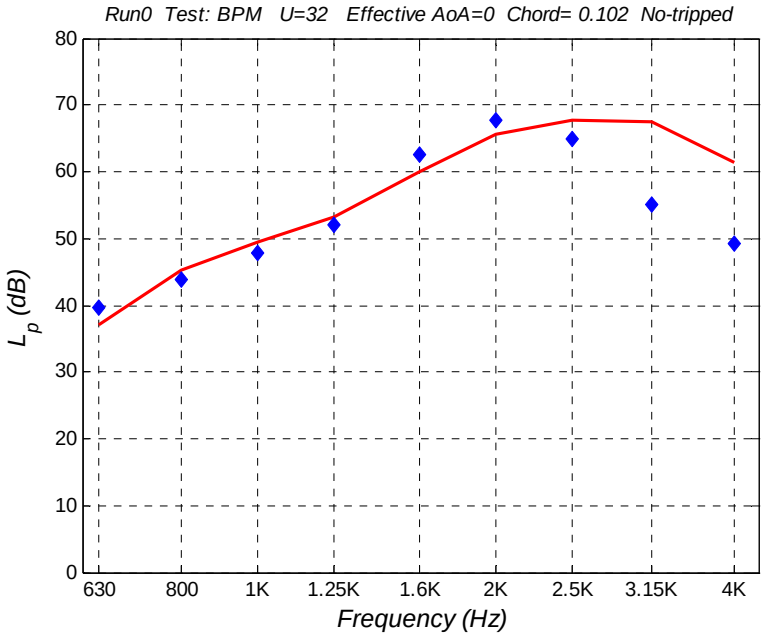

Figure F2: *Example of spectral comparison of experimental results and prediction using Model I-e and the ATANA approach.*

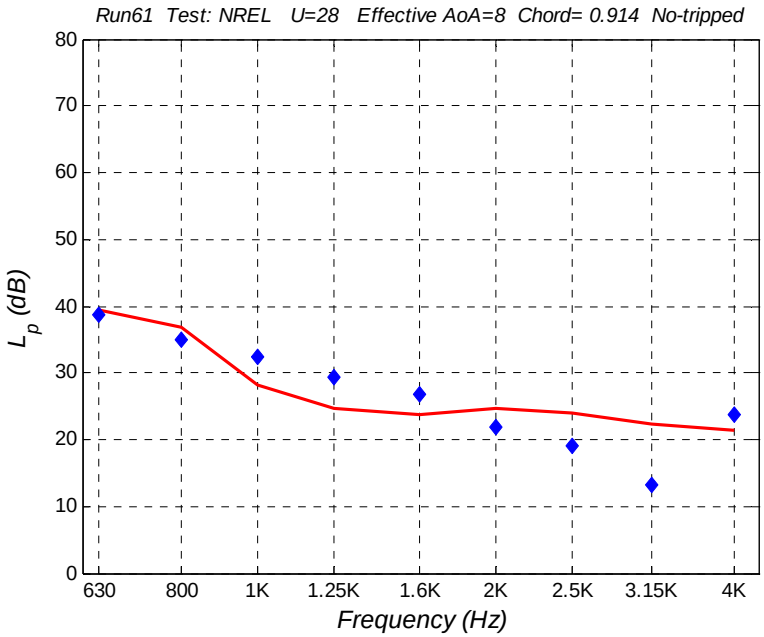

Figure F3: *Example of spectral comparison of experimental results and prediction using Model I-e and the ATANA approach.*

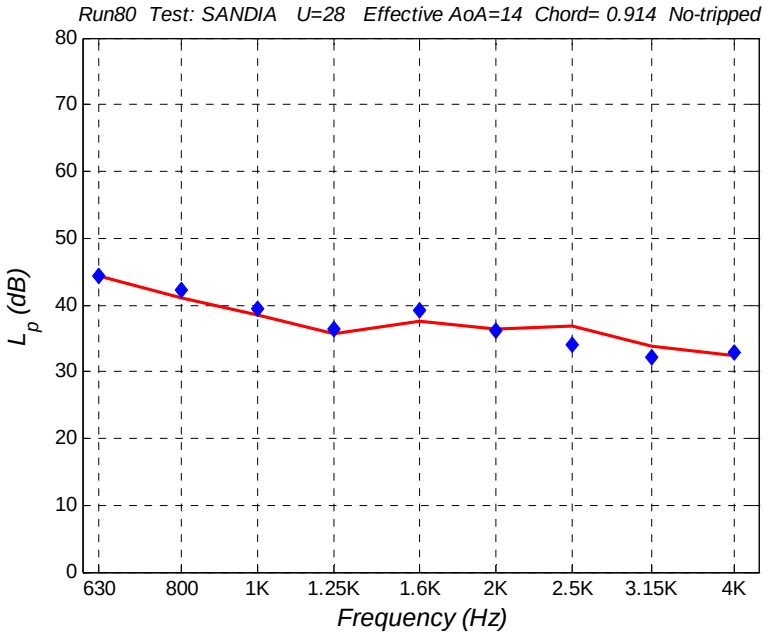

Figure F4: *Example of spectral comparison of experimental results and prediction using Model I-e and the ATANA approach.*

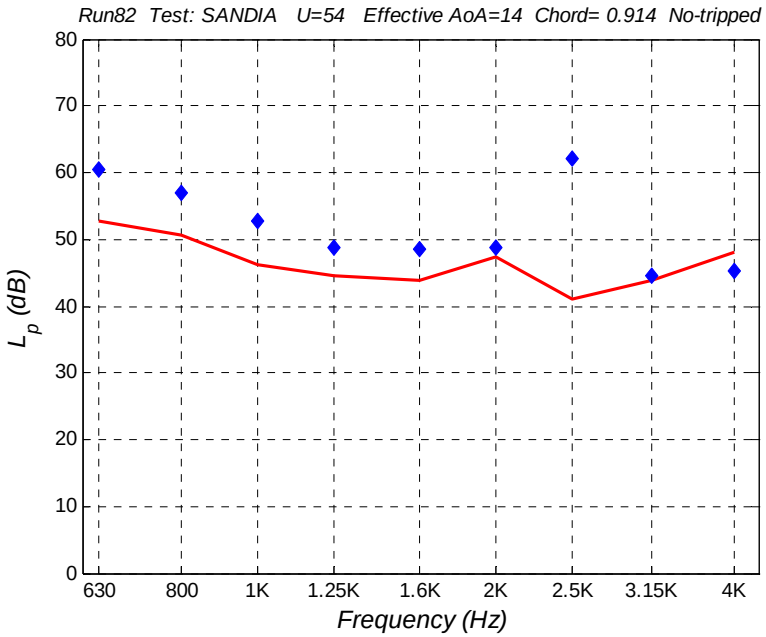

Figure F5: *Example of spectral comparison of experimental results and prediction using Model I-e and the ATANA approach.*

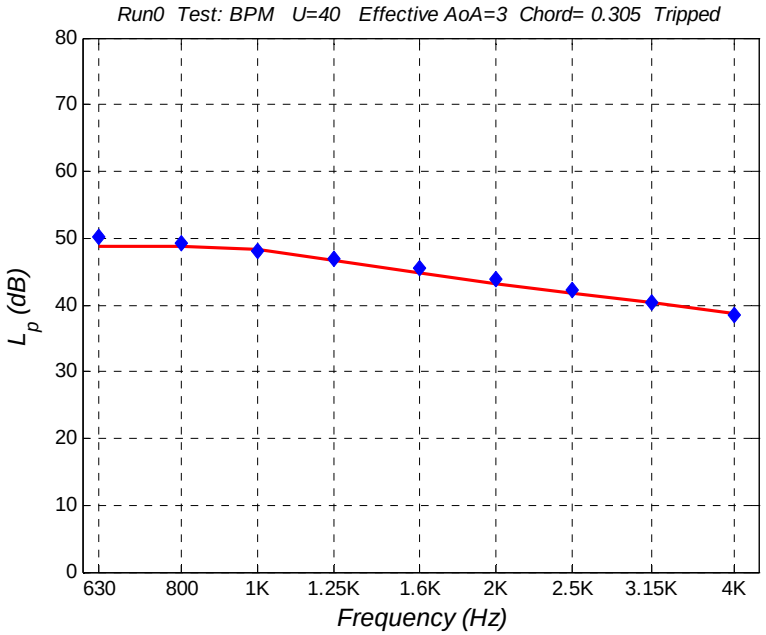

Figure F6: *Example of spectral comparison of experimental results and prediction using Model I-e and the ATANA approach.*

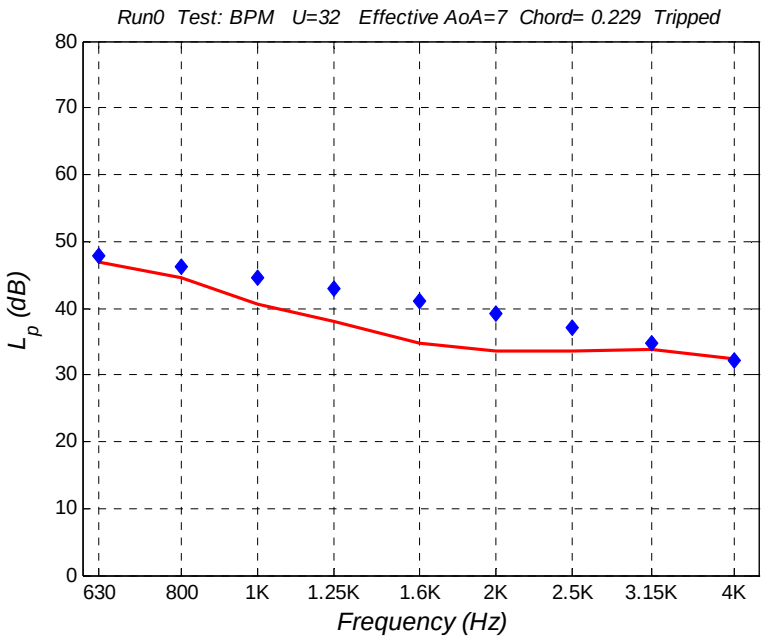

Figure F7: *Example of spectral comparison of experimental results and prediction using Model I-e and the ATANA approach.*

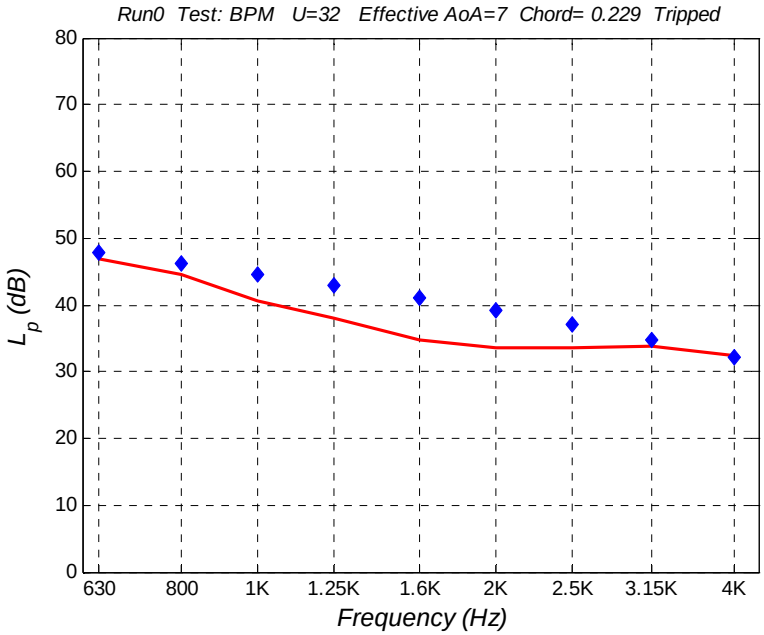

Figure F8: *Example of spectral comparison of experimental results and prediction using Model I-e and the ATANA approach.*

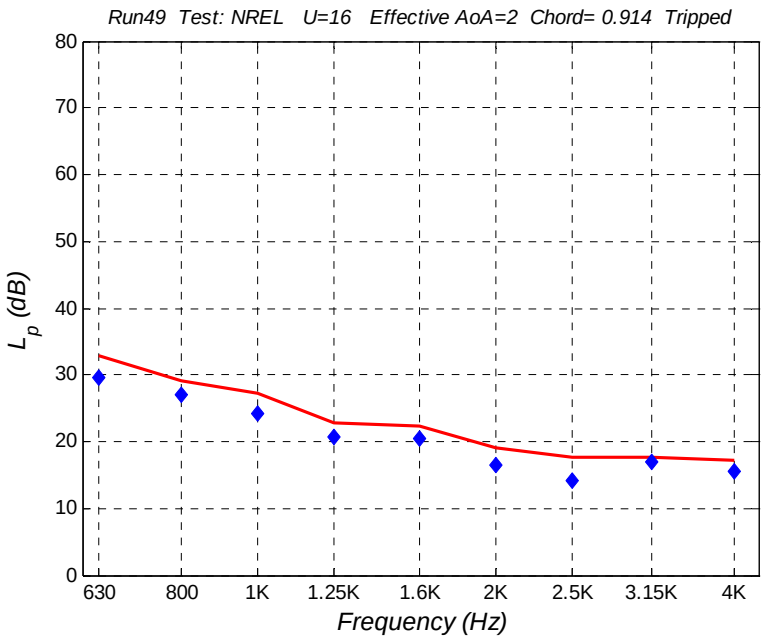

Figure F9: *Example of spectral comparison of experimental results and prediction using Model I-e and the ATANA approach.*

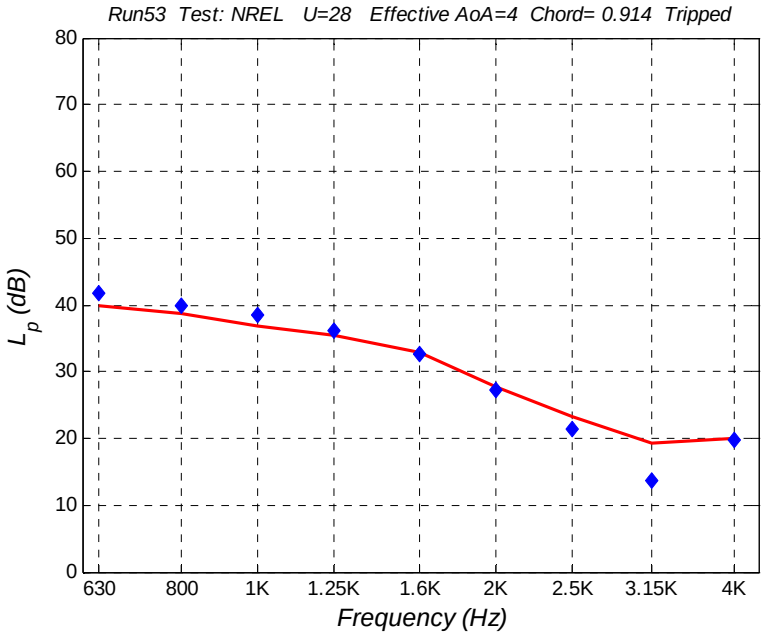

Figure F10: *Example of spectral comparison of experimental results and prediction using Model I-e and the ATANA approach.*

F.2 Model I-*e* using the CTNN approach

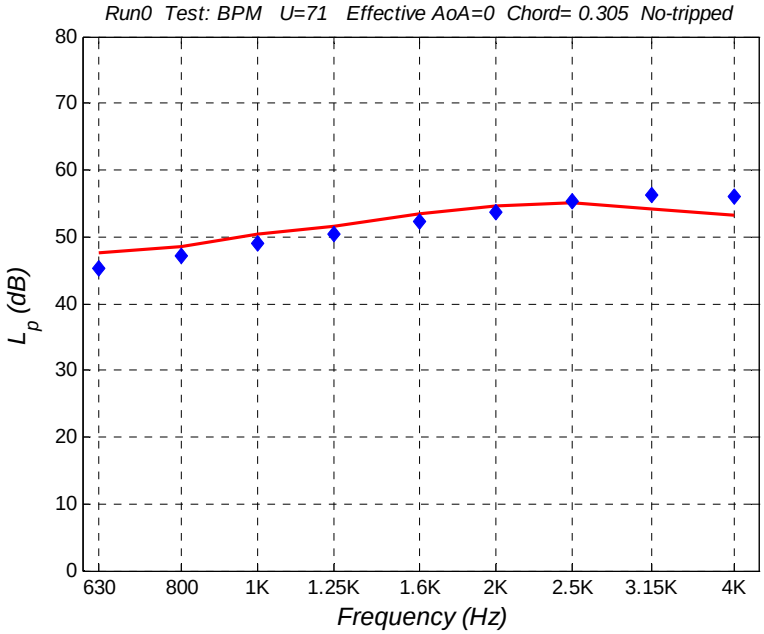

Figure F11: *Example of spectral comparison of experimental results and prediction using Model I-e and the CTNN approach.*

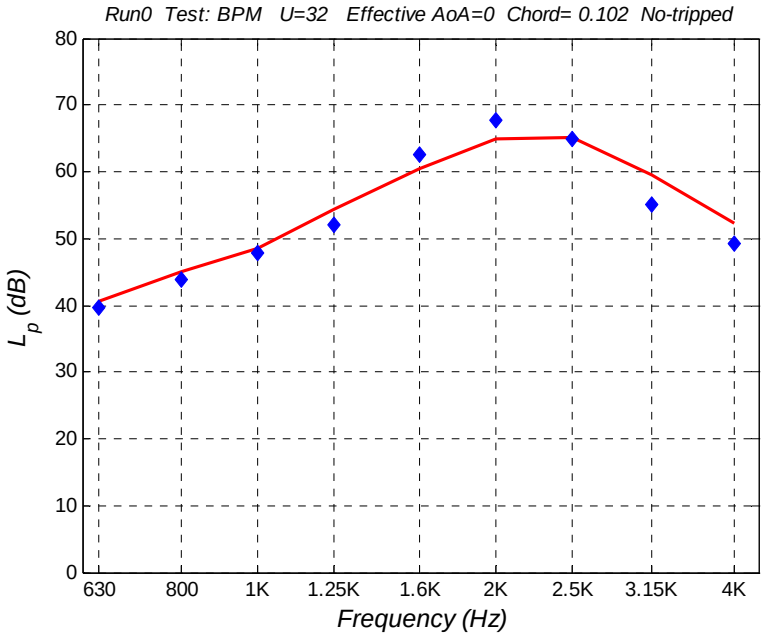

Figure F12: *Example of spectral comparison of experimental results and prediction using Model I-e and the CTNN approach.*

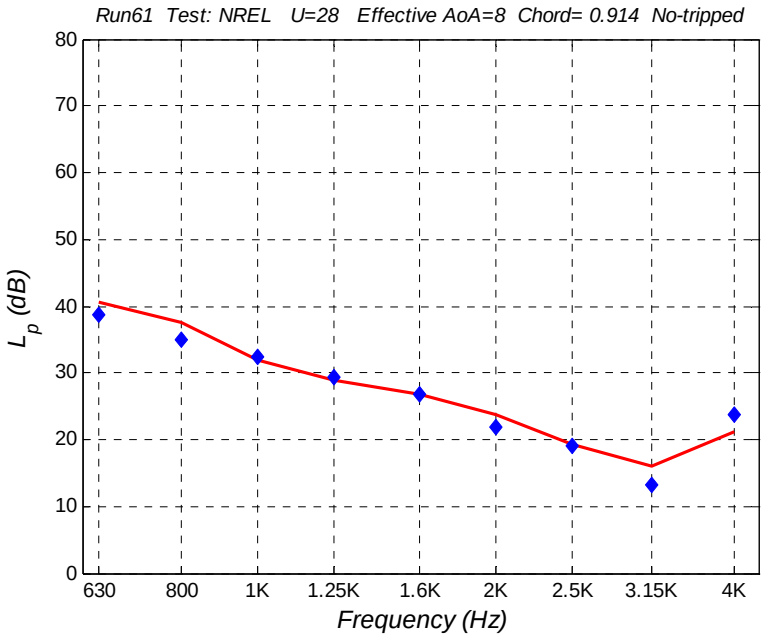

Figure F13: *Example of spectral comparison of experimental results and prediction using Model I-e and the CTNN approach.*

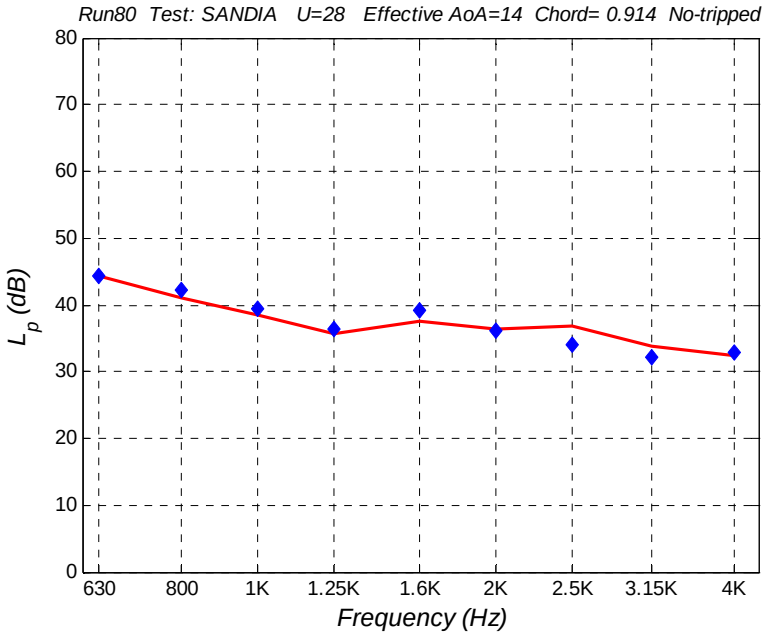

Figure F14: *Example of spectral comparison of experimental results and prediction using Model I-e and the CTNN approach.*

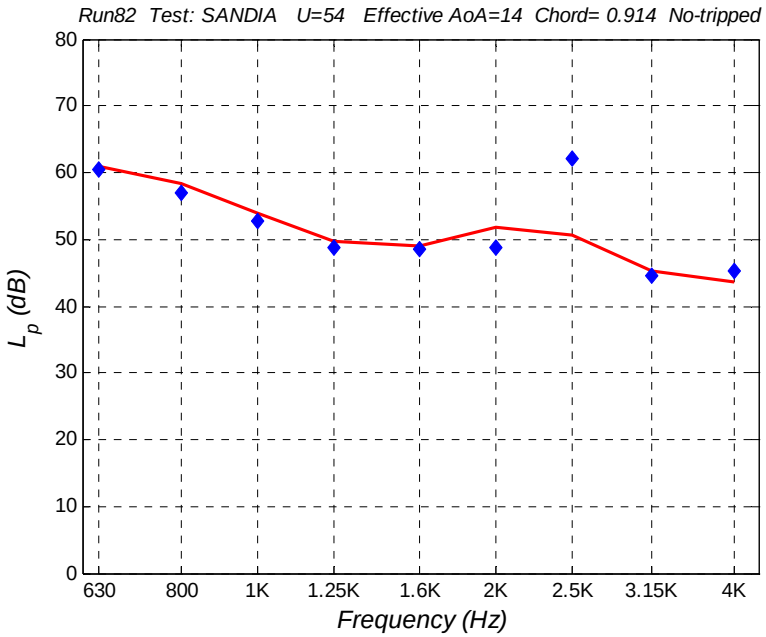

Figure F15: *Example of spectral comparison of experimental results and prediction using Model I-e and the CTNN approach.*

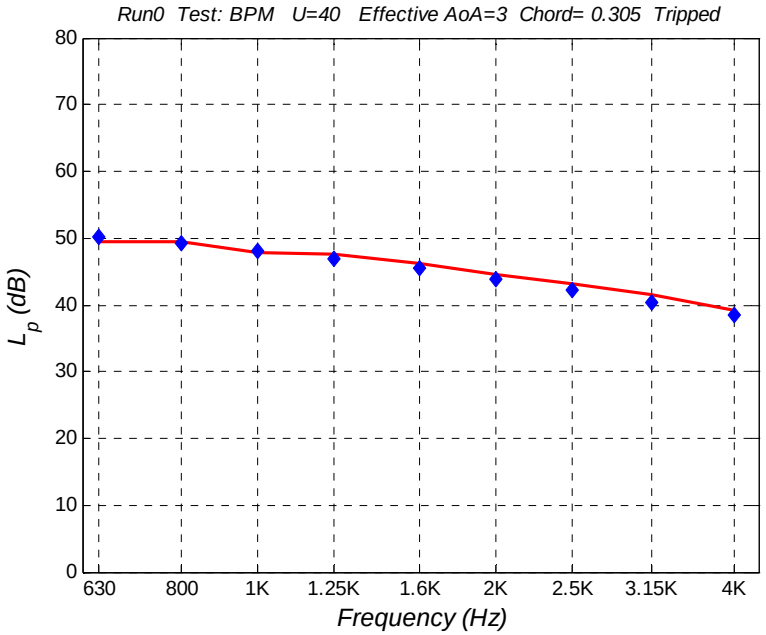

Figure F16: *Example of spectral comparison of experimental results and prediction using Model I-e and the CTNN approach.*

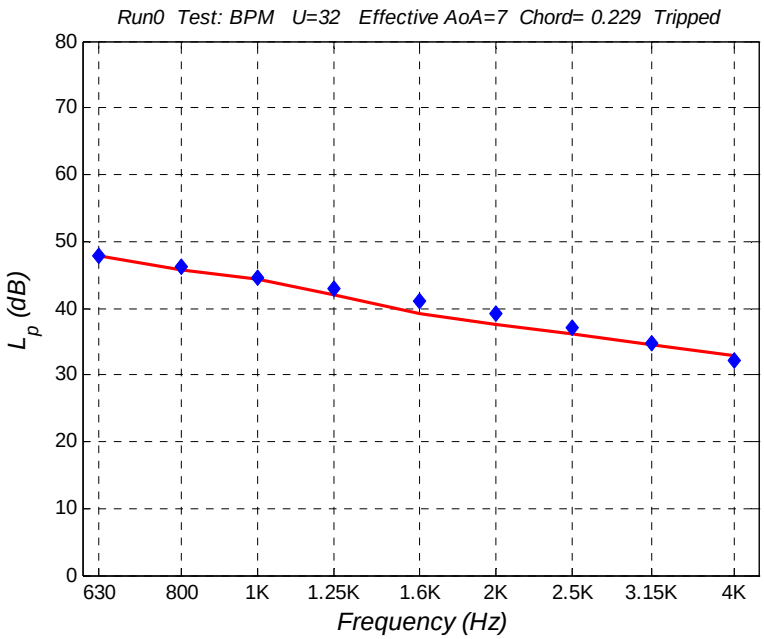

Figure F17: *Example of spectral comparison of experimental results and prediction using Model I-e and the CTNN approach.*

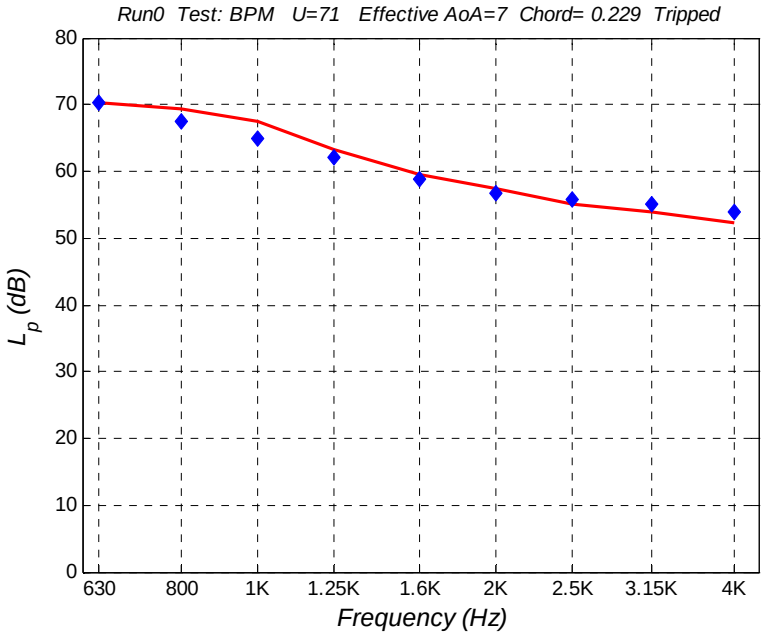

Figure F18: *Example of spectral comparison of experimental results and prediction using Model I-e and the CTNN approach.*

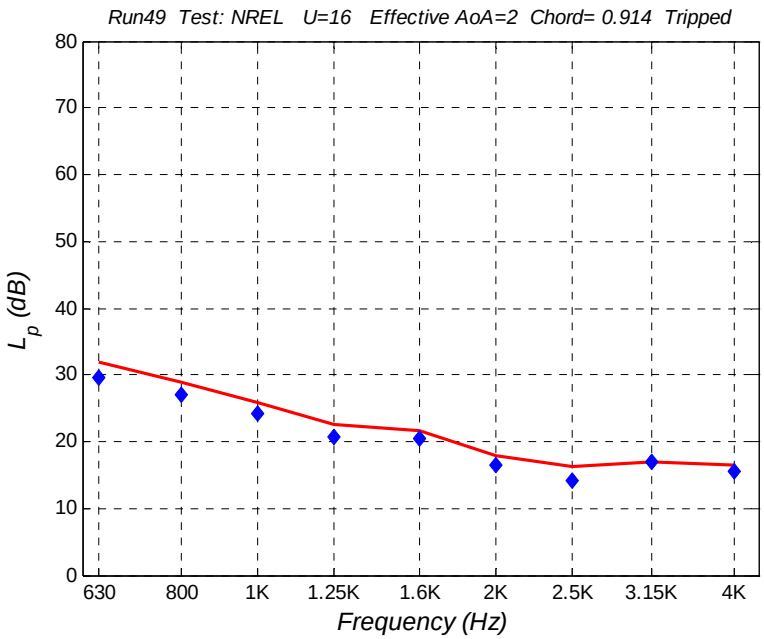

Figure F19: *Example of spectral comparison of experimental results and prediction using Model I-e and the CTNN approach.*

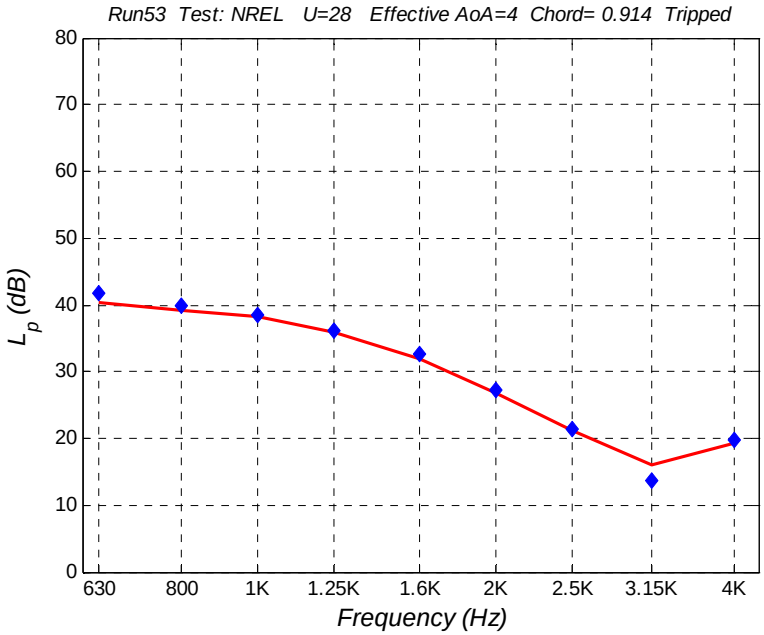

Figure F20: *Example of spectral comparison of experimental results and prediction using Model I-e and the CTNN approach.*

F.3 Model II-*h* using the ATANA approach

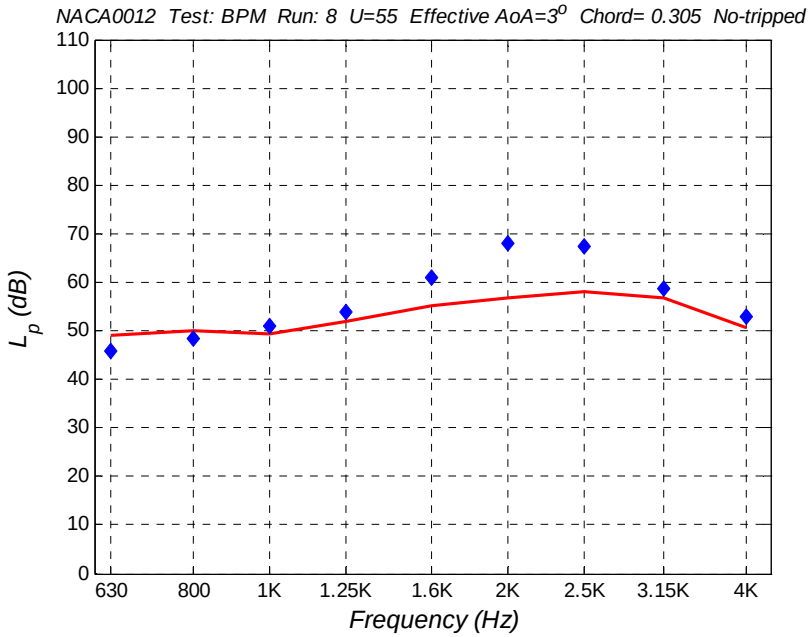

Figure F21: *Example of spectral comparison of experimental results and prediction using Model II-h and the ATANA approach.*

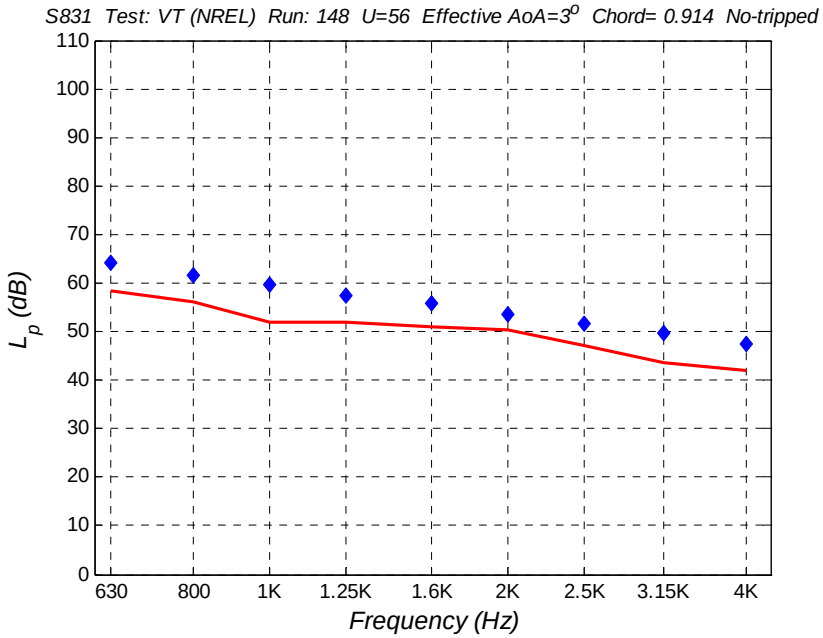

Figure F22: *Example of spectral comparison of experimental results and prediction using Model II-h and the ATANA approach.*

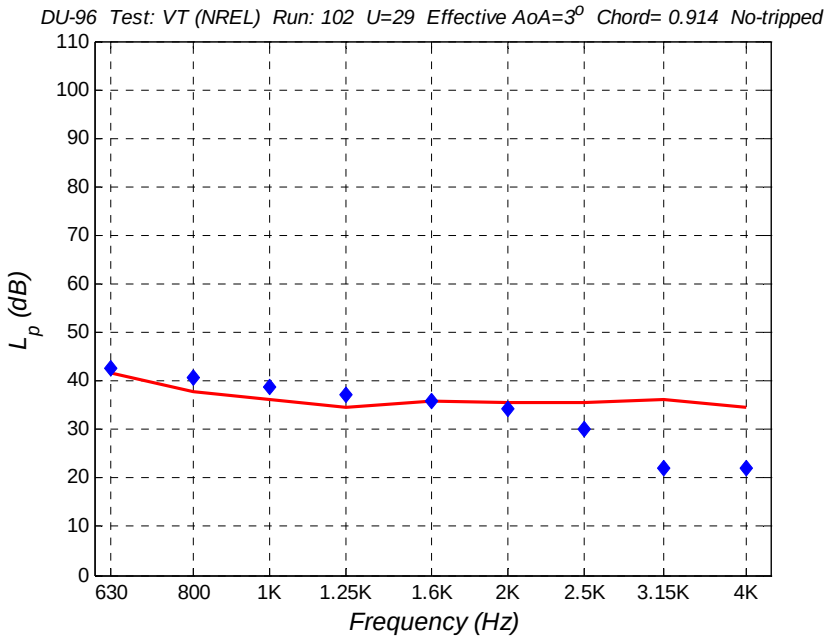

Figure F23: *Example of spectral comparison of experimental results and prediction using Model II-h and the ATANA approach.*

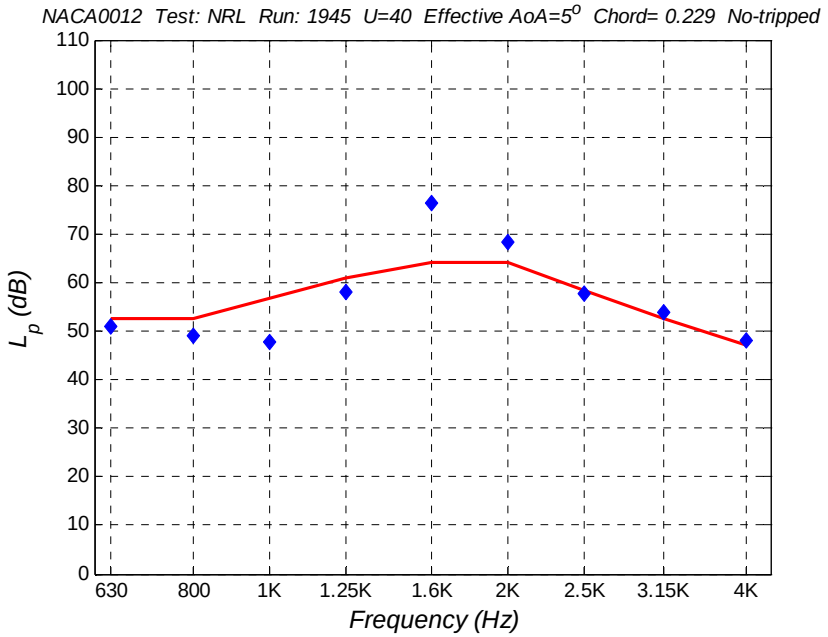

Figure F24: *Example of spectral comparison of experimental results and prediction using Model II-h and the ATANA approach.*

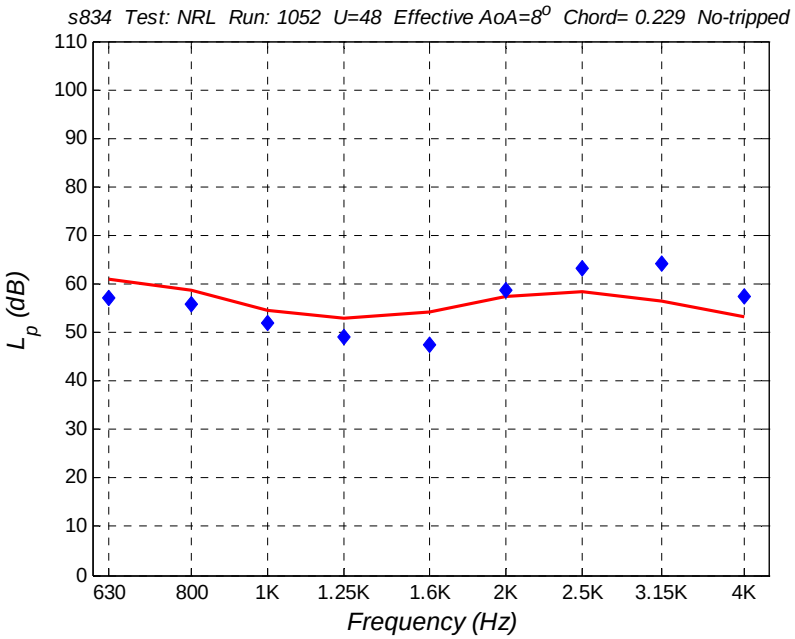

Figure F25: *Example of spectral comparison of experimental results and prediction using Model II-h and the ATANA approach.*

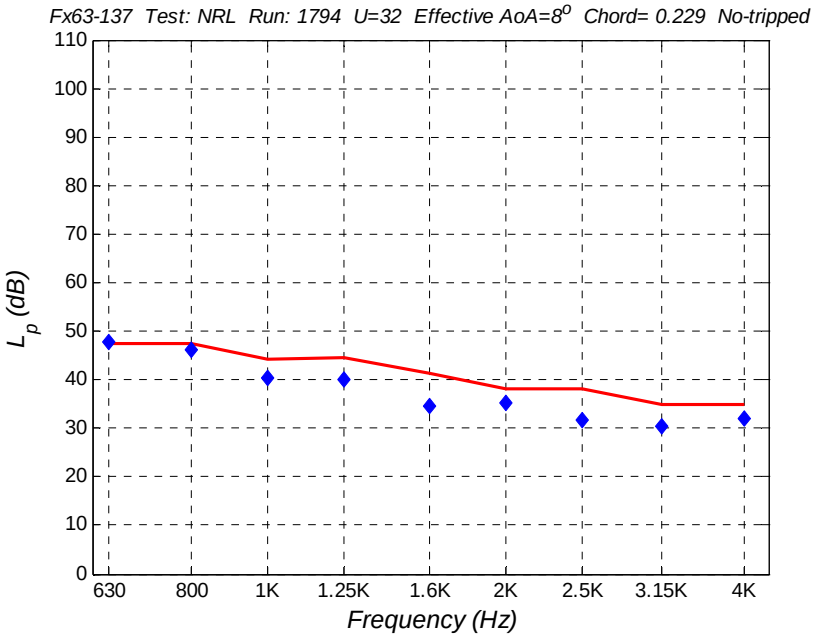

Figure F26: *Example of spectral comparison of experimental results and prediction using Model II-h and the ATANA approach.*

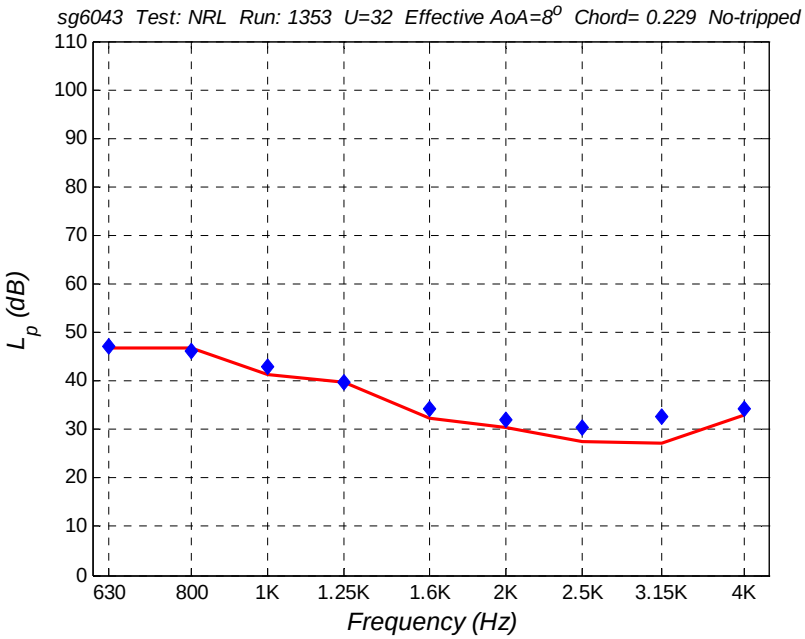

Figure F27: *Example of spectral comparison of experimental results and prediction using Model II-h and the ATANA approach.*

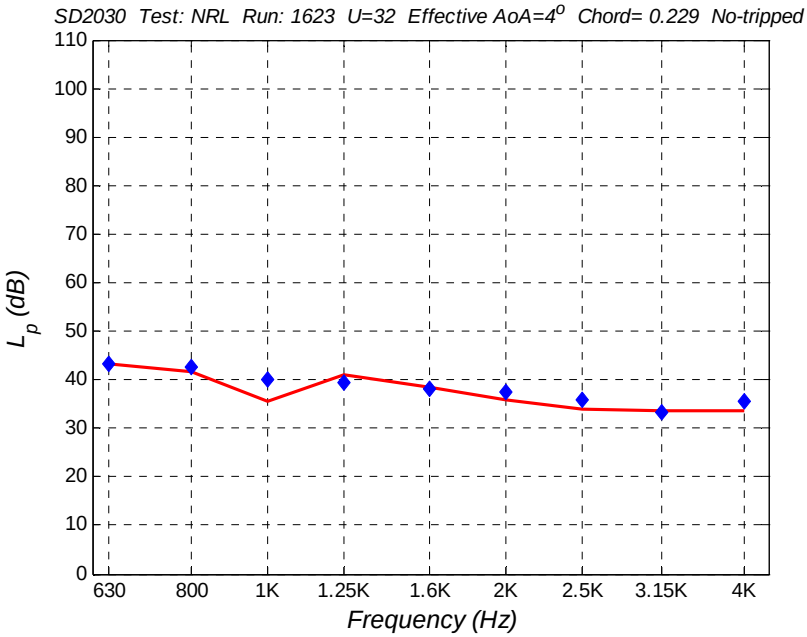

Figure F28: *Example of spectral comparison of experimental results and prediction using Model II-h and the ATANA approach.*

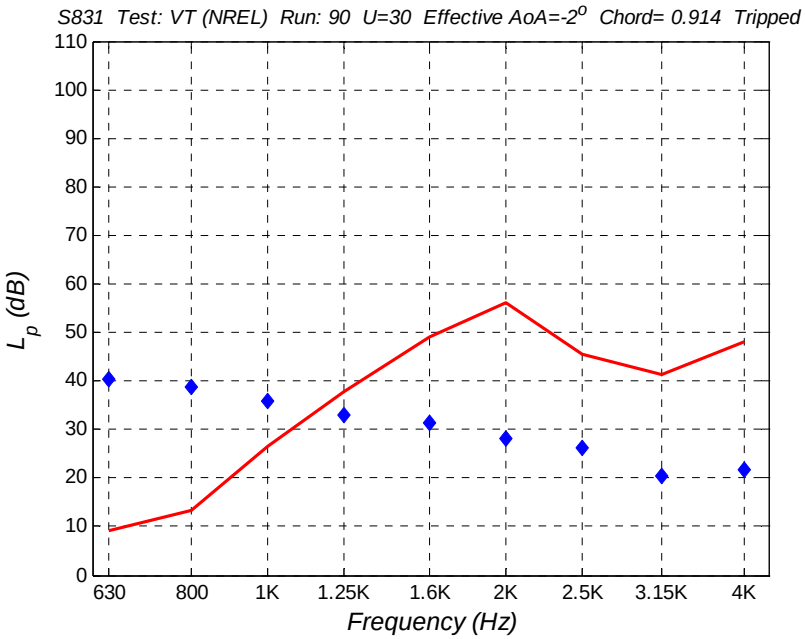

Figure F29: *Example of spectral comparison of experimental results and prediction using Model II-h and the ATANA approach.*

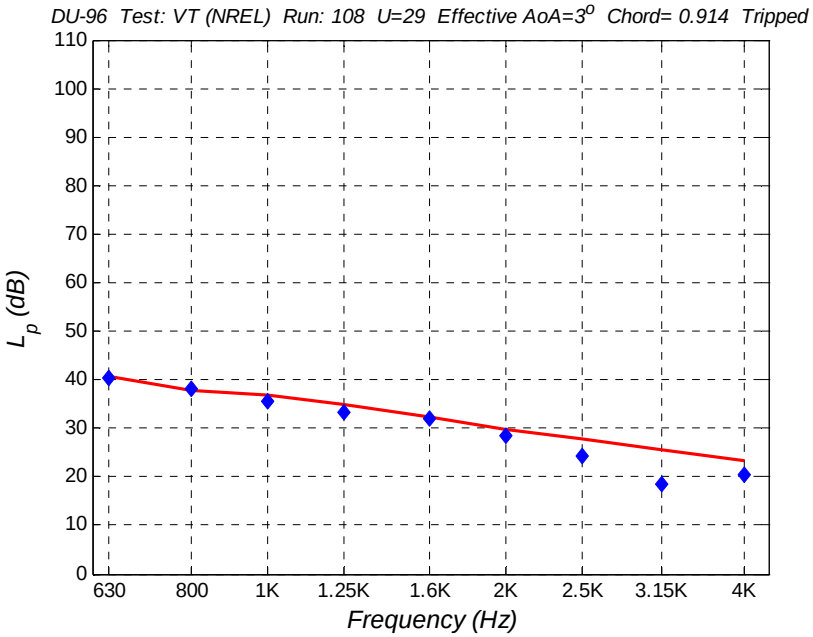

Figure F30: *Example of spectral comparison of experimental results and prediction using Model II-h and the ATANA approach.*

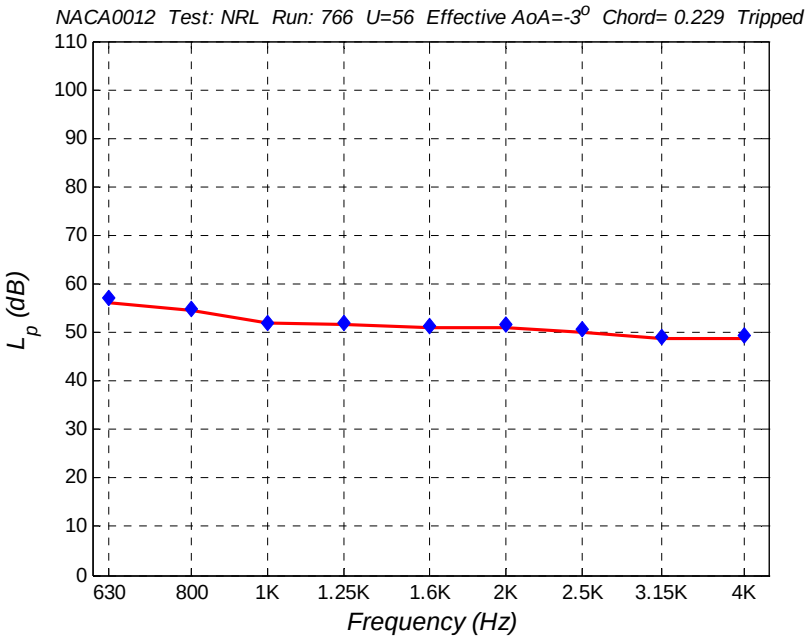

Figure F31: *Example of spectral comparison of experimental results and prediction using Model II-h and the ATANA approach.*

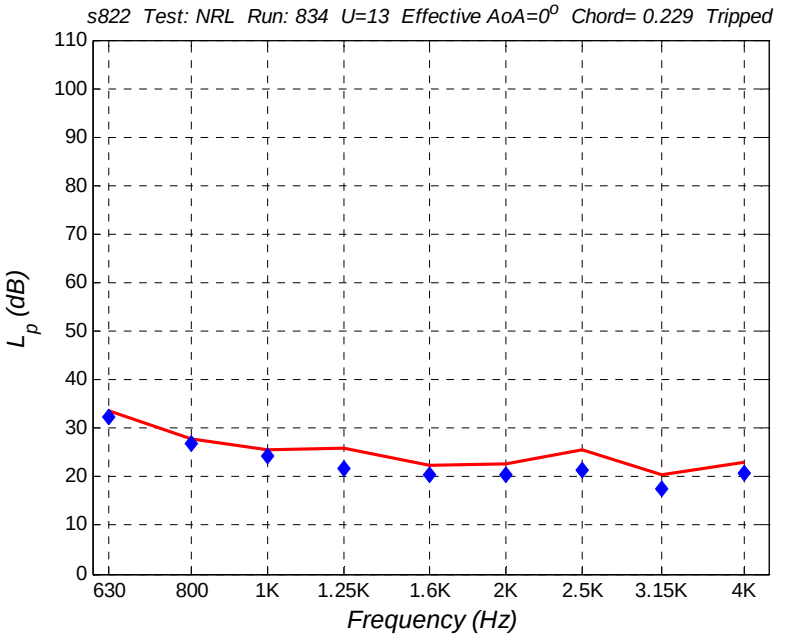

Figure F32: *Example of spectral comparison of experimental results and prediction using Model II-h and the ATANA approach.*

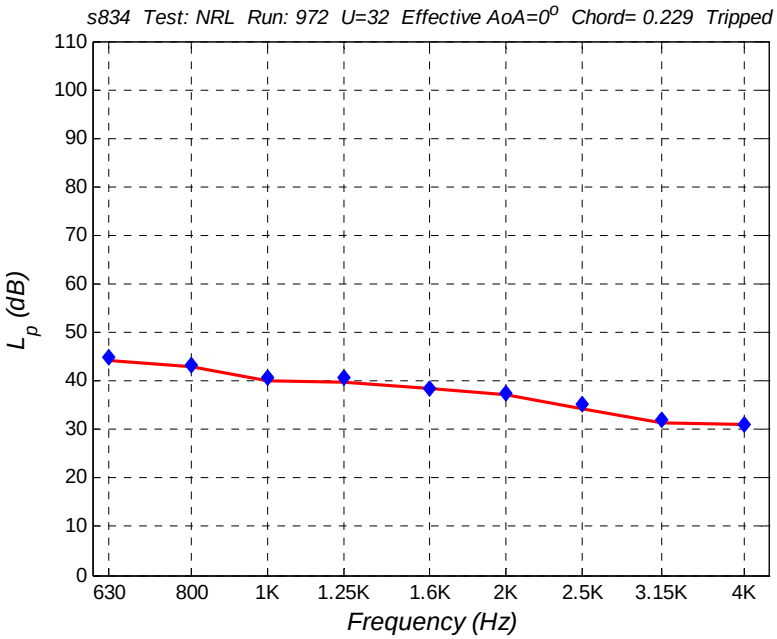

Figure F33: *Example of spectral comparison of experimental results and prediction using Model II-h and the ATANA approach.*

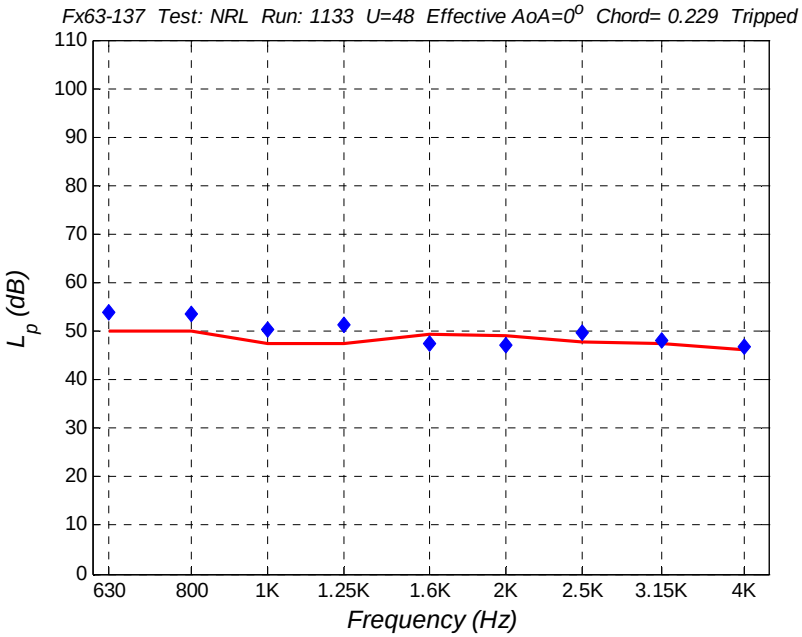

Figure F34: *Example of spectral comparison of experimental results and prediction using Model II-h and the ATANA approach.*

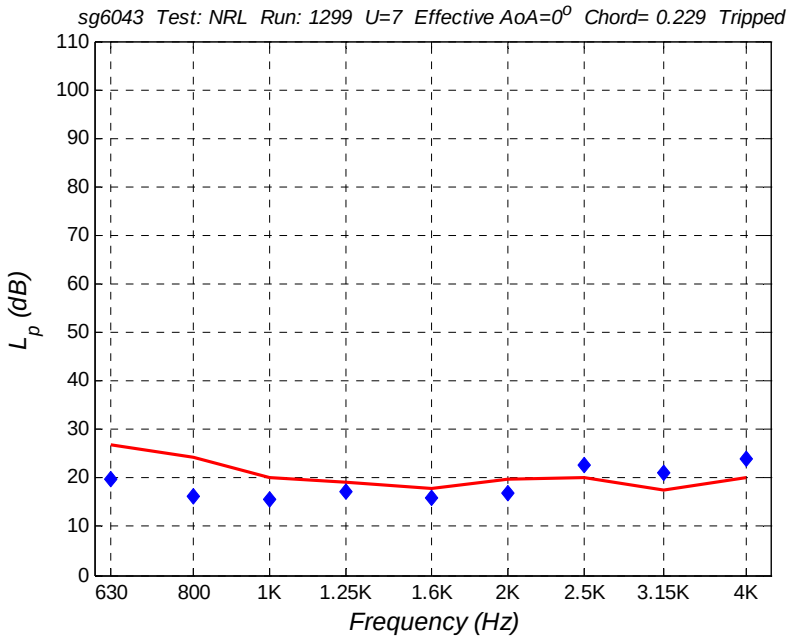

Figure F35: *Example of spectral comparison of experimental results and prediction using Model II-h and the ATANA approach.*

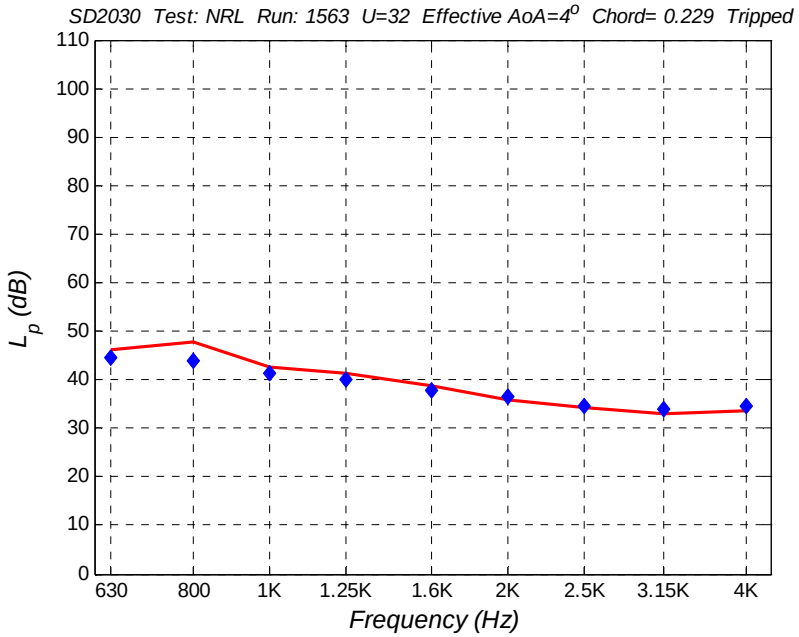

Figure F36: *Example of spectral comparison of experimental results and prediction using Model II-h and the ATANA approach.*

F.4 Model II-*h* using the CTNN approach

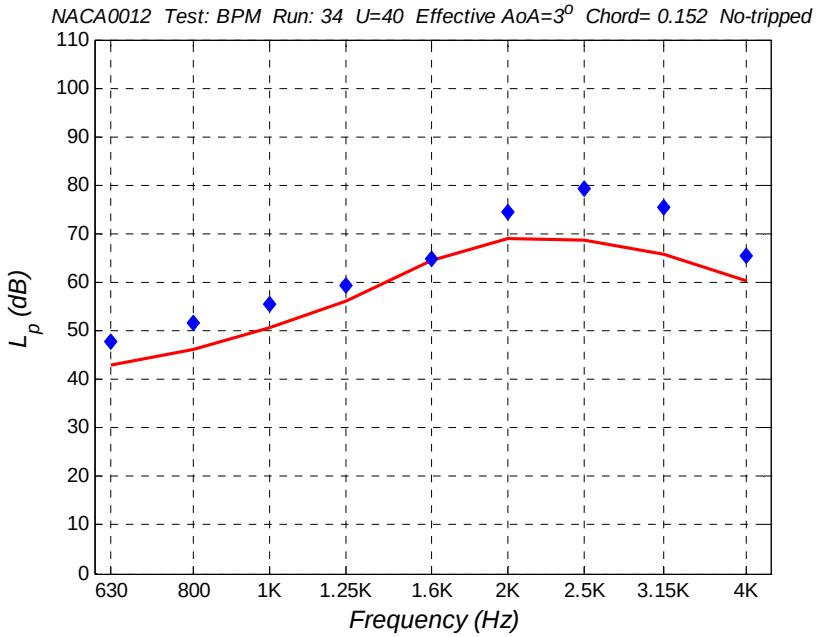

Figure F37: *Example of spectral comparison of experimental results and prediction using Model II-h and the CTNN approach.*

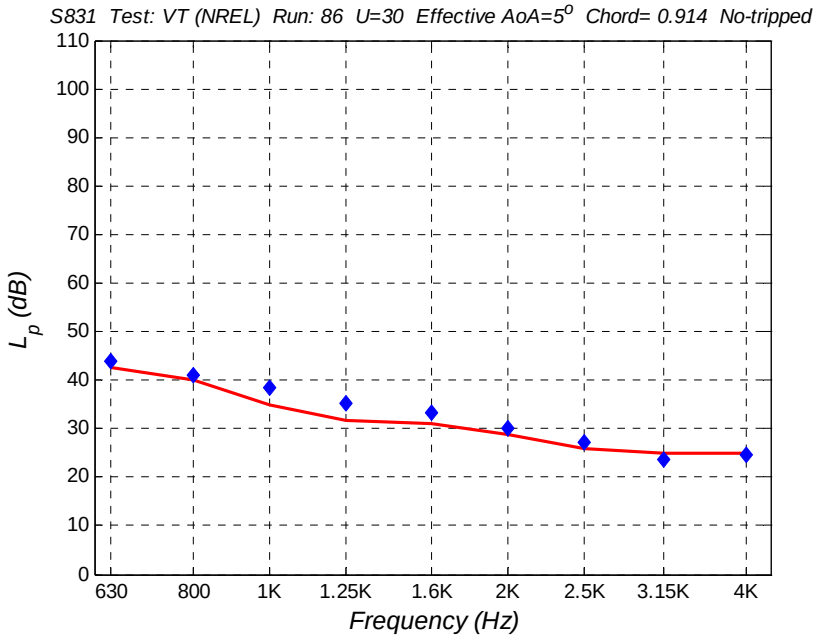

Figure F38: *Example of spectral comparison of experimental results and prediction using Model II-h and the CTNN approach.*

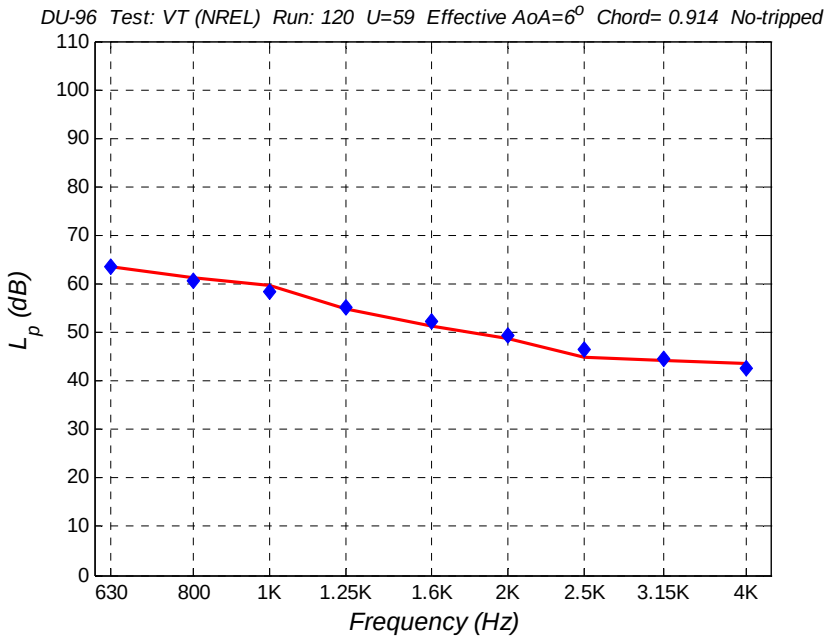

Figure F39: *Example of spectral comparison of experimental results and prediction using Model II-h and the CTNN approach.*

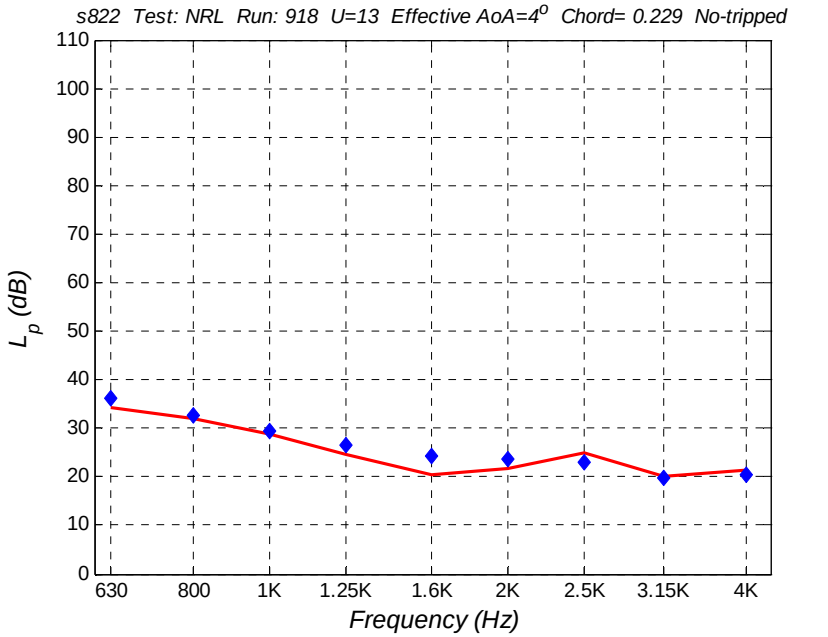

Figure F40: *Example of spectral comparison of experimental results and prediction using Model II-h and the CTNN approach.*

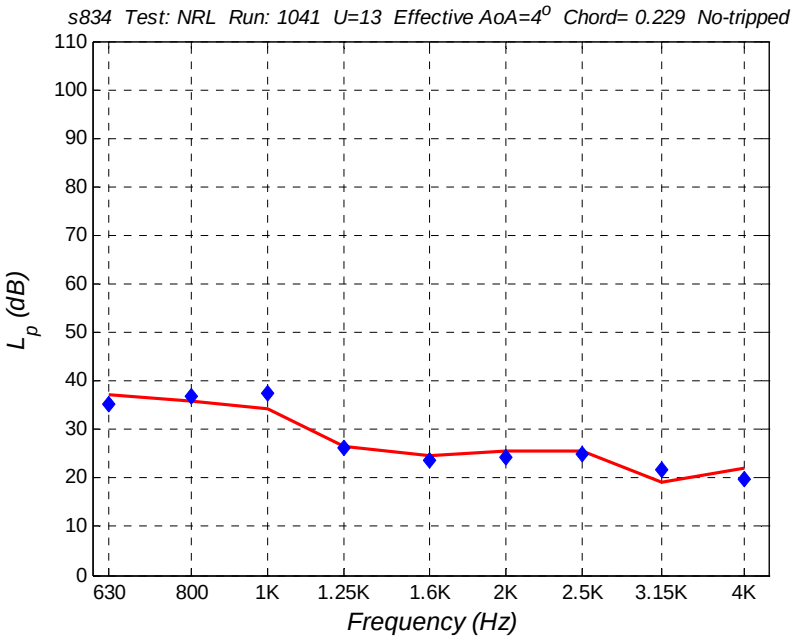

Figure F41: *Example of spectral comparison of experimental results and prediction using Model II-h and the CTNN approach.*

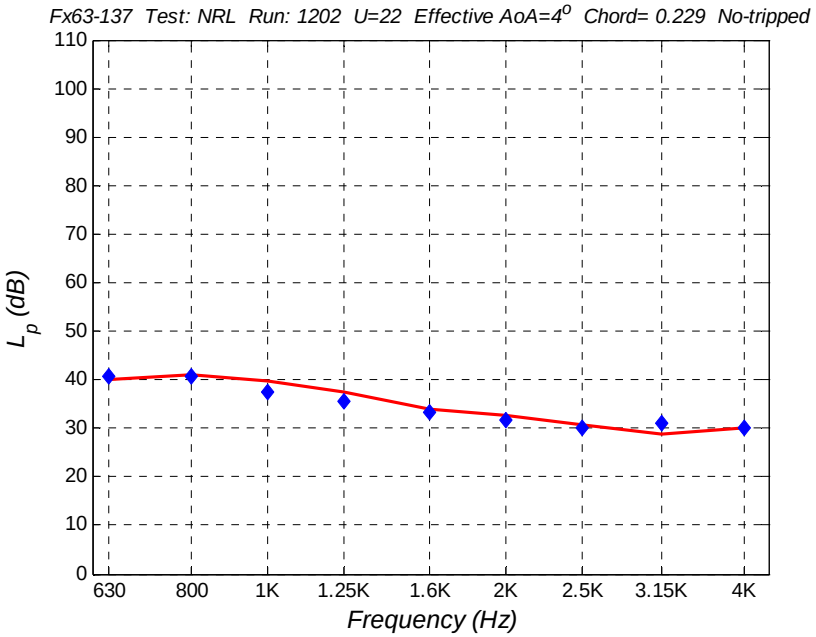

Figure F42: *Example of spectral comparison of experimental results and prediction using Model II-h and the CTNN approach.*

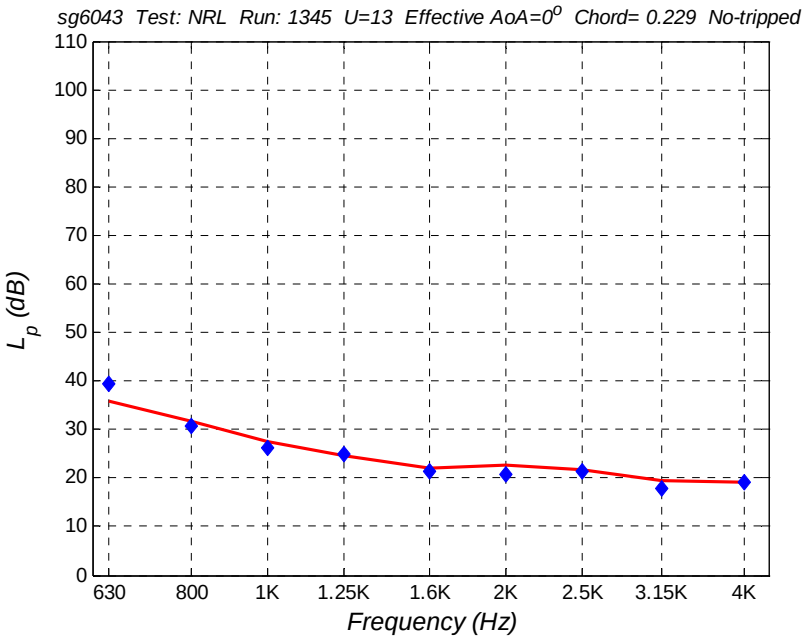

Figure F43: *Example of spectral comparison of experimental results and prediction using Model II-h and the CTNN approach.*

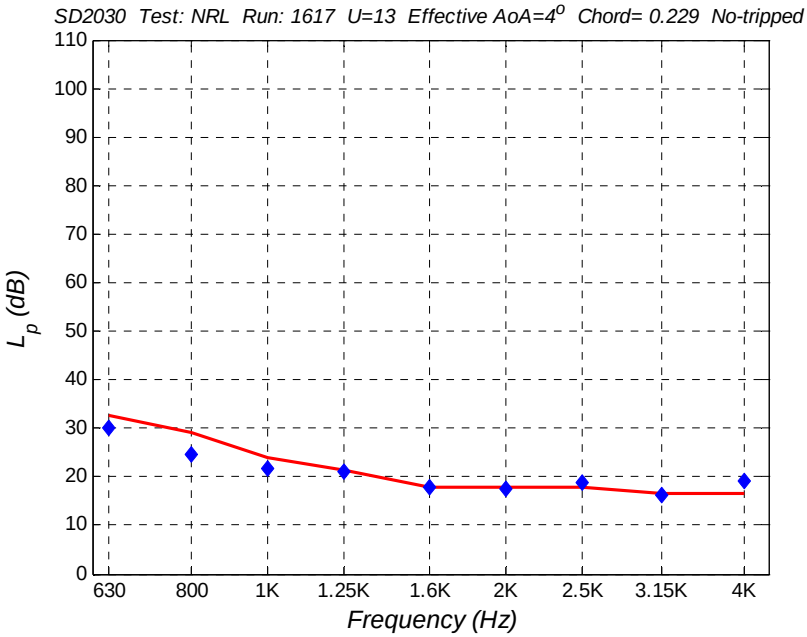

Figure F44: *Example of spectral comparison of experimental results and prediction using Model II-h and the CTNN approach.*

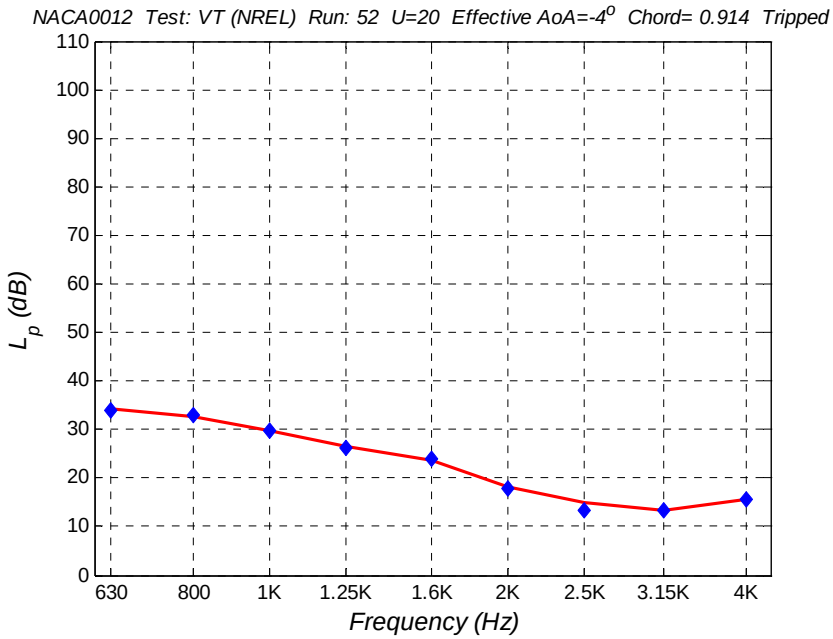

Figure F45: *Example of spectral comparison of experimental results and prediction using Model II-h and the CTNN approach.*

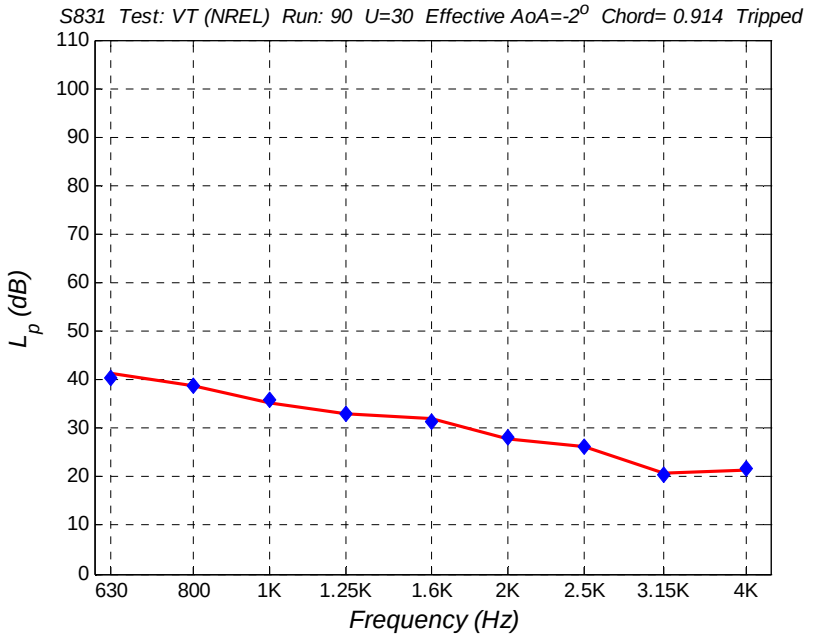

Figure F46: *Example of spectral comparison of experimental results and prediction using Model II-h and the CTNN approach.*

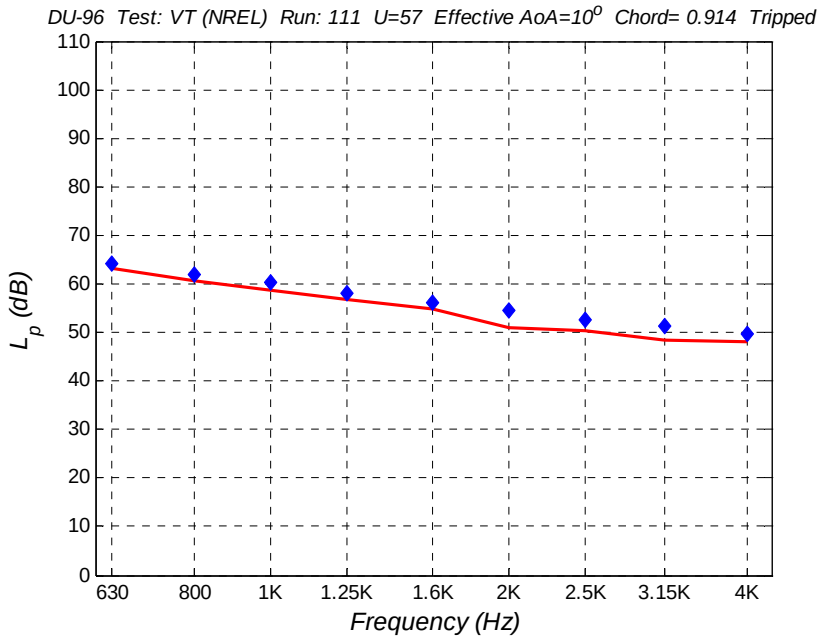

Figure F47: *Example of spectral comparison of experimental results and prediction using Model II-h and the CTNN approach.*

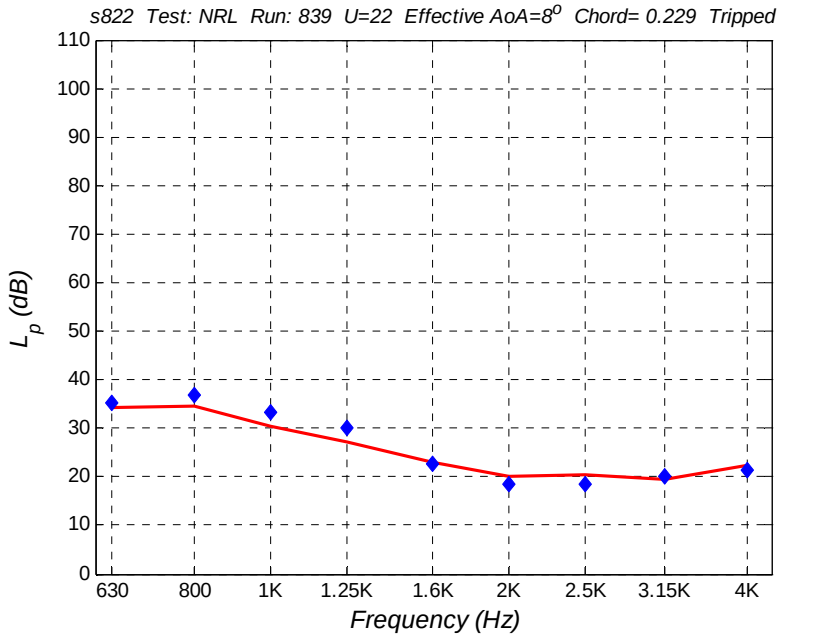

Figure F48: *Example of spectral comparison of experimental results and prediction using Model II-h and the CTNN approach.*

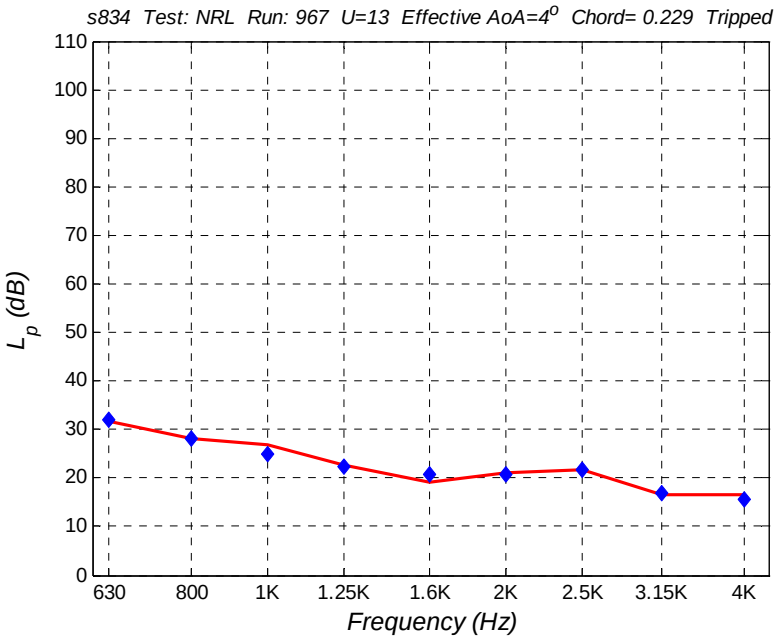

Figure F49: *Example of spectral comparison of experimental results and prediction using Model II-h and the CTNN approach.*

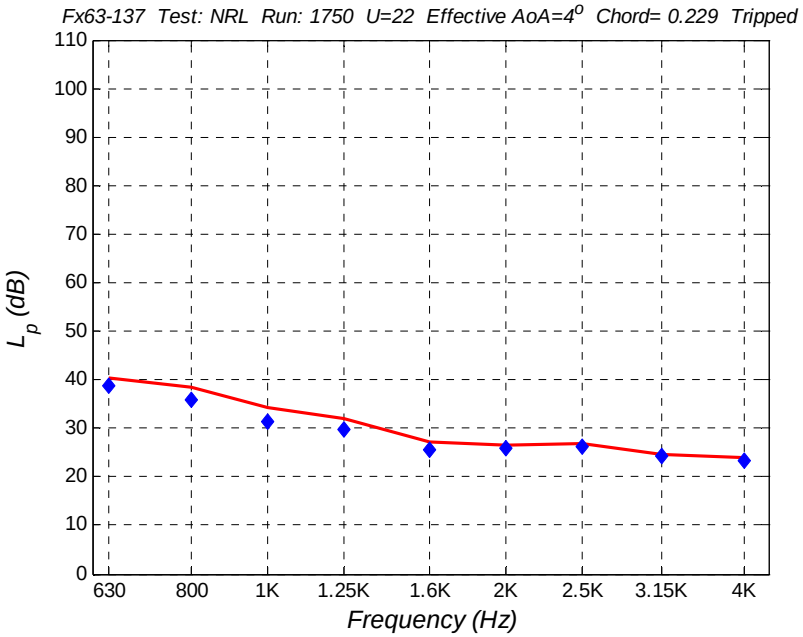

Figure F50: *Example of spectral comparison of experimental results and prediction using Model II-h and the CTNN approach.*

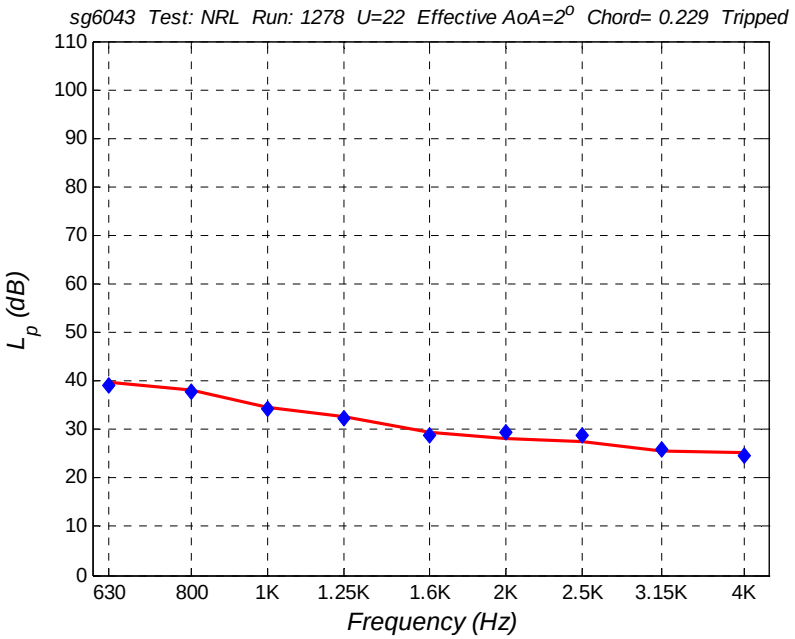

Figure F51: *Example of spectral comparison of experimental results and prediction using Model II-h and the CTNN approach.*

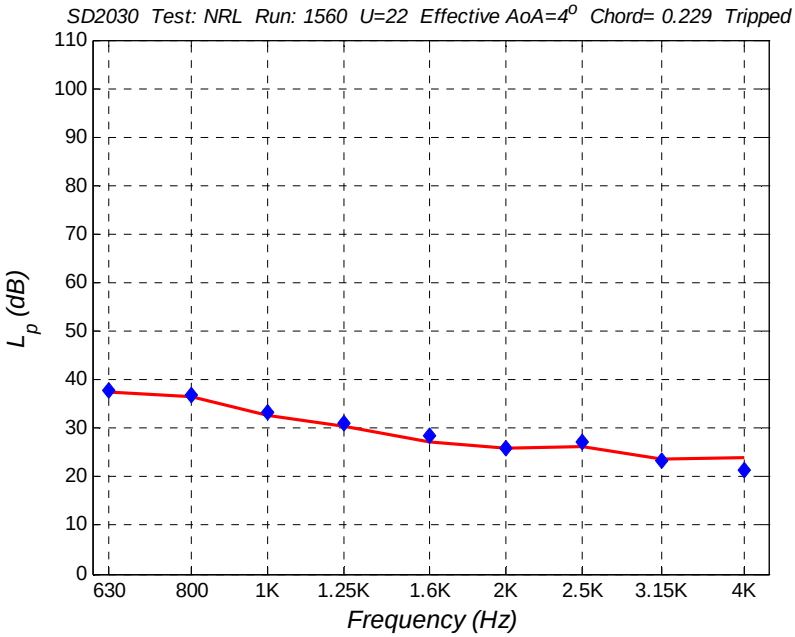

Figure F52: *Example of spectral comparison of experimental results and prediction using Model II-h and the CTNN approach.*